UNIVERSITY OF
LIVERPOOL

Resonant tunnelling nanostructures for THz energy harvesting

PhD student: Ibrahim Nemr Noureddine

Primary supervisor: Prof Steve Hall

Department of Electrical Engineering and Electronics

Submitted in June 2018
in accordance with the requirements for
the award of the degree of Doctor of Philosophy
of the University of Liverpool

Abstract

Photovoltaic (PV) cells are currently the only mature technology for solar energy harvesting. As a quantum device, the efficiency of PV cell is a function of the bandgap, and ultimately fundamentally limited by the match of the bandgap to the solar spectrum. The average efficiency of a solar PV module is between 6 and 15%. Hence 85-94% of the solar radiation is rejected as waste heat at about 333K. An alternative approach to photovoltaics is the rectenna concept, which is a combination of a receiving antenna and a rectifier. The sunlight is collected in the antenna as an alternating current and rectified to direct current (DC). The rectenna concept has been successfully demonstrated for microwave power transmission with high efficiency of ~84%. The capture and conversion of solar energy >200 THz and therefore efficiency of rectennas in the infrared and visible regime, is currently limited by the lack of a diode nanostructure that can work at THz frequencies. High-frequency response of semiconductor diodes, like p-n junctions or Schottky, is limited by charge storage and parasitic capacitance respectively, making them inoperable for rectification at frequencies beyond 5 THz. The practical rectifying mechanism proposed is based on a tunnelling effect of electrons having fast response times of the order of femto-seconds. The device is based on a Metal Insulator Insulator Metal (MIIM) structure, where electrons tunnel from one metal electrode to the other under forward bias, with the aid of a 'stepping stone' offered by a notch between the two dielectric (insulator layers:) resonant tunnelling. In the reverse bias direction, electrons have to tunnel directly through the combined thickness of the two dielectrics making the 'off current' much smaller. The dielectric layers are a few nms thick only and are realised by atomic layer deposition (ALD). The project is aimed at solar energy harvesting but is also of interest in the general area of THz electronics, at lower THz frequencies.

Acknowledgements

I wish to thank all people who have promoted this project.

Especially, I would like to express my gratitude to my primary supervisor, Prof Steve Hall, who has inspired me over five years in the field of microelectronics. I also wish to thank him for his revision, arrangements, discussions, and fruitful guidance.

I am also so grateful to my secondary supervisor Dr Ivona Mitrovic for the practical arrangements and for making my thesis successful. She is a very kind person.

Many thanks are directed to the solid-state electronics group and the antenna group who were answering my questions and to all colleagues who motivated me to cross the finish line. In particular, I would like to thank the following for their help during my lab work: Dr Naser Sedghi (discussions and all lab work), Dr Harm Van Zalinge (AFM), Dr Jidong Jin and Dr Dave Donaghy (photolithography), Prof Yi Huang (antennas), Dr Jenny Hanson (confocal microscope), Dr Jacqueline Wrench from Prof Paul Chalker group (ALD), Dr Robert Treharne from Stephenson institute (sputtering), Dr Chen Li (FF-OCT), Dr Yaochun Shen (rectenna testing and FF-OCT), and Dr Vin Dhanak and Partha Das (XPS). Their assistance made lab experiments full of joy and fun.

I would like to thank Dr Ali Al-Ataby, Dr Saqib Khursheed, Dr Miguel Lopez-Benitez, Dr John Marsland, and Dr Waleed Al-Nuaimy for their assistance during my part-time demonstrating work at the university. This indeed enriched my experience in electronic engineering at an academic level.

I would like to thank National Tsing Hua University for the wonderful ten-month experience in Taiwan, particularly Prof Yen-Chieh Huang who enriched my knowledge in photonics.

I am very pleased with all the staff of the University of Liverpool who have been so cooperative especially Ms. Hannah Fosh.

I am so grateful for the financial support of my parents and for their encouragement and for the studentship provided by University of Liverpool and National Tsing Hua University.

Table of Contents

Abstract i

Acknowledgements ii

Table of Contents iii

List of Figures vii

List of Tables xv

List of abbreviations xvii

1. Introduction 1

1.1 Motivation 1

1.2 Energy harvesting in the electromagnetic spectrum 3

1.3 IR/THz applications 4

1.4 Outline of thesis contents 6

2. Energy harvesting: the challenge at THz 8

2.1 Rectennas towards THz 8

2.2 THz rectification through metal–insulator–(insulator)–metal diodes 10

2.3 State of the art devices 11

2.4 Rectenna array design 12

2.4.1 Efficiency considerations 13

2.4.2 Diode–antenna coupling 14

2.4.3 Circular patch parameters 16

2.4.4 Photolithography and Shadow Mask 17

2.4.5 Microfabrication process flow 19

3. Fabrication and characterisation technologies 24

3.1 Deposition techniques 24

3.1.1 Atomic Layer Deposition 24

3.1.2 Sputtering 26

3.1.3 Thermal Evaporation 28

3.2 Scanning electron microscopy and transmission electron microscopy 29

3.3 Electron-beam lithography 30

3.4 Atomic force microscopy 32

3.5 Spectroscopic ellipsometry 33

3.6 X-ray Photoelectron spectroscopy 36

4. The Physics of quantum mechanical tunnelling 38

4.1 Overview of the concept 38

4.2 The generalised tunnelling current formula 40

4.3 Tsu-Ezaki equation 42

4.4 WKB Approximation 43

4.5 Fowler-Nordheim tunnelling 45

4.6 Direct tunnelling 47

4.7 Transfer-Matrix Method 49

4.8 Trap-assisted mechanisms 51

4.1 The resonant tunnelling mechanism 53

4.2 Summary of conduction mechanisms in MIM/MIIM diodes 55

4.3 The model used for optimizing the structures 57

5. Engineering the rectifying characteristics in tunnelling structures 65

5.1 Verifying homogeneity of the dielectrics using the ellipsometry 66

5.2 Imaging the structure (FF-OCT, AFM, and HR-TEM) and the native oxide issue 71

5.3 XPS analysis of Al_2O_3/Ta_2O_5/Si stacked sample 80

5.4 J-V characterisation of the first MIIM batches 83

5.4.1 The dielectric and the bottom contact 83

5.4.2 Etching the native oxide 88

5.4.3 Optimal structure: choice of metal and dielectric thickness 94

5.4.4 Varying thicknesses of Cr-sandwiched dielectrics 100

5.5 Summary 103

6. Optimizing the structures for THz rectification 104

6.1 Barrier tuning of atomic layer deposited Ta_2O_5 and Al_2O_3 in double dielectric diodes 104

6.1.1 Fabrication 104

6.1.2 Material Selection 105

6.1.3 Results and discussion 107

6.2 Improved rectification in MIIM tunnelling diodes via dielectric defects 113

6.2.1 Fabrication 114

6.2.2 Results and discussion 116

6.3 The role of oxygen vacancies 126

6.3.1 Fabrication 127

6.3.2 Results and discussion 128

6.4 Effect of area scaling 139

6.5 Summary 141

7. Towards integrating the nanostructures in THz rectennas 142

7.1 Fabricating the 0.14 THz rectennas 142

7.2 Devising the 2 THz rectenna array 143

7.2.1 Material choice 144

7.2.2 Process flow 145

7.2.3 Modelling the rectifying performance 148

8. Conclusions and suggestions for further work 153

References 156

List of Figures

Figure 1.1 The electromagnetic spectrum indicating the different frequency regimes: radio frequency (RF), microwaves (MW), far, mid and near infrared (IR), visible (VIS), and ultraviolet (UV). Terahertz (THz) regime covers parts of MW and far-IR regimes. Infrared: 700nm–1mm/430THz–300GHz, Microwave: 1mm-1m/300GHz–300MHz. 3

Figure 1.2 The spectral power density of sunlight.[6] The different spectra refer to the extra-terrestrial AM0 radiation at upper atmosphere and the AM1.5 radiation at sea level. The inset shows the solar spectrum absorption with different solar cell materials.[7] 4

Figure 2.1 A terahertz solar rectenna structure proposed for the project for each device (left) and for an array used for a practical system.[1] 9

Figure 2.2 Single (MIM) and double (MIIM) dielectric diode structures: bottom metal (green), dielectrics (yellow and red), and top metal (blue)... 10

Figure 2.3 The equivalent circuit of the THz rectenna element coupling the antenna with the rectifier. 14

Figure 2.4 a_{diode} is the side length of the square diode active area. a) The coupling efficiency for a 0.14 THz rectenna for a matching antenna-diode impedence of 300-300Ω, and when the diode impedances larger by an order of magnitude (3000Ω). b) The coupling efficiency of 0.14 THz (solid) as compared with 2 THz rectenna assuming a perfect matching of the diode-antenna impedance. 15

Figure 2.5 CST simulations for a 1×2 rectenna showing high directivity and high return loss response (s11) at 0.14 THz for copper patches. 17

Figure 2.6 a) The photolithography approach process flow: 1) spin-on the resist, 2) UV exposure through a mask, 3) development, 4) metal deposition, and 5) lifting-off to leave the patterned metal (yellow). b) The final structure of the device using the designed shadow mask. The active device is magnified and shown in the upper right inset. The shadow mask is shown on the upper left inset where evaporated metal (indicated by blue arrows) gets patterned through it and sticks to the substrate fixed under it with a magnet sheet. 18

Figure 2.7 The 4 photomasks used to fabricate the rectennas (1×2 here). The radius of each circle is 255 µm as designed for the patch antennas in Table 2.3. The linewidth of the attached extension used for the diode electrodes varies gradually until it settles at 2 µm. 19

Figure 2.8 The process flow for patterning the bottom metal. 20

Figure 2.9 The process flow for patterning the dielectric stack. 21

Figure 2.10 Part of the fabricated rectenna array: a) Bottom metal (green) patterned using Photomask1; b) Dielectric (transparent pink) patterned over the bottom metal using Photomask2; c) Top metal (blue) patterned using Photomask3; and d) the antenna patches (red) using Photomask4. 22

Figure 2.11 a) The actual size of the 1×2 and 1×6 rectenna arrays of diode junction area: 2×2, 4×4, 6×6, 8×8, 10×10, and 12×12 μm^2; b) The actual size of MIM/MIIM diodes with junction area: 20×20, 50×50, 100×100, 150×150, 200×200, and 250×250 μm^2; c) A 3D drawing of the plasmonic diode set in Kretschmann coupling system. 23

Figure 3.1 Schematic diagram of ALD reactor. Film growth requires precursors and reactant gases (H2O and NH3) in addition to either O3 supply or plasma source. 25

Figure 3.2 Typical ALD process illustrated in 4 steps. 25

Figure 3.3 Schematic of RF sputtering system: Argon is ionized and accelerates towards the target (cathode) with high energy which releases atoms from the target surface and are forced to move towards the grounded anode by the strong electric field created by V_{RF}. 27

Figure 3.4 Schematic diagrams of the light microscope, the TEM, and the SEM[73] 29

Figure 3.5 The history and projection of the resolution trends in lithography.[76] 31

Figure 3.6 Illustration of linear, circular, and elliptical polarised light and of beam path in ellipsometry.[80] 35

Figure 4.1 Quantum tunnelling through a barrier (or more) results in the same energy of the tunnelled electrons but with smaller amplitude. (a) Tunnelling could be direct or Fowler-Nordheim (FN). (b) When two or more dielectrics are used, a quantum well (yellow) can be formed for resonance to occur. 39

Figure 4.2 Energy band diagram showing the conduction band and the parameters used to calculate Fowler-Nordheim tunnelling current. 45

Figure 4.3 Energy band diagram showing the conduction band and the parameters used to calculate direct tunnelling current. 47

Figure 4.4 The energy barrier of a single-layer dielectric. The potential energy Ux is the conduction band energy. 50

Figure 4.5 Energy band diagram illustrating the Schottky (SE), Poole-Frenkel (PFE), and trap assisted tunnelling (TAT) mechanisms in MIM diodes. The same principle applies for the mechanisms in multi-insulator diodes. 53

Figure 4.6 Two dielectrics of dissimilar thicknesses and permittivities in an MIIM structure. The surface charge density is $\sigma 1$ at I1/M1 interface and $\sigma 2$ at I2/M2 interface. (a) The electric displacement $D1$ and $D2$ at any region in I1 and I2 dielectrics respectively. (b) The electric fields across the dielectrics: $E1$ across I1 and $E2$ across I2. 54

Figure 4.7 Simulated energy band diagrams of the Al/Ta_2O_5-4nm/Al_2O_3-1nm/Al structure (Batch 1) for opposite injection of electrons. Given that the left electrode is grounded, the voltage is applied to the right electrode as shown in (a) and set at (from left to right) +1.5, 0, and -1.5V. The tunnelling direction of electrons is represented by the red dashed arrow. The materials, the low and high barrier heights, and the potential well are illustrated in (b). 55

Figure 4.8 J-V characteristic modelling for double dielectric diodes with different structures and Ta_2O_5 thicknesses (2 and 4 nm) keeping Al_2O_3 thickness at 1 nm. The voltage step size is 10 mV. 58

Figure 4.9 The J-V characteristics a1-a5, b1-b5, c4, and d4 (M1/I1/I2/M2) structures varying the thickness of Ta_2O_5 (1, 2, 3, 4, and 5 nm) considering 1 nm Al_2O_3 (a) and 0.5 nm Al_2O_3 (b, c) simulated using the model. The former structures is modelled based on WKB approximation (c).[26] The voltage step size is 100 mV. 59

Figure 4.10 The x-directed transmission probability of different MIIM (b1, b4, c4) and MIM (d4) structures (Table 4.1). 61

Figure 4.11 Conduction band diagrams of M1/I1/I2/M2 structures (M1 is the right electrode): a4, b4, c4, d4 at -2 V (a, b, c, d) and +2V (e, f, g, h). 62

Figure 4.12 The rectifying characteristics of the modelled structures (a1-a5, b1-b5, c4, d4): the J-V characteristics (a), the asymmetry (b), the non-linearity (c), and the dynamic resistance (d). 63

Figure 5.1 Fitting psi (Ψ) and delta (Δ) using Tauc-Lorentz or Cody-Lorentz oscillators (using *CompleteEase*) to a reference Si model with a minimum mean squared error (MSE) and consistency at 3 Brewster angles (65, 70, and 75°) ensures correct extraction of the oxide parameters. 67

Figure 5.2 Refractive index (n) and extinction coefficient (k) versus the photon energy (*E*) for the 27nm sputtered Ta_2O_5, 10.1 nm sputtered Al_2O_3, and 2.2 nm native SiO_2. All oxides were grown on separate Si substrates. 67

Figure 5.3 $(\alpha h\upsilon)^2$ as a function of the photon energy (E = h.υ) in eV. The full scale is shown in (a) to show the linear fit for Ta_2O_5 whereas (b) is a zoom-in to show the plots of other samples. 68

Figure 5.4 Mapping profile of the native SiO_2 grown on 525µm thick Meiningen Si substrate modelled using *CompleteEase* and measured using the ellipsometer at 65°: a) native SiO_2 thickness (with an average MSE 1.5 and average thickness of 21.73 Å), b) surface roughness in Å, c) MSE. Measurements were done at the black dots. 70

Figure 5.5 Mapping profile of the 47 nm ALD deposited Al_2O_3 grown over Si substrates (using *CompleteEase*) showing the oxide thickness profile at 65 (a), 70 (b), and 75° (c), the optical surface roughness profile (d) (the same at all angles), and the MSE at 65 (e), 70 (f), and 75° (g). 71

Figure 5.6 AFM images scanned on two different regions of 47 nm thick ALD deposited Al_2O_3 on silicon substrates: a) RMS roughness 0.85 nm, average roughness 0.58 nm b) RMS roughness 0.84 nm, average roughness 0.57 nm. 72

Figure 5.7 FF-OCT image of device B1-4 (a) and confocal microscope images of device B3-2 (b and c). 73

Figure 5.8 AFM images created using WSxM[121] showing the textured surface of the 60nm-Al top electrode of B1-4 junction (a), 60nm-Al of B1-4 top electrode (b), 30nm-Al of B1-4 bottom electrode (c), sandwiched oxides of B1-4 (d), and a corner of B1-4 (e) and B3-2 (f) junctions. 76

Figure 5.9 SEM and HR-TEM images of device c1. 78

Figure 5.10 SEM and HR-TEM images of device c3. 79

Figure 5.11 XPS core level spectra plots: Al 2p deconvoluted (a), Ta 4f deconvoluted (b), Si 2p deconvoluted (c). 81

Figure 5.12 The J-V characteristics (a), the asymmetry plots (b), the non-linearity plots (c) and the dynamic resistance plots (d) of several MIIM devices (dashed) and 4nm (solid) Ta_2O_5/Nb_2O_5 from batches 1 (black), 2 (red), and 3 (blue). 85

Figure 5.13 Linear fits of Fowler-Nordheim plots for B1-4 and B2-4. A good fit was observed in the high field at positive bias which does not necessarily indicate Fowler-Nordheim tunnelling in this region. 86

Figure 5.14 The experimental J-V characteristics as compared to the in-house model and the closed form expressions of direct and Fowler-Nordheim tunnelling for the structures B1-4 (a) and B2-4 (b). 88

Figure 5.15 AFM image of sample B4-2 processed using WSxM. 89

Figure 5.16 J-V characteristics for the same device B5-3 before and after annealing, in the dark and under illumination. The dashed orange curve represents the direct tunnelling closed form expression considering a 6.4 nm thick Ta_2O_5 dielectric and a 0.5 eV low barrier height between the Al and the Ta_2O_5. 90

Figure 5.17 Simulated J-V curves for Al/Al_2O_3/Ta_2O_5/Al. The low barrier height was considered to be 0.45 eV (Work Function of Al: 4.2 eV, Electron affinities of Ta_2O_5 and Al_2O_3: 3.75 and 1.35 eV respectively). 91

Figure 5.18 The J-V characteristics (a), the asymmetry plots (b), and the non-linearity plots (c) of selected B4 and B5 devices having 3 (black), 4 (blue), and 5 nm (red) low barrier oxide from batches 1 (red), 2 (blue), and 3 (green). 92

Figure 5.19 Simulated conduction band energy band diagrams of 50nm-Al/1nm-Al_2O_3/4nm-Ta_2O_5/50nm-Al structure. The voltage above each diagram represents the voltage applied at the same polarity as that of the J-V curves. 93

Figure 5.20 Fowler-Nordheim plot for the annealed devices of batch 5 showing a good fit at high electric field at both polarities. 94

Figure 5.21 The energy band diagrams of the 4 batches at 0.5 V voltage increment from -1.5 to 1.5 V. The diagrams are shown in this way to further illustrate the structure effect on the potential well for enhancing resonant tunnelling. 96

Figure 5.22 The rectifying characteristics versus the applied dc voltage for the 4 batches with Ta_2O_5 thickness of 3 (dashed) and 4 nm (solid). 97

Figure 5.23 Fowler-Nordheim plots for 7 devices of the four batches using Ta_2O_5 of dielectric stack total thickness (a and b), and individual layer voltage distribution across Ta_2O_5 (c and d) and A_2O_3 (e and f). 99

Figure 5.24 Temperature dependence of the J-V characteristics for the device B9-4 at 300, 325, 350, and 375 K. 99

Figure 5.25 The dynamic resistance (a), the non-linearity (b), the asymmetry (c), and the current voltage curves for different dielectric thicknesses. 101

Figure 5.26 Energy band diagrams for different structures showing the conduction band and the electron injection. 102

Figure 5.27 J-V characteristics at different temperatures 300, 325, 350, and 375K for the devices. 102

Figure 6.1 Energy band diagrams (conduction band) of four structures at −1 (a) and +1 V (b). Direction of electron injection is indicated by red arrows. Top electrode is always referred to zero. One tick on the x-axis corresponds to 1 nm. 106

Figure 6.2 AFM images scanned at 1×1 μm^2 regions of the as-deposited bottom layers Cr, Au, and Al revealing an RMS average surface roughness of 0.42, 0.44, and 2.8 nm. 107

Figure 6.3 J-V characteristics of the MIM devices S1 (Al_2O_3) and S2 (Ta_2O_5), measured at 300, 325, 350, and 375 K. 108

Figure 6.4 PFE (a) and SE (b) plots of the MIM device S2 (Ta_2O_5) at 300, 325, 350, and 375 K. 108

Figure 6.5 Arrhenius plots of the MIM device S2 from 0 to +1.5 (a) and to −1.5 V (b) at a 0.1 V step voltage. 110

Figure 6.6 Activation energy (E_a) versus square root of voltage plots for the MIM device S2 at 300, 325, 350, and 375 K. 110

Figure 6.7 Rectifying characteristics of the MIIM devices (S3, S4, S5, and S6) showing the: (a) J-V characteristics, (b) asymmetry, (c) nonlinearity, and (d) dynamic resistance. 111

Figure 6.8 Simulated conduction band diagrams at +1.5 V showing 0, 1, 2, and 3 bound states (solid lines) for S3, S4, S5, and S6, respectively, using a work function difference of 0.2 eV (Ref. [129]). One tick on the x-axis corresponds to 1 nm. 112

Figure 6.9 Band diagrams of structures S1, S3, S5, and S7 at negative (a) and positive (b) bias. Electron injection is indicated by the red arrow. 116

Figure 6.10 The rectifying characteristics of the Au/Ta_2O_5/Al_2O_3/Al structures showing the: J-V characteristics (a), asymmetry (b), non-linearity (c), and dynamic resistance (d). 117

Figure 6.11 The temperature dependent J-V measurements of the devices measured using the cryostat (a-d) at 77K and 100-to-375K with 25K-step or using the heating stage (e-g) at 300-to-375K with 25K-step: S1a (a), S3a (b), S5a (c), S7a (d), S1b (e), S5s (f), and S3s (g). 119

Figure 6.12 FN plot for S1b at negative polarity assuming Ta_2O_5 of total thickness equal to that of the sandwiched dielectric stack. The extracted barrier height is 0.59, 0.58, 0.58, and 0.62 eV at 300, 325, 350, and 375 K respectively. 120

Figure 6.13 FN plots considering the electric field distribution across each dielectric Ta_2O_5 (a and b) and Al_2O_3 (c and d). 121

Figure 6.14 The J-V characteristics of S1a (a), S5s (b), and S5a (c), based on fitting the extracted parameters from the experimental J-V characteristics to the equation of PFE (ln(I/V)-$V^{1/2}$), SE (ln(I/T^2)-$V^{1/2}$), and TAT (ln(J)-V^{-1}). The J-V^2 characteristics of these 3 devices indicate no linearity over the applied voltage (d). 123

Figure 6.15 J-V characteristics of selected devices measured at negative sweep from maximum positive voltage to maximum negative voltage (+to-) and positive sweep from maximum negative voltage to maximum positive voltage (-to+). 124

Figure 6.16 Microscope images of two devices fabricated using lift-off photolithography: 250×250 μm^2 device after M1 deposition (a), after developing (b), and after M2 deposition (c), and another 20×20 μm^2 device (d). 128

Figure 6.17 Rectifying characteristics of the MIIM devices (g1, g3, g5, S3s, and S5s) showing the: (a) J-V characteristics, (b) asymmetry, (c) nonlinearity, and (d) dynamic resistance. 129

Figure 6.18 Simulated conduction band diagrams of the structures g1, g3, g5, S5s, and S3s at -1.1 (a) and +1.1 V (b) showing 0/2, 5/0, 0/0, 0/1, and 3/0 bound states (solid lines) for S3, S4, S5, and S6 respectively at negative/positive bias. One tick on the x-axis corresponds to 1 nm. The electrons move from an electrode to another as indicated by the red arrows. The red polarity symbols represent how the device is connected for the current-voltage measurements. 130

Figure 6.19 The temperature dependent J-V measurements of g1, g3, and g5 devices measured using the heating stage at 300, 325, 350, and 375 K. 131

Figure 6.20 PFE (a, c, e) and SE (b, d, f) plots of the MIIM devices g1, g3, and g5 at 300, 325, 350, and 375 K. 133

Figure 6.21 TAT (a, c, e) and SCL (b, d, f) plots of the MIIM devices g1, g3, and g5 at 300, 325, 350, and 375 K. ... 134

Figure 6.22 J-V characteristics of g1, g3, and g5 devices measured at negative sweep from maximum positive voltage to maximum negative voltage (+to-) and positive sweep from maximum negative voltage to maximum positive voltage (-to+). ... 135

Figure 6.23 Comparison between experimental and modelled J-V characteristics for S5s and S3s devices. The onset of resonant and FN tunnelling is indicated by arrows for the modelled J-V curves. ... 137

Figure 6.24 The J-V characteristics of different MIIM structures varying their lateral area. ... 140

Figure 7.1 Confocal microscope images of selected fabricated rectenna circular patches with integrated rectifiers of an active area equal to 2µm×2µm (a) and 6µm×6µm (b). ... 142

Figure 7.2 The set-up used to test the rectenna devices. ... 143

Figure 7.3 Five times the skin depth calculated using the resistivity of different metals. ... 145

Figure 7.4 The process flow for patterning the layers of rectenna array FN2 at the cross-section of the integrated rectifier. ... 146

Figure 7.5 Top view of the patterned structure: a) the bottom electrode (red) at the corner of the array with the connection b) the oxide (green), and c) the top electrode (blue). ... 147

Figure 7.6 Fabricating the rectifying nanostructures of varying active area between 100×100 nm^2 and 100×100 μm^2: a) the bottom electrode (blue), b) the oxide(s) (yellow), and c) the top electrode (red). d) The rectenna array (of 14×14 mm^2 total actual size) connected to two metal lines for measurements and surrounded by rectifying nanostructures for dc measurements. e) Zoomed in image of the rectenna array. ... 148

Figure 7.7 Conduction band diagrams simulated using the in-house model (described in section 4.11). ... 149

Figure 7.8 The rectifying characteristics of FN2, RT2, RT3, and RT4 structures simulated using the in-house model (described in section 4.11): the J-V characteristics (a), the asymmetry (b), the non-linearity (c), and the dynamic resistance (d). ... 150

Figure 7.9 The diode-antenna coupling efficiency assuming an antenna impedance of 300 Ω. Calculations are based on equation (2.2) described in section 2.4.1. ... 151

List of Tables

Table 2.1 The state of the art devices suitable for THz rectennas... 12

Table 2.2 The rectenna coupling efficiencies for a diode assuming an antenna resistance of 300Ω. 15

Table 2.3 Parameters considered for the 0.14 and 2 THz rectenna design. 16

Table 2.4 Etchants suitable for Ta_2O_5 and Al_2O_3 films as deposited. 21

Table 4.1 Modelled structures. 59

Table 5.1 The extracted refractive index (n) and bandgap (E_g) as compared to literature values. 68

Table 5.2 Binding energy of the peaks. 82

Table 5.3 Device structure of selected samples from 3 batches.. 83

Table 5.4 Diode impedance [Ω] near zero volt for the different structures fabricated: noticeable improvement with Cr. Al_2O_3 is 1 nm thick, while Ta_2O_5 is 2 or 4 nm thick............................ 86

Table 5.5 Several materials and their corresponding barrier heights. 87

Table 5.6 The device structure and layer thickness of batches 4 and 5. 89

Table 5.7 The slopes and intercepts of the linear fits of FN plots and the extracted barrier height $\emptyset_B$. 94

Table 5.8 The device structure of the fabricated devices of batches 6, 7, 8, and 9. 95

Table 5.9 Extracted barrier heights from each FN plot at negative and positive bias across each dielectric. 99

Table 6.1 Device structure and layer thickness. 105

Table 6.2 Extracted CF when $\varepsilon_{r,PFE}$ is matched to $\varepsilon_{r,opt}$ (CF_m), the voltage range in which PFE fitting is done (V_{PFE}), and the trap depth at zero bias φ_{t0} for the 4 nm thick Ta_2O_5 at negative (−) and positive (+) polarities at 300 K. 109

Table 6.3 ALD pulse and purge times. 114

Table 6.4. Device structure and layer thickness: Substrate/M1/I1/I2/M2, where substrate could be glass (Gl) or Si, M1 and M2 are the bottom and top electrodes respectively, and I1 and I2 are the insulators. 115

Table 6.5 The extracted barrier heights from FN plots across each dielectric. 122

Table 6.6 Device structure and layer thickness. 128

Table 6.7 The reversal voltage for the devices S5s, S3s, g1, g3, and g5 at 300, 325, 350, and 375 K at negative (-) and positive (+) bias, defined as the voltage at which a non-linearity of 3 is achieved. 131

Table 6.8 The structures of this section and the previous section (6.2) showing the change in the minimum switching voltage swept at opposite polarities ΔV_{sweep} 136

Table 6.9 Extracted parameters from PFE, SE, and TAT plots of g1, g3, and g5 devices: ε_r trap depth ϕ_t and ϕ_{BTAT}. 137

Table 7.1 Device structure 145

List of abbreviations

AFM	Atomic Force Microscopy
Ag	Silver
Al_2O_3	Alumina
ALD	Atomic Layer Deposition
ALE	Atomic Layer Epitaxy
AC	Alternating Current
Ar	Argon
Au	Gold
BE	Binding Energy
CF	Compensation Factor
Cu	Copper
CVD	Chemical Vapour Deposition
DC	Direct Current
DIW	De-Ionized Water
E_a	Activation Energy
EBL	Electron Beam Lithography
E_g	Bandgap
FF-OCT	Full-Field Optical Coherence Tomography
FN	Fowler-Nordheim
FWHM	Full Width at Half Maximum
GPC	Growth Per Cycle
H2O	Water
HR-TEM	High-Resolution Transmission Electron Microscopy

I	Current
IR	Infrared
Ir	Iridium
J	Current density
MFC	Mass Flow Controller
MFM	Magnetic Force Microscopy
MIIM	Metal-Insulator- Insulator-Metal
MIM	Metal-Insulator-Metal
MSE	Mean Squared Error
MW	Maxwell-Wagner
MW	Microwave
n	Refractive Index
NL	Non-linearity
O2	Oxygen
Os	Osmium
Pd	Palladium
PFE	Poole-Frenkel Emission
PSP	Photostimulable Phosphor
Pt	Platinum
PV	Photovoltaic
PVD	Physical Vapor Deposition
R_d	Dynamic Resistance
RF	Radio Frequency
Rh	Rhodium

RMS	Root Mean Squared
RT	Resonant tunnelling
Ru	Ruthenium
sccm	standard cubic centimeter per minute
SCL	Space Charge Limited
SE	Schottky Emission
SE	Spectroscopic Ellipsometry
SEM	Scanning Electron Microscopy
SThAFM	Scanning Thermal Atomic Force Microscopy
STM	Scanning Tunnelling Microscopy
Ta_2O_5	Tantalum
$TaSi_2$	Tantalum Silicide
$TaSi_2$	Tantalum Silicide
$TaSiO_X$	Tantalum Silicate
$TaSiO_X$	Tantalum Silicate
TAT	Trap Assisted Tunnelling
TEM	Transmission Electron Microscopy
THz	Terahertz
TMM	Transfer Matrix Method
UHV	Ultra-High Vacuum
UV	Ultraviolet
V	Voltage
VIS	Visible
V_{ON}	Turn-on Voltage

WF	Work Function
WKB	Wentzel-Kramers-Brillouin
XPS	X-ray Photoelectron Spectroscopy

1. Introduction

1.1 Motivation

The use of fossil energy resources was basically triggered by the industrial revolution and was growing rapidly after that attributing to the oil-dependent technological advances in combination with the global population growth. Due to the limited petroleum reserves, the production is continuously decreasing and is endangered to be exhausted in a few decades. The rise of crude oil prices combined with the growing global energy demand sparked the need for inexhaustible renewable energy sources. In addition, global warming and air pollution as a result of the emissions from fossil sources raised environmental awareness towards the use of clean energy sources. Furthermore, the earlier nuclear power plant crisis unfolding in Japan after the massive earthquake in Fukushima in 2011 was a further motivation to usher a new era of renewable energy in the world.

Among the various renewable energy sources, solar energy draws attention because this source of energy is unlimited and, although intermittent, available everywhere. However, the low price of oil combined with the high costs of developing new technology has prevented the widespread adoption of solar power. By governmental support, the faith of strong investors in solar energy conversion and the efforts of research and development aim on the common target to get the solar power costs down to make it price-competitive with fossil fuels.

Solar cells are optoelectronic devices in which solar energy is directly converted to electrical energy. Photovoltaics are currently the only mature technology for harvesting part of this energy, corresponding to the visible part of the spectrum, converting the photons from solar illumination to useful DC current through a process known as the inner photovoltaic effect. However, photovoltaic cells are limited to harvesting energy in the visible regime and are unable to extend their potential towards other frequency/wavelength regimes in the wider electromagnetic spectrum. An alternative approach is the rectenna concept, which is a combination of an antenna collecting selected electromagnetic waves and an electrical rectifier making these waves into useful electricity at DC.

These low power devices have been proven in harvesting artificial energy sources in the radio/microwave regime of the energy spectrum making them successful for wireless power transmission applications. They have the potential to harvest energy at higher THz frequencies converting collected electromagnetic waves to DC current, to recycle industrial waste heat energy, and to cool electronic devices taking the advantage of their capability to be easily integrated into

microelectronic devices. These devices have been proposed to be used as rectenna arrays for solar energy harvesting[1], and are still under development at IR/THz with a maximum efficiency of 1%[2].

Rectennas are dielectric based solar cells. The advantages of rectennas are the high reliability, low operation cost, low fabrication cost (dielectric based), and low (cumulated) emission of greenhouse gases. They work day and night with wide absorption band, orientation insensitivity, and are independent of weather conditions. To increase the output power, these devices can be made into arrays taking the advantage of their tiny size. They can be selected for space use because of their lightweight and the ability to supply spacecraft and space stations with energy independent of fuels.

The criteria are the ability of the antenna structure to collect a substantial fraction of wave radiation from the electromagnetic spectrum and integrated diode to rectify the induced current in the antenna(s) into useful DC current. The diode types which are used at present are the semiconductor-based p-n junction, Schottky and the dielectric-based metal-insulator- -metal (MIM) . The p-n diodes cannot operate in the terahertz (THz) regime as they operate based on injection of minority charge carriers which must be removed when switching to reverse bias which in turn slows down their operation. Schottky diodes, however, do not suffer from this charge storage effect and can operate at THz but are limited by parasitic capacitance and associated RC time constants. Additionally, there are engineering and fabrication complications for coupling them with antennas and integration in arrays. Therefore, in theory, single (MIM) and double dielectric diodes (MIIM) are the only structures which can be used efficiently in rectenna arrays in the terahertz (THz) frequency regime due to their ultra-fast tunnelling conduction mechanism and their ability to be integrated in arrays of nanoscale features.

Metals and dielectrics used are highly abundant in the earth's crust. While thin film solar cells require several layers of materials and a total semiconductor thickness of less than 2 microns (processed on rigid glass substrates), rectennas require a 400 times thinner dielectric stack (considering it 5 nm in total). Hence, material input, which presents an important cost share of any renewable energy source, is also greatly reduced in the production of rectenna arrays. Rectenna arrays are realized by structuring the functional thin films allowing for an integrated series connection of rectenna elements.

The potential of rectennas to operate at higher IR/THz frequencies has been hindered by the lack of a diode nanostructure that can work efficiently when coupled to antennas. The practical rectifying mechanism proposed is based on a quantum tunnelling effect of electrons having fast response times of the order of femto-seconds.[3] This concept happens in MIIM (metal-insulator-insulator-metal) diodes which needs to be engineered for enhanced resonant tunnelling, and their

size needs to be minimized towards nanostructures for efficient operation at THz. The rise of nanotechnology – bringing the patterning capability down to the nanoscale – makes it possible therefore to move these devices towards the THz regime. This work focuses on optimizing the diode structures giving a further understanding of their suitability of being integrated into rectenna scavengers. It is aimed at enhancing the rectifying characteristics of THz rectifiers, devising the rectenna arrays, specifying the technological requirements, and attempt to move THz/IR rectenna arrays from proof-of-concept to prototype. It is aimed to demonstrate the feasibility of rectenna technology at optical frequencies and to open the road towards energy harvesting ranging from the surface of the earth, infrared emissions to space and towards solar energy (100's THz).

1.2 Energy harvesting in the electromagnetic spectrum

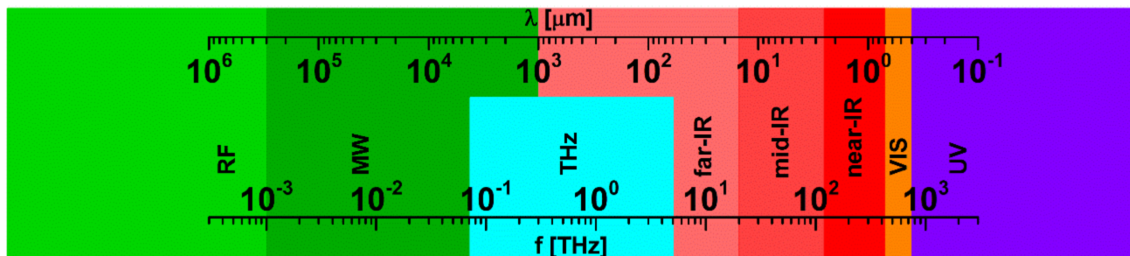

Figure 1.1 The electromagnetic spectrum indicating the different frequency regimes: radio frequency (RF), microwaves (MW), far, mid and near infrared (IR), visible (VIS), and ultraviolet (UV). Terahertz (THz) regime covers parts of MW and far-IR regimes. Infrared: 700nm–1mm/430THz–300GHz, Microwave: 1mm-1m/300GHz–300MHz.

The current successful technology in the market for energy harvesting from the electromagnetic spectrum is based on photovoltaic solar cells which have a thermodynamic efficiency limit, and the highest lab-scale record achieved recently is an efficiency of 38.8% for multi-junction solar cells.[4] However, there still exist cost hurdles in making it competitive with non-renewable technologies. A typical efficiency in the market for solar modules is 15%, and hence around 85% of the solar radiation is rejected as waste heat and reflection. Furthermore, the solar spectrum is only a part of the wide-ranging electromagnetic spectrum (Figure 1.1) which surrounds the universe covering other forms of radiation ranging from low energy (low frequency) radio waves to high energy (high frequency) gamma rays. The part corresponding to wavelengths of 0.1–30 μm is called the THz band corresponding to frequencies of 10^{11}–10^{12} Hz, while the optical spectrum includes the infrared (1–429 THz) including thermal IR around 30 THz, the visible (429–750 THz), and the ultraviolet (750 THz – 30 PHz) bands.[5]

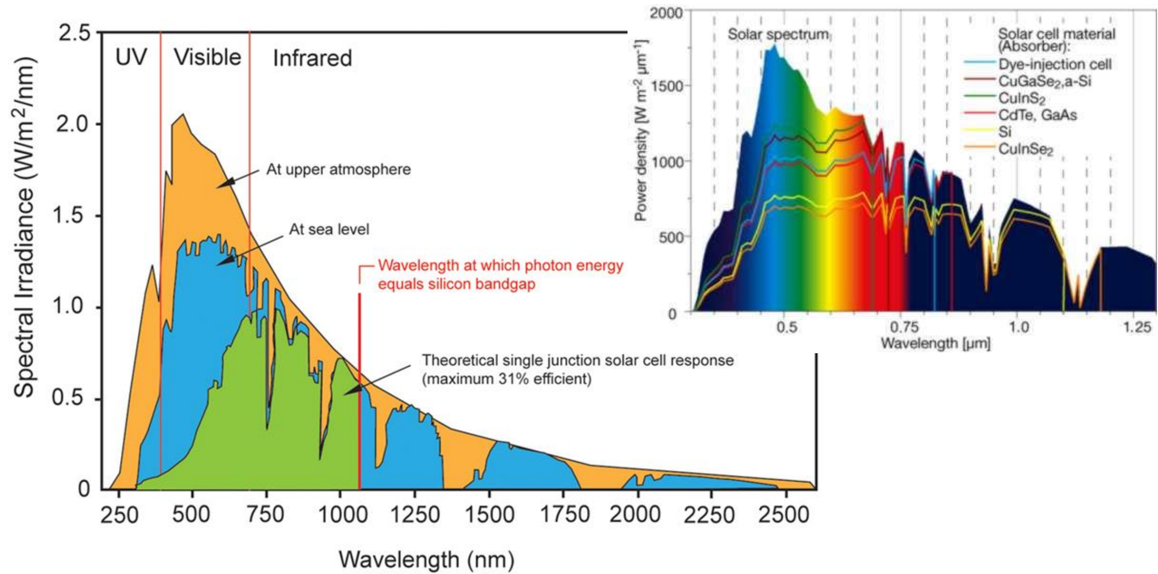

Figure 1.2 The spectral power density of sunlight.[6] The different spectra refer to the extra-terrestrial AM0 radiation at upper atmosphere and the AM1.5 radiation at sea level. The inset shows the solar spectrum absorption with different solar cell materials.[7]

The rectenna approach can be designed to absorb selected resonant frequency range of electromagnetic waves by varying its area and thus making use of the electromagnetic waves in the infrared and microwave regions. This is an advantage over the existing semiconductor photovoltaic technology which is limited to absorbing electromagnetic waves mainly in the visible region due to the band gap matching requirement. This is further illustrated in Figure 1.2 showing the solar energy spectrum in the ultraviolet-visible-infrared region along with the absorbed energy in solar cells having diverse absorber materials. The selection of the semiconductor material has a remarkable influence as shown in the inset but is still limited mainly to the visible and the near infrared regions. The rectenna concept is however limited to wide-ranging wavelengths in the terahertz region. Therefore, a large part of wasted energy would be useful in the rectenna applications in addition to being functional at night as they are designed to operate in the infrared and microwave regimes.

1.3 IR/THz applications

Applications of IR/THz rectennas include satellite wireless communication, energy harvesting by THz-to-DC conversion, infrared sensors, non-linear optics, medical therapies, explosive and biochemical detection, mine detection, nano-photonics, data transfer, and through-the-wall imaging. Despite the success of semiconductor-based photovoltaic cells in the visible regime and rectennas in the RF and microwave frequency regimes, the THz regime situated in between is still not exploited due to the lack of sources and detectors working efficiently at THz.

THz signal used to be generated from thermal radiation sources in conjunction with IR spectrophotometers until the generation of far-IR light using picosecond laser pulses was demonstrated in 1972.[8] A photoconductive switch was introduced in 1975,[9] where a picosecond time-dependent transient current radiating with generated THz components was demonstrated opening the road for THz realm till the present time. This principle is still used as a source in the commercial THz systems. A photonic-based approach is used to generate tunable THz pulses rectified from a laser source using non-linear optics[10,11]. Further enhancement to this approach is needed as the sources still suffer from very low efficiency and power.

THz rectennas can be used for scavenging thermal infrared radiation (which is emitted at 30 THz considering human body temperature) and for THz imaging by detecting hot object emissions. They can be used for wireless (instead of fiber) THz communication with large bandwidth potential (up to 100 GHz) for data transfers exceeding 1 Gb per second. This is a big advantage over the currently available IEEE standard WiFi systems providing up to 433 Mbit/s for 80 MHz bandwidth at 5 GHz band. One challenge for THz wireless communication is the free space attenuation which increases with waves of higher frequencies (scattering and absorption by clouds, rain, air particles, etc) and the strong water vapour absorption of THz radiation. This limits the range between the transmitter and the receiver which could be an advantage to prevent spying and intercepting THz signals, e.g. in military applications. This is however not a problem for communications outside the atmosphere between satellites, which tend to get smaller if designed for THz waves.

THz rectennas can also be used as detectors for THz imaging with high resolution (sub-mm) in biomedical applications[12] with the potential to distinguish skin cancer from healthy skin.[13]. As THz radiation has the ability to pass through low-loss dielectrics (e.g. textile and paper), passive imaging becomes theoretically possible.[14] This would be applicable for security such as luggage inspection and detection of weapons or hidden explosives from a distance.

THz rectennas have also been proposed to be used for energy harvesting applications with the ability to be tuned for a broadband waste energy collection such as that of residual heat ranging from small electronic devices to large industrial machinery. Heat at temperature between 400 and 2000K emitted from any object is in fact a form of infrared wave radiating between 2 and 11 μm in the electromagnetic spectrum. Such radiation results in the vibration of electrons in metals acting as antenna patches, which creates tiny induced current flowing internally. This current can be useful when rectified between two antenna patches, which needs to be smaller at higher frequencies. The tiny size needed for a rectenna in the nanoscale offers a great advantage of

putting them in an array to maximize the output power for detectable electricity along with low fabrication cost due to the necessity of small amounts of materials.

These arrays have been proposed for harvesting the energy emitted from Earth (7-17 μm) which is emitted all year regardless of weather conditions and all day even during the darkness. Unlike conventional solar cells, THz rectennas are broadband, which is an advantage for harvesting heat emitted in the form of black body radiation of continuous spectrum. They could be applicable to electric devices and vehicles such as combustion engines cooling them by recycling their dissipated heat to useful electricity enhancing their efficiency. They can also be used for cooling electronic devices and recycling their heat – such as laptops extending their running time – estimated by around 20%[15] considering thermal-to-electric conversion rate of 100 W/cm^2.[16]

The concept of THz rectennas can be used for extending these devices towards harvesting solar energy consisting of the VIS regime and part of IR radiation as an alternative to conventional solar cells as originally proposed in 1972[17] and patented in 2012[1] to be fabricated as an array.

Diodes based on tunnelling through one or more insulator layers are attractive rectifying devices for electronics and energy harvesting applications at terahertz (THz) and infrared (IR) frequencies[18] offering rectification into these regimes due to their short tunnelling transit time in the range of femtoseconds.[3] Due to their ultrafast operation, these diodes are of interest for optical frequency applications[19,20] including infrared detection[21,22] and solar energy harvesting[23,24]. Integrating them into rectenna arrays[1] offers the distinct advantage over photovoltaics of harvesting IR energy during night time hours. The main challenges remain in achieving sufficient nonlinearity, high asymmetry, and low dynamic resistance[25] to achieve sufficiently high efficiency. Resonant tunnelling (RT) can serve to bring further enhancement to the current asymmetry and nonlinearity[26] with demonstrated operation at THz frequencies.[27,28]

1.4 Outline of thesis contents

Motivation linking this work to proposed THz devices used for recycling energy and other THz applications has been introduced in this chapter. It includes an overview of energy harvesting in the electromagnetic spectrum pointing to where THz frequencies regime is situated and the ambition of moving these energy scavenging devices towards harvesting solar and thermal energy.

In chapter 2, the performance of rectennas at low frequencies (Radio/Microwave) is investigated including the challenges at larger (IR/THz) frequencies. An overview is given about the success of RF Rectennas for wireless transmission, the importance of extending these devices towards energy harvesting through THz radiation, the proof-of-concept situation of THz rectennas, the

significance of developing THz diode nanostructures for successful integration, an update of the state-of-the-art devices, and the challenges of the project.

Chapter 3 contains the theory of the techniques used for fabricating the devices and how they are relevant for this work. This includes the fabrication equipment, shadow mask and photolithography, and imaging techniques.

Chapter 4 explains the physical concept of resonant tunnelling giving the mathematical calculations used for optimising the rectifying performance. The conduction mechanisms in MIM/MIIM diodes are summarised. The model used in this thesis is described through simulations for some structures.

Chapter 5 concerns rectification using metal–insulator–(insulator)–metal diodes including experimental work particularly with the ultra-thin Ta_2O_5 and Al_2O_3 dielectrics for high speed MIIM rectifiers. The rectifying performance metrics of turn-on voltage, asymmetry, non-linearity, and dynamic resistance is linked to the different tunnelling and thermal emission mechanisms through the dielectrics and shown using different types of electrodes and compared according to their compatibility with THz rectennas. Issues in fabrication such as the native oxide supported with HR-TEM images is put forward.

Chapter 6 includes optimization of tunnelling structures according to the individual dielectric layer thickness explaining. It discusses the role of interfacial and bulk defects modified with the ALD parameters in tuning the characteristics. Significant performance is reported showing the impact of scaling down the area.

Chapter 7 includes design of 0.14/2 THz rectennas and underlying theory behind them. This covers the rectenna array design done for the project with the efficiency considerations and area required for efficient coupling with antenna patches. The challenges in nanofabrication and the device structure are described with the attempt done for prototype fabrication of THz rectenna arrays using integrated MIM nanostructures.

Chapter 8 gives a brief overview summarizing how rectifiers can be optimised for rectenna integration and giving a roadmap for rectenna arrays towards THz energy harvesting.

2. Energy harvesting: the challenge at THz

2.1 Rectennas towards THz

The proposed concept is based on an antenna in conjunction with a rectifier forming a rectenna device. The electromagnetic waves are collected and converted to high frequency current through an antenna and then converted to dc power by the rectifier.

Rectennas have been demonstrated successfully for microwave power transmission using a half-wave dipole antenna with 85% conversion efficiency at 2.45 GHz when coupled to GaAs Schottky diode[29] and 82% at 5.8 GHz for a 50 mW input when coupled to Si Schottky diode[30]. The concept was first proposed for solar energy collection in 1972[17], and not re-examined till 2005 suggesting an array of antennas prior rectification for efficiencies equivalent to photovoltaic cells and stating some issues at the optical frequencies.[31] A record rectenna efficiency of 90.6% was reached in 1977 using GaAs-Pt Schottky diode at 2.45 GHz for 8 W input,[32] and a 72% efficiency was achieved in 1991 at 35 GHz.[33]

Research in this field was focused at the traditional frequencies of 2.45 and 5.8 GHz until it was proposed to extend into the optical regime of the electromagnetic spectrum in 1981[34] and 1984.[35] The rectenna concept in the visible regime was first experimentally proven on fabricated nanostructures in 1996 where resonance light absorption and high frequency rectification was observed.[36] Further attempts at 30 THz done in 2002[2] led to a better understanding of the concept despite the low efficiency obtained.

Rectennas are theoretically limited by Landsberg efficiency of 93%[37] for full-wave rectification with a loss mechanism limiting it experimentally including antenna radiation efficiency, resistive losses in the antenna, antenna-to-diode power transfer, and diode efficiency in converting AC to DC. The overall power efficiency, by which an antenna is able to convert the incoming electromagnetic energy into DC output power, approaches 90% at single microwave frequencies using a Schottky diode-coupled rectenna with full-wave rectification.[38] However, the rectenna efficiency drops to 0.1-1% at 30 THz using MIM diode-coupled nano-antenna arrays[2] and is unable to attain a quantum efficiency larger than 0.01% for light harvesting using a Schottky diode-coupled plasmonic nano-antenna.[39]

The energy conversion efficiency can be further improved by the proper matching of the rectifier with the antenna in terms of having lower impedance and parasitic capacitance. To rectify the high frequency THz electromagnetic radiation efficiently, the rectenna RC constant must be smaller than the reciprocal of the angular frequency,[40] where R is the total resistance of the diode

and antenna in parallel. Obtaining lower capacitance requires either a lower dielectric constant or a smaller area of the active device. However, in the latter case as it gets smaller, the diode resistance increases limiting the coupling efficiency from the antenna. Thus, smaller area is sought for the device to reduce the intrinsic capacitance and thus make it operative for solar energy harvesting in the visible regime.

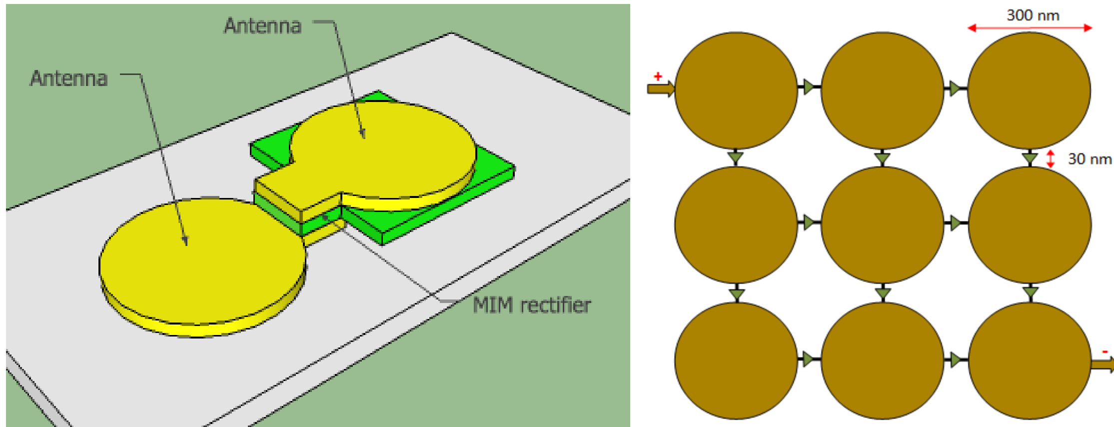

Figure 2.1 A terahertz solar rectenna structure proposed for the project for each device (left) and for an array used for a practical system.[1]

The proposed rectenna array is made up of a rectifier sandwiched inside a two-patch antenna and reproduced into an array as shown in Figure 2.1. Electromagnetic energy is collected in the antenna as an alternating current and then rectified to direct current using a huge array of small area devices for an enlargement of the output power having the advantage of a proper antenna-to-rectifier matching.

The popular rectifier used in rectennas at present is the Schottky diode which is attractive for rectenna applications because of its low series resistance, high forward bias current, low substrate losses, and very fast switching properties.[41] However, this rectifier becomes inefficient in the high frequency regime[42] where it is limited by series resistance and junction capacitance. The series resistance limitation becomes more prominent at THz frequencies due to the plasma resonance effect[43] which constrain the current to flow along the surface of the semiconductor substrate and the skin effects whereby the current is confined to the edges of the metal contact.[44] Resonant tunnelling diodes have a promising potential in the THz frequency range especially with the single and double dielectric structures. The main challenges remain in obtaining sufficient rectifying characteristics (low non-linearity and asymmetry) especially for nanostructures in addition to their high impedance which makes them inefficient when incorporated in THz rectennas due to mismatch of impedances.

2.2 THz rectification through metal–insulator–(insulator)–metal diodes

Rectification and detection for RF applications is typically done using pn junction diodes at kHz-MHz frequency regime. Schottky diodes, specifically GaAs, are characterised by their low turn-on voltage, lower forward resistance, and lower noise generation with scalability of their active area for lower junction capacitance characteristics which enables their operation at higher GHz-THz frequencies with demonstrated detection at 2.5 THz[45]. However, their performance degrades drastically at THz frequencies and are unable to operate beyond 5 THz. This is in addition to their overheating, large series resistance, current saturation effect, and their very low experimental efficiency with $1/f^3$ power drop[46]. Integrating these devices in THz rectenna arrays becomes more challenging with fabrication in coupling them with antennas. Efficiency of a diode becomes more complex when integrated in rectennas, which are used for harvesting low and fluctuating incident power, and require using structures of easier integration capability and of faster charge transport mechanism to operate at THz frequencies.

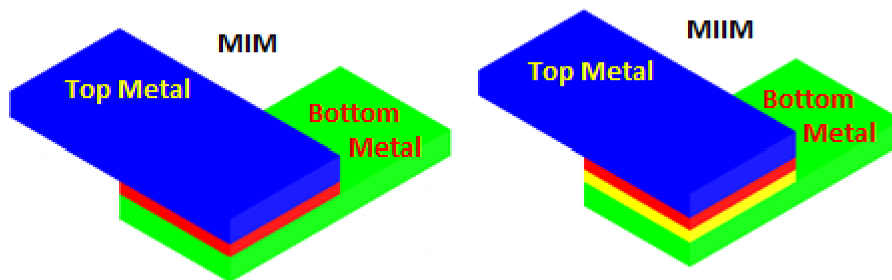

Figure 2.2 Single (MIM) and double (MIIM) dielectric diode structures: bottom metal (green), dielectrics (yellow and red), and top metal (blue).

The mechanism of the proposed device is based on the principle of quantum mechanical tunnelling of electrons occurring through ultra-thin dielectric layers. This structure is composed of one or two dielectric layers of few nanometres thickness sandwiched in between two metal electrodes as shown in Figure 2.2. Being sufficiently thin, the direct tunnelling mechanism would dominate the leakage current in the dielectric making it possible to flow at low voltage bias with a fast response of femtoseconds[3] – and thus enabling it to operate in the visible regime. These rectifying diodes can be made into nanostructures to be easily integrated in THz/IR rectennas offering full functionality without the need of cooling and applying an external bias.

The device fabrication is aimed to develop diodes with high forward-to-reverse current ratio for sufficiently non-linear and asymmetric J-V characteristics. Asymmetry in the characteristics can be enhanced with the usage of different electrodes and geometric field scheme.[47] The non-linearity is defined as $V.dI/I.dV$ which is unity for a resistor and more than 3 for a typical diode. Further

significant enhancement in asymmetry and non-linearity was observed with metal-insulator-insulator-metal (MIIM) diodes.[26] This double-dielectric structure will be mainly used and optimized in terms of obtaining higher non-linearity and lower resistance as required by rectenna applications at high THz frequencies.

Both single and double insulator structures work on the same physical principle: tunnelling of electrons from one electrode to the other. They both operate at high THz frequencies which is required for the rectennas, making it several of orders of magnitude faster than the other electronic devices with a tunnelling time in the order of femtoseconds. The response time is however limited by several factors including the capacitance and matching the diode impedance to that of the antenna.

2.3 State of the art devices

MIIM diodes have been demonstrated at THz frequencies[27,28] with the capability of achieving good rectifying characteristics with resonant tunnelling[26] and their integration in THz rectenna arrays[1]. The characteristics of the state of the art diodes needed for good performance of the rectifying devices when integrated in THz rectennas including the responsivity and the dynamic resistance are listed in Table 2.1.

The responsivity, which is a measure of diode non-linearity, is the ratio of the rectified dc current to the incident ac power: $Resp = 0.5 \times (dr_d/dV)/r_d$. It can be noticed that most papers focus on the performance of the MIM structure solely. As the structures are intended for THz energy harvesting, rectification near zero bias for devices of the smallest possible active area and the lowest dynamic resistance becomes extremely important as discussed in sub-sections 2.4.1 and 2.4.2. For this, the Choi MIM structure of 60 nm^2 active area with a responsivity of 12-31 A/W at 0-80 mV applied bias are indeed the most interesting. However, an estimate using the current-voltage (I-V) characteristics implies a dynamic resistance $R_d = dV/dI$ in the order of 10^{13} Ω, which is very large for THz rectennas. The Grover MIIM structures of unidentified area showed noticeably improved R_d in the order of 10^9 Ω near 0 V with sufficient responsivity. This is in addition to good matching between the measured and modelled characteristics, which is rarely found in papers. More interesting is the Berland report of rectenna arrays fabricated using 100×100 nm^2 MIM nanostructures, of very low non-linearity (and consequently insufficient responsivity) near 0 V, integrated in rectenna arrays showing a coupling efficiency of 0.1-1% at 30 THz.

Concisely, the reported diodes still suffer from a high dynamic resistance and relatively low asymmetry. Furthermore, a sufficiently low turn-on voltage towards zero bias[48] is required for efficient operation in low-power applications in rectenna arrays.

Table 2.1 The state of the art devices suitable for THz rectennas.

Author / Year	Device		Responsivity [A/W]		R_d [Ω]	Performance when integrated in rectennas
	Structure	Area [μm²]	Max	Near 0V	Near 0V	
Hoofring 1989[49]	Ni/NiO/Au	0.64	5.5	2.8	-	-
Wilke 1994[50]	Ni/NiO/Ni	0.0576	1.6	-	100	-
Berland 2002[2]	$Au/Nb_2O_5/Nb$	0.01	-	Very low	4.9×10^4	**0.1-1% at 30 THz**
Abdel-Rahman 2004[51]	Ni/NiO/Ni	0.075/ 0.0014	2.75/1.65	-	180	-
Esfandiari 2005[52]	Ni/NiO/Pt	0.0025	13	3	-	-
Krishnan 2008[53]	Ni/NiO/Cr/Au	1	5	1	5×10^5	-
Choi 2010[54]	$PolySi/SiO_2/PolySi$	60	**31 at 80 mV**	**12**	-	-
Dagenais 2010[47]	$PolySi/SiO_2/Au$	0.35	14.5	2.5	1.2×10^8	-
Bean 2011[55]	$Al/AlO_x/Pt$	0.5625	2.3	0.5	2.2×10^5	-
Grover 2012[26]	**$W/Nb_2O_5/Ta_2O_5/W$**	-	**12**	**4.5**	**10^8/ 10^9**	-
Zhang 2013[56]	Ni/NiO/Cu	0.008	7.3	-	1.2×10^6	-
Kinzel 2013[57]	$Al/Al_2O_3/Pt$	0.008	0.03	0.00124	**124.6**	-
Zhu 2013[58]	Graphene-graphene geometric Diode	0.01	0.24	0.12	10^3	QE[1] 0.01% at 28.3 THz
Gadallah 2014[59]	Cu/CuO/Au	0.0045	6	4	505	-

[1]*The Quantum Efficiency*

2.4 Rectenna array design

Rectennas are devices used to convert electromagnetic waves into useful energy captured by antennas and rectified by diodes. The dc component extracted from the non-linear characteristics of the diode can be fed into a load. Rectenna arrays will be fabricated consisting of inter-connected rectenna elements in an array and a description of the design is given in the following subsections. The aim is to devise rectenna arrays for energy harvesting at 0.14 and 2 THz, selected based on the available THz measurement sources at the University of Liverpool and National Tsing Hua University respectively.

2.4.1 Efficiency considerations

The overall efficiency of a rectenna is defined by:

$$\eta_{overall} = \eta_a . \eta_s . \eta_c . \eta_j \tag{2.1}$$

where η_a is the efficiency of coupling the incident electromagnetic wave to the receiving antenna, η_s is the efficiency of the collected energy at the antenna-diode junction governed by resistive losses at high frequencies, η_j is the rectifying efficiency of the diode, and η_c is the antenna-to-diode power coupling efficiency governed by the impedance mismatch. The latter is frequency dependent and given by:

$$\eta_c = \frac{4\frac{R_A . R_D}{(R_A + R_D)^2}}{1 + [\omega . C_D . \frac{R_A . R_D}{(R_A + R_D)}]^2} \tag{2.2}$$

where R_A and R_D are the resistances of the antenna and the diode respectively, ω is the angular frequency, and C_D is the diode capacitance. Thus, for an efficient power transfer, it is required to match the resistance of the diode to that of the antenna and to have the second term in the denominator much less than 1 which can be achieved by minimizing the diode area. The latter, however, causes an increase in the diode resistance, and thus a trade-off exists, and an optimum occurs at a certain area. This means that for a higher coupling efficiency, $C_D . R_D \ll 2/\omega$, and thus it's required to have $C_D . R_D \ll 2.27 \times 10^{-12}\ s$ for 0.14 THz and $C_D . R_D \ll 1.59 \times 10^{-13}\ s$ for 2 THz. Assuming a double dielectric structure of 1 and 4 nm of Al_2O_3 and Ta_2O_5 respectively, the resulting capacitance is found to be $1.4 \times 10^{-5}\ F/cm^2$. Therefore, for an efficient coupling, it is required to have a diode resistance $R_D \ll 1.7 \times 10^{-7}\ and\ 1.2 \times 10^{-8}\ \Omega cm^2$ for 0.14 and 2 THz respectively. Such low resistance can never be achieved, and thus the only way is to minimize the diode capacitance by minimizing the diode active area.

For an efficient power transfer, the diode needs to be matched with the antenna which has typical impedances as low as few hundred ohms. This can be achieved when having low barrier heights between the metal and the dielectric which conversely limits the asymmetry. Consequently, the double dielectric structure is preferable for the diode where the asymmetry can be managed using similar electrodes keeping the nonlinearity high with resonant tunnelling structures.

2.4.2 Diode–antenna coupling

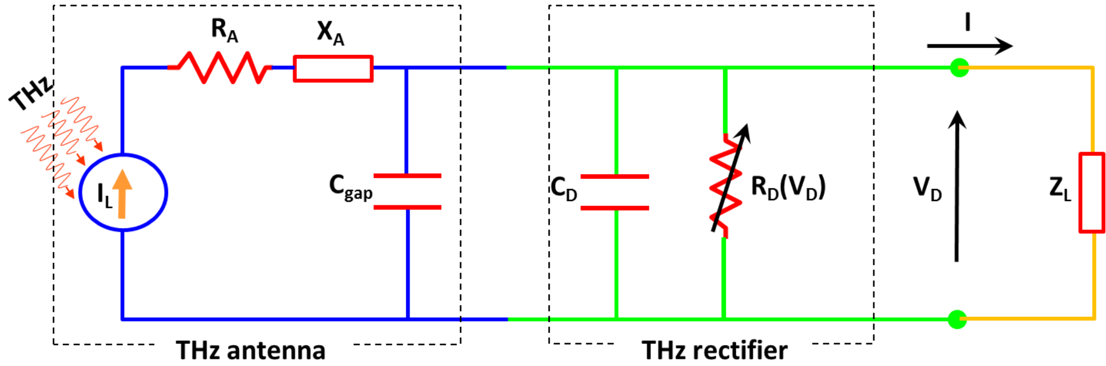

Figure 2.3 The equivalent circuit of the THz rectenna element coupling the antenna with the rectifier.

As depicted in Figure 2.3, the antenna collects the incident THz waves and transforms them into current. This current becomes useful DC when coupled to a rectifying diode. R_A and X_A are the antenna impedance and reactance respectively. C_{gap} is the capacitance generated in the antenna by the air gap. C_D is the diode junction capacitance and R_D is the non-linear series resistance.

For the double dielectric structure, the total capacitance of the device is the series capacitance across each dielectric expressed by:

$$C = \varepsilon_0 \varepsilon_r A/d \quad (2.3)$$

where ε_0 is the vacuum permittivity, ε_r is the relative permittivity of the dielectric, A is the active area, and d is the thickness of the dielectric.

For efficient coupling, diode-antenna impedance matching is necessary, and the diode side is a trade-off between the coupling efficiency and the nonlinearity. Assuming dielectric thicknesses of 1 nm-Al_2O_3 and 4 nm-Ta_2O_5 and a perfectly matched antenna-diode impedance of 300 Ω, the coupling efficiency is calculated based on equation (2.2). and shown in Figure 2.4 as a function of the side length of a squared diode. The efficiency curves in Figure 2.4 and the values given in Table 2.2 show the necessity to use the smallest possible area for the diode to improve the coupling efficiency. The fabrication of the required nanostructures cannot be done with the available facilities, where the smallest possible line-width which can be fabricated is not less than 2 µm.

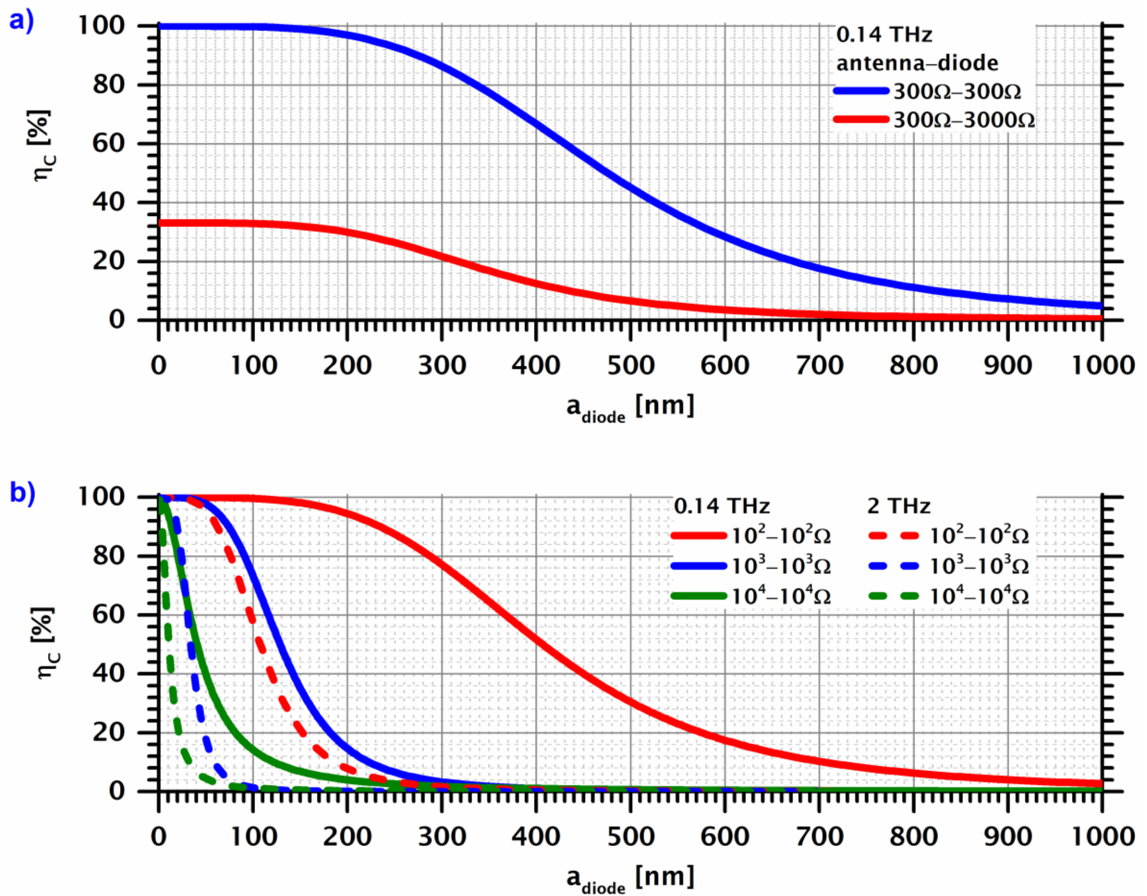

Figure 2.4 a_{diode} is the side length of the square diode active area. a) The coupling efficiency for a 0.14 THz rectenna for a matching antenna-diode impedence of 300-300Ω, and when the diode impedances larger by an order of magnitude (3000Ω). b) The coupling efficiency of 0.14 THz (solid) as compared with 2 THz rectenna assuming a perfect matching of the diode-antenna impedance.

Table 2.2 The rectenna coupling efficiencies for a diode assuming an antenna resistance of 300Ω.

	0.14 THz rectenna coupling efficiency	
Diode Area	300Ω-diode	3000Ω-diode
100nm×100nm	100%	33%
1µm×1µm	4.89%	0.51%
2µm×2µm	0.32%	0.03%

2.4.3 Circular patch parameters

The antenna design consists of a thin dielectric sandwiched between two conducting layers: lower ground and upper circular patch, where the fringing fields in between cause radiation. The patch must be thin enough of thickness much less than the free space wavelength which is defined by the following equation:

$$\lambda = c/f_0 \qquad (2.4)$$

where c is the speed of light and f_0 is the wavelength of the electromagnetic wave.

Considering a frequency of 0.14 THz, the free space wavelength is then calculated to be 2.14 mm. Thick substrates with low permittivity are desirable which provides better efficiency, larger bandwidth, and higher radiation.[60] Corning glass substrates having a relative permittivity of 5.84 will be used. The diode will be designed having the smallest possible area, which is necessary for matching with the antenna. At THz frequency, the skin effect occurs, driving the current to flow within a small thickness at the surface. Thus, copper (Cu) patch thickness will be chosen to be equal to at least double the skin-depth δ_s which was found to be 175 nm at 0.14 THz according to the following equation:

$$\delta_s = \sqrt{\rho/(\pi.f.\mu)} \qquad (2.5)$$

where ρ is the resistivity (Ωm), f is the wave frequency (Hz), and μ is the permeability (Ωs/m).

The appropriate values for the rectenna design parameters were found to be as listed in Table 2.3 including the height of the dielectric substrate, the relative dielectric constant of the substrate ε_r, and the radius of the circular patch r_{patch}. The required radius of the patch at an electromagnetic radiation of 0.14 THz was found to be optimum (in terms of bandwidth and radiation pattern) at 255 µm using CST Microwave Studio simulations as shown in Figure 2.5.

Table 2.3 Parameters considered for the 0.14 and 2 THz rectenna design.

	Antenna				Diode
Frequency	$\varepsilon_{r,\mathrm{CG}}$	h_{CG}	r_{patch}	δ_s (Cu)	$a_{diode,eff}$
THz	-	µm	µm	nm	nm
0.14	5.84	700	255	175	200
2	5.84	700	-	46	50

where $a_{diode,eff}$ is the diode side assuming it a square, required for efficient coupling

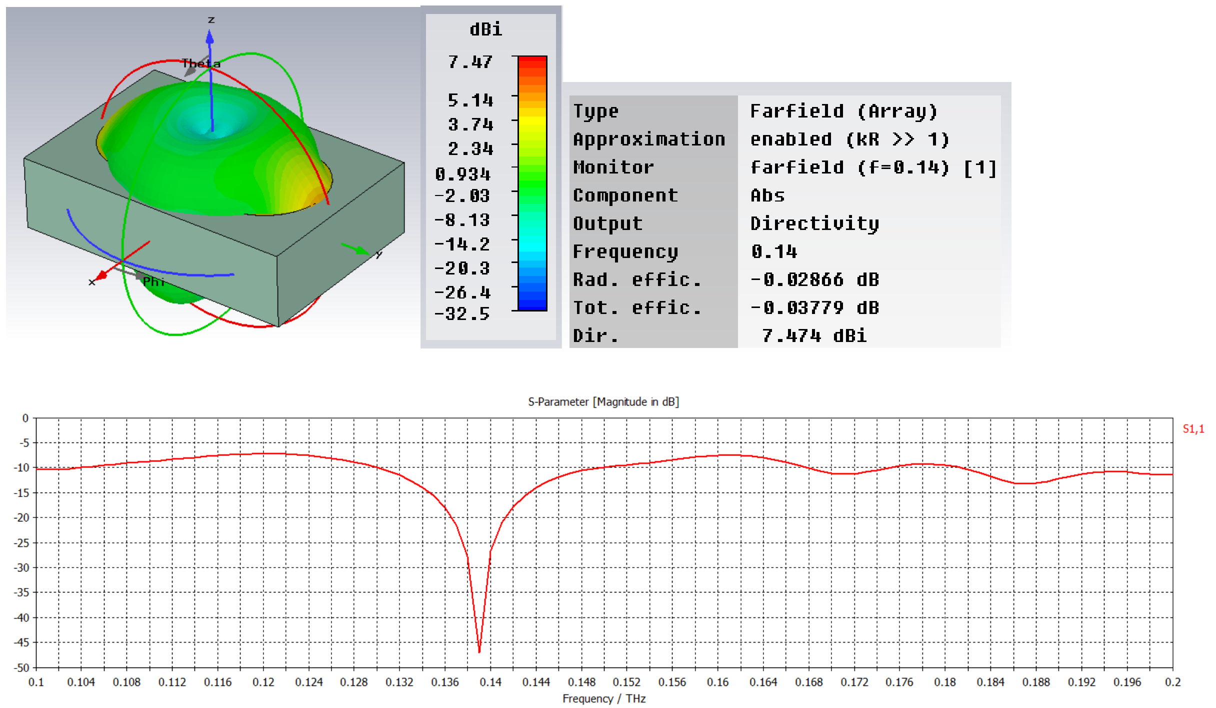

Figure 2.5 CST simulations for a 1×2 rectenna showing high directivity and high return loss response (s11) at 0.14 THz for copper patches.

2.4.4 Photolithography and Shadow Mask

Patterning the metal electrodes is done using shadow mask and the photolithography approaches. The latter approach will be mainly done using the lift-off process[61] for the top electrode as wet etching of the metal is not reliable for ultra-thin nanostructures[62]. Wet-etching cannot be easily controlled to etch the metal without attacking the thin oxides. After careful consideration of the different available methods, the following lift-off process is proposed based on the ease of use, the reliability of the method, and the inexpensive chemicals needed. This is demonstrated in the process flow shown in Figure 2.6(a). The conventional lift-off method requires a single layer resist with a simple photolithography process which allows patterning the device structure to a minimum line-width reproduced reliably at ≈2 µm.[62] The prebake time and temperature, exposure time, and the developer type and time are the variables needed to control the process.

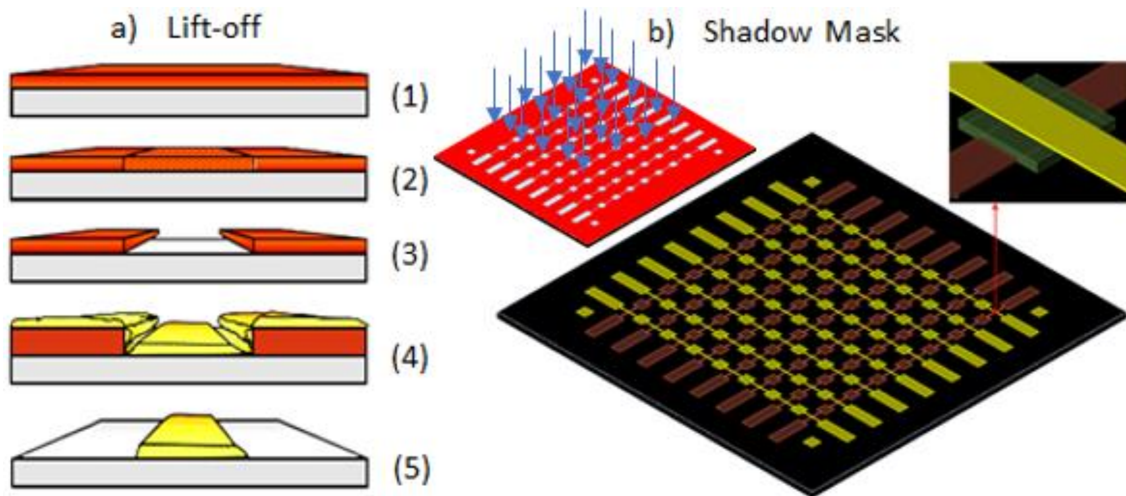

Figure 2.6 a) The photolithography approach process flow: 1) spin-on the resist, 2) UV exposure through a mask, 3) development, 4) metal deposition, and 5) lifting-off to leave the patterned metal (yellow). b) The final structure of the device using the designed shadow mask. The active device is magnified and shown in the upper right inset. The shadow mask is shown on the upper left inset where evaporated metal (indicated by blue arrows) gets patterned through it and sticks to the substrate fixed under it with a magnet sheet.

Referring to Figure 2.6(a), a standard cleaning process is done for the substrate using acetone and isopropanol to remove oil, organic contaminant and metal, and atomic or ionic components. If the substrates are not cleaned properly, the diodes could otherwise be easily shorted or damaged by particulate contamination. The positive photoresist *Shipley S1805* is then spun onto the substrate using a spin-coater followed by prebaking on hot plate. The substrate/resist stack is then exposed to ultraviolet (UV) light using the designed photomask and the mask-aligner. After that, the resist is developed using *Microposit* developer. The sample is then rinsed in de-ionized water (DIW) and blown dry with nitrogen.

In parallel to photolithography, the devices are aimed to be fabricated using a shadow mask which was designed as shown in Figure 2.6(b) for a device area of 100 μm×100 μm. The bottom metal is patterned on the substrate using thermal evaporation through the shadow mask. After the dielectric(s) are deposited over the entire surface (not shown) using ALD, plasma etching is done on the sides using a non-patterned shadow mask to build contact with the bottom metal. Top metal is then patterned through the same shadow mask (rotated perpendicularly) using thermal evaporation to get the final structure. The MIM/MIIM device is located at the junction: the dielectric layer(s) (green) sandwiched in between the bottom metal (brown) and the top metal (yellow).

For both approaches, the metal is deposited onto the substrate by thermal evaporation. In the case of gold, it could be easily scraped away by tungsten probes as observed in some fabricated samples. This can be avoided by depositing a chromium layer for good adhesion, while the gold layer is evaporated on top, immediately after to minimise oxidation. The photoresist is then stripped away by immersing the sample into acetone. Finally, the sample is dipped into isopropanol to remove the acetone, rinsed in DIW, and blown dry with nitrogen.

After the procedure is done with the base metal attached to substrate, the dielectric layers is deposited over the entire surface using atomic layer deposition (ALD). It is important to minimize surface roughness prior to deposition of these ultra-thin layers.[63] The ALD technique allows good control of the few nanometres thickness with pinhole-free and highly uniform layers[64] which can result in the enhancement of the J-V non-linearity. The same lift-off procedure as described before is repeated with the front metal contact to obtain the final diode structure.

2.4.5 Microfabrication process flow

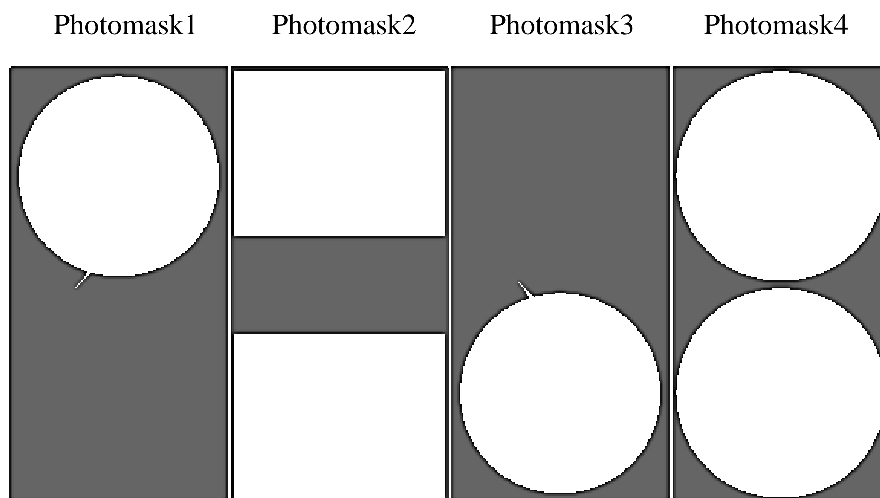

Figure 2.7 The 4 photomasks used to fabricate the rectennas (1×2 here). The radius of each circle is 255 µm as designed for the patch antennas in Table 2.3. The linewidth of the attached extension used for the diode electrodes varies gradually until it settles at 2 µm.

The cleaning procedure of the Corning glass substrate is done in a similar way to the description in 3.1 using Decon90, Acetone, and Isopropanol. The photomasks are shown in Figure 2.7. The bottom metal contact is then deposited over the substrate and patterned using the lift-off process as shown in Figure 2.8 and described as follows.

- The positive photoresist *Shipley S1805* is spun onto the substrate using a spin coater at 6000 rpm for 30 s, followed by prebaking in oven at 90ºC for 25 min.
- The substrate/resist stack is then exposed to UV light for 20 s using the designed Photomask1.
- After that, the resist is developed using *Microposit* developer. The sample is then rinsed in DIW for 3 times 30 s, and blown dry with nitrogen.
- Then the metal is deposited onto the substrate by thermal evaporation.
- The resist is then stripped away by immersing the sample into acetone for 15-20 minutes. Finally, the sample is dipped into Isopropanol for 2 minutes to remove the acetone, rinsed in DIW for 1 minute, and blown dry with nitrogen.

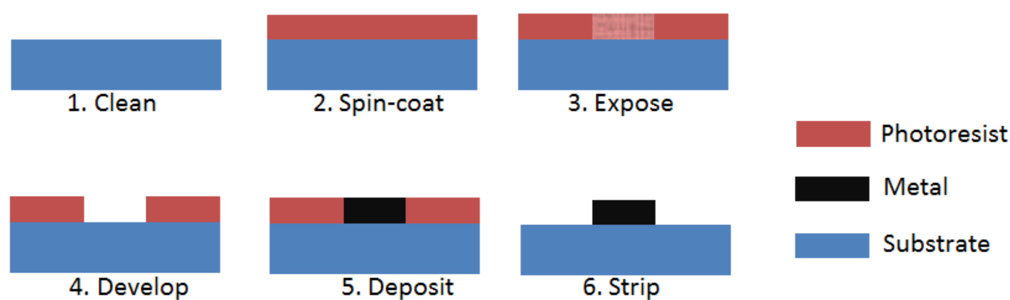

Figure 2.8 The process flow for patterning the bottom metal.

After the bottom metal attached to the substrate is realised, the dielectric(s) need to be patterned. The photoresist has a certain thermal sensitivity if exceeding a certain temperature which makes the lift-off process not appropriate for the oxide layers deposited by high temperature ALD. Thus, wet etching is chosen for patterning the surface as shown in Figure 2.9 and described in the following steps.

- The dielectrics are deposited over the entire surface using ALD.
- The positive photoresist *Shipley S1805* is spun onto the substrate using a spin coater at 6000 rpm for 30 s, followed by prebaking in oven at 90ºC for 25 min.
- The substrate/resist stack is then exposed to UV light for 20 s using the designed Photomask2 and the mask-aligner.
- After that, the resist is developed using *Microposit* developer. The sample is then rinsed in DIW for 3 times 30 s, and blown dry with nitrogen.
- The sample is then immersed in an etchant solution selective to the oxide layers. Metal oxides of interest, Ta_2O_5 and Al_2O_3, can be etched using the etchants described in Table 2.4:
- If not successful, the whole layer surface is etched using ion sputter dry etching. Photomask2 is used to pattern the photoresist (1µm thick) which would still have some thickness after dry

etching the whole surface completely. This ensures removing the dielectrics of few nanometres thickness and keeping a photoresist layer over the rectifier region. The photoresist can then be stripped away using acetone.

Table 2.4 Etchants suitable for Ta_2O_5 and Al_2O_3 films as deposited.

	Etchant		
Oxide (as deposited)	HF-H_2O[65]	BHF[65]	6:1 BHF etch rate[66]
Al_2O_3	H	H	350 nm/min
Ta_2O_5	M	L	0.2 nm/min

Etch rate: H=High, M=Medium, L=Low

- The resist is then stripped away by immersing the sample into acetone for 15-20 minutes. Finally, the sample is dipped into isopropanol for 2 minutes to remove the acetone, rinsed in DIW for 1 minute, and blown dry with nitrogen.

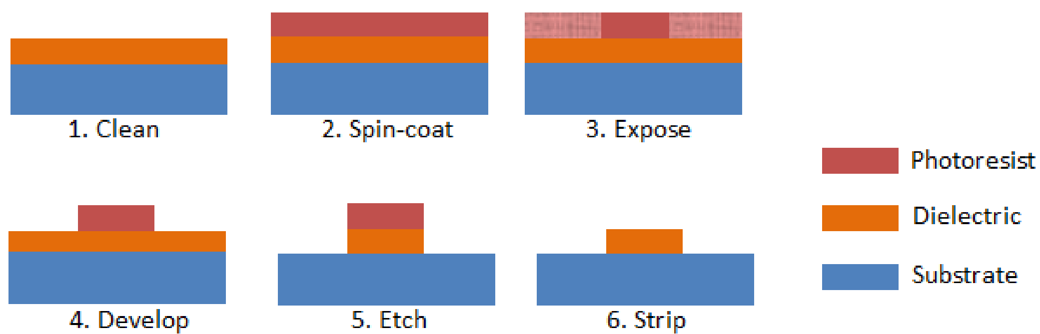

Figure 2.9 The process flow for patterning the dielectric stack.

- The following are then deposited and patterned using the same lift-off process described for the first metal using Photomask3 and Photomask4 respectively:
    - The top metal as the second electrode of the diode.
    - The metal for the antenna patches. This step was added to avoid the skin effect discussed in section *2.4.3*.

(a) (b) (c) (d)

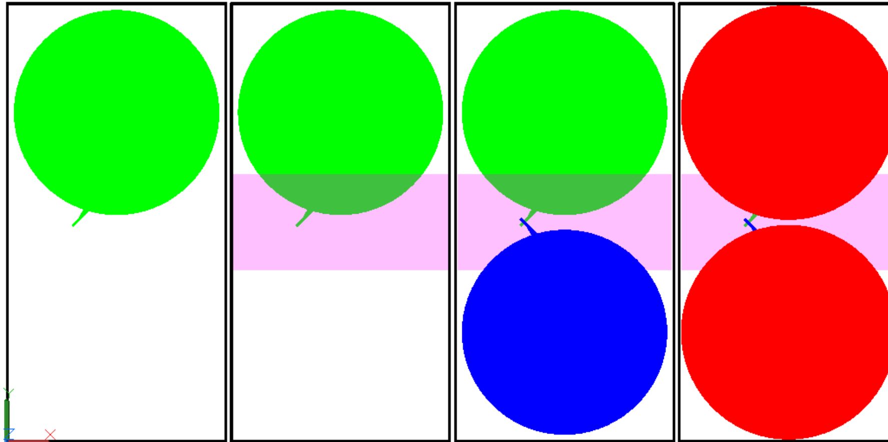

Figure 2.10 Part of the fabricated rectenna array: a) Bottom metal (green) patterned using Photomask1; b) Dielectric (transparent pink) patterned over the bottom metal using Photomask2; c) Top metal (blue) patterned using Photomask3; and d) the antenna patches (red) using Photomask4.

The rectenna fabrication steps are shown in Figure 2.10. The electromagnetic radiation is radiated towards the antenna patches, where the generated current is then rectified from one of the electrodes towards the other via the dielectric stack. The rectenna arrays are tested using a 20 mW source operating at 0.14 THz.

Diodes of smallest possible area should be fabricated at the junction rectifying the current collected at each 1×2 and 1×6 array sets as shown in Figure 2.11(a). This design shows flexibility in depositing different material composition for the diode and antenna which enhances the coupling and prevents the skin effect at THz frequency. Another advantage is the precision of the diode area at the junction which was chosen to be varying as follows: 2×2, 4×4, 6×6, 8×8, 10×10, and 12×12 μm^2.

In addition, new diodes based on surface plasmon excitation and hot electron extraction[67,68] were designed as they could be promising for THz energy harvesting. The same process flow used for fabricating the antennas will be used to fabricate these plasmonic diodes and 4 more photomasks were fitted in the same photomask set for this purpose (Figure 2.11).

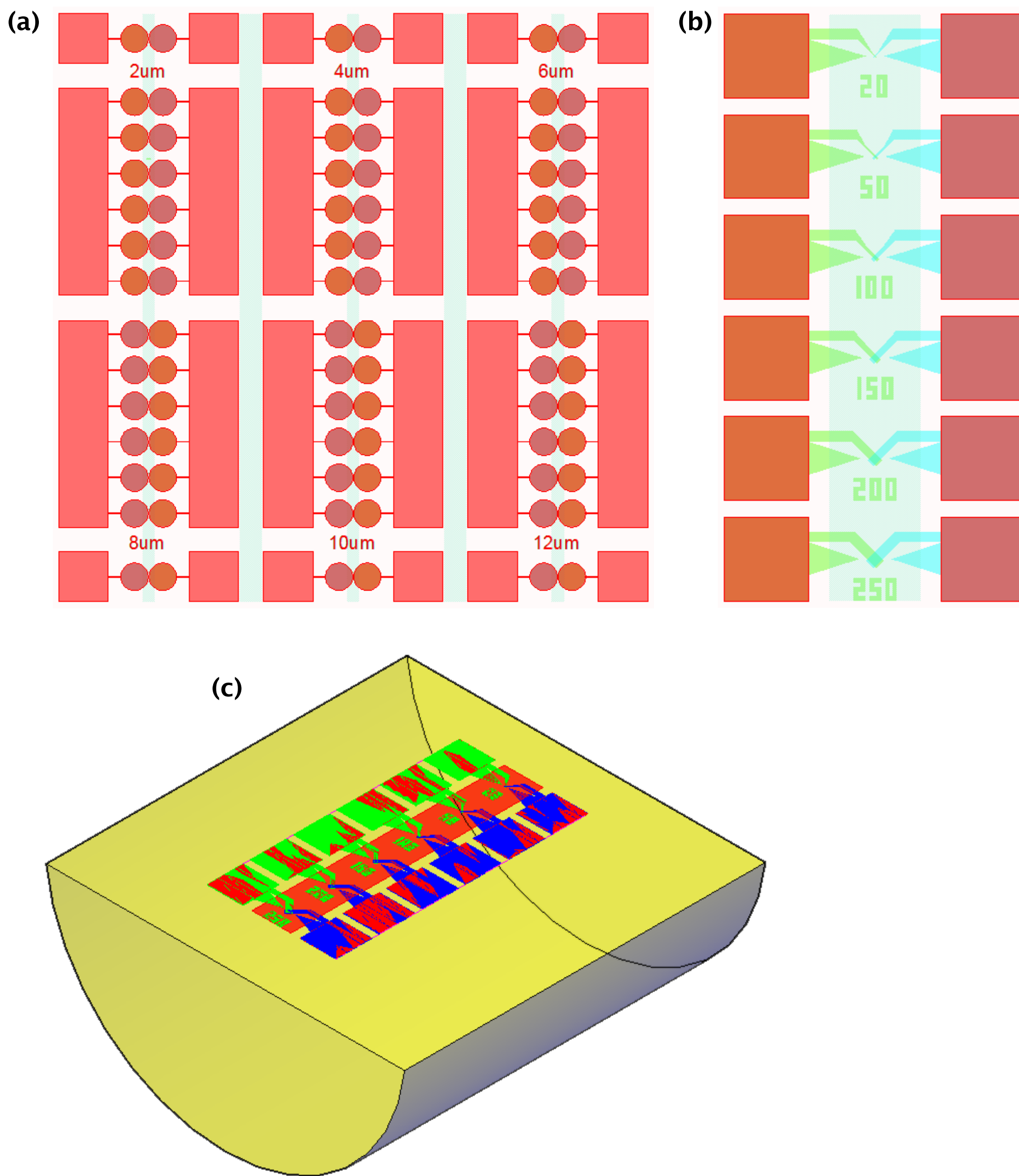

Figure 2.11 a) The actual size of the 1×2 and 1×6 rectenna arrays of diode junction area: 2×2, 4×4, 6×6, 8×8, 10×10, and 12×12 μm^2; b) The actual size of MIM/MIIM diodes with junction area: 20×20, 50×50, 100×100, 150×150, 200×200, and 250×250 μm^2; c) A 3D drawing of the plasmonic diode set in Kretschmann coupling system.

3. Fabrication and characterisation technologies

3.1 Deposition techniques

Thin films can be classified into thermal oxides, dielectrics, epitaxial layer, polycrystalline silicon, and metal films. The choice of deposition techniques is essential for the success of the devices, requiring pin-hole free thin films of excellent homogeneity especially for the dielectrics. Metals are generally deposited using physical vapor deposition (PVD) techniques not involving any chemical reaction, whereas semiconductors and dielectrics are often deposited using chemical vapour deposition (CVD) techniques. Metal films ranging from low work function (WF) aluminum to high WF gold are used as electrodes to form low-resistance contacts with the measurement system. PVD of metals can be done using thermal evaporation, electron-beam evaporation, plasma spraying, and sputtering.

3.1.1 Atomic Layer Deposition

Atomic layer deposition (ALD) is a technique, highly modified from chemical vapour deposition (CVD) process, used for depositing thin films in the form of polycrystalline or amorphous monolayers at the nanometre level. These monolayers are grown on a substrate by two or more cyclically self-limiting surface reactions offering conformality with high aspect ratio. ALD gives the deposited film exceptional conformality, excellent homogeneity, and tunable film composition. This technique was invented in 1974 as atomic layer epitaxy (ALE) for single crystal (epitaxial) layer.[69] It wasn’t until the mid1990’s that the progressive reduction of fabricated structures following Moore’s law and the higher demand for good aspect ratio needed for integrated circuits in made this technique of great attention as a promising coating technology for microelectronics.[70]

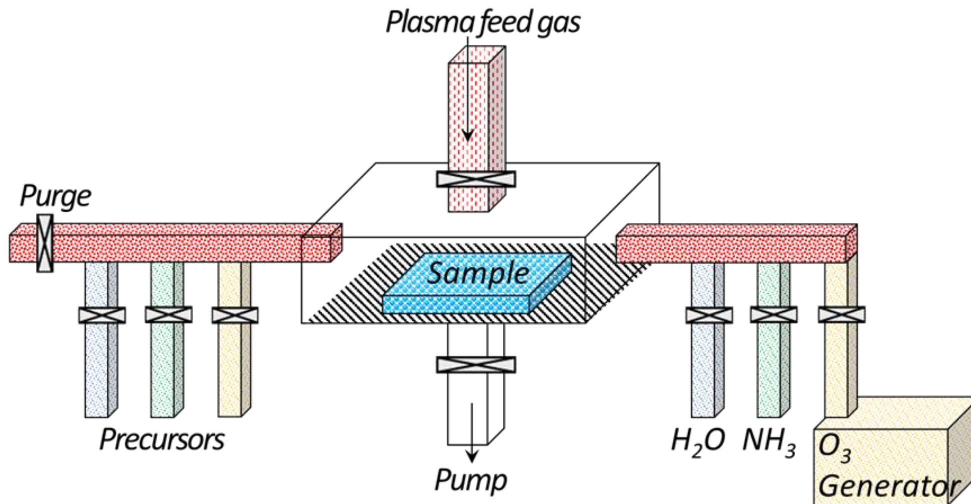

Figure 3.1 Schematic diagram of ALD reactor. Film growth requires precursors and reactant gases (H2O and NH3) in addition to either O3 supply or plasma source.

Layer formation is carried out by means of a chemical reaction of at least two starting materials called precursors. These precursors are admitted into the reaction chamber at regular intervals (cycles) one after the other. Between the gas inlets of the precursors, the reaction chamber is normally purged with an inert gas (usually argon) so that the partial reactions are separated from each other and limited to the surface. These partial reactions for layer growth are of self-limiting nature, that is, the precursor of a partial reaction does not react with itself and no further adsorption takes place.

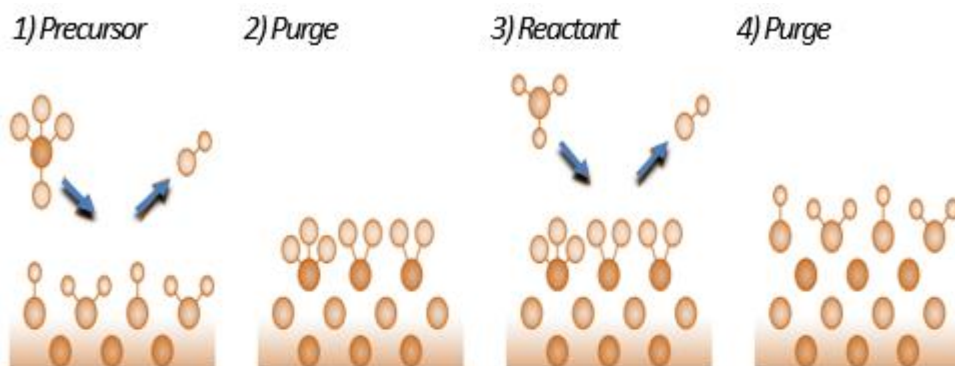

Figure 3.2 Typical ALD process illustrated in 4 steps.

For tantalum (V) oxide (Ta_2O_5), the components tantalum pentachloride ($TaCl_5$) and water (H_2O) are guided into the chamber alternately and separately through flushing steps:

a) The first reactant or precursor ($TaCl_5$) is pulsed creating a self-limiting reaction on surface.

b) Purging with inert carrier gas (Ar) to remove unreacted precursor gas and reaction products.
c) The second reactant (H_2O) is pulsed creating a self-limiting reaction on surface.
d) Purging with inert carrier gas (Ar) to remove unreacted precursor gas and reaction products.

The occurence of these 4 steps form what is so called the reaction cycle, which is repeated until the desired layer thickness is obtained. Ideally, each step runs completely the precursor molecules are chemisorbed until the surface is completely occupied. The amount of the layer material deposited in each reaction cycle is constant. Depending on the process parameters, the material, and the reactor, a layer of 0.1-3 Å thickness can be generated per cycle. The deposition rate of the ALD or growth per cycle (GPC) need to take into consideration:

1) the spatial expansion of the starting materials leading to the steric hindrance (relating to the spatial arrangement of atoms in molecule) which causes parts of the surface to be partitioned and thus prevents good adsorption.
2) incomplete partial reactions, where areas which cannot participate in the partial reaction are available on the surface.

Deposition in real processes is, however, non-ideal. The pulse time should be not too long to avoid affecting the precursor in the next ALD cycle with undesirable gas phase reactions in the sample chamber. It should also be not too short resulting in non-uniformity and poor quality of the high-k oxides. Giving enough time for each reaction step to complete results in high-purity coatings even at relatively low temperatures. Neglecting the different growth rate at the beginning of the deposition due to the surface chemistry of the substrate material, ALD has very good control of layer thickness below 10 nm which grows in proportion to the number of reaction cycles. Despite its low throughput and large gas consumption, ALD is characterised by excellent homogeneity making it suitable for coating more structured surfaces and particularly needed for research and development.

3.1.2 Sputtering

Sputtering is a PVD coating technology where positive ions created by plasma are bombarded towards the metal or oxide target inside the vacuum chamber causing the material to sputter, as indicated in Figure 3.3. Sputtering can be one of four types: RF, magnetron DC, bias, and collimated sputtering. RF sputtering is the only one which can be used to deposit dielectric films, which is done in a vacuum chamber at a pressure of 10^{-3} Torr in the presence of Ar gas. DC

sputtering can only be done on conductive targets (metals), whereas RF sputtering can be used for both metal and dielectrics.

The vacuum chamber is evacuated to a pressure in the scale of 10^{-6} torr to remove water, oxygen, nitrogen, and other gas molecules, followed by filling it with argon gas and applying a very large negative dc bias to the cathode. A plasma glow discharge is then generated between the plates resulting in the loss of an electron for each argon atom which makes them positively charged ions (cations). A very large electric field is applied between the two electrodes using voltages typically in the range 1-to-2 kV applied across a distance of ~8-to-12 cm between the target and the sample. Argon cations are accelerated by this electric field towards the cathodic target at the bottom, thus bombarding the target. The transfer of their high energy causes the target particles to be sputtered from the bottom cathodic target towards the top rotating anodic sample holder. The electrons emitted during this process interact with neutral Ar atoms creating more Ar cations thus forming a self-sustained plasma glow discharge. This self-sustainability is impeded if an insulating material is used as the target due to the accumulation of positive charges on the target surface from the Ar cations. However, radio frequency (RF) sputtering, where the power supply is operated at 13.56 MHz, involves bombarding the target with cations and electrons consecutively at low pressure and temperature resulting in charge neutralization. This enables using dielectrics as the target material, which is an advantage over DC sputtering.

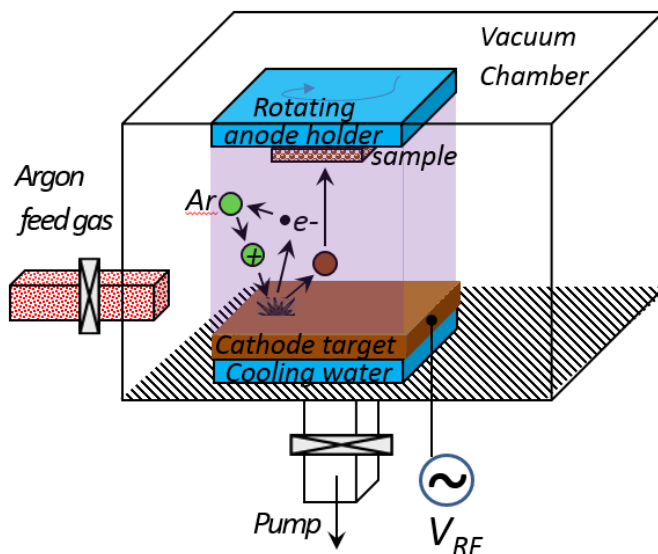

Figure 3.3 Schematic of RF sputtering system: Argon is ionized and accelerates towards the target (cathode) with high energy which releases atoms from the target surface and are forced to move towards the grounded anode by the strong electric field created by V_{RF}.

3.1.3 Thermal Evaporation

Thermal evaporation is frequently used in microfabrication due to its simplicity and low cost. The source material is heated inside a filament in vacuum chamber until its surface atoms obtain sufficient energy to leave the surface. The metal melts and turns into vapour particles moving at one to two times the thermal energy ($3k_BT/2$) in the order of 0.1-0.2 eV[71] under vacuum towards the target substrate where they condense to solid state. In this work, the substrate is positioned under rotation above the evaporating material for upward evaporation using a Moorfield evaporator, whereas it is positioned fixed below the evaporating material for downward evaporation using the Edwards evaporator. The pressure in the chamber must be low at the 10^{-6} mbar scale or below to minimize the traces of water, oxygen, and nitrogen molecules in the chamber and avoid the collision between the remaining traces of these gas molecules and the evaporated metal. At such low pressure, the particle mean free path is longer than the distance between the substrate and the source material. The mean free path is the average distance the particles can travel in the vacuum chamber before colliding with a trace material. The vapourized metal particles move from the filament towards the cooler substrate surface, where they condense by nucleation. This results in the growth of the film to the desired thickness at controllable depositing rate which could be chosen between 0.1 and 10 nm per second depending on the power and the melting temperature of the metal, which becomes lower with higher vacuum. Cr as compared to Au and Al, for instance, requires much higher vacuum than Au and Al to be deposited at much lower rate.

The samples are loaded into the chamber which is pumped with a diffusion pump (Edwards), cryo-pump, or a turbo-pump (Moorfield) to attain vacuum. The diffusion pump contains oil at the bottom which turns to vapour moving upwards when heated. The water cooling system surrounding the diffusion pump condenses the evaporated oil inside the diffusion pump to oil droplets which fall to the bottom where they get heated. Before these droplets get evaporated again, they push air molecules forcing them to get sucked by the mechanical pump. Liquid nitrogen is used for the Edwards system to stop vacuum gases entering the chambers. The turbo-pump, however, has a large number of blades which push the air molecules forcing them to be sucked by the mechanical pump. It also has water cooling system and requires no liquid nitrogen.

The melting point of each metal depending on the pressure and the choice of filament carrying the metal (boat, coil, basket, crucible) is referred to *Lesker* supplier website[72].

3.2 Scanning electron microscopy and transmission electron microscopy

Scanning electron microscopy (SEM) and transmission electron microscopy (TEM) are important tools to investigate the structures of electronic devices in the micro and nano scales respectively. Referring to Figure 3.4, both techniques operate by placing the sample in high vacuum, bombarding it downwards with an electron beam created by heating a tungsten or LaB6 filament at very high electric field; typically with an applied voltage between 60 and 120 kV. The image is detected on a phosphour fluorescent screen with electromagnetic lenses used for magnification and focusing the beam. Electron microscopy is characterised by the short wavelength of an electron associated with the DeBroglie wavelength of 1.23 nm which makes it capable of imaging nanostructures with very high (voltage-dependent) resolution of typically 1-5 nm. Optical microscopy offers a resolution not lower than 200 nm with its associated photons of larger electromagnetic wavelengths in the visible regime.

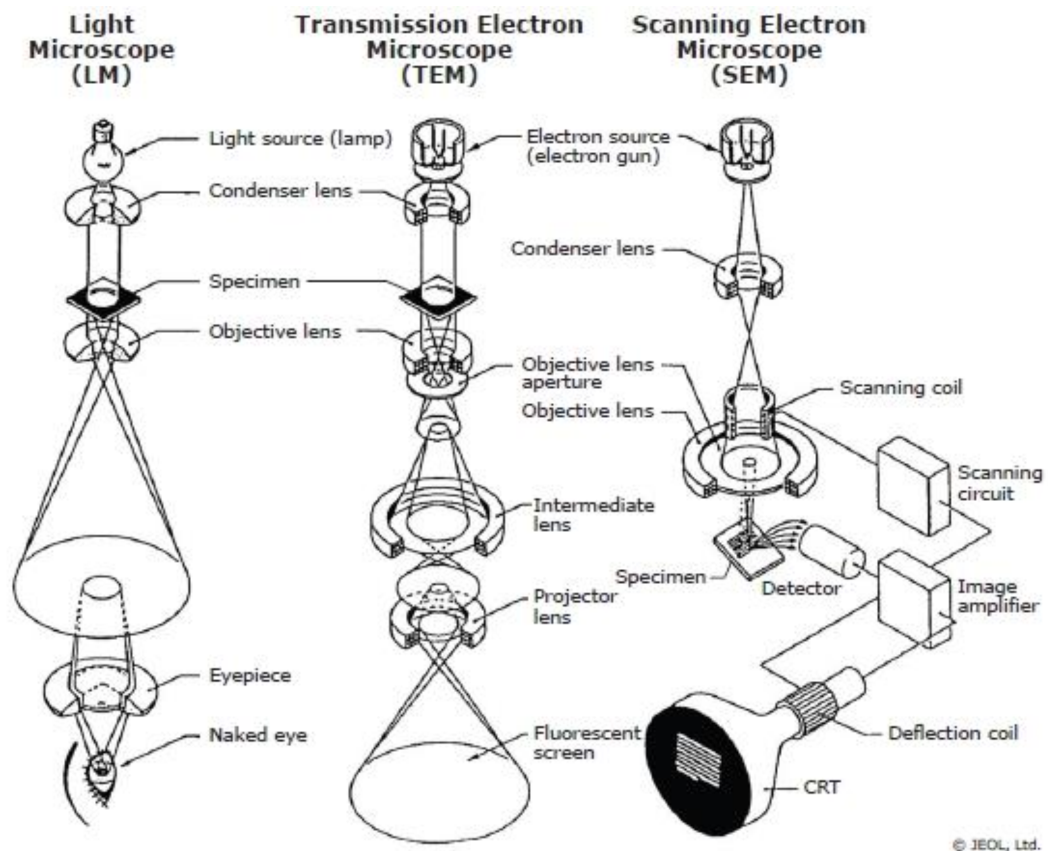

Figure 3.4 Schematic diagrams of the light microscope, the TEM, and the SEM[73]

SEM produces 3-D images of 2 nm average resolution, whereas TEM produces 2-D images of 0.2-0.5 nm average resolution[74] and requires 1 day for preparing the sample by carbon coating, ultra-microtome sectioning, and staining with electron-absorbing heavy metals. However, SEM is limited to imaging the surface topography by detecting the scattered secondary electrons emitted from the sample surface after excitation by the energy transfer by the electrons in the electron beam. It cannot be used to create a cross-sectional image of the layer structure, and its magnification is limited to 0.1 million X. TEM can do this where the electron beam can pass through the layers (of total thickness typically less than 200 nm) forming the image from the primary electron beam electrons with 5 million X magnifying capability. HR-TEM or high resolution mode of transmission electron microscopy allowing the formation of nanoscale images based on phase contrast, which could reach a resolution as small as 0.5 Å[75] where atoms and defects can be distinguished.

3.3 Electron-beam lithography

Electron-beam or e-beam lithography is a maskless nanotechnology deposition technique of patterning capability in the sub 2 um down to several tens of nanometres and of precision (Figure 3.5). A focused beam of electrons patterns the surface by exposure of an electron-sensitive resist. This is done through a layout used for direct-writing which can be changed anytime with no need to fabricate the mask for each new pattern as required for the photolithography technique. The electron beam changes the solubility of the resist. The samples are then immersed in developer to get the desired solubility pattern. Using positive resist, the regions exposed to e-beam becomes soluble leaving the unsoluble non-exposed regions, whereas using negative resist, the regions exposed to e-beam becomes unsoluble leaving the soluble non-exposed regions. As with photolithography, etching or lift-off can be used for patterning the material structure.

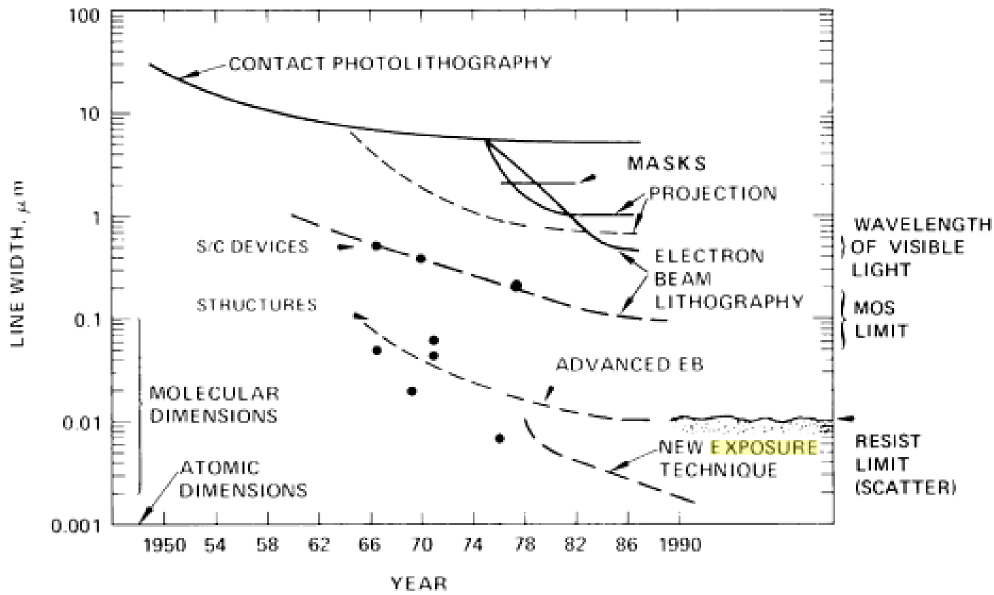

FIG. 1.21 History and projection of the resolution trends in lithography. ———, Production, - - -, R&D.

Figure 3.5 The history and projection of the resolution trends in lithography.[76]

The writing process is extremely slow and follows the exposure parameters related by the following formula:

$$D \times A = T \times I \qquad (3.1)$$

where D, A, T, I are the dose, exposed area, exposure time, beam current respectively.

E-beam lithography is limited to very low throughput due to its slow exposure time with an extremely small field scanning resolution of less than a mm^2 requiring the stage to move in between. This requires the minimization of patterned area to minimize the exposure time, which would also increase the writing resolution and requires increasing the minimum dose to maintain the noise level. Patterning with this technique can take million times longer than the standard photolithography with photomask projection which has a resolution lower than 40 mm2 and requires no stage movement. This technique suits THz rectenna arrays where sub-micron dimensions are required for the rectifiers and patterning area can be small enough for the exposure to be done in 1 day.

The pattern is made on silicon substrates which are first spin coated with a polymer resist layer sensitive to electron beam exposure, followed by soft baking on a hot plate. While SEM is commonly used for e-beam exposure, STEM (Scanning Transmission Electron Microscope), FIB (Focused Ion Beam), or helium ion microscope can also be used for this purpose. The samples are

placed inside the e-beam chamber (SEM is commonly used for this), where an electron beam is bombarded onto the sample following the design pattern of the structure. After that the sample is immersed in developer removing the resist parts irradiated by the electron beam in the case of positive resist. It's then cleaned and blown with nitrogen gun. Metal deposition is then done all over the substrate surface using thermal evaporation or sputtering. The unwanted metal is then removed by lift-off using acetone which dissolves the undeveloped resist, whereas the remaining metal stays intact over Si following the e-beam exposure pattern.

3.4 Atomic force microscopy

Scanning probe microscopy techniques are used to create an image of the surface topography of materials by regulating the gap distance between the sample and the probe using a feedback loop. These techniques include: atomic force microscopy (AFM), magnetic force microscopy (MFM), scanning thermal AFM (SThAFM), and scanning tunnelling microscopy (STM), which record the image signal based on van der Waals forces, magnetic stray field, heat-to-electricity conversion, and tunnelling current respectively.

AFM or atomic force microscopy is an imaging technique with very high lateral resolution, less than 1 nm, used typically to study the topography of the deposited film surface, analyse the surface roughness, and calibrate film thickness for deposition techniques. This technique requires no vacuum and minimum sample preparation. It creates a 3-D topographical image of the surface of any material by scanning a cantilever (typically 50-400 µm) of very sharp tip (typically 5-20 nm radius and 10-25 µm hight) over a certain region by piezoelectric positioning system along X and Y directions. The cantilever deflects up or down according to the fine sub-nanometre features of the material surface. These deflections are governed by forces into and away from the surface: the attractive force bringing the cantilever tip towards the surface, and another repulsive force deflecting the tip away from the surface upon approaching it (when the tip-to-sample separation distance becomes close to zero). AFM can run in contact mode with interatomic forces of short-range interactions (Å) requiring a cantilever of low stiffness so that it does not deform the surface upon contact. In non-contact mode, the amplitude of the tip is typically a few nanometres, where van der Waals forces become stronger reducing the cantilever resonance frequency to adjust the tip-to-sample distance, where this distance is associated to Z position forming the topographical image. AFM can also run in tapping mode governed by long-range forces (van der Waals, electrostatic, and magnetic) where the tip oscillations are damped to maintain its amplitude when close to the surface (5-15 nm) keeping an intermittent contact. Using any mode, a laser beam is incident on the top of the cantilever tip and reflected towards a photodiode which detects and

monitors all cantilever deflections from the surface in 0.5 nm range. A constant laser position is maintained using a feedback loop which keeps a constant accurate distance between the tip and the surface to ensure forming an accurate topographic image of the surface features.

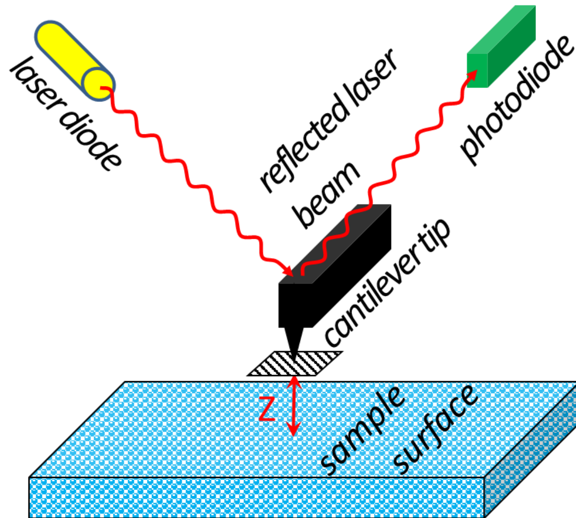

AFM: cantilever tip scans the surface with its up and down movement (Z-direction) at constant force recorded by position sensing photodiode and moves in an arbitrary X direction (parallel to surface plane) certain number of times to create a 3-D topographical image.

All AFM images in the thesis are scanned using a Veeco CP-II AFM on contact mode up to 512×512 data points. It has a maximum DAC (digital-to-analog converter) lateral/vertical resolution of 0.25/0.025 Å and a maximum lateral/vertical scan range of 90/7.5 um.[77] However, the actual lateral resolution of the measurement is limited by the ratio of the side of the squared AFM image to the data points. Assuming a 1-5 μm image scanned at 512×512 data points, the lateral resolution is then calculated to be ~2-10 nm for each data point.

3.5 Spectroscopic ellipsometry

Spectroscopic ellipsometry (SE) is an optical characterisation technique, emerging in 1945,[78] used to find the composition, crystallinity, doping concentration, surface roughness, conductivity, and thickness of thin films, mainly dielectrics. The change of polarization (Ψ) and the phase difference (Δ) upon reflection or transmission of an elliptically polarized light beam incident to the material surface as a function of the energy spectra of light is measured and compared to an assumed model of the structure. These measured terms allow the determination of the thickness of the film, which could range in thickness between a few Angstroms and several micrometres, and the optical

constants of the material in the near-UV, VIS, and near-IR. It works best for layer thickness not much smaller or greater than the incident light wavelength, e.g. 5-1000 nm thick layers using light of 500 nm wavelength, and for roughness not less than ~10% of incident light wavelength, and for thickness variation not more than 10% over the spot width of the incident light.[79]

Light is composed of the visible electromagnetic waves traveling through space. The way that the electric and magnetic fields of these waves behave with respect to time and space is described by their polarization. It must be of specific orientation and phase at a given point, of distinct shape following a specific path, in order to be polarised so that it can be measured by SE. Light propagates in the z-direction (Figure 3.6) and the electric field is a linear combination of the x and y components describing the polarization of light as described by the following equation:

$$E_x(z,t) = A_x \times cos(\omega t - k_z + \varphi_x)$$
$$E_y(z,t) = A_y \times cos(\omega t - k_z + \varphi_y) \tag{3.2}$$

The relative phase is $\varphi = \varphi_y - \varphi_x$ and the relative amplitude is a relation between A_x and A_y.

Light can be linearly polarised when E(z,t) propagates on a bounded straight line in the xy-plane of centre (0,0) assuming φ = ±kπ , for k = 0,1,2, · · · (in phase) in equation (3.2) which leads to the following equation:

$$E_y = \pm \frac{A_y}{A_x} \times E_x \tag{3.3}$$

Light is circularly polarized when E(z,t) propagates on a circle in the xy-plane of centre (0,0) assuming φ = π/2 ± pπ , for p = 0,1,2, · · · (out of phase) and the same amplitude which leads to the following equation:

$$E_x^2 + E_y^2 = A^2 \tag{3.4}$$

Ellipsometry polarization is elliptical which combines orthogonal waves of arbitrary phase and amplitude and can be described by the following equation:

$$\frac{E_y^2}{A_y^2} + \frac{E_x^2}{A_x^2} = 1 \tag{3.5}$$

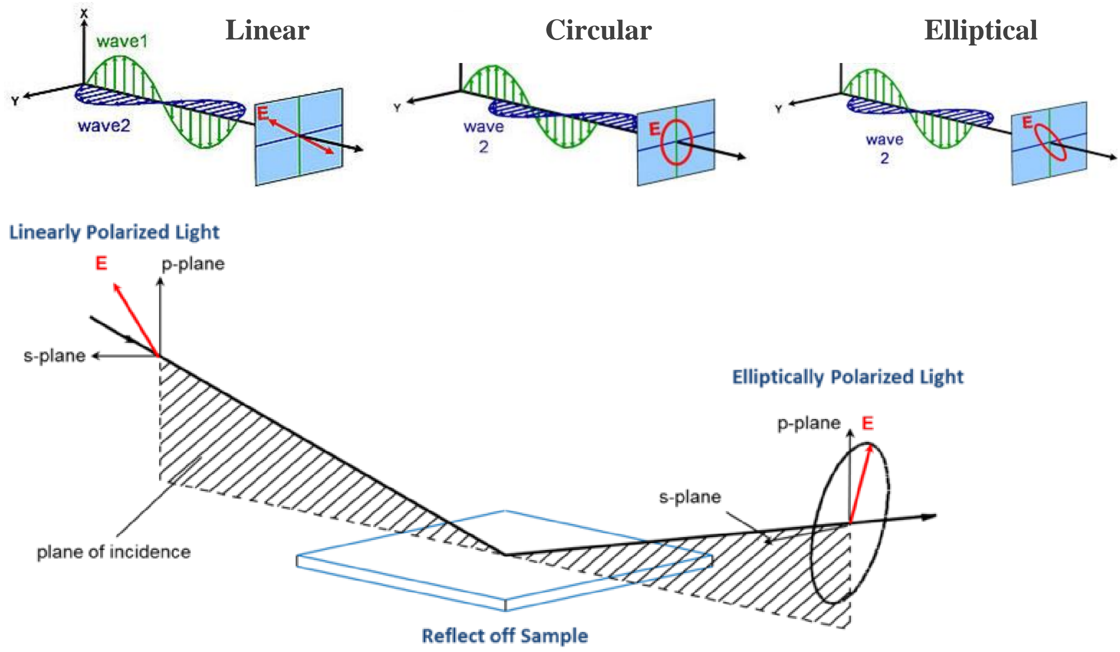

Figure 3.6 Illustration of linear, circular, and elliptical polarised light and of beam path in ellipsometry.[80]

While light wave travels across the materials, phase velocity and wavelength change depending on the refractive index and some light wave energy is lost to the material. Reflection and refraction of light occurs at each interface according to Snell's law, which forms multiple beam in the layer. While light is transmitted or reflected, ellipsometry uses the mutual reaction between s and p components to measure the polarization change (amplitude and phase) according to the following equation[81]:

$$\rho = tan(\psi)e^{i\Delta} \tag{3.6}$$

A light beam is illuminated and filtered using a polarizer, maintaining the requisite field orientation to make it linearly polarized. After reflection from the surface of the sample, the beam becomes elliptically polarized and is analysed by another rotating polarizer. It is then converted to an electronic signal by a detector and compared to input polarization to measure the beam/sample interaction parameters defining the polarization change Psi (Ψ) and Delta (Δ): $\Psi = A$ and $\Delta = 2P + \pi/2$, where A and P are the analyser and polarizer angles respectively under null conditions. Using a standard model for each material, thickness and optical constants of the deposited material are calculated from Fresnel's equations. The difference between the model and measured data is calculated as the Mean Squared Error (MSE) which needs to be less than 6 for reliable results. Film thickness is determined from the light portion travelling through the layer

and returning to the surface, where the interference between the reflected light and the light that travels through the film includes amplitude and phase information. The optical constant of a material depends on wavelength and is best described by the Cauchy equation for transparent films such as ultra-thin oxides:

$$n(\lambda) = A + \frac{B}{\lambda^2} + \frac{C}{\lambda^4} \tag{3.7}$$

where A, B, and C are constants to be fitted for a model-measurement matching at a minimum MSE.

3.6 X-ray Photoelectron spectroscopy

X-ray photoelectron spectroscopy (XPS) is a technique which uses X-rays of 200-2000 eV photon energy to study the elemental composition, chemical state, and electronic state of the surface region of a material to a depth of approximately ~8 nm. A spectrum is produced, which is the number of detected photoelectrons (emitted electrons) versus the corresponding kinetic energy. During irradiation by X-ray, the measured kinetic energy and the number of photoelectrons within this depth are determined by the photon energy and the respective binding energies which gives rise to a peak for each element in the photoelectron spectrum. This allows a quantitative analysis of the surface composition associated to the intensity peaking at certain kinetic energy. Only the elements with an atomic number (Z) of 3 and above can be detected in the parts per thousand range, whereas it is difficult to detect hydrogen (Z = 1) or helium (Z = 2).

The sample is placed in ultra-high vacuum (UHV) of pressure in the order of 10^{-9} mbar. X-ray sources create either Mg Kα radiation (hν = 1253.6 eV) or Al Kα radiation (hν = 1486.6 eV) which give rise to kinetic energy (KE) of photoelectrons in the range of 0-1250 eV or 0-1480 eV respectively. This KE measured by the instrument is defined by:[82]

$$KE = h\upsilon - BE - \phi_s \tag{3.8}$$

where $h\upsilon$ is the photon energy from the x-ray source, BE is the binding energy which is the energy difference between the ionized (after leaving the atom) and neutral atoms, and ϕ_s is the work function dependent on the spectrophotometer and the material.

XPS involves detection of photoelectrons travelling through the sample, escaping into the vacuum, and reaching the detector without any energy loss. Detection can be considered strong

and reliable at depth of 8 nm or below where the measured photoelectron KE is unique enough to identify each element. The number of photoelectrons escaping into the vacuum is exponentially attenuated with the depth of the material where they interact with the material undergoing inelastic collisions, recombination, or trapping in different excited states. XPS can be used for tunnelling structures to identify the elements of the ultra-thin oxide layers and any interfacial layer.

4. The Physics of quantum mechanical tunnelling

4.1 Overview of the concept

The first motivation on resonant tunnelling was by Gurney in 1929[83] giving attention of how a particle of low energy equal to the quasi-stationary discrete energies of the nucleus can penetrate it. The invention of transistors in 1947 gave further attention to quantum tunnelling until tunnel diodes were discovered experimentally for the first time by Esaki in 1957[84] in p-n junction devices, and the results were explained by him in 1974[85] suggesting resonant transmission in tunnelling.

According to classical mechanics, a particle can either pass over the barrier or rebound back after colliding with it according to the law of conversation of energy where the sum of the kinetic energy and potential energy must stay constant. However, this transport is not allowed when the barrier is higher than the kinetic energy of the particle. Quantum mechanical tunnelling is a physical phenomenon whereby the particles penetrate or pass through one or more potential barriers which are classically forbidden. Each particle moves through the barrier as an electromagnetic wave described by Schordinger equation in 1926. The wave has an amplitude, related to the probability of finding it (de Broglie in 1923), which decreases exponentially while penetrating through the barrier. Heisenberg uncertainty principle ($\Delta E.\Delta t$ < constant) implies that it is possible to violate the principle of conversation of energy by the electron by borrowing some energy ΔE for some time not exceeding Δt in order to tunnel through a barrier. Based on this, the relative probability of tunnelling occurrence increases with higher particle energy, lower barrier height, and thinner barrier thickness (width), as these factors allow sufficient time for the electron to return back its borrowed energy after tunnelling.

There have been several attempts on calculating the tunnelling current in MIM structures using the WKB approximation which first appeared in 1963 by Simmons using similar electrodes.[86] The first calculations on tunnelling were reported in 1951 by Holm[87] and later extended in 1962 by including the temperature dependence and the image force correction.[88] The model used to design the diodes in this work[89] is based on the Tsu-Esaki method[90] for calculating the tunnelling current using a piecewise transfer matrix approach. The calculations used are described in the next sections. The model is applicable for multi-barrier tunnelling, i.e. MIM and MIIM diodes.

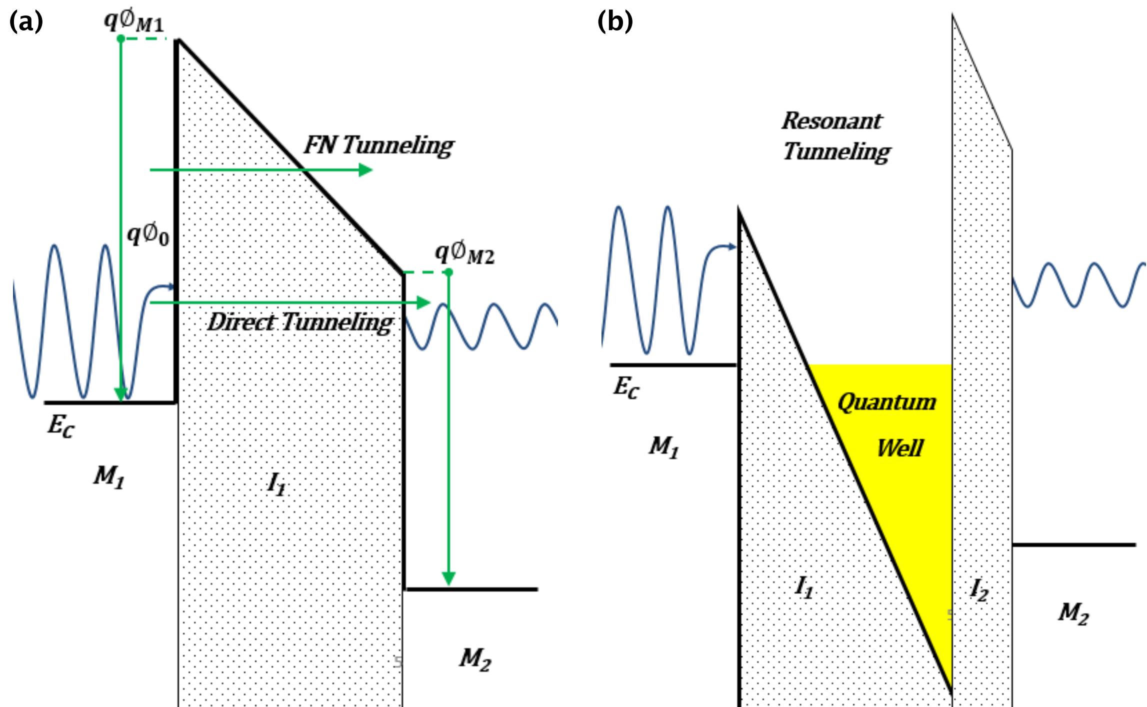

Figure 4.1 Quantum tunnelling through a barrier (or more) results in the same energy of the tunnelled electrons but with smaller amplitude. (a) Tunnelling could be direct or Fowler-Nordheim (FN). (b) When two or more dielectrics are used, a quantum well (yellow) can be formed for resonance to occur.

Direct tunnelling [Figure 4.1(a)] is predicted for ultra-thin oxide layers going into the conduction band of the other metallic contact and becomes negligible through a relatively thick oxide layer of more than several nanometers.[91] This type of tunnelling occurs at low electric field when the potential across the dielectric is lower than the potential barrier at the metal/dielectric interface. Fowler-Nordheim (FN) tunnelling [Figure 4.1(a)] is predicted to affect the J-V characteristic in the high electric field regime for thin and thick dielectrics. This mechanism is strongly dependent on the oxide electric field and occurs above a critical value approaching 6 MV/cm for SiO_2[92] and as low as 1 MV/cm for Ta_2O_5 and Nb_2O_5[93].

Resonant tunnelling can occur in structures of two or more barriers forming a quantum well when the energy level of the mobile charge carrier (electron) is aligned with one or more eigen- states in the well [Figure 4.1(b)]. The probability of resonant tunnelling increases by the way the structure is engineered, i.e. deeper and wider quantum wells allow more bound states to be formed. The barriers could be semiconductors, typically GaAs layer (as a quantum well) sandwiched in between two AlGaAs semiconductor layers contacted with doped n+ GaAs electrode layers. However, semiconductor-based diodes are not suitable for integration with dielectric antennas in rectenna energy harvesters. Dielectric based diodes offer additional advantages over other

semiconductor based diodes. They offer easier nano-scalability in planar fabrication and tuning capability of the structures using different thicknesses of ultra-thin layers and different materials to enhance the resonance level in double dielectric structures.

4.2 The generalised tunnelling current formula

Tunnelling can be described from many-particle[94] and independent-particle[95] points of views. The interactions between the electrons will be ignored here. The electron is transferred from the first metal M_1 of occupation state $\psi_1(x_1)$ passing through the dielectric layer barrier. The wave function representing the electrons inside the barrier is considered to drop exponentially before reaching the interface with the second metal M_2 of occupation state $\psi_2(x_2)$.

The total tunnelling current density is the difference of current flowing from M_1 electrode to M_2 electrode J_{M1-M2} and the current flowing in the opposite directions such that J_{M2-M1}:

$$J = J_{M1-M2} - J_{M2-M1}$$

$$dJ_{M1-M2} = q.\upsilon_x.g_1(k_x).T(k_x).f_1(E).[1 - f_2(E)].dk_x \quad (4.1)$$

$$dJ_{M2-M1} = q.\upsilon_x.g_2(k_x).T(k_x).f_2(E).[1 - f_1(E)].dk_x$$

where k_x is the wave vector, $T(k_x)$ is the transmission probability, $g_1(k_x)$ and $g_2(k_x)$ are the density of states of the metals M1 and M2 respectively near their interfaces with the dielectric, υ_x is the velocity of the electrons, and $f_1(E)$ and $f_2(E)$ are the energy distribution functions representing the probability of occupation of states near the dielectric interfaces.

The calculations used to derive the tunnelling current are based on the De Broglie dispersion relation between the total energy of the particle (E), its mass (m), and its momentum (P): $E^2 = (m.c^2)^2 + (P.c)^2$. The particle here is the electron which behaves as a matter and wave at the same time. Thus, its kinetic energy can be expressed as $E = \hbar\omega$ and its momentum P as $E = \hbar k$ where $k = k_x + k_y + k_z$ is the wave vector. Substituting these terms into equation leads to the following dispersion relation: $E = \frac{\hbar^2 k^2}{2m} = \frac{\hbar^2}{2m}k_x^2 + \frac{\hbar^2}{2m}k_y^2 + \frac{\hbar^2}{2m}k_z^2$

Thus, assuming tunnelling to be in the x-direction, $E_x = \frac{\hbar^2}{2m}k_x^2$ and the velocity and energy components can be expressed as: $\upsilon_x = \frac{1}{\hbar}\frac{dE}{dk_x} = \frac{\hbar}{m}k_x$ and thus:

$$v_x . dk_x = \frac{dE_x}{\hbar} \tag{4.2}$$

Given the density of k_x states $g(k_x) = \int_0^\infty \int_0^\infty g(k_x, k_y, k_z)\, dk_y dk_z$, and the wave vector components in L³ cube $\Delta k_x = \Delta k_y = \Delta k_z = 2\pi/L$, the density of states can be expressed as $g(k_x, k_y, k_z) = 2/[L^3(\Delta k_x . \Delta k_y . \Delta k_z)] = 1/4\pi^3$. Thus $g_1(k_x) = g_2(k_x) = 1/4\pi^3$ and:

$$g(k_x) = \int_0^\infty \int_0^\infty \frac{1}{4\pi^3} dk_y dk_z \tag{4.3}$$

Substituting equations (4.2) and (4.3) into the integration of equations (4.1)

$$J_{M1-M2} = \frac{q}{\hbar . 4\pi^3} . T(E_x) . dE_x . \int_0^\infty \int_0^\infty f_1(E) . [1 - f_2(E)]\, dk_y dk_z \tag{4.4}$$

$$J_{M2-M1} = \frac{q}{\hbar . 4\pi^3} . T(E_x) . dE_x . \int_0^\infty \int_0^\infty f_2(E) . [1 - f_1(E)]\, dk_y dk_z$$

Equations (4.4) in cartesian coordinates can be transformed into polar coordinates using $k_y = k_\rho \cos(\tan^{-1} \frac{k_z}{k_y})$ and $k_z = k_\rho \sin(\tan^{-1} \frac{k_z}{k_y})$ where $k_\rho = \sqrt{k_y^2 + k_z^2}$. Thus, $E_\rho = \frac{\hbar^2}{2m} k_y^2 + \frac{\hbar^2}{2m} k_z^2 = \frac{\hbar^2}{2m} k_\rho^2$ and $E_x = \frac{\hbar^2}{2m} k_x^2$, and thus equations (4.4) can be expressed as:

$$J_{M1-M2} = \frac{4\pi . m . q}{h^3} \int_{E_{min}}^{E_{max}} T(E_x) . dE_x \int_0^\infty f_1(E) . [1 - f_2(E)]\, dE_\rho \tag{4.5}$$

$$J_{M2-M1} = \frac{4\pi . m . q}{h^3} \int_{E_{min}}^{E_{max}} T(E_x) . dE_x \int_0^\infty f_2(E) . [1 - f_1(E)]\, dE_\rho$$

The charge transport is assumed to be due to electrons tunnelling from the conduction band. The energies, E_{min} and E_{max} are the highest conduction band edges of the two electrodes and the dielectric respectively. The total tunnelling current density is:

$$J = J_{M1-M2} - J_{M2-M1} = \frac{4\pi.m.q}{h^3}\int_{E_{min}}^{E_{max}} T(E_x).dE_x \int_0^{\infty} [f_1(E) - f_2(E)]\ dE_\rho \tag{4.6}$$

4.3 Tsu-Ezaki equation

$\int_0^{\infty}[f_1(E) - f_2(E)]\ dE_\rho$ is the difference in the supply of electrons at the dielectric interfaces.

The probability that a particle will have energy E is described by the Fermi-Dirac energy distribution function at thermal equilibrium: $f(E) = \frac{1}{1+\exp\left(\frac{E_x+E_\rho-E_f}{k_B T}\right)}$

$$\int_0^{\infty} f(E)dE = \int_0^{\infty} \frac{1}{1+\exp\left(\frac{E_x+E_\rho-E_f}{k_B T}\right)} dE_\rho = \left[k_B\text{T}.\,ln\left(\frac{1}{1+e^{-\left(\frac{E_x+E_\rho-E_f}{k_B T}\right)}}\right) + C\right]_{\rho=0}^{\rho=\infty}$$

$$= k_B\text{T}.\ln[1 + e^{-\left(\frac{E_x-E_f}{k_B T}\right)}]$$

Thus,

$$\int_0^{\infty} [f_1(E) - f_2(E)]\ dE_\rho = k_B\text{T}.\ln\left[\frac{1+e^{-\left(\frac{E_x-E_{f1}}{k_B T}\right)}}{1+e^{-\left(\frac{E_x-E_{f2}}{k_B T}\right)}}\right]$$

Therefore, equation (4.6) can be expressed as:

$$J = \frac{4\pi.m.q.k_B\text{T}}{h^3}\int_{E_{min}}^{E_{max}} T(E_x).\ln\left[\frac{1+e^{-\left(\frac{E_x-E_{f1}}{k_B T}\right)}}{1+e^{-\left(\frac{E_x-E_{f2}}{k_B T}\right)}}\right] dE_x \tag{4.7}$$

which is Tsu-Ezaki equation used for resonant tunnelling diodes.

Assuming $T = 0\ K$, Fermi-Dirac function $f(E)$ can be replaced by a step function as follows:

$$f_1(E) = f(E - E_{f1}) = \begin{cases} 1\ for\ E \le E_{f1} \\ 0\ for\ E > E_{f1} \end{cases}$$

$$f_2(E) = f(E - E_{f2}) = \begin{cases} 1\ for\ E \le E_{f2} \\ 0\ for\ E > E_{f2} \end{cases}$$

And thus,

$$\int_0^{\infty} [f_1(E) - f_2(E)]\ dE_\rho = \begin{cases} E_{f1} - E_{f2}\, for\, E_x \leq \\ E_{f1} - E_x\, for\, E_{f2} \leq \\ 0\, for\, E_x > E_{f1} \end{cases}$$

Substituting it into equation (4.6):

$$J = J_{M1-M2} - J_{M2-M1} \tag{4.5}$$

$$= \frac{4\pi.m.q}{h^3}\left[\int_{-\infty}^{E_{f2}} T(E_x).dE_x \overbrace{\int_{-\infty}^{E_{f2}} [f_1(E) - f_2(E)]\,dE_\rho}^{\approx 0}\right.$$

$$+ \int_{E_{f2}}^{E_{f1}} T(E_x).dE_x \int_{E_{f2}}^{E_{f1}} [f_1(E) - f_2(E)]\,dE_\rho$$

$$\left. + \int_{E_{f2}}^{+\infty} T(E_x).dE_x \overbrace{\int_{E_{f1}}^{+\infty} [f_1(E) - f_2(E)]\,dE_\rho}^{=0}\right]$$

$$= \frac{4\pi.m.q}{h^3}\int_{E_{f2}}^{E_{f1}} T(E_x).\left[E_{f1} - E_x\right] dE_x$$

4.4 WKB Approximation

The WKB (Wentzel-Kramers-Brillouin) approximation is commonly used in calculating the transmission coefficient $T(E)$ needed for modelling quantum mechanical tunnelling current. Substituting the wave function $\psi(x) = R(x).\exp(i\frac{S(x)}{\hbar})$ in the time-independent Schrödinger equation[96] for $\psi(x)$: $\left[-\frac{\hbar^2}{2m}\frac{d^2}{dx^2} + U(x)\right]\psi(x) = E.\psi(x)$ where $U(x)$ is the potential energy.

The solution of its imaginary part is: $R\frac{d^2S}{dx^2} + 2\frac{dR}{dx}\frac{dS}{dx} = 0 \longrightarrow \frac{dS}{dx} = \frac{C}{R^2}$

Substituting it into its real part: $\frac{d^2R}{dx^2} - \frac{1}{\hbar^2}\left(\frac{dS}{dx}\right)^2 R + \frac{2m}{\hbar^2}[E - U(x)]R = 0$

$\longrightarrow \frac{1}{R}\frac{d^2R}{dx^2} - \frac{1}{\hbar^2}\left(\frac{dS}{dx}\right)^2 + \frac{2m}{\hbar^2}[E - U(x)] = 0$

Assuming the approximation $\frac{1}{R}\frac{d^2R}{dx^2} \ll \frac{1}{\hbar^2}\left(\frac{dS}{dx}\right)^2$:

$$-\left(\frac{dS}{dx}\right)^2 + 2m[E - U(x)] = 0 \longrightarrow S(x) \approx \int \sqrt{2m[E - U(x)]}\, dx$$

$$\longrightarrow \psi(x) = R(x).\exp\left(\frac{i}{\hbar}\int \sqrt{2m[E - U(x)]}\, dx\right)$$

The wave is assumed to be incident towards the dielectric barrier till the point x_1 at the interface with M_1 and transmitted from the point x_2 at the interface with M_2 such that $x_1 < x_2$:

$$\psi_1(x \le x_1) = R(x).\exp\left(\frac{i}{\hbar}\int_{-\infty}^{x_1} \sqrt{2m[E - U(x)]}\, dx\right)$$

$$\psi_2(x \ge x_2) = R(x).\exp\left(\frac{i}{\hbar}\int_{-\infty}^{x_2} \sqrt{2m[E - U(x)]}\, dx\right)$$

The transmission probability $T(E)$ is then expressed as:

$$T(E) = \left|\frac{\psi_2(x_2)}{\psi_1(x_1)}\right|^2 = \frac{\exp\left(\frac{i}{\hbar}\int_{-\infty}^{x_2} \sqrt{2m[E - U(x)]}\, dx\right)}{\exp\left(\frac{i}{\hbar}\int_{-\infty}^{x_1} \sqrt{2m[E - U(x)]}\, dx\right)} = \left|\exp\left(\frac{i}{\hbar}\int_{x_1}^{x_2} \sqrt{2m[E - U(x)]}\, dx\right)\right|^2$$

$$= \exp\left(-\frac{2}{\hbar}\int_{x_1}^{x_2} \sqrt{2m[E - U(x)]}\, dx\right)$$

$$T(E) = \exp\left(-\frac{2}{\hbar}\int_{0}^{x_1} \sqrt{2m_{ox}(E_C - E_x)}\, dx\right) \tag{4.8}$$

4.5 Fowler-Nordheim tunnelling

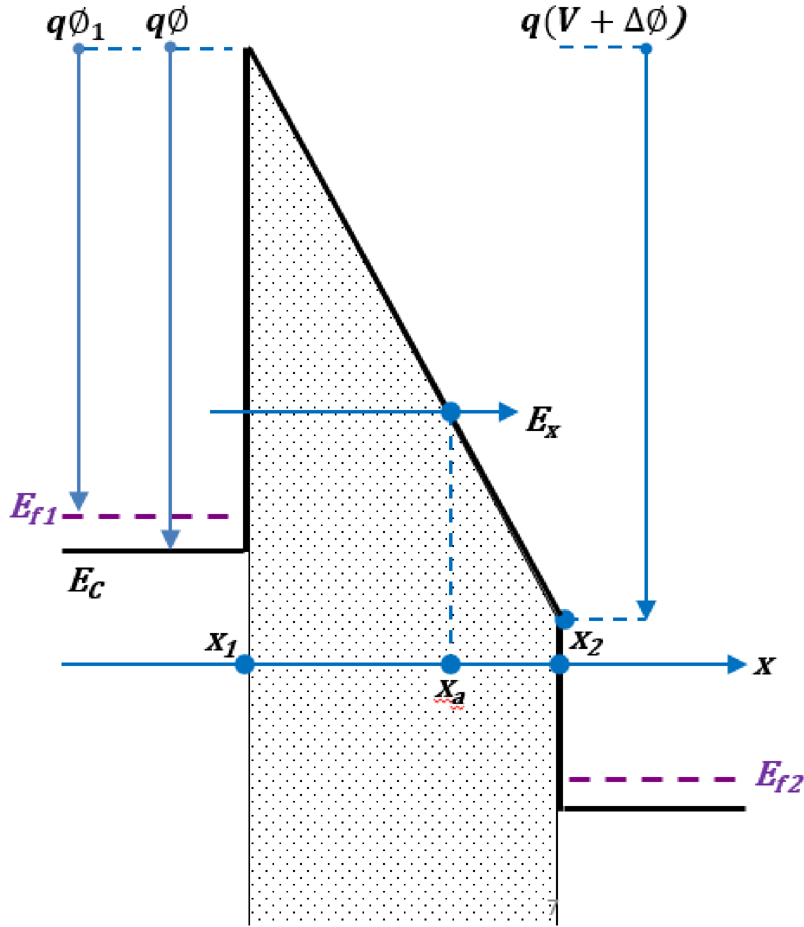

Figure 4.2 Energy band diagram showing the conduction band and the parameters used to calculate Fowler-Nordheim tunnelling current.

The electric field across the dielectric F_{ox} created by the difference in Fermi level $E_{f1} - E_{f2}$ and the work functions of the electrodes $q(\Delta\emptyset)$. Considering a triangular band bending of the conduction band of the dielectric the following relations are derived using Figure 4.2:

$$F_{ox} = \frac{E_{f1} - E_{f2} + q\overbrace{\Delta\emptyset}^{\approx 0\ approximation}}{qt_{ox}}$$

$$x_a = \frac{E_{f1} + q\emptyset_1 - E_x}{qF_{ox}}$$

$$E_C(x) = E_{f1} + q\emptyset_1 - qF_{ox}x$$

The transmission probability $T(E)$ [equation (4.8)] can then be calculated:

$$T(E) = \exp\left(-\frac{2\sqrt{2m_{ox}}}{\hbar}\int_0^{x_1}\sqrt{\left(E_{f1} + q\emptyset_1 - qF_{ox}x - E_x\right)}\,dx\right)$$

$$= \exp\left(4\frac{\sqrt{2m_{ox}}}{3\hbar qF_{ox}}\left(E_{f1} + q\emptyset_1 - qF_{ox}x - E_x\right)^{\frac{3}{2}}\right)\Bigg|\begin{matrix}x_a\\0\end{matrix}$$

$$= \exp\left(4\frac{\sqrt{2m_{ox}}}{3\hbar qF_{ox}}\left(-E_{f1} - q\emptyset_1 - E_x\right)^{\frac{3}{2}}\right)$$

$$= \exp\left\{-4\frac{\sqrt{2m_{ox}}}{3\hbar qF_{ox}}\left[q\emptyset_1 - \left(E_x - E_{f1}\right)\right]^{3/2}\right\}$$

To solve the above $T(E)$ equation, Taylor expansion series to the first order is used to simplify it:

$$\left[q\emptyset_1 - \left(E_x - E_{f1}\right)\right]^{3/2} \approx q\emptyset_1^{\frac{3}{2}} + \frac{3}{2}\left(E_x - E_{f1}\right)q\emptyset_1^{\frac{1}{2}}$$

Equation (4.6) of tunnelling current becomes:

$$J = \frac{4\pi.m.q}{h^3}\int_{E_{f2}}^{E_{f1}}\exp\left\{-4\frac{\sqrt{2m_{ox}}}{3\hbar qF_{ox}}\left[(q\emptyset_1)^{\frac{3}{2}} + \frac{3}{2}\left(E_x - E_{f1}\right)(q\emptyset_1)^{\frac{1}{2}}\right]\right\}.\left[E_{f1} - E_x\right]dE_x$$

$$= \frac{4\pi.m.q}{h^3}exp\left(-4\frac{\sqrt{2m_{ox}}}{3\hbar qF_{ox}}\right)(q\emptyset_1)^{\frac{3}{2}}\int_{E_{f2}}^{E_{f1}}\exp\left\{-2\frac{\sqrt{2m_{ox}}}{\hbar qF_{ox}}.\left(E_x - E_{f1}\right)(q\emptyset_1)^{\frac{1}{2}}\right\}.\left(E_{f1} - E_x\right)dE_x$$

$$J = \frac{4\pi.m.q}{h^3}exp\left[-4\frac{\sqrt{2m_{ox}}}{3\hbar qF_{ox}}(q\emptyset_1)^{\frac{3}{2}}\right]\int_0^{E_{f2}-E_{f1}}\exp\left\{2\frac{\sqrt{2m_{ox}}}{\hbar qF_{ox}}(q\emptyset_1)^{\frac{1}{2}}.\left(E_x - E_{f1}\right)\right\}.\left(E_x - E_{f1}\right)d\left(E_x - E_{f1}\right)$$

Using constant $a = 2\frac{\sqrt{2m_{ox}}}{\hbar qF_{ox}}(q\emptyset_1)^{\frac{1}{2}}$, the equation above can be simplified as $\int\exp(a.x).x\,dx = \frac{(a.x-1)}{a^2}\exp(a.x)$. Substituting $w = E_x - E_{f1}$:

$$J = \frac{4\pi.m.q}{h^3}exp\left[-4\frac{\sqrt{2m_{ox}}}{3\hbar qF_{ox}}(q\emptyset_1)^{\frac{3}{2}}\right]\int_0^{E_{f2}-E_{f1}}\exp\{a.w\}.w\,dw$$

$$J = \frac{4\pi.m.q}{h^3}exp\left[-4\frac{\sqrt{2m_{ox}}}{3\hbar qF_{ox}}(q\emptyset_1)^{\frac{3}{2}}\right]\frac{1}{a^2}\exp\{a.\left(E_{f2} - E_{f1}\right)\}.\{a.\left(E_{f2} - E_{f1}\right) - 1\}$$

Assuming $E_{f1} \gg E_{f2}$, the above equation can be approximated to:

$$J \approx \frac{q^3 m}{8\pi h q \emptyset_1 m_{ox}} F_{ox}^2 exp\left(-4\frac{\sqrt{2m_{ox}}}{3\hbar q F_{ox}}(q\emptyset_1)^{\frac{3}{2}}\right) \quad (4.9)$$

which is the same FN equation[97] $J = AF_{ox}^2 \exp\left\{-\frac{B}{F_{ox}}\right\}$ where $A = \frac{q^3 m}{8\pi h q \emptyset_1 m_{ox}}$ and $B = 4\frac{\sqrt{2m_{ox}}}{3\hbar q F_{ox}}$

4.6 Direct tunnelling

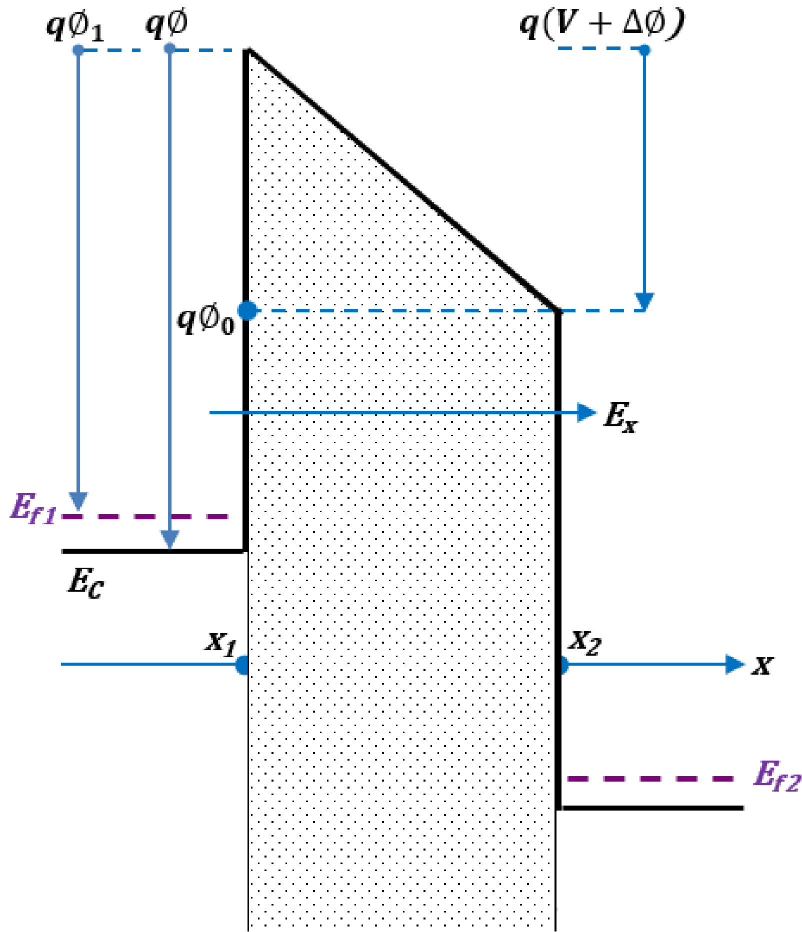

Figure 4.3 Energy band diagram showing the conduction band and the parameters used to calculate direct tunnelling current.

The electric field across the dielectric F_{ox} created by the difference in Fermi level $E_{f1} - E_{f2}$ and the work functions of the electrodes $q(\Delta\emptyset)$. Considering a rectangular band bending of the conduction band of the dielectric of thickness t_{ox} the following relations are derived using Figure 4.3 for $E < q\emptyset_0$:

$$q\emptyset = E_{f1} + q\emptyset_1$$

$$q\emptyset_0 = E_{f1} + q\emptyset_1 - qF_{ox}t_{ox}$$

$$E_C(x) = E_{f1} + q\emptyset_1 - qF_{ox}x$$

The transmission probability $T(E)$ [equation (4.8)] can then be calculated:

$$\begin{aligned} T(E) &= \exp\left(-\frac{2}{\hbar}\int_0^{t_{ox}} \sqrt{2m_{ox}(E_C - E_x)}\, dx\right) \\ &= \exp\left(-\frac{2\sqrt{2m_{ox}}}{\hbar}\int_0^{t_{ox}} \sqrt{(q\emptyset - qF_{ox}x - E_x)}\, dx\right) \\ &= \exp\left(-\frac{4\sqrt{2m_{ox}}}{3\hbar qF_{ox}}(q\emptyset - qF_{ox}x - E_x)^{3/2}\right)\Bigg|_{0}^{t_{ox}} \\ &= \exp\left(-\frac{4\sqrt{2m_{ox}}}{3\hbar qF_{ox}}\left[(q\emptyset - E_x)^{3/2} - (q\emptyset_0 - E_x)^{3/2}\right]\right) \end{aligned}$$

To solve the above $T(E)$ equation, Taylor expansion series to the first order is used to simplify it:

$$\begin{aligned} (q\emptyset - E_x)^{\frac{3}{2}} - (q\emptyset_0 - E_x)^{\frac{3}{2}} &= \left(E_{f1} + q\emptyset_1 - E_x\right)^{\frac{3}{2}} - \left(E_{f1} + q\emptyset_1 - qF_{ox}t_{ox} - E_x\right)^{\frac{3}{2}} \\ &= \left(q\emptyset_1 - \left(E_x - E_{f1}\right)\right)^{\frac{3}{2}} - \left(q\emptyset_1 - qF_{ox}t_{ox} - \left(E_x - E_{f1}\right)\right)^{\frac{3}{2}} \\ &\approx (q\emptyset_1)^{\frac{3}{2}} + \frac{3}{2}\left(E_x - E_{f1}\right)(q\emptyset_1)^{\frac{1}{2}} - (q\emptyset_1 - qF_{ox}t_{ox})^{\frac{3}{2}} \\ &\quad - \frac{3}{2}\left(E_x - E_{f1}\right)(q\emptyset_1 - qF_{ox}t_{ox})^{\frac{1}{2}} \\ &= (q\emptyset_1)^{\frac{3}{2}} - (q\emptyset_1 - qF_{ox}t_{ox})^{\frac{3}{2}} + \frac{3}{2}\left(E_x - E_{f1}\right)\left[(q\emptyset_1)^{\frac{1}{2}} - (q\emptyset_1 - qF_{ox}t_{ox})^{\frac{1}{2}}\right] \end{aligned}$$

$$\begin{aligned} J = \frac{4\pi.m.q}{h^3}\exp\left(-\frac{4\sqrt{2m_{ox}}}{3\hbar qF_{ox}}\right)\int_{E_{f2}}^{E_{f1}} \exp\Big\{(q\emptyset_1)^{\frac{3}{2}} - (q\emptyset_1 - qF_{ox}t_{ox})^{\frac{3}{2}} \\ + \frac{3}{2}\left(E_x - E_{f1}\right)\left[(q\emptyset_1)^{\frac{1}{2}} - (q\emptyset_1 - qF_{ox}t_{ox})^{\frac{1}{2}}\right]\Big\}.\left[E_{f1} - E_x\right] dE_x \end{aligned}$$

Using the constants $a = \frac{4\pi.m.q}{h^3}$, $b = -\frac{4\sqrt{2m_{ox}}}{3\hbar qF_{ox}}\left[(q\emptyset_1)^{\frac{3}{2}} - (q\emptyset_1 - qF_{ox}t_{ox})^{\frac{3}{2}}\right]$, and $c = -\frac{2\sqrt{2m_{ox}}}{\hbar qF_{ox}}\left[(q\emptyset_1)^{\frac{1}{2}} - (q\emptyset_1 - qF_{ox}t_{ox})^{\frac{1}{2}}\right]$, the equation above can be simplified as $J = a.\exp(b)\int_{E_{f2}-E_{f1}}^{0} exp\{c\left(E_x - E_{f1}\right)\}.\left[E_{f1} - E_x\right] d(E_x - E_{f1})$. Substituting $w = E_x - E_{f1}$:

$$J = a.\exp(b)\int_0^{E_{f2}-E_{f1}} exp\{cw\}.w\,dw$$

$$= \frac{a.exp(b)}{c^2}\{1 - \exp[c(E_{f2} - E_{f1})][1 + c(E_{f2} - E_{f1})]\}$$

Assuming $E_{f1} \gg E_{f2}$, the above equation can be approximated to:

$J = \frac{a.exp(b)}{c^2}$ where

Equation (4.6) of tunnelling current becomes:

$$J = \frac{m.q^3.F_{ox}^2}{8\pi m_{ox} h\left[(q\emptyset_1)^{\frac{1}{2}} - (q\emptyset_1 - qF_{ox}t_{ox})^{\frac{1}{2}}\right]^2} \exp\left\{-\frac{8\pi\sqrt{2m_{ox}}}{3hqF_{ox}}\left[(q\emptyset_1)^{\frac{3}{2}} - (q\emptyset_1 - qV_{ox})^{\frac{3}{2}}\right]\right\} \tag{4.10}$$

which is the same direct tunnelling equation[97] $J = AF_{ox}^2 \exp\left\{-\frac{B}{F_{ox}}\right\}$

where $A = \frac{m.q^3}{8\pi m_{ox} h\left[(q\emptyset_1)^{\frac{1}{2}} - (q\emptyset_1 - qF_{ox}t_{ox})^{\frac{1}{2}}\right]^2}$ and $B = \frac{8\pi\sqrt{2m_{ox}}}{3hq}\left[(q\emptyset_1)^{\frac{3}{2}} - (q\emptyset_1 - qV_{ox})^{\frac{3}{2}}\right]$

4.7 Transfer-Matrix Method

The wave function was shown with WKB approximation to be:
$\psi(x) = R(x).\exp\left(\frac{i}{\hbar}\int\sqrt{2m[E - U(x)]}\,dx\right)$. This can be rewritten as:

$$\psi_j(x) = A_j(x).\exp(i.k_j.x) + B_j(x).\exp(-i.k_j.x) \tag{4.11}$$

where $k_j = \sqrt{2m_j[E - U_j(x)]}/\hbar$, $U(x)$ is the potential energy which is the conduction band here.

The electron moving in M_1 till it reaches x_1, which the classical turning point at the interface with the dielectric is described by: $\psi_1(x) = A_1(x).\exp(i.k_1.x)$ for $x < x_1$. The wave is then damped by the energy barrier created by the dielectric(s) before reaching the interface with other electrode M_2 at x_2 with a wave described by: $\psi_N(x) = A_N(x).\exp(i.k_N.x)$ for $x > x_2$.

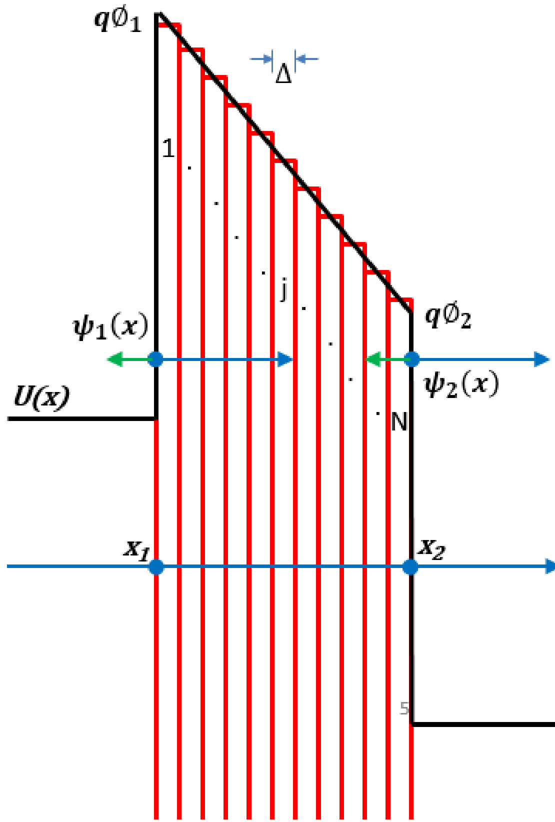

Figure 4.4 The energy barrier of a single-layer dielectric. The potential energy $U(x)$ is the conduction band energy.

The dielectric layer is divided into N number of sublayers (Figure 4.4), and each sublayer is assumed to be under constant voltage where electrons have constant mass m_j of waves amplitudes A_j if incident, and B_j if reflected.

$$\psi_j(x) = \psi_{j+1}(x)$$

$$A_j(x).\exp\left(i.k_j.x\right) = A_{j+1}(x).\exp\left(i.k_{j+1}.x\right)$$

$$\frac{1}{m_j}\frac{d\psi_j(x)}{dx} = \frac{1}{m_{j+1}}\frac{d\psi_{j+1}(x)}{dx}$$

The relation between subsequent waves can be expressed as a complex transfer matrix for $1 \ll j \ll N-1$

$$T_j \begin{pmatrix} A_j \\ B_j \end{pmatrix} = \begin{pmatrix} A_{j+1} \\ B_{j+1} \end{pmatrix} \tag{4.12}$$

Assuming the phase factor $\gamma = \exp[i\Delta(j-1)]$, the transfer matrix is:

$$T_j = \frac{1}{2}\begin{pmatrix} (1 + k_j/k_{j+1})\gamma^{-k_{j+1}} & (1 - k_j/k_{j+1})\gamma^{-k_{j+1}} \\ (1 - k_j/k_{j+1})\gamma^{+k_{j+1}} & (1 + k_j/k_{j+1})\gamma^{+k_{j+1}} \end{pmatrix}\begin{pmatrix} \gamma^{+k_j} & 0 \\ 0 & \gamma^{-k_j} \end{pmatrix} \tag{4.13}$$

The waves describing the moving electron at x_1 and x_2 are described by $\psi_1(x)$ and $\psi_N(x)$ respectively. The region between them is divided into a total number sof N regions. Thus, the transfer matrix of total transmission across the dielectric(s) is the subsequent multiplications of the transfer matrices in these regions, which can be described by the following relation:

$$\prod_{j=1}^{N} T_j \begin{pmatrix} A_1 \\ B_1 \end{pmatrix} = \begin{pmatrix} A_N \\ B_N \end{pmatrix} \tag{4.14}$$

Assuming no reflected wave in the last region beside x_2 and that the amplitude of $\psi_1(x)$ at x_1 is 1, the total transfer matrix can be reduced to:

$$\begin{pmatrix} T_{11} & T_{12} \\ T_{21} & T_{22} \end{pmatrix}\begin{pmatrix} 1 \\ B_1 \end{pmatrix} = \begin{pmatrix} A_N \\ 0 \end{pmatrix}$$

The transmission coefficient is the ratio of the current reaching x_2 to that at x_1:

$$T(E) = \frac{J_N}{J_1} = \frac{k_1 m_1}{k_N m_N}\frac{|A_N|^2}{|A_1|^2} \tag{4.15}$$

The total current density is then calculated using Tsu-Ezaki equation (4.7). E_{min} and E_{max} are respectively the minimum and the maximum energy levels, between the input and output fermi levels of the electrodes, included in calculations. dE_x is the energy segment taken by specifying certain number of states included between the lower and upper limits.

4.8 Trap-assisted mechanisms

In addition to FN and direct tunnelling, there could be other thermal conduction mechanisms affecting the current-voltage characteristics. These mechanisms stem from the existence of defects in the oxides such as oxygen vacancies, which are physically described by traps. The transit time of the charge transport via these defect states becomes inevitably slower than that of tunnelling. The charge carriers (electrons) moving from M1 to M2 electrodes can get trapped in defects

existing in the bulk of the oxide. These defects are located at an energy level equal to the trap depth φ_T below the conduction band of the dielectric. Poole Frenkel emission (Figure 4.5) describes the excitation of these trapped electrons into the conduction band of the dielectric. The effective barrier is then reduced by the applied electric field increasing the probability of thermal excitation which moves the electrons out of the traps. Schottky emission (Figure 4.5) is the process of thermal activation of electrons to be injected over the barrier between M1 and the dielectric, into the conduction band of the dielectric. It is similar to PFE, however, the trap depth φ_T is replaced with the barrier height φ_B between M1 and the first dielectric in addition to doubling the band bending of the dielectric. Schottky (SE) and Poole-Frenkel emission (FPE) are described by the following equations[98]:

$$J_{SE} = A^{*}.T^{2}\ exp\frac{-q(\varphi_B - \sqrt{qE/4\pi\varepsilon_r\varepsilon_0})}{kT} \tag{4.16}$$

$$J_{FPE} = E\ exp\frac{-q(\varphi_T - \sqrt{qE/\pi\varepsilon_r\varepsilon_0}}{kT} \tag{4.17}$$

where A^{*} is the effective Richardson constant, T is temperature, k is Boltzmann constant. φ_T is the trap depth.

Trap assisted tunnelling (TAT)[99] is the process where the electrons tunnel from M1 to M2 via the defects in the dielectric bulk (Figure 4.5). TAT plays major role for barriers of large number of traps and consists of the following two-step process:

1) Tunnelling from the injecting electrode to traps.

2) One of these mechanisms:

    a) PFE from traps where electrons are activated to the conduction band of the dielectric.

    b) FNT directly from traps to the other electrode.

TAT tunnelling can be described by the following equation[100]:

$$J_{TAT} = A_0 \exp\left(-\frac{q}{kT}\varphi_B\right) \exp\left(-\frac{8\pi\sqrt{2qm_s}\varphi_{BTAT}^{3/2}}{3hE}\right) \tag{4.18}$$

where A_0 is a constant, h is Planck's constant, φ_{BTAT} is the barrier height, and m_s is the electron effective mass considered to be 0.05 m_e (the free electron mass).

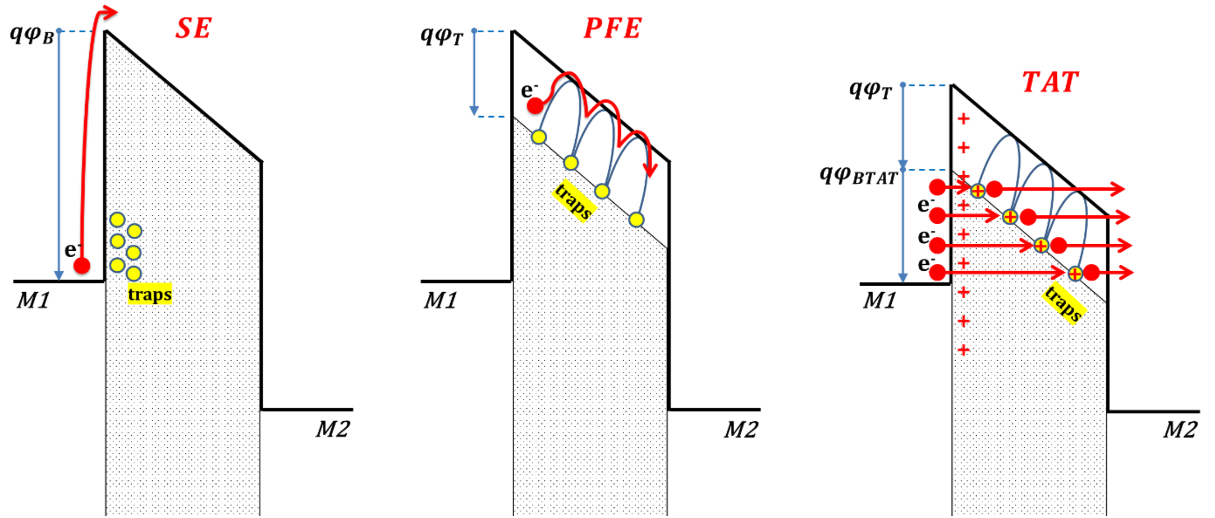

Figure 4.5 Energy band diagram illustrating the Schottky (SE), Poole-Frenkel (PFE), and trap assisted tunnelling (TAT) mechanisms in MIM diodes. The same principle applies for the mechanisms in multi-insulator diodes.

Trap-to-trap hopping is possible between TAT steps 1 and 2. This process describes the electrons tunnelling through impurity energy levels and is dependent on temperature and the overlap of the electron wave functions. There are two types of hopping:

a) Nearest neighbouring hopping (NNH)[101] where the trapped electrons hop into the nearest trap through tunnelling effect: $J_{TAT} = \sigma_0 \exp(-T_0/T)\,.\,\mathrm{E}$
b) Variable range (or Mott) hopping (VRH)[102] where the trapped electrons hop into far traps with lower trap energy: $J_{TAT} = \sigma_0 \exp(-T_0/T)^{1/4}\,.\,\mathrm{E}$

where E is the electric field in the dielectric and σ_0 is its conductivity at temperature T_0.

4.9 The resonant tunnelling mechanism

In the case of double dielectric structures, the situation becomes more complex as there would be voltage drop across each barrier and the tunnelling current across both dielectrics depends on the barrier height of each metal-insulator (Figure 4.6). The dielectrics are assumed to be homogeneous and isotropic: $\vec{D_1} = \varepsilon_1 \vec{E_1}$ and $\vec{D_2} = \varepsilon_2 \vec{E_2}$. According to electrostatics rule and assuming no free charges at the interface, the normal components of the electric displacement vectors are equal at

the boundary surface between the two dielectrics: $\vec{D}_1 = \vec{D}_2$. The voltage across each dielectric of thicknesses d_1 and d_2 can then be described by the following equations respectively:

$$V_1 = V\frac{d_1}{\varepsilon_1}\left(\frac{d_1}{\varepsilon_1}+\frac{d_2}{\varepsilon_2}\right)^{-1}$$ (4.19)

$$V_2 = V\frac{d_2}{\varepsilon_2}\left(\frac{d_1}{\varepsilon_1}+\frac{d_2}{\varepsilon_2}\right)^{-1}$$

where each of V, V_1, and V_2 is the voltage applied between the electrodes, across the first insulator of thickness d_1 and relative permittivity ε_1, and across the second insulator of thickness d_2 and relative permittivity ε_2.

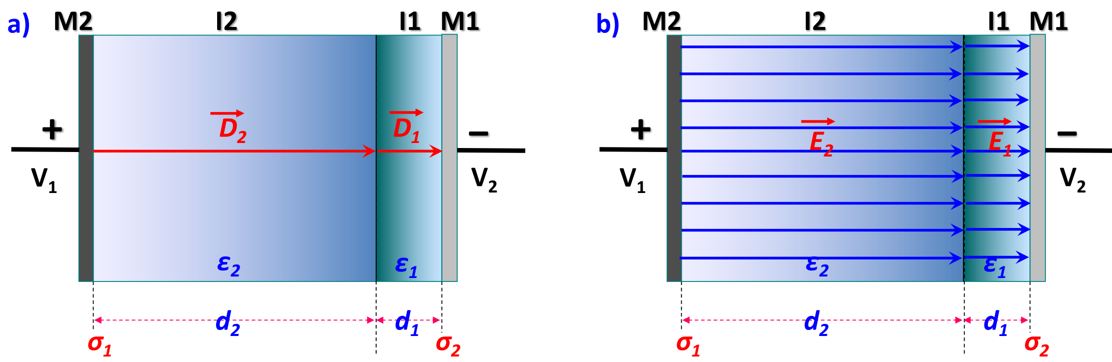

Figure 4.6 Two dielectrics of dissimilar thicknesses and permittivities in an MIIM structure. The surface charge density is σ_1 at I1/M1 interface and σ_2 at I2/M2 interface. (a) The electric displacement $\vec{D}_1$ and $\vec{D}_2$ at any region in I1 and I2 dielectrics respectively. (b) The electric fields across the dielectrics: $\vec{E}_1$ across I1 and $\vec{E}_2$ across I2.

The current passing through the dielectrics must be the same according to Poisson's equation. However, these insulating layers have different conductance and thus different charge transport flux in each material. Thus, the additional charge flowing in the dielectric with higher conductance is assumed to be flowing to the interface between the dielectrics until equilibrium is reached, which is known as the Maxwell-Wagner (MW) effect.[103] This effect is expected for all devices having two or more dielectrics sandwiched between two metal layers[104], i.e. for all MIIM devices but not MIM.

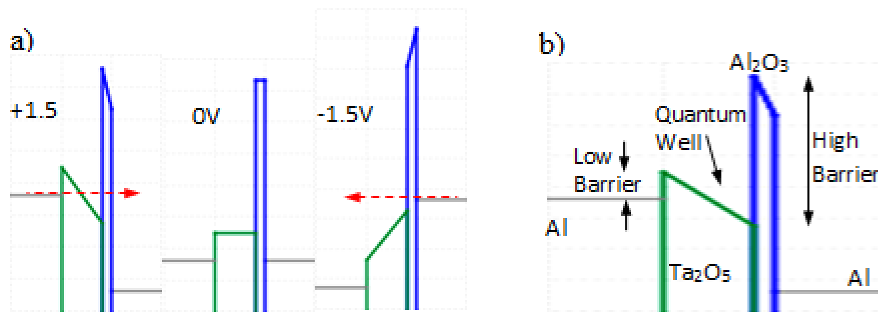

Figure 4.7 Simulated energy band diagrams of the Al/Ta_2O_5-4nm/Al_2O_3-1nm/Al structure (Batch 1) for opposite injection of electrons. Given that the left electrode is grounded, the voltage is applied to the right electrode as shown in (a) and set at (from left to right) +1.5, 0, and -1.5V. The tunnelling direction of electrons is represented by the red dashed arrow. The materials, the low and high barrier heights, and the potential well are illustrated in (b).

Energy band diagrams are plotted using *Multi-Dielectric Energy Band Diagram Program*[105] in Figure 4.7 showing the conduction band for the same Al/Ta_2O_5/Al_2O_3/Al structure. If the conduction band of the lower barrier falls below the metal Fermi level, the tunnelling distance narrows allowing tunnelling to occur thus making it more likely for an electron to pass through the barrier. The double dielectric configuration can be designed to have either step tunnelling or resonant tunnelling. Step tunnelling occurs when an abrupt decrease in tunnel distance with increasing voltage for electrons tunnelling from the metal on the right (-1.5V). When the electron injection is from the electrode on the left side with an applied voltage of +1.5V, a quantum well is formed at the interface between the barriers having quantized energy levels and bound states. Resonant tunnelling occurs when the quantum well is wide enough to produce resonant energy levels through bound states within the well. Step and resonant tunnelling mechanisms can both occur in the same diode, and the overall asymmetry of the J-V curve can be regulated by the one which dominates.

4.10 Summary of conduction mechanisms in MIM/MIIM diodes

The conduction mechanism in a diode can be composed of different tunnelling and thermal emission processes dominating in different voltage regions.[98] Each mechanism is described by an equation which can be fitted using the measured J-V data. If a linear fit of $R^2 > 0.995$ can be obtained and the extracted parameters are sensible with literature values, the domination of the

corresponding mechanism in that voltage regime can be indicated. E is the electric field across the dielectric, often denoted by F_{ox}. The electric field distribution according to equation (4.19) can be considered in the case of double dielectrics.

The current in MIM/MIIM diodes can be described by one of the following mechanisms:

1. Fowler-Nordheim tunnelling (FN):

$$J \sim E^2 \exp(-b/E)$$

   Drawing FN plot, $\ln\left(\frac{J}{E^2}\right)$ vs $\frac{J}{E}$, allows the determination of the barrier height from the slope in the voltage regimes where the data can be fitted.

2. Space charge limited conduction (trap free):

$$J \sim V^2$$

   It can be indicated in case the plot of J vs V^2 gives a linear fit in any voltage regime.

3. Resonant tunnelling in MIIM structures (RT), where resonance arises from bound states in the quantum well between the two dielectrics.[106]

   This can be predictable from the band diagrams, where the probability of its occurrence increases with the bound states in the quantum well formed between the dielectrics.

4. Direct tunnelling across the dielectric stack of thickness less than 3 nm:

$$J \sim E^2 \exp\left(-\frac{B}{E}\right)$$

5. Cathode thermionic Schottky emission (SE):

$$J \sim T^2 \exp(-q\varphi_B + aE^{\frac{1}{2}}/kT)$$

   Drawing SE plots, $\ln\left(\frac{I}{T^2}\right)$ vs $V^{1/2}$, allows the determination of the dynamic relative permittivity ε_r from the slope in the voltage regimes where the data can be fitted.

6. Trap field-enhanced Poole-Frenkel emission (PFE):

$$J \sim E^2 \exp(-q\varphi_B + 2aE^{\frac{1}{2}}/kT)$$

   Drawing PFE plots, $\ln\left(\frac{I}{V}\right)$ vs $V^{1/2}$, allows the determination of the dynamic relative permittivity ε_r from the slope in the voltage regimes where the data can be fitted. The trap depth φ_T can be extracted using J-V measurements at 4 or more temperatures:

- Arrhenius plot $\ln\left(\frac{I}{V}\right)$ vs $\frac{1}{kT}$
  - Extracting E_a from the slopes of Arrhenius plots for each voltage $I_{PFE} \propto Vexp(-E_a/kT)$
- Activation energy plot E_a vs $V^{1/2}$
  - φ_T is the intercept of activation energy plot at V = 0

7. Ohmic conduction:

$$J \sim E \exp(-c/kT)$$

8. Ionic conduction:

$$J \sim E/T \exp(-d/kT)$$

9. Trap assisted tunnelling (TAT):

$$J_{TAT} = A \exp(-B\, \varphi_{BTAT}^{\frac{3}{2}})$$

Drawing TAT plots $\ln(J)$ vs V^{-1}, allows the determination of the barrier height φ_{BTAT} from the slope in the voltage regimes where the data can be fitted.

4.11 The model used for optimizing the structures

A model, written as a MATLAB code, was developed by the team in the department and will be referred in this thesis as the in-house model.[48,107] It allows the simulation of the band diagrams containing the bound states and the tunnelling current for multi insulator diodes including resonant, FN, and direct tunnelling. Trap-assisted mechanisms are not considered in this model. The model is based on the transfer matrix method using all the equations described in section 4.7, where the current density is calculated using Tsu-Ezaki equation (4.7) and the subsequent multiplications of the transfer matrix T_j in equation (4.14). It allows the option of selecting the number of sections for each dielectric layer (Figure 4.4). The more sections, the more precise the simulation but the longer the run duration. Each run can take up to 1 day or longer depending on the piecewise step, the voltage step, and the applied voltage range. Typically, 50 sections per nanometre is sufficient.

An example of a diode DC response is shown below in Figure 4.8. Based on the model, the J-V curves for different double-dielectric structures were simulated. The results indicate an asymmetry

with a high forward-to-reverse current ratio. The difference in the barrier heights at the electrodes causes the asymmetry in the J-V characteristics of single dielectric diodes.[108] However, the usage of similar electrodes maintained the asymmetry in the double-dielectric case because of the resonant tunnelling occurring in the forward bias direction. These two, reverse and forward, mechanisms allow the double-dielectric diode to have an enhanced non-linearity in the J-V curves. A larger current at positive bias could make a sharp rise for sufficient dielectric thickness leading to a high responsivity which can be further enlarged by using high barrier diodes.[55] This is desirable but could result in a high resistance which limits the asymmetry, and thus 3-4 nm thick Ta_2O_5 is desired as a trade-off. It can be noticed that the current density rises more rapidly at the point where resonant tunnelling arises indicating a lower diode resistance and thus a better match to the antenna for an efficient power transfer. The model is altered in figures other than Figure 4.8 and Figure 5.14 to remove the spikes which appear in the J-V curves and keep the current continuous. However, these spikes are helpful to understand where resonant tunnelling occurs.

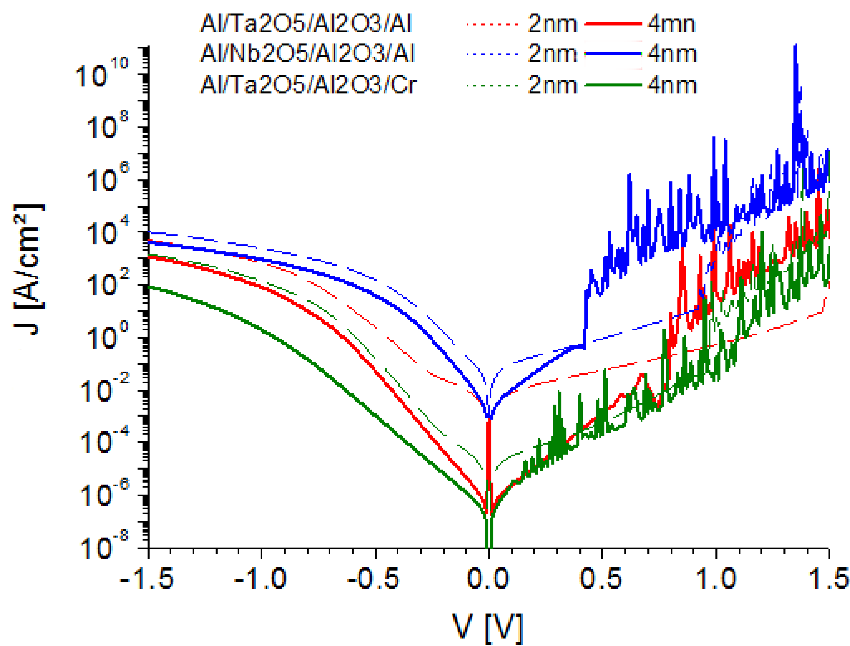

Figure 4.8 J-V characteristic modelling for double dielectric diodes with different structures and Ta_2O_5 thicknesses (2 and 4 nm) keeping Al_2O_3 thickness at 1 nm. The voltage step size is 10 mV.

Table 4.1 Modelled structures.

Structure	a1	a2	a3	a4	a5	b1	b2	b3	b4	b5	c4	d4
M2	Al	Al	Al	Al	Al	Al	Al	Al	Al	Al	Au	Al
I2 thickness (Ta_2O_5) [nm]	1	2	3	4	5	1	2	3	4	5	4	4
I1 thickness (Al_2O_3) [nm]	1	1	1	1	1	0.5	0.5	0.5	0.5	0.5	0.5	-
M1	Al	Al	Al	Al	Al	Al	Al	Al	Al	Al	Au	Au

The in-house model is used to optimise the structures according to the individual layer thickness of each dielectric. The model assumes grounded M2 simulating the J-V characteristics (Figure 4.9) from -2 to 2 V at a step voltage of 0.1 V. The thickness of Ta_2O_5 is varied (1, 2, 3, 4, and 5 nm) while keeping the thickness of Al_2O_3 at 1 nm (a) and 0.5 nm (b). Both graphs show steeper rise in current at positive bias as Ta_2O_5 thickness is increased. This steep rise cannot be observed using WKB approximation which does not take into consideration resonant tunnelling.

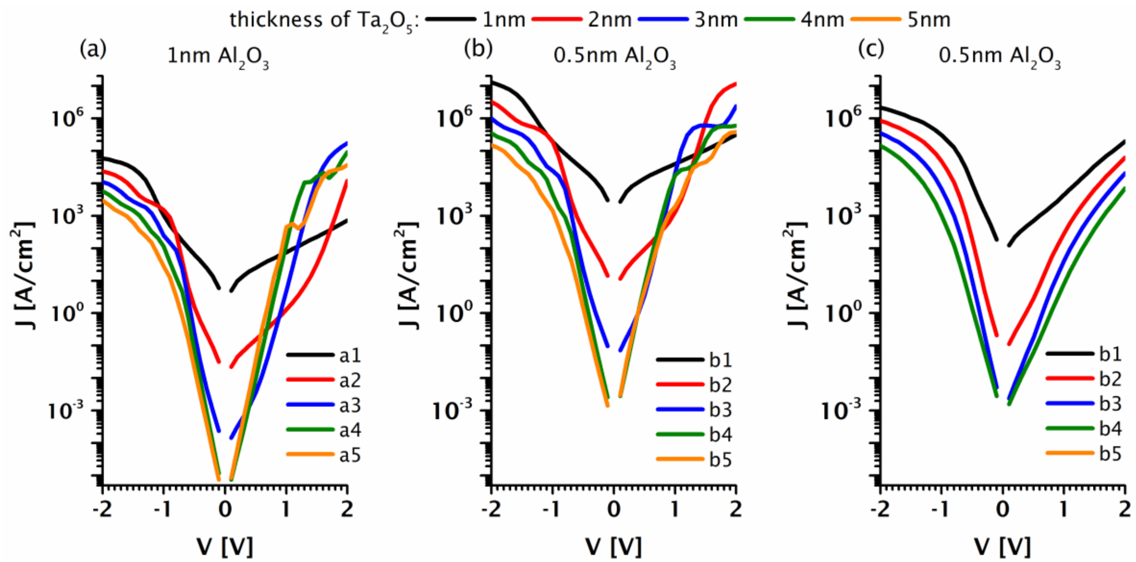

Figure 4.9 The J-V characteristics a1-a5, b1-b5, c4, and d4 (M1/I1/I2/M2) structures varying the thickness of Ta_2O_5 (1, 2, 3, 4, and 5 nm) considering 1 nm Al_2O_3 (a) and 0.5 nm Al_2O_3 (b, c) simulated using the model. The former structures is modelled based on WKB approximation (c).[26] The voltage step size is 100 mV.

To understand this, the transmission probability is calculated using the model for four different structures (b4, c4, b1, d4) as a function of the x-directed incident energy of the electron at -2, -1, 0, 1, and 2 V. The fermi level of the ungrounded M2 electrode is fixed at 0 eV for Al. The incident electron energy E_x contributing to the net current for all structures is $0<E_x<2$ eV at -2V, $0<E_x<1$

eV at -1V, E_x=0 eV at 0 V, $-1<E_x<0$ eV at -1V, $-2<E_x<0$ eV at +2V. Resonant tunnelling peaks appear at +1 and +2 V for b4 (a), giving rise to transmission. These peaks do not appear for $T(E_x)$ (see Figure 4.10) calculated using the WKB approximation (dashed lines),[26] which indicates the unsuitability of this method for resonant tunnelling structures. The resonant peaks give rise to $T(E_x)$ of b4 MIIM structure exceeding that of d4 MIM structure despite the additional 0.5 nm Al_2O_3 barrier for b4. At -2 V, however, no peaks can be observed, and $T(E_x)$ of b4 remains below that of b1 due to the absence of resonance peaks. This is reflected on the J-V simulated curves in Figure 4.9 where the current of b4 exceeds that of b1 at +2 V, whereas it does not at any negative bias regime.

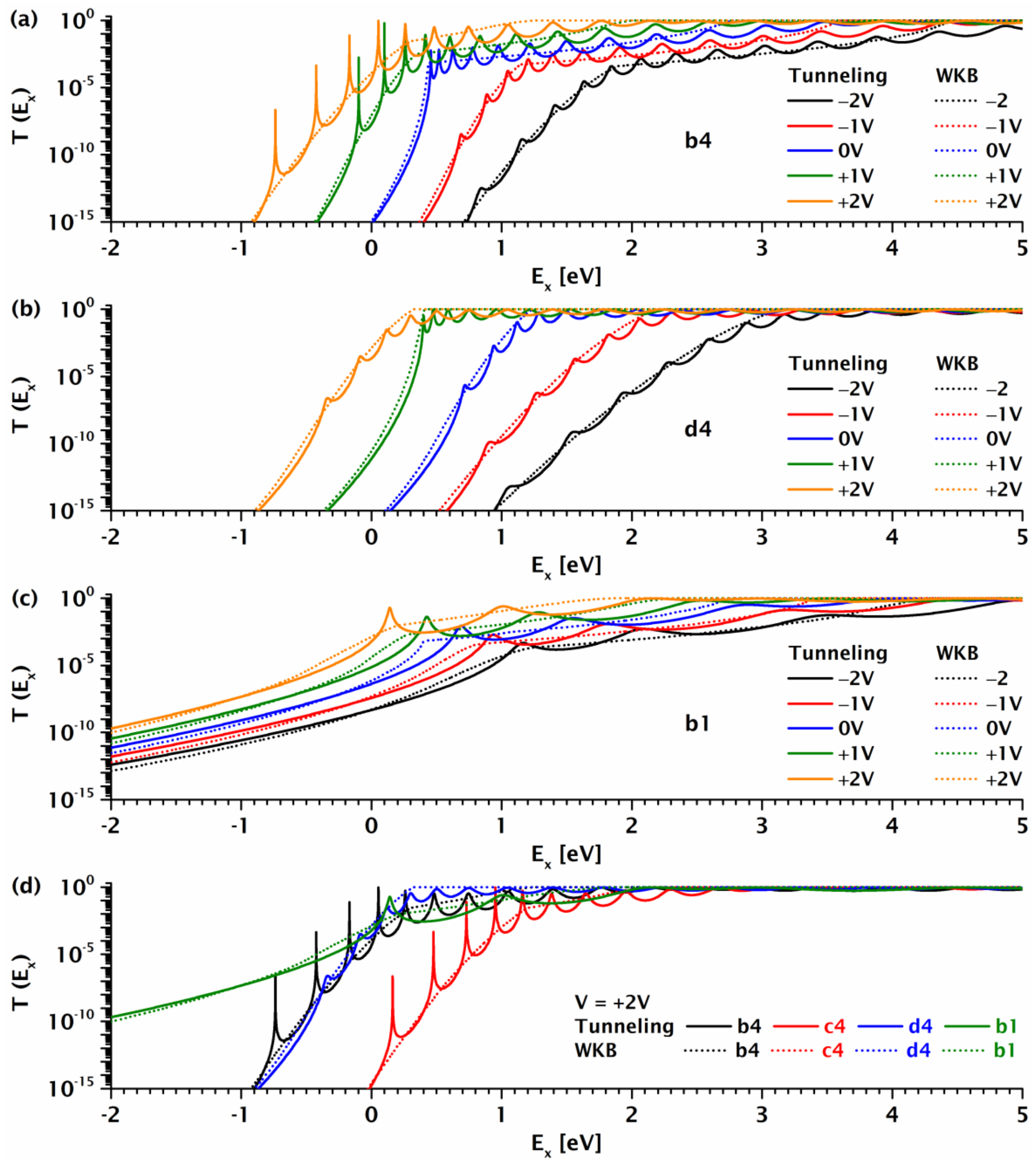

Figure 4.10 The x-directed transmission probability of different MIIM (b1, b4, c4) and MIM (d4) structures (Table 4.1).

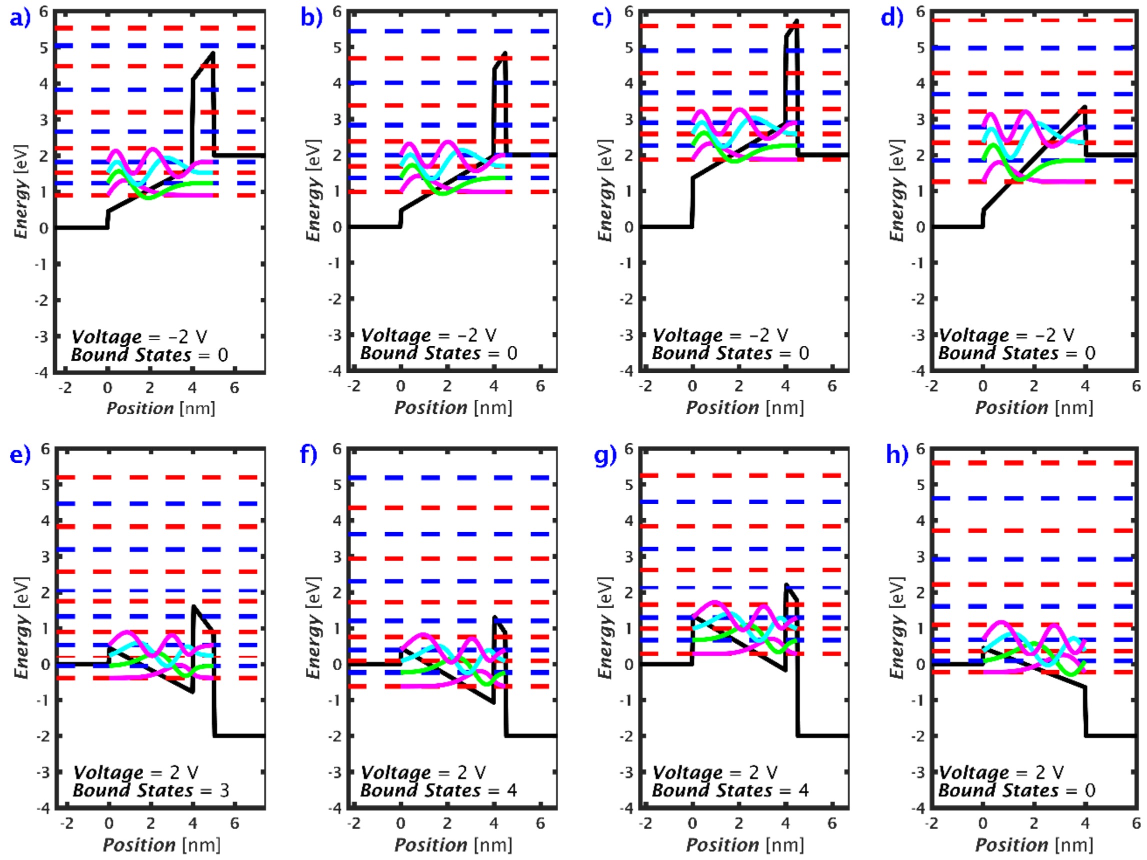

Figure 4.11 Conduction band diagrams of M1/I1/I2/M2 structures (M1 is the right electrode): a4, b4, c4, d4 at -2 V (a, b, c, d) and +2V (e, f, g, h).

If the energy of an incident electron E_x is equal to the energy state in the quantum well in between the dielectrics in double dielectric structures, the transmission probability becomes unity ideally defining a resonant tunnelling structure. For further understanding, the band diagrams are shown for the four structures at -2 and +2 V (Figure 4.11). Four resonance states exist for b4 in the quantum well are consistent with the transmission probability curves which also show four resonant peaks at the same applied voltage (+2V). The four resonance states existing in the quantum well for c4, of Au electrodes, also appear in $T(E_x)$ curves for E_x>0 V, which essentially does not contribute to the net tunnelling current at +2 V. The reduced Al_2O_3 thickness of b4, not only helps in reducing the dynamic resistance, but also increases the bound states in the quantum well. Hence, b4 represents an optimised resonant tunnelling structure based on modelling.

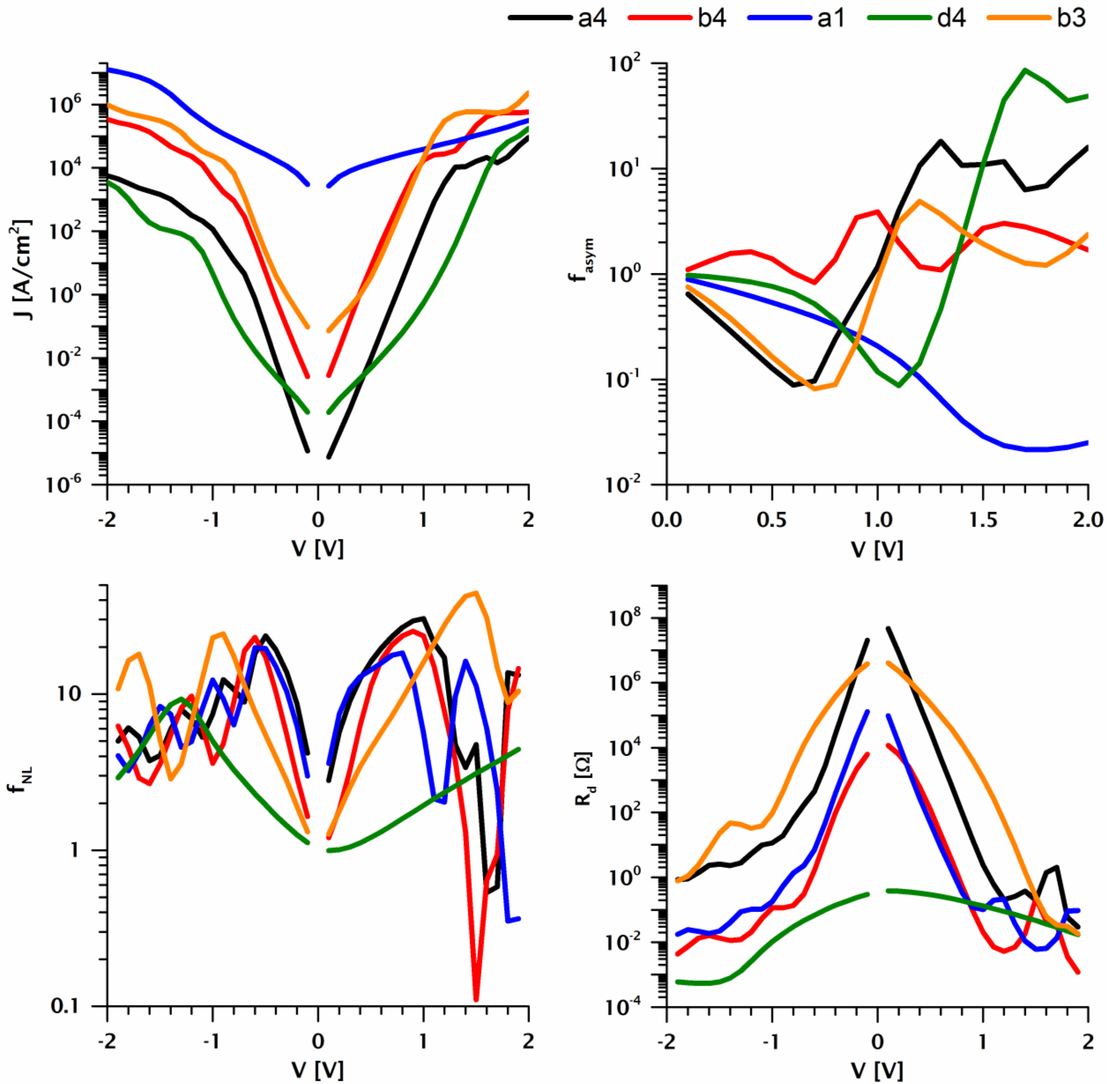

Figure 4.12 The rectifying characteristics of the modelled structures (a1-a5, b1-b5, c4, d4): the J-V characteristics (a), the asymmetry (b), the non-linearity (c), and the dynamic resistance (d).

The rectifying characteristics of all structures in Table 4.1 are shown in Figure 4.12. These are the figure of merits of the rectifying characteristics of a diode. They are used for device optimisation based on what is needed for THz rectennas: some asymmetry enough to rectify the incoming radiation into useful DC power, non-linearity larger than three, and a dynamic resistance as low as possible ideally less than 10^3 Ω. These should occur at a voltage near 0 V as the rectifier should not require an external bias which would add considerable complexity. Although high asymmetry helps increase the efficiency of a rectenna, it is not as critical as the non-linearity for rectification and the dynamic resistance (R_d) for coupling with antennas. A simple simulation of a rectifier indicates that an asymmetry of 20, 10, 5, 2, and 1.2 results in a dc voltage of 90%, 80%, 67%, 33%, and 10% respectively. Integrating the devices into rectenna arrays, any small dc

voltage would add up to make larger voltage. A trade-off between R_d and the non-linearity can be seen with the MIM structure d4 (of the lowest R_d along with the lowest non-linearity) as compared to a4 and b4 resonant tunnelling structures (of higher R_d and higher non-linearity). Significant reduction in R_d can be observed with b4 as compared with a4 of 0.5 nm thicker Al_2O_3.

5. Engineering the rectifying characteristics in tunnelling structures

In this chapter different structures of resonant tunnelling probability are fabricated and analysed starting from the one of best modelled resonance probability, varying the oxide thickness, and using electrodes of similar and dissimilar work functions. The aim is to grasp basic understanding of the optimizing keys of the diodes and point out their issues.

The atomic layer deposition was done by placing each sample at the centre of the chamber with no rotation and at a temperature of 200 ºC. ALD1 and ALD2 denote the growth conditions of the oxides. For ALD1, oxides are deposited using deionized water as the oxidant for Ta_2O_5 and Al_2O_3 at 0.04s/10s pulse/purge times, tantalum ethoxide precursor for Ta_2O_5 at 0.3s/2s pulse/purge time, and trimethylaluminium (TMA) precursor for Al_2O_3 at 0.02s/5s pulse/purge time. ALD2 is described and used in chapter 6.

Sput1 denotes RF sputtering conditions done at the Stephenson institute for renewable energy. Al_2O_3 and Nb_2O_5 oxides are deposited at room temperature under the flow of argon gas at a pressure of 20 mTorr and at plasma power of 180 and 100 Watts respectively. The samples are fixed to a rotating sample holder and kept in the chamber in vacuum till pressure is in the 10^{-5} torr range. The oxides are sputtered using two separate targets for Al_2O_3 and Nb_2O_5 in the chamber.

Sput2 denotes RF sputtering done at a power of 45 W and at an argon flow rate of 0.5 sccm (standard cubic centimeter per minute) controlled by the mass flow controller (MFC). The samples are fixed to a rotating sample holder and kept in the chamber in vacuum till pressure is below 5×10^{-7} Torr to ensure moisture free surface prior sputtering. Al_2O_3 and Ta_2O_5 are sputtered using two separate targets in the chamber at a rate of 0.095 A/s and 0.54 Å/s respectively, and the thickness was verified on small Si substrates using spectroscopic ellipsometry.

For all devices in this thesis, each measurement was done at least three times on different devices having the same structure, and only the result which is more typical as compared to others was selected. J-V measurements were done in the dark (unless stated illuminated) using an *Agilent B1500 Semiconductor Device Analyzer* on a heating stage. The thicknesses of the dielectric layers were measured by variable angle spectroscopic ellipsometry using a *XLS-100 J.A. Woollam* instrument.

5.1 Verifying homogeneity of the dielectrics using ellipsometry

In this section, the dielectrics which are used in fabricating the devices are characterised using the atomic force microscopy and spectroscopic ellipsometer. The aim is to verify the homogeneity of the deposited oxides on the whole surface and the surface roughness which needs to be smooth for planar fabrication, and the dielectric material properties are extracted. The dielectrics were deposited using the atomic layer deposition ALD1 and RF sputtering (Sput2) on the top of Silicon substrates, cleaned with isopropanol and blown dry with nitrogen gun.

The variable angle spectroscopic ellipsometry (XLS-100 Spectroscopic Ellipsometer J.A. Woollam Co., Inc) was used to find the thicknesses and the optical constants of the ultra-thin Ta_2O_5 and Al_2O_3 oxide layers (for all MIM and MIIM rectifiers) deposited on a silicon substrate using atomic layer deposition (ALD) - 14 and 8 cycles/nm respectively. The change of polarization (Ψ) and the phase difference (Δ) are then extracted as a function of the photon energy (E) and fitted using *CompleteEase* software (provided specifically for the ellipsometer) from which the material properties are derived. The ellipsometry is capable of illuminating light beam at wavelength ranging between 241.1 and 1686.7 nm corresponding to an energy ranging between 0.7 and 5.2 eV. Measurements are done at a certain Brewster angle which can be adjusted according to the substrate type to enhance the light intensity.

Ellipsometry gives more precise and reliable thickness measurements for oxides deposited on Si than for those deposited on glass substrates even for layers as thin as 1 nm. This was confirmed by obtaining an extracted native oxide thickness on top of silicon very close to the native oxide thickness given by the company. For each oxide deposition (using the ALD or sputtering), a small piece of silicon was loaded beside the sample to validate, using the ellipsometry, the thickness of the deposited dielectrics in the fabricated diodes.

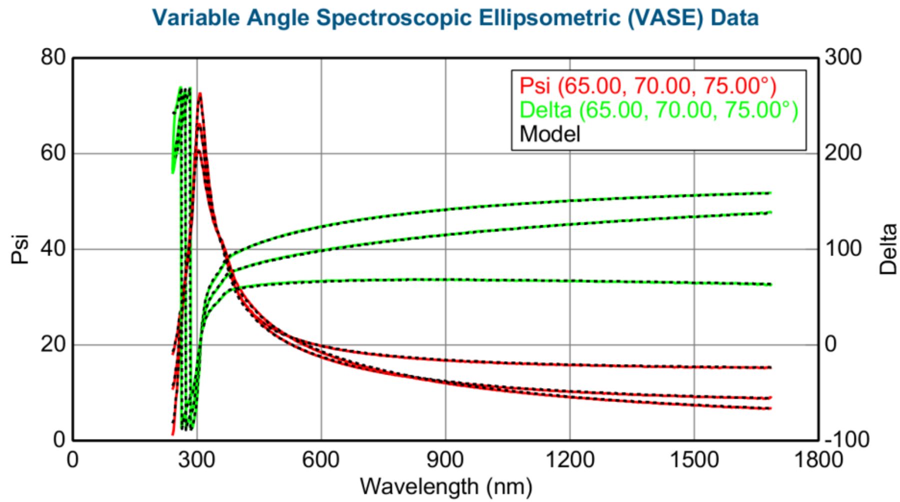

Figure 5.1 Fitting psi (Ψ) and delta (Δ) using Tauc-Lorentz or Cody-Lorentz oscillators (using *CompleteEase*) to a reference Si model with a minimum mean squared error (MSE) and consistency at 3 Brewster angles (65, 70, and 75°) ensures correct extraction of the oxide parameters.

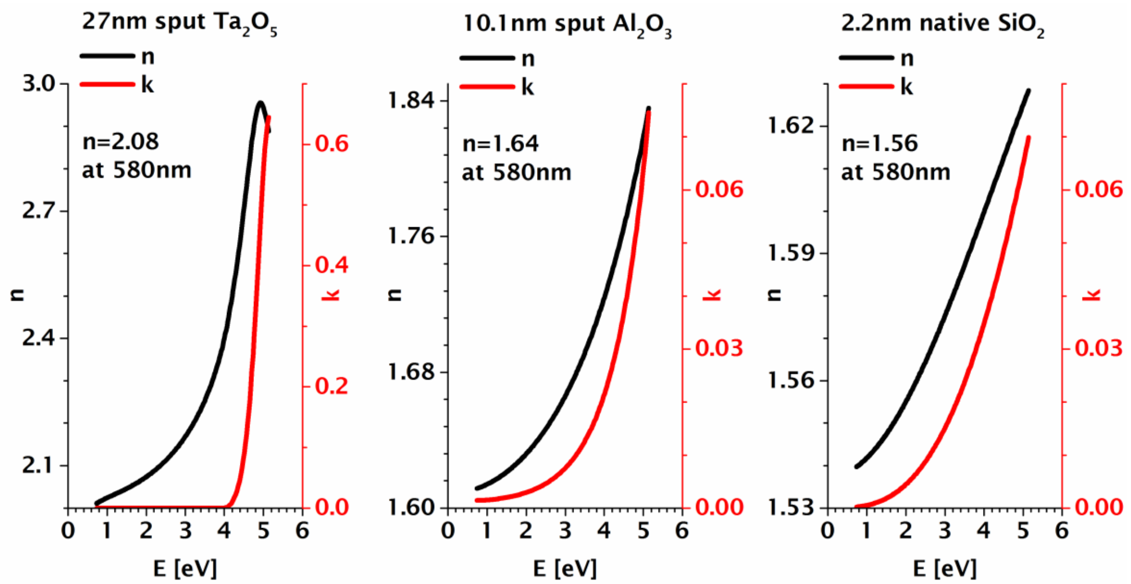

Figure 5.2 Refractive index (n) and extinction coefficient (k) versus the photon energy (E) for the 27nm sputtered Ta_2O_5, 10.1 nm sputtered Al_2O_3, and 2.2 nm native SiO_2. All oxides were grown on separate Si substrates.

The plots of the dielectric optical constants, n and k, as a function of the photon energy are shown in Figure 5.2. The extracted n for each dielectric is given in Table 5.1 showing consistency with literature values.

Table 5.1 The extracted refractive index (n) and bandgap (E_g) as compared to literature values.

	n at 580 nm		n^2 at 400-1200 nm		Eg [eV]	
	exp	literature	exp	literature	exp	literature
Ta_2O_5	2.08	2.13[109] 2.2-2.3[110]	4.1-4.76	4.6-4.95[111]	4.8	4.4[112]
Al_2O_3	1.64	1.77[113]	2.61-2.79		--	8.8[112] 6.5[114]
SiO_2	1.56	1.46[115,116]	2.38-2.49		--	9[112]

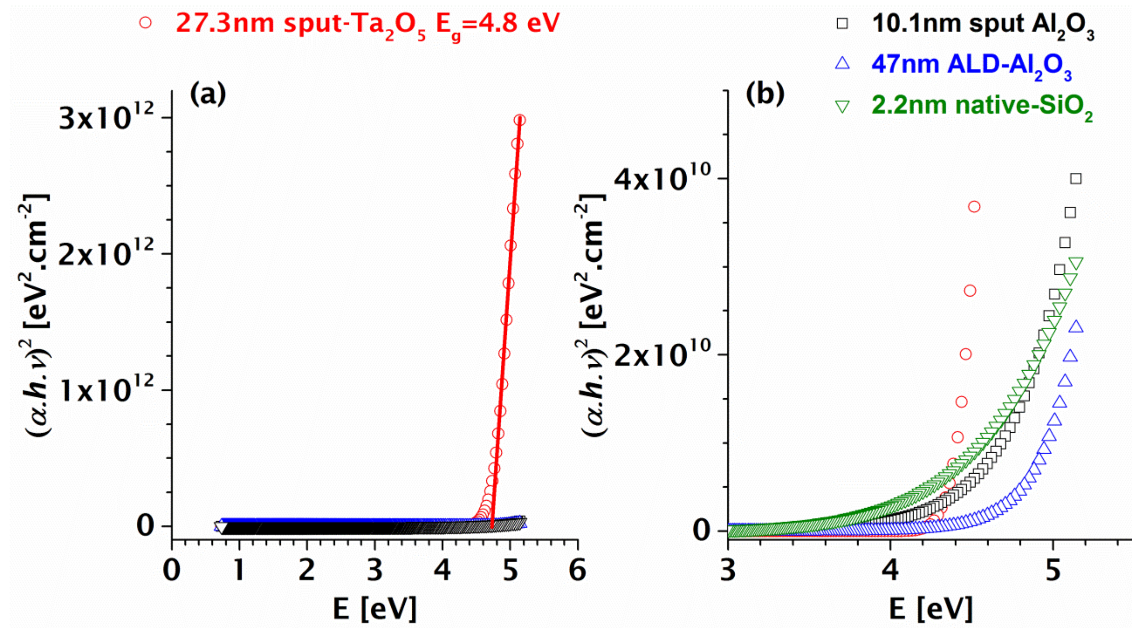

Figure 5.3 $(\alpha h\upsilon)^2$ as a function of the photon energy (E = h.υ) in eV. The full scale is shown in (a) to show the linear fit for Ta_2O_5 whereas (b) is a zoom-in to show the plots of other samples.

The relation between the energy bandgap and the absorption coefficient is described by the following Urbach equation:[117]

$$\alpha = \frac{A(h\upsilon - E_g)^{\frac{1}{2}}}{h\upsilon} \tag{5.1}$$

where α is the absorption coefficient, A is a constant, E_g is the energy bandgap, h is the Plank's constant, and υ is the frequency.

The slope of the curves in (Figure 5.3) indicates the transition between the valence and conduction bands. The bandgap is extracted by extrapolating the linear region of α^2 up to the value of energy

where $\alpha = 0$. These curves represent Tauc plots which describe $(\alpha h\upsilon)^n$ as a function of the photon energy (E = h.υ) in eV where n = 2 for direct bandgap and n = 0.5 for indirect bandgap material. An energy bandgap of 4.8 eV was extracted from the intercept of the plot using the absorption coefficient of the sputtered deposited Ta_2O_5 extracted from ellipsometry measurements at 65°. The bandgap of Al_2O_3 and SiO_2 could not be extracted as their bandgaps (Table 5.1) lie outside the ellipsometry spectral range capability (0.7-5.2 eV).

The thickness and roughness profiles of a silicon substrate with native oxide on top as indicated by the manufacturer and of a 47-nm thick ALD deposited Al_2O_3 are shown in Figure 5.4 and Figure 5.5 respectively. The measurements were mapped for both samples and taken at 3 different Brewster angles for the second sample showing general consistency and lower MSE at 70°. The mapping profile of native SiO_2 on Si substrate showed very low MSE (1.4-1.6) and very good homogeneity with thickness of 2.1 nm around the centre and peaking at the edges at 2.2 nm. The thickness at single point for one of the measurements is calculated using *CompleteEase* and found to be 20.89 ± 0.251 Å. With a resolution of ± 0.1 nm, this can be read as 2.1 nm. Surface roughness generally rises at the edges. The native SiO_2 thickness was also verified at approximately 2 nm with HR-TEM images (section 5.2). This thickness mapping pattern for SiO_2 becomes completely different with the 47 nm ALD deposited Al_2O_3 where thickness increases gradually in a wavy pattern from an edge (46.5 nm) to the other (47.4 nm) which is expected with the ALD deposition flowing horizontally from one side to the other. Surface roughness appears constant over the whole surface (between 1.67 and 2 nm). The 0.9 nm (1.9 %) thickness variation is essentially very small indicating excellent homogeneity and uniformity of the ALD technique. The excellent smoothness of the surface and the gradual and very small thickness variation indicate that the ALD technique allows good control of few nanometres thickness with pinhole-free and highly uniform oxide layers. Any pinhole increases the risk of short circuits especially in MIM/MIIM devices of ultra-thin oxide films. Short circuit was frequently occurring for fabricated devices.

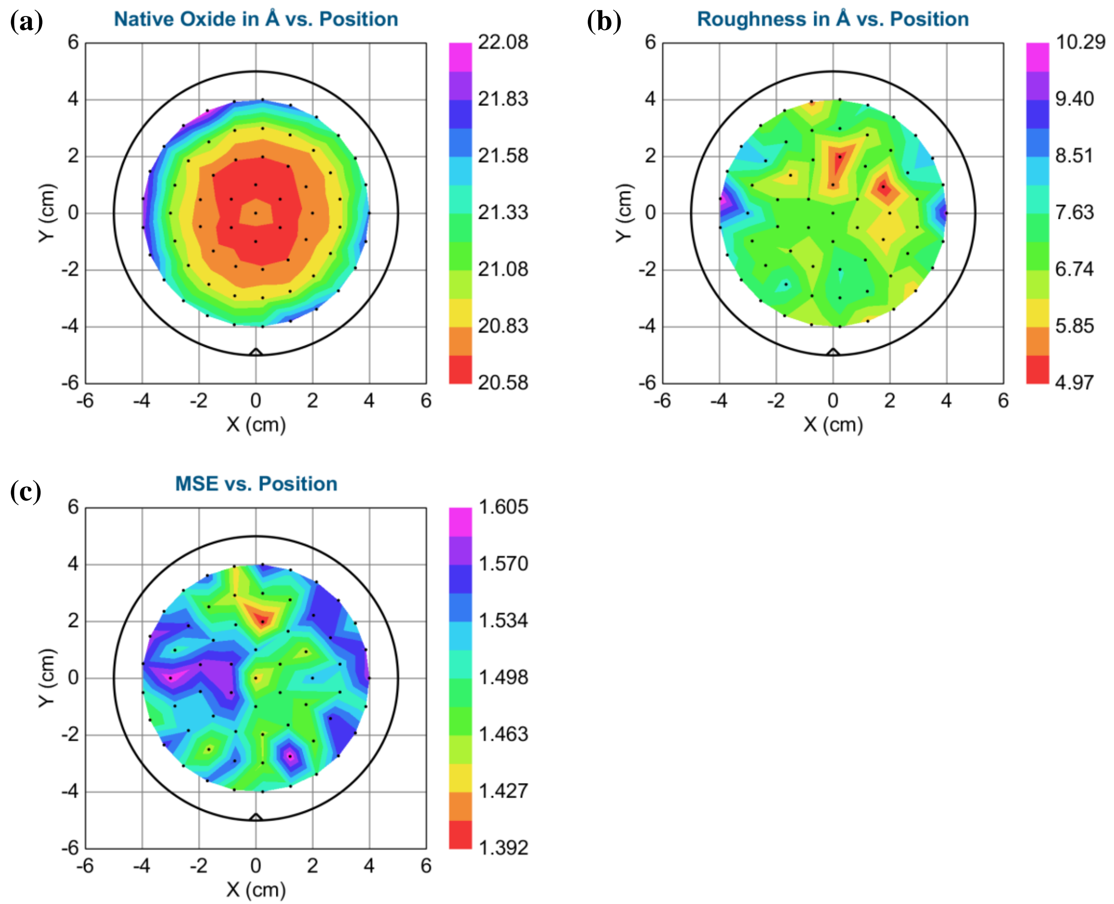

Figure 5.4 Mapping profile of the native SiO_2 grown on 525μm thick Meiningen Si substrate modelled using *CompleteEase* and measured using the ellipsometer at 65°: a) native SiO_2 thickness (with an average MSE 1.5 and average thickness of 21.73 Å), b) surface roughness in Å, c) MSE. Measurements were done at the black dots.

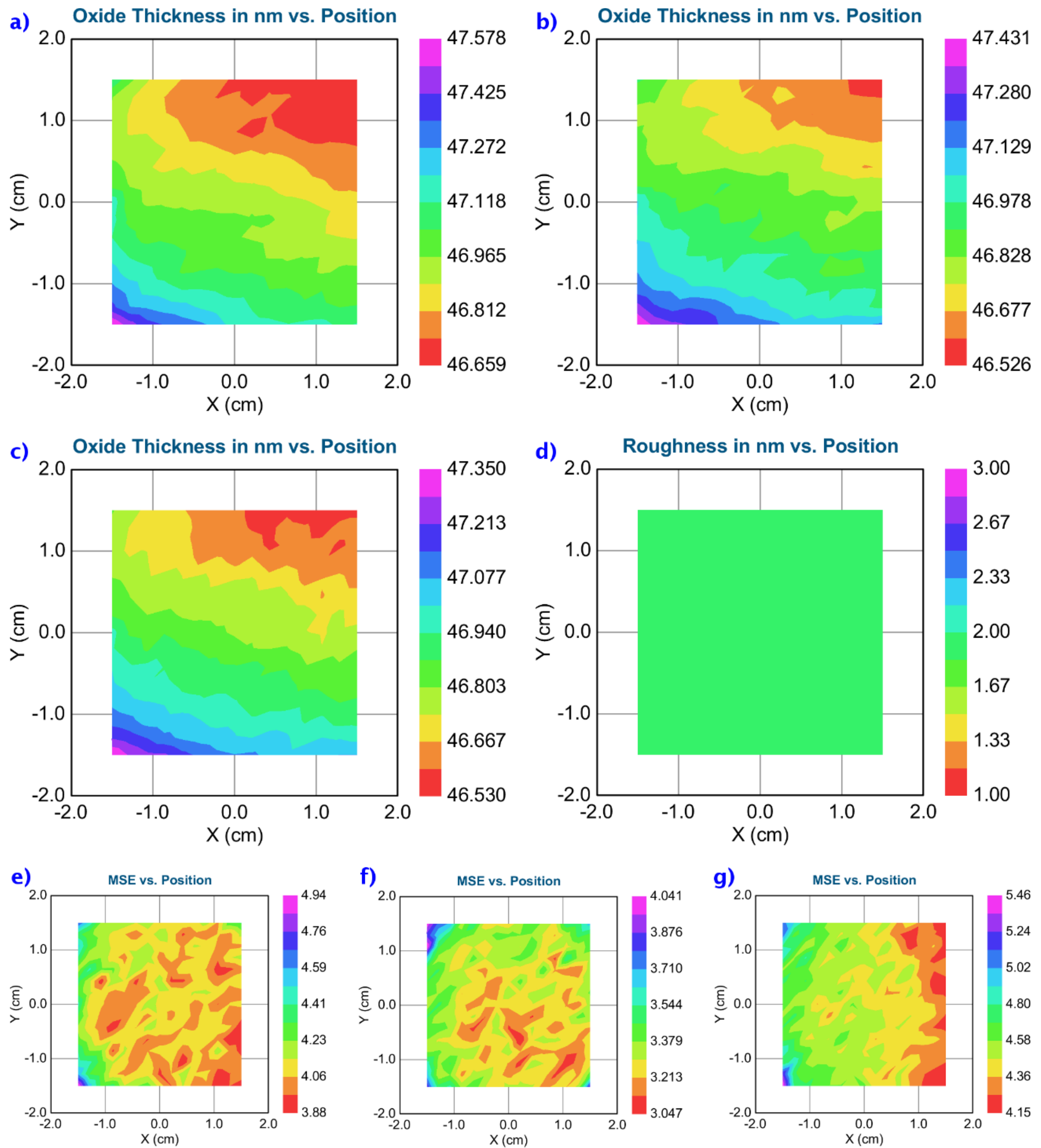

Figure 5.5 Mapping profile of the 47 nm ALD deposited Al_2O_3 grown over Si substrates (using *CompleteEase*) showing the oxide thickness profile at 65 (a), 70 (b), and 75° (c), the optical surface roughness profile (d) (the same at all angles), and the MSE at 65 (e), 70 (f), and 75° (g).

5.2 Imaging the structure (FF-OCT, AFM, and HR-TEM) and the native oxide issue

In this section, images of different device structures are shown aiming to understand what is fabricated and what happens at the interface. Physical roughness of the metal and dielectrics, which is important for MIM/MIIM performance especially for resonant tunnelling to occur, and metal film thickness is checked with the AFM. The growth of native oxide is investigated using

HR-TEM images, which give a deeper insight into the ultra-thin oxide layers deposited using the RF sputtering, where the interface and deposition quality of the oxides and metals are examined.

AFM images are scanned using *Veeco Digital Instruments CP-II system APEM-1000*. All AFM images in this thesis were scanned on contact mode as it produced better topography of the surface for the device materials used. The physical surface roughness of the dielectric surface of Al_2O_3 deposited using ALD was checked with AFM measurements scanned at two different 2×2 μm^2 regions (Figure 5.6). The low surface roughness of ~0.85 nm reveals an atomically smooth surface (< 1 nm). This physical roughness is more reliable than the 1.67-2 nm optical roughness indicated using ellipsometry. AFM was also used in contact mode to validate the nominal thickness values of the metals deposited for all samples. A comparison with thicknesses estimated using the quartz monitor during deposition allowed the estimation of a calibration factor.

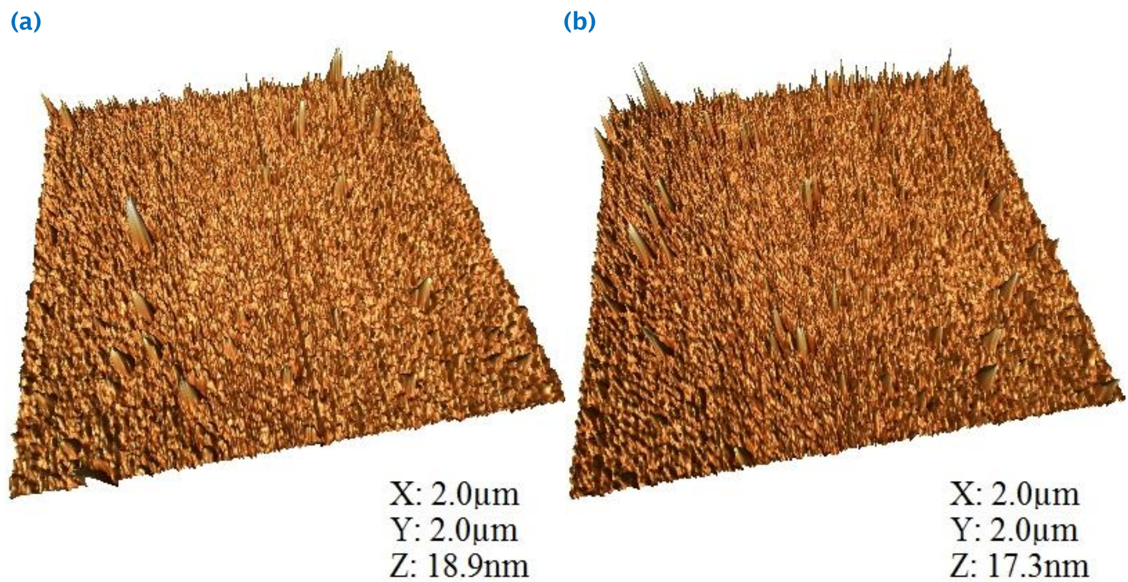

Figure 5.6 AFM images scanned on two different regions of 47 nm thick ALD deposited Al_2O_3 on silicon substrates: a) RMS roughness 0.85 nm, average roughness 0.58 nm b) RMS roughness 0.84 nm, average roughness 0.57 nm.

Images shown in Figure 5.7 show the active device at the junction using the AFM, confocal microscope, and FF-OCT. The full-field optical coherence tomography (FF-OCT) system is used to take an image of a device by full-field illumination of the sample. An infrared light beam of $\lambda_0 = 850\ nm\ \Delta\lambda = \ 90\ nm$ is split into the sample and a reference using non-polarising beam splitter. The beam scattering back from the sample recombines with the light reflecting from the reference. The reference moves while the recombined beam gets detected by an image sensor at a rate of 120 frames per second. This results in scanning an image at depth interval depending on

the reference speed and at two lateral dimensions to get the 3-D image. More details about the in-house FF-OCT technique used can be found elsewhere.[118] A shadowing effect can be noticed clearly on the FF-OCT image for batch 1 (B1-4) for the bottom Al contact and on the confocal image of batch 3 (B3-2) for the bottom Cr contact. This issue was observed for the electrodes deposited downwards using the Edwards evaporator. The linewidth of the metal electrodes look to be consistent as can be seen in Figure 5.7(c).

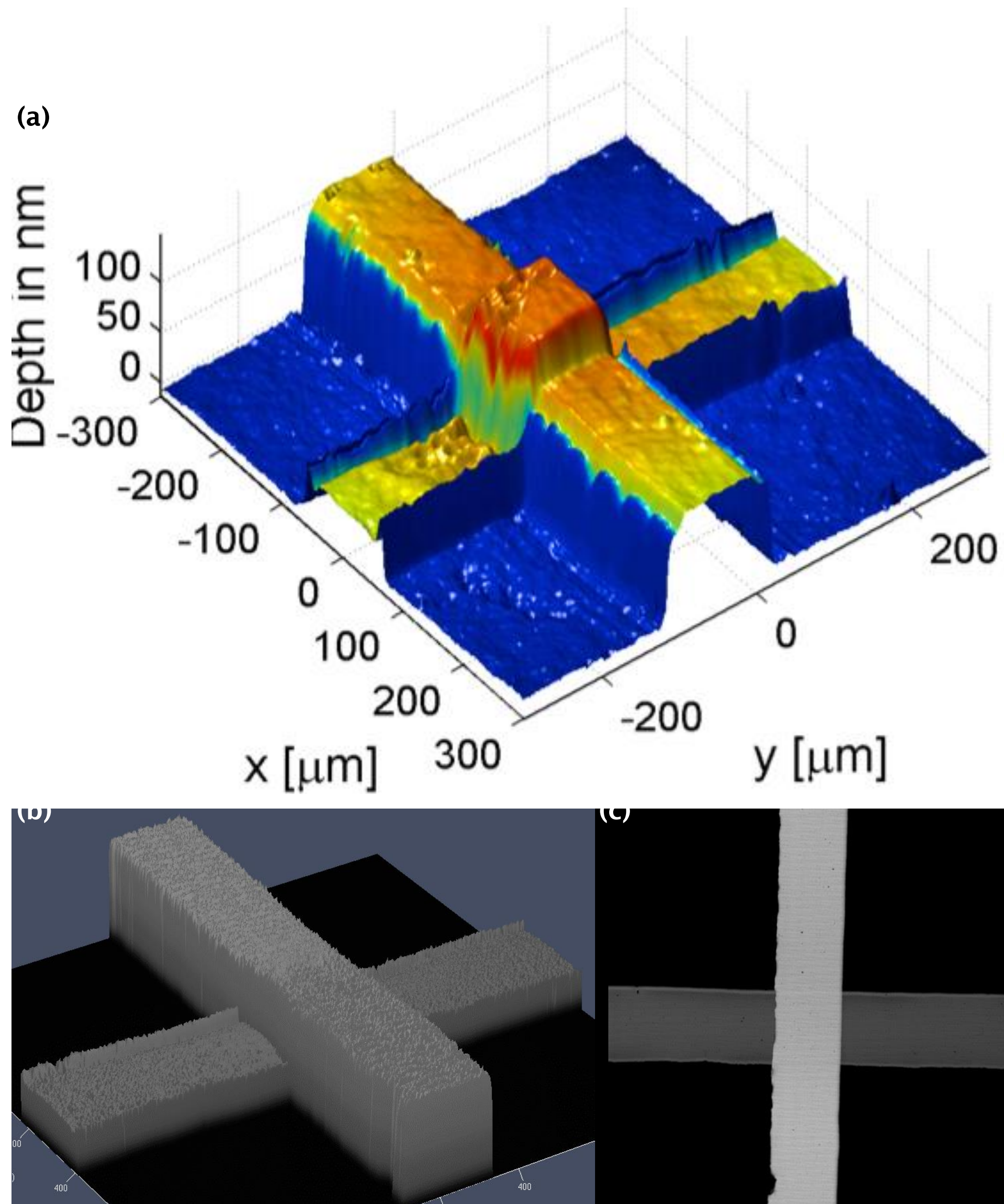

Figure 5.7 FF-OCT image of device B1-4 (a) and confocal microscope images of device B3-2 (b and c).

AFM images have been taken for many samples. The selected B1-4 and B3-2 (Table 5.3) show the typical topography and roughness of Edwards-thermally evaporated samples (Figure 5.8). The RMS/average roughness values were found to be (in nm) 0.45/0.32 nm for the corning glass substrate, 2.2/1.5 nm for top 60 nm-Al at the junction, 2.15/1.5 nm for the top 60 nm-Al, 1.4/1.1 nm for the bottom 30 nm-Al, and 0.9/0.7 nm for the oxide stack (1 nm-Al_2O_3 on top of 4 nm-Ta_2O_5). This indicates a reasonable smoothness of the fabricated Al metal due to the tendency of elemental metals to crystallize even at room temperature.[119] However, further improvement is needed to reduce the surface roughness of the bottom contact and dielectric films which is essential for the bottom metal for optimal performance of the MIM/MIIM diodes. This could not be achieved for the first 3 batches using the Edwards metal evaporator, which evaporates downwards at a pressure in the order of 10^{-6} mbar at deposition rate not easy to be kept constant and difficult to be lowered to the Angstrom (Å) per second level (~1 nm per second for Al). Deposition of batches in the next sections are done using a Moorfield system, which deposits upwards towards a rotating stage holding the samples at a pressure in the order of 10^{-7} mbar and easily controllable rate in the order of Å/s. The ALD1 oxide stack with 0.9 nm RMS roughness is atomically smooth (< 1 nm) but can still be slightly improved knowing that 150 nm-thick RF-sputtered Ta_2O_5 had 0.7 nm RMS roughness in another study.[120]

Additionally, it is essential to investigate the native oxide expected to grow on the top of the bottom metal electrode which is critical in understanding the role of the native oxide in the conduction process. Literature review and ellipsometry measurements on in-house fabricated samples indicate that this layer (AlO_x) is fairly thick on Al; 2.6-3 nm estimated by ellipsometry with higher values reported in the literature. The growth rate is very high in most metals and it can reach to saturation thickness in a few hundreds of seconds. Other physical characterization techniques such as HR-TEM cross-sectional image would be useful since the elliposmetry is not very accurate due to the reflective metal surface underneath the native oxide. A complete understanding of this is clarified in sections 6.2 and 6.3 with the assistance of electrical characterisation.

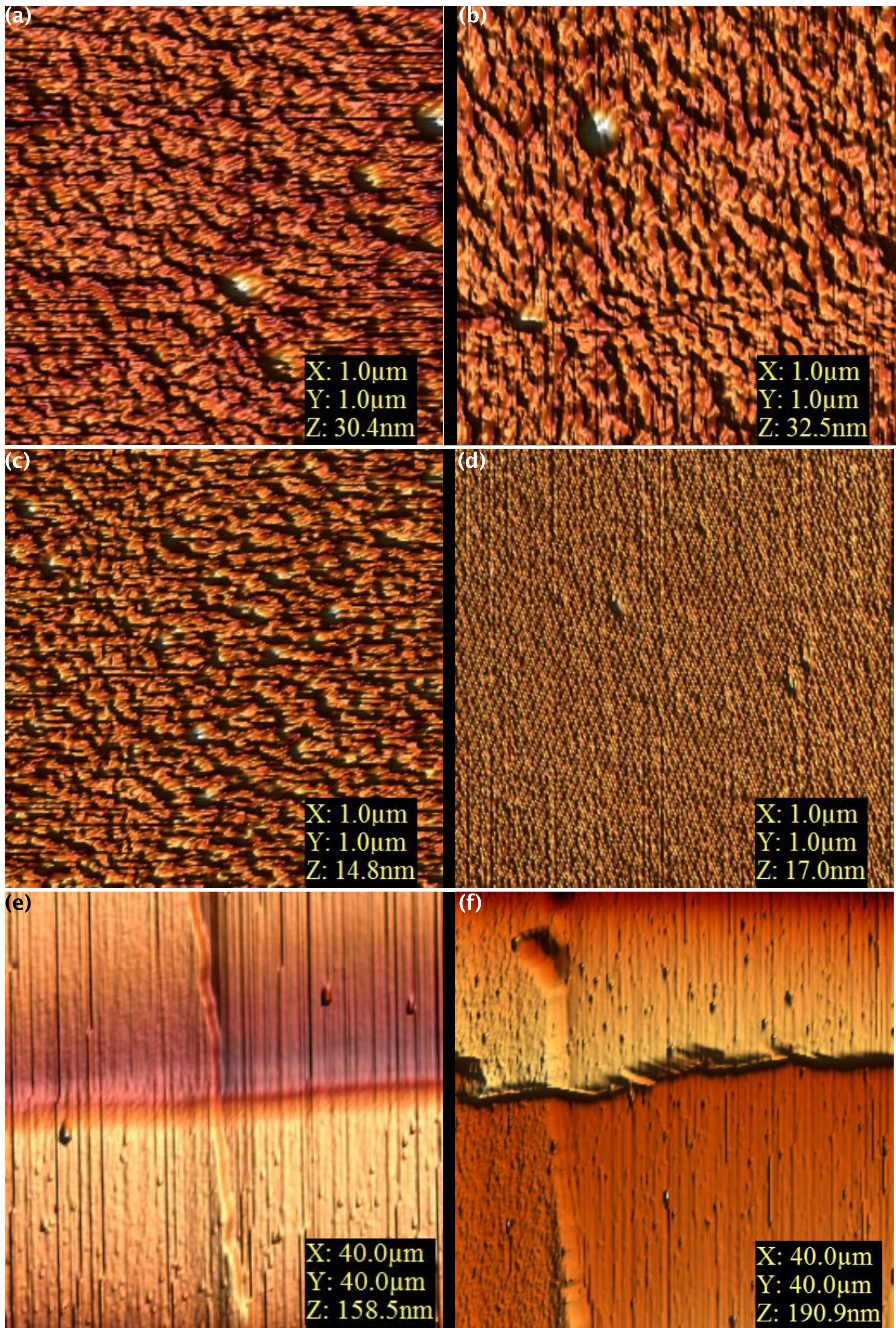
(a)
X: 1.0μm
Y: 1.0μm
Z: 30.4nm
(b)
X: 1.0μm
Y: 1.0μm
Z: 32.5nm
(c)
X: 1.0μm
Y: 1.0μm
Z: 14.8nm
(d)
X: 1.0μm
Y: 1.0μm
Z: 17.0nm
(e)
X: 40.0μm
Y: 40.0μm
Z: 158.5nm
(f)
X: 40.0μm
Y: 40.0μm
Z: 190.9nm

Figure 5.8 AFM images created using WSxM[121] showing the textured surface of the 60nm-Al top electrode of B1-4 junction (a), 60nm-Al of B1-4 top electrode (b), 30nm-Al of B1-4 bottom electrode (c), sandwiched oxides of B1-4 (d), and a corner of B1-4 (e) and B3-2 (f) junctions.

HR-TEM images in Figure 5.9 and Figure 5.10 show the cross-sectional structure, respectively, of two devices of the following structures:

1. c1: 120nm-Al/AlO_x/4nm-Ta_2O_5/1nm-Al_2O_3/AlO_x/120nm-Al/2nm-SiO_2/Si
2. c3: 120nm-Al/AlO_x/1nm-Al_2O_3/4nm-Ta_2O_5/AlO_x/120nm-Al/2nm-SiO_2/Si

The Al electrodes were deposited upwards using Moorfield thermal evaporator at a rate of 5 Å/s and patterned using the lift-off process, whereas the oxides were RF sputtered (Sput2). Thermal evaporation and sputtering (Sput2) were done when the pressure in the chamber is lower than 5×10^{-7} Torr. Details of the lift-off process are described section 6.3.1.

As can be observed, the growth of ~3-to-4 nm native oxide is confirmed on the top of bottom Al electrode and surprisingly on the bottom of the top Al electrode at the interface with the oxides. This is much larger than 1.5 nm native oxide grown at the interface between the 100 nm thick bottom metal (Al/ZrCuAlNi) and the 10 nm Al_2O_3, as observed on HR-TEM images of another study.[122] These samples were deposited at a pressure of 2.5×10^{-7} mbar, low enough to prevent the oxidation of the Al while depositing which is evident from the failure to observe any oxide layer on the bottom of bottom Al electrode. The layer observed on the top of top Al contact is the carbon coating needed for TEM imaging. Thus, the more likely explanation of the formation of native oxide layer on the bottom of top electrode is that Al, which has a high affinity to oxygen and which can diffuse from the overlying dielectric. It is also possible that Ta_2O_5 oxide layer is altered when in contact with Al, losing oxygen molecules especially at the interface resulting in a barrier between Al and the dielectric. This possibility will be further investigated in sections 6.2 and 6.3.

Based on these aspect, removal of the native oxide layer deposited on the top of the bottom Al when exposed to air during ion sputter dry etching prior to oxide deposition without breaking the vacuum will not prevent the formation of AlO_x. This procedure was attempted on some samples (before using HR-TEM) without observing any remarkable improvement of the J-V characteristics for any of the samples. In fact, dry etching worsens the surface roughness, which is needed to be as low as possible for better rectifying performance in tunnelling MIM structures.[123] The existence of native oxide is undesirable and can affect the tunnelling mechanisms and the calculations of the barrier height from FN plots.

To tackle this issue, it is suggested to use noble metallic chemical elements of outstanding resistance to corrosion/oxidation: ruthenium (Ru), rhodium (Rh), palladium (Pd), silver (Ag), osmium (Os), iridium (Ir), platinum (Pt), and gold (Au). Further research is needed to investigate the effect of deposition techniques and parameters on the quality of Ta_2O_5 and whether this can enhance the chemical bonds in this compound to prevent the loss of oxygen molecules to the oxidising metals. Cr can be used as bottom contact as the native oxide growing on Cr is of small band gap which provides a barrier to Cr similar to that with Ta_2O_5.

Another issue in the fabrication of planar MIM/MIIM structures as observed on HR-TEM images is the inhomogeneity of Al growth despite the low growth rate of 2 Å/s and the very low vacuum pressure in the chamber while depositing (2.5×10^{-7} mbar). This is a limitation of either thermal evaporation technique or Al material. A study[122] showed good homogeneity of Al and ZrCuAlNi as observed on HR-TEM images and that RMS roughness and z-peak excursions are as low as 0.2 nm and 1.7 nm respectively for 100 nm thick DC magnetron sputtered amorphous ZrCuAlNi and as high as 5 nm and 70 nm for 100 nm thick thermally evaporated Al respectively. Other studies confirm the ultra-smoothness of ZrCuAlNi with an average roughness Ra of 0.65[124] and 0.2[125] nm deposited using RF magnetron sputtering. Unfortunately, this metal cannot be deposited with the available facilities, and it is not desirable for the topic of this thesis since it has a large work function of 4.8 eV[122] which makes it difficult for resonant tunnelling to occur. However, using Au of better smoothness and no native oxide issue which a large work function of 4.8/5.1 eV as the bottom electrode is advantageous for the rectifying devices as investigated in the next sections.

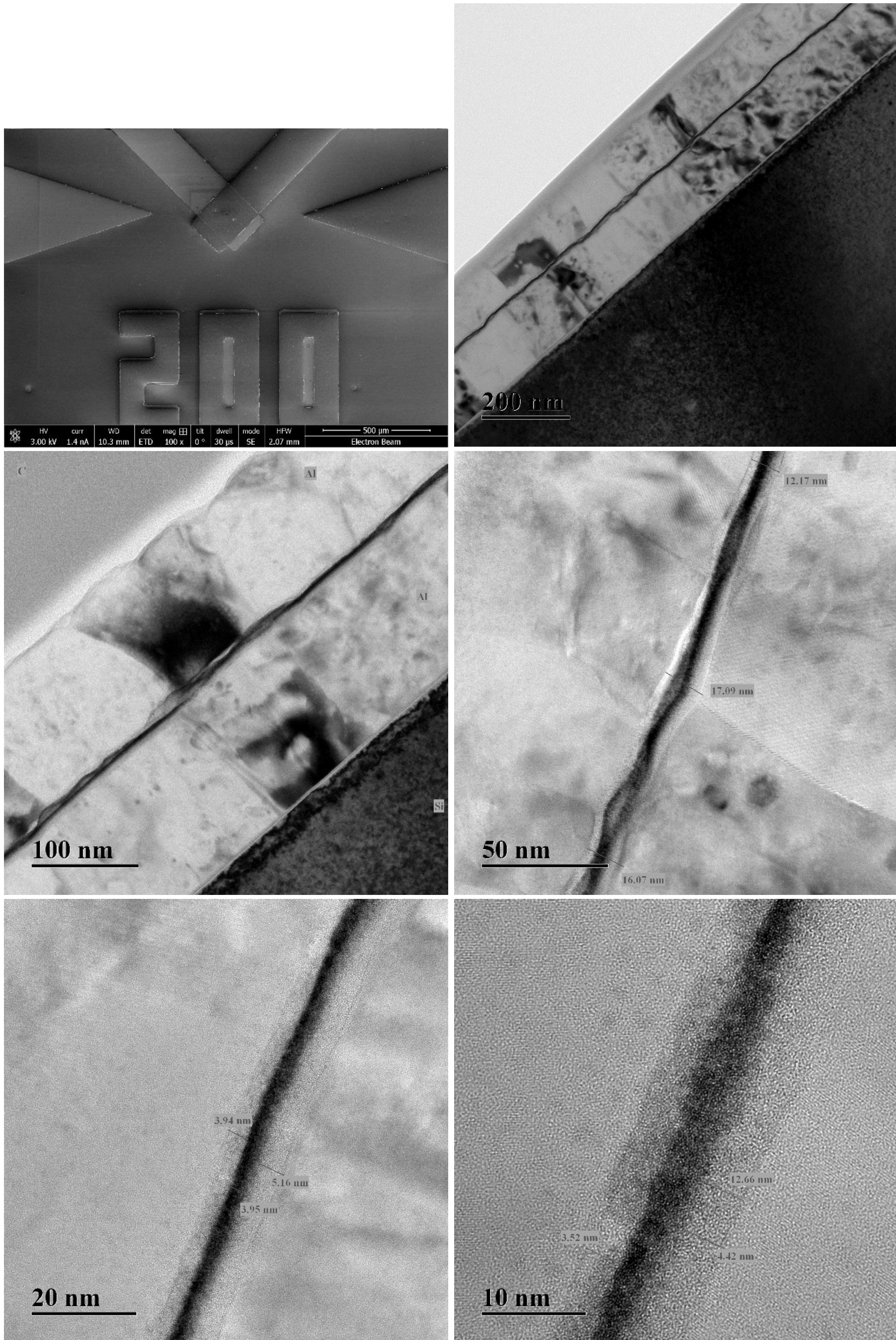

Figure 5.9 SEM and HR-TEM images of device c1.

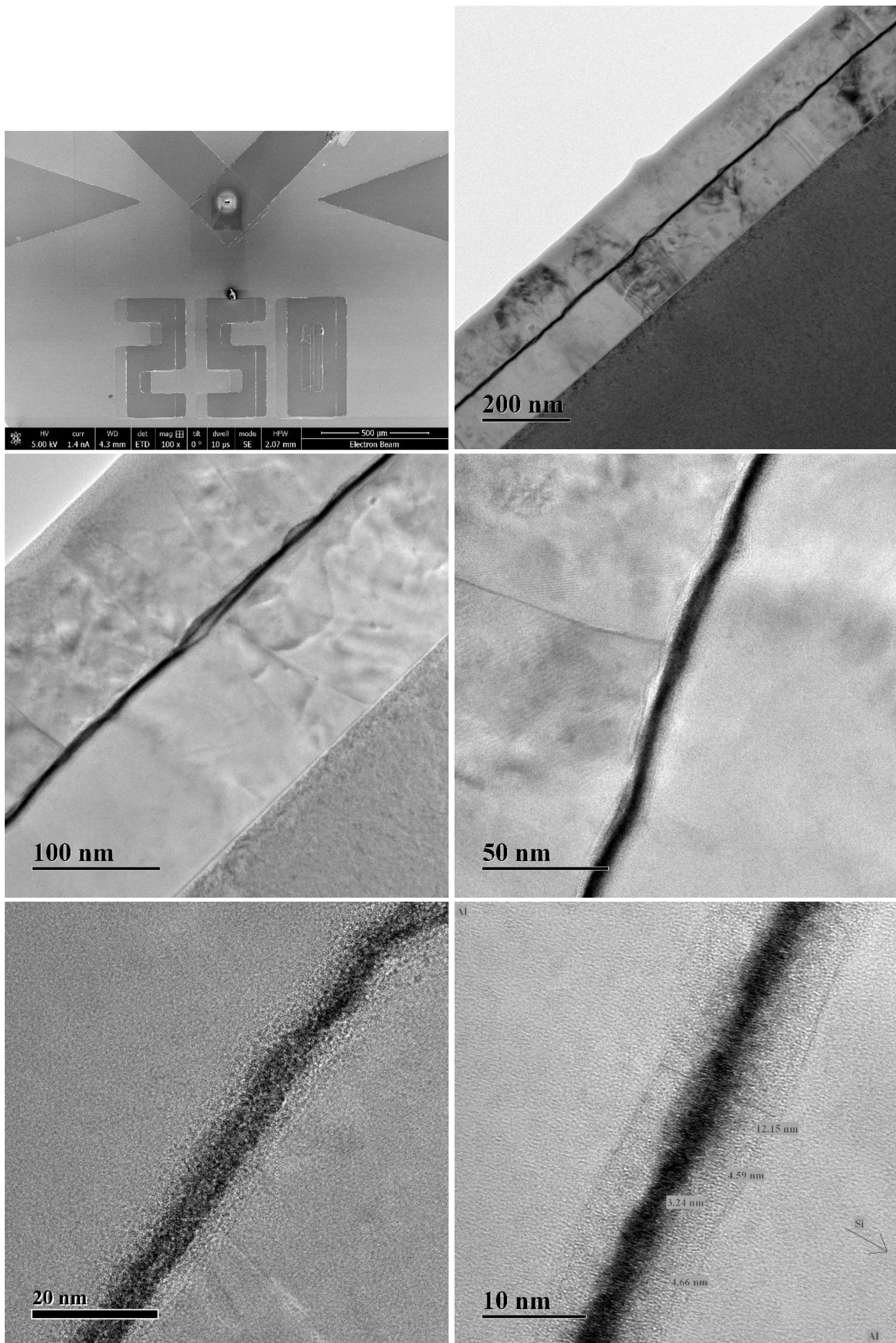

Figure 5.10 SEM and HR-TEM images of device c3.

5.3 XPS analysis of $Al_2O_3/Ta_2O_5/Si$ stacked sample

The aim of this section is to confirm the expected chemical nature of Sput2 RF sputtered oxides Al_2O_3 and Ta_2O_5. Sput2 is used for c1, c3, and devices in section 6.2 and the sections following it.

XPS measurements were performed in a standard ultra-high vacuum (UHV) system consisting of a PSP (photostimulable phosphor) Vacuum Technology dual anode (Mg/Al) x-ray source and a hemispherical electron energy analyser equipped with five channeltrons. The spectrometer was calibrated so that the Ag 3d5/2 photoelectron line had a binding energy (BE) of 368.27 eV with a full width at half maximum (FWHM) of 0.8 eV. The electron binding energies were calibrated by setting the C 1s peak in the spectra (due to stray carbon impurities) at 284.6 eV for all samples. All the spectra were measured with a precision of 0.2 eV. The measurement was performed using Al Kα (1486.6 eV) radiation as the source. The X ray source used 12 mA emission current and 12 KV accelerating voltage. The survey scan was performed using pass energy of 50 eV and the region scan with 20 eV. The step was 0.05 eV for survey and quick regions and 0.03 eV for region scan. A Shirley type background correction was used and Lorentzian–Gaussian (30) components were used to fit all spectra. The Casa XPS Version software, version 2.3.17 PR1.1, was used for all data analysis.

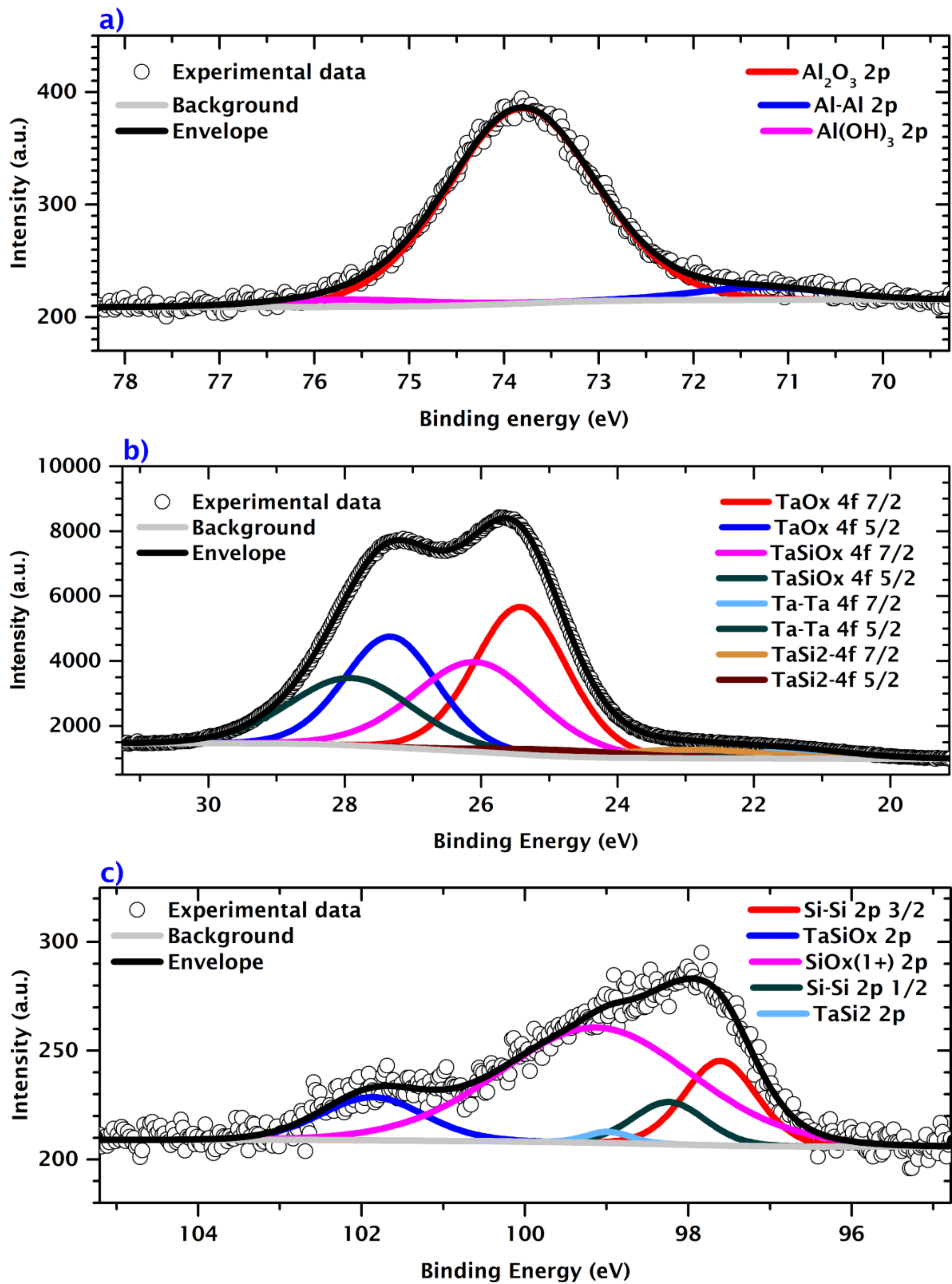

Figure 5.11 XPS core level spectra plots: Al 2p deconvoluted (a), Ta 4f deconvoluted (b), Si 2p deconvoluted (c).

The O 1s, Si 2p, Al 2p and Ta 4f core levels have been analysed and the following details have been observed (Figure 5.11 and Table 5.2). Apart from Al_2O_3, very small peaks of elemental aluminium and $Al(OH)_3$ is observed in deconvoluted Al 2p spectrum [Figure 5.11(a)]. Referring to Figure 5.11(b), Tantalum silicide ($TaSi_2$) and tantalum silicate ($TaSiO_X$) peaks can be seen at the interface along with a very small peak of elemental tantalum and significant tantalum sub-oxide peak. The intensity ratio of $TaSiO_X$ and $TaSi_2$ Ta 4f peak area is 8.82. Referring to Figure 5.11(c), an elemental Si peak can be seen at the binding energy of 97.61 (2p-3/2) and 98.24 eV (2p-1/2). The spin orbit splitting for Si 2p-3/2 & 2p-1/2 is typically 0.63 eV and intensity ratio of the two-spin orbit component is 0.5. No spin orbit splitting is seen for Si compounds (i.e., SiO_X, $TaSi_2$ & $TaSiO_X$). The intensity ratio of $TaSiO_X$ and $TaSi_2$ –Si 2p peak area is 8.81.

Table 5.2 Binding energy of the peaks.

	Serial no.	Peak	Binding Energy (eV)
Ta 4f deconvoluted	1.	Ta-Ta 4f 7/2	21.36
	2.	Ta-Ta 4f 5/2	23.28
	3.	TaSi2-4f 7/2	22.91
	4.	TaSi2-4f 5/2	24.83
	5.	TaOx 4f 7/2	25.42
	6.	TaOx 4f 5/2	27.32
	7.	TaSiOx 4f 7/2	26.08
	8.	TaSiOx 4f 5/2	27.90
Si 2p deconvoluted	1.	Si-Si 2p 3/2	97.61
	2.	Si-Si 2p 1/2	98.24
	3.	$TaSi_2$ 2p	98.98
	4.	SiO_X (1+) 2p	99.13
	5.	$TaSiO_X$	101.86

5.4 J-V characterisation of the first MIIM batches

The main aim of this section is to gain an initial understanding of the rectifying potential of the tunnelling structures which can be fabricated using the available facilities and how to proceed with the ones suitable for THz rectennas.

For all devices, corning glass substrates are cleaned using Decon-90 diluted with deionised water (DIW), acetone, and isopropanol while blowing dry with nitrogen gun after each step. Si substrates were cleaned with isopropanol and blown dry with nitrogen gun. The J-V measurements were done in the dark using an *Agilent B1500 Semiconductor Device Analyzer* on a temperature-controlled heating stage. Voltage was swept with 10 mV step size from 0 V from negative to positive bias, and from positive to negative bias.

5.4.1 The dielectric and the bottom contact

The first three batches of MIIM devices were successfully fabricated by depositing the oxides using the sputtering and atomic layer deposition techniques, varying the oxide thickness as described in Table 5.3. The devices have active area 100×100 μm^2 and were fabricated using the shadow mask approach. The shadow mask was attached to the glass substrates using magnet sheets and placed in the vacuum chamber of Edwards evaporator which evaporates the metals downward while the samples are fixed without rotation. Al_2O_3 and Nb_2O_5 oxides of B2-2 and B2-4 devices were deposited using RF sputtering (Sput1). The oxides in B1, B2, and B3 devices are deposited using ALD1.

Table 5.3 Device structure of selected samples from 3 batches.

Device		Substrate	Metal 1		Oxide 1	Oxide 2	Metal 2
Batch 1	**B1-2**	7mm CCG	30nm Al TESM	ALD1	2nm Ta_2O_5	1nm Al_2O_3	60nm TESM
	B1-4	7mm CCG	30nm Al TESM	ALD1	4nm Ta_2O_5	1nm Al_2O_3	60nm TESM
Batch 2	**B2-2**	7mm CCG	50nm Al TESM	Sput	1nm Al_2O_3	2nm Nb_2O_5	50nm Al TESM
	B2-4	7mm CCG	50nm Al TESM	Sput	1nm Al_2O_3	4nm Nb_2O_5	50nm Al TESM
Batch3	**B3-2**	7mm CCG	60nm Cr TESM	ALD1	1nm Al_2O_3	2nm Ta_2O_5	45nm Al TESM

Abbreviations: ALD = Atomic Layer Deposition, TESM = Thermal Evaporation via Shadow Mask, CCG = Cleaned Corning Glass, Sput = Sputtered

J-V measurements were done for several devices for each structure where the voltage was swept from 0 to maximum positive and negative bias at a sweep rate *dV/dt* of 9.8 mV/s and steps of either 1 or 10 mV. The 1 mV measurements were reduced to 10 mV step data to simplify the analysis and avoid measurement errors which can significantly change the rectifying characteristics derived from the J-V measurements. Sweeping in both polarities was done to exclude the shift in the J-V curves which was observed in previous measurements. This can be explained by electron trapping in the dielectric during the measurement. This trapping effect depends on fabrication conditions and will be studied in sections 6.2 and 6.3. Some devices were swept at higher voltage to check the breakdown voltage which was ranging at around 1.1 and 1.35 V for the 2 and 4 nm thick Ta_2O_5 respectively. 64 devices of each structure of the first batches were fabricated in each sample as many devices broke after sweeping the voltage; some were intentionally sacrificed, others broke suddenly after a few measurements. Some samples were already short circuited, which could possibly be due to metal spikes connecting the electrodes. These can be indicated in the z-excursion peaks and surface roughness obtained from AFM images which need to be significantly improved considering the planar structures of few nanometres thick dielectrics.

MIIM devices of 1 nm Al_2O_3 sandwiched with 6 and 8 nm-Ta_2O_5 devices were also fabricated but will not be presented and will not be fabricated in next batches due to their very high dynamic resistance making them useless for THz energy harvesters, which is the aim of this work.

Some measurements were conducted under illumination but showed no reaction to light. The first two batches (B1 and B2) were measured at room temperature, whereas all others were measured at fixed temperature of 300 K for consistency and some at varied temperature with 25 K steps using a temperature-controlled heating stage or a cryostat. The difference between the J-V measurements done at room temperature (roughly 293 K as checked all over the year in the laboratory) and those done at 300 K is slight (~7 K) but cannot be neglected due to the strong temperature dependence of some current mechanisms. The positive voltage source of the device analyser is connected to the bottom electrode while the top electrode is grounded for J-V measurements of all devices in this thesis except for batch 1 which is measured with opposite connection.

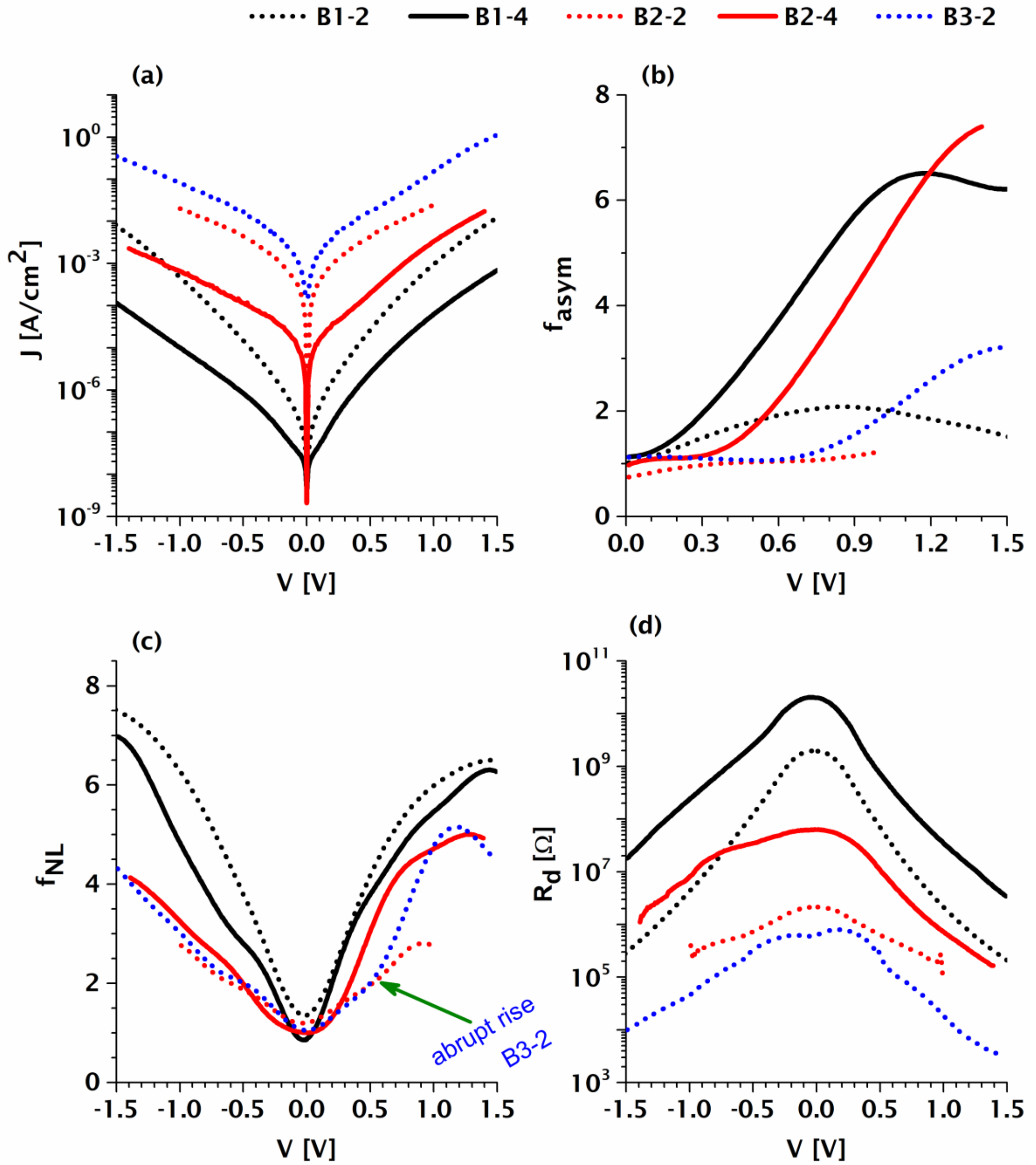

Figure 5.12 The J-V characteristics (a), the asymmetry plots (b), the non-linearity plots (c) and the dynamic resistance plots (d) of several MIIM devices (dashed) and 4nm (solid) Ta_2O_5/Nb_2O_5 from batches 1 (black), 2 (red), and 3 (blue).

Selected characteristic curves of devices having different structures are shown in Figure 5.12 where the current density (J) can be seen to increase with increasing thickness of the oxide at the low barrier (Ta_2O_5). For smaller Ta_2O_5 thickness, the tunnelling distance becomes shorter resulting in larger direct tunnelling current. The J-V asymmetry is defined as the positive to negative current ratio $f_{asym} = J_+/J_-$, while the non-linearity defined by $f_{NL} = V.dJ/J.dV$. The first and second batches showed high asymmetry despite batch 3 which showed the highest non-linearity. The similarity in asymmetry behaviour between batches 1 and 2 is due to having the

same electrode material. The usage of different dielectrics could not achieve high asymmetry in batch 3 as expected for single dielectric devices. This low asymmetry could be attributed to roughness, defects, and the presence of other conduction mechanisms affecting the charge transport.[111] Although B1-4 showed the highest non-linearity and asymmetry at the lowest turn on voltage, it suffers from a very high dynamic resistance. Considering the devices of 2nm-thick Ta_2O_5 from the 3 batches, the dynamic resistance, defined by $R_d = dV/dI$, was the lowest for B3-2 found to be less than 1×10^6 Ω near 0 V making the device structure best for matching with the antenna for THz rectennas.

The average dynamic resistances of the previous batches near 0 V are summarized in Table 5.4 showing large values where the structure $Cr/Al_2O_3/Ta_2O_5/Al$ had the smallest resistance of 1 MΩ with the 2 nm Ta_2O_5 needed for asymmetry. Assuming this resistance, which is equivalent to 118 Ωcm^2, diodes with $100\ \mu m \times 100\ \mu m$ area obviously cannot be coupled efficiently to antennas.

Table 5.4 Diode impedance [Ω] near zero volt for the different structures fabricated: noticeable improvement with Cr. Al_2O_3 is 1 nm thick, while Ta_2O_5 is 2 or 4 nm thick.

Ta_2O_5 thickness	B1	B2	B3
2nm	2.5×10^9	2.3×10^6	$1E\times10^6$
4nm	2.8×10^{10}	1.2×10^8	

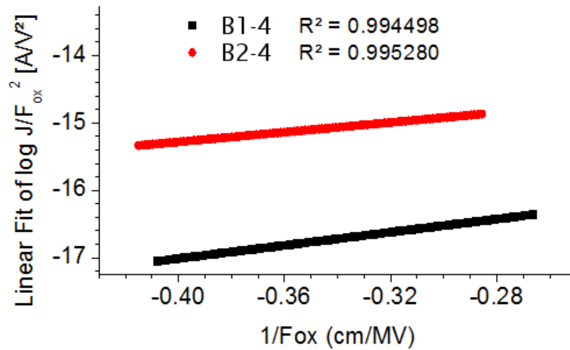

Figure 5.13 Linear fits of Fowler-Nordheim plots for B1-4 and B2-4. A good fit was observed in the high field at positive bias which does not necessarily indicate Fowler-Nordheim tunnelling in this region.

To analyse the J-V data, several tunnelling mechanisms are taken into consideration. Tunnelling of electrons at high electric field is described by Fowler-Nordheim plots and shown in Figure 5.13 to extract the barrier height from the slopes by fitting equation (4.9). Fowler-Nordheim (FN) tunnelling was assumed to dominate for the thicker dielectric having the lower barrier height. The

barrier height was then extracted between the metal and the oxide and found to be 0.3 eV for Al/Nb_2O_5 for B2-4 and 0.38 for Al/Ta_2O_5 for B1-4. A comparison between experimental and literature values is shown in Table 5.5. The table includes the work functions and electron affinities for several materials which are used later in the thesis. It is worth noting that literature values differ which could explain the mismatch observed with experimental values. This indicates the necessity to find the work function and electron affinities of the deposited materials using other techniques so as to be helpful in choosing the right materials for the next batches. However, FN tunnelling is expected to be more dominant at opposite negative polarity rather than at negative polarity, and thus this current reversal could be due to another mechanism which will be argued on in the next sections and investigated thoroughly in chapter 6. The possibility of resonant tunnelling is suggested at positive polarity especially for B3-2, indicated by a green arrow in Figure 5.12 where an abrupt steep rise in non-linearity can be observed at ~0.5 V.

Table 5.5 Several materials and their corresponding barrier heights.

Work Function of Metals [eV]					Electron Affinity of Oxides [eV]		
Al	Cr	Au	Ag	Pt	Al_2O_3	Ta_2O_5	Nb_2O_5
4.2	4.4	4.8	4.7	5.3	1.35	3.75	4

Barrier Heights [eV]				
Cr/Al_2O_3	Al/Al_2O_3	Al/Ta_2O_5	Al/Nb_2O_5	Cr/Nb_2O_5
3.05	2.85	0.45	0.2	0.4

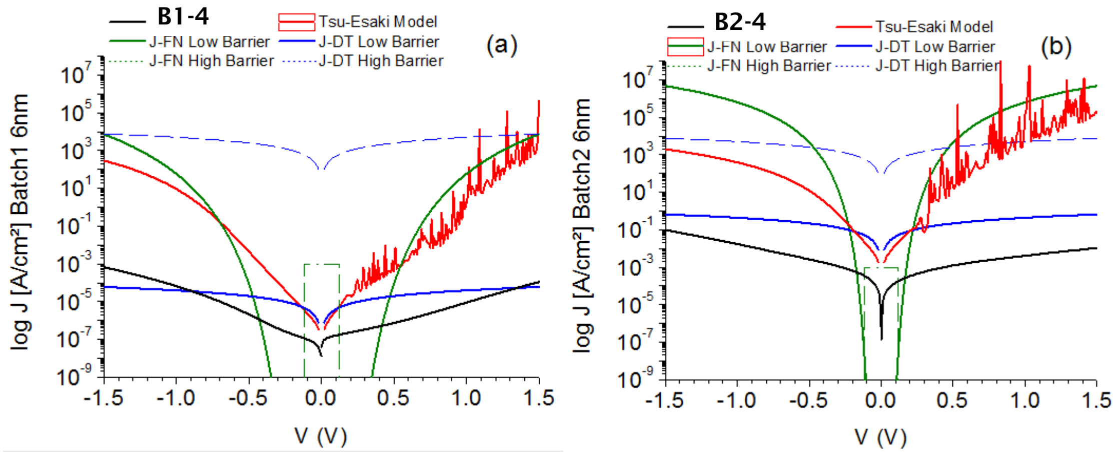

Figure 5.14 The experimental J-V characteristics as compared to the in-house model and the closed form expressions of direct and Fowler-Nordheim tunnelling for the structures B1-4 (a) and B2-4 (b).

The closed form expressions of the FN and direct tunnelling mechanisms based on equations (4.9) and (4.10) respectively were plotted with the J-V curves obtained from the in-house model for 1 device from each batch and compared to experimental characteristics as shown in Figure 5.14. The behaviour of the experimental devices was surprisingly far from the model and close to direct tunnelling and shifted up by FN tunnelling especially in the negative bias regime. The model shows peaks at positive polarity describing resonant tunnelling. These noise-resembling peaks were corrected later in the model to show the current increasing steadily, however, they are good here to understand the occurrence of resonant tunnelling in different structures.

5.4.2 Etching the native oxide

Batches 4 and 5 of the following device structure Glass/Al/Al_2O_3/Ta_2O_5/Al were repeated with some modifications in the fabrication process to investigate why the dynamic resistance at 0 V was so high (2×10^{10} Ω) for device B1-4 and to see if it can be reduced. These batches were annealed unlike all other devices in this work which were as-deposited. Thermal evaporation was done upwards using Moorfield evaporator at a deposition rate of ~10 Å/s. The conditions of sputtering the oxides are the same as described in section 5.4.1. Ion sputtering was used to dry etch the native oxide on the bottom deposited metal. This is done using the same sputtering kit at a power of 50 W for 10 minutes, which is sufficient to etch several nanometres. The oxides are then sputtered in the same chamber without breaking vacuum.

Table 5.6 The device structure and layer thickness of batches 4 and 5.

Device	Substrate	M1		Native[1]	I 1	I 2	Native[1]	M2	
	CG [µm]	Al-TE_M [nm]	Rq/R_a[2] [nm]	AlO_x [Å]	Al_2O_3 [nm]	Ta_2O_5 [nm]	AlO_x [Å]	Al-TE_M[2] [nm]	Rq/R_a[2] [nm]
B4-3	700	44	5.4/3.6	-	-	3	-	60	3.7/2.8
B4-5	700	47	7.3/5.5	-	-	5	-	120	3.7/2.9
B5-3	700	44	5.0/3.0	-	1	3	-	45	2.6/2.0
B5-4	700	43	5.7/3.5	-	1	4	-	47	1.9/1.5
B5-5	700	45	7.6/4.6	-	1	5	-	85	2.2/1.7

CG = Corning Glass, TE_M = Thermal Evaporation Moorfield, [1]discussed in section 5.2,
[2]Roughness extracted from AFM images, Rq/R_a or RMS/Average roughness

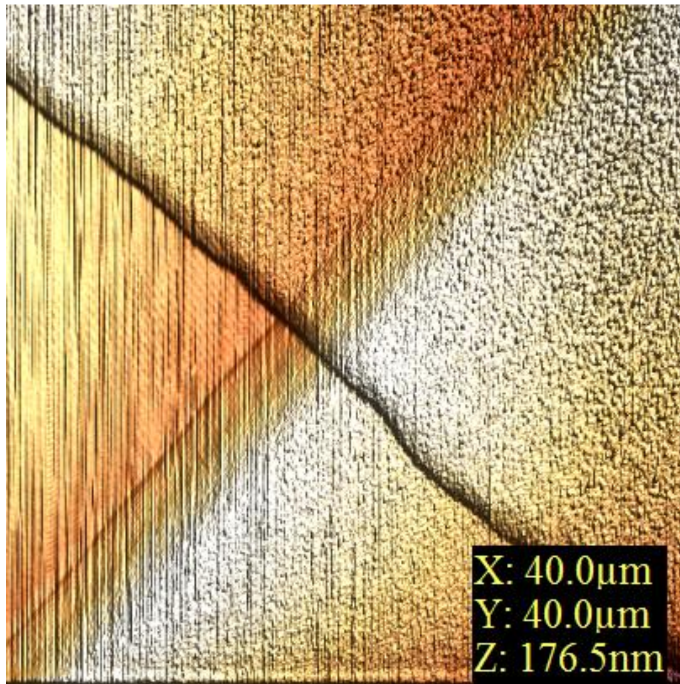

Figure 5.15 AFM image of sample B4-2 processed using WSxM.

An AFM image of the device structure at a corner of the junction is shown in Figure 5.15 where the dielectric is on the left triangle, the bottom Al metal at the lower triangle, the top Al metal at the upper triangle, and the junction corner at the right triangle. The thickness of the metal layers was validated using the AFM showing non-uniformity and high roughness for thick regions as shown in Table 5.6. This step, despite its advantage of removing the native oxide, is thought to be the reason for the very high surface roughness observed for the etched bottom Al electrodes.

The J-V measurements were swept at positive and negative bias with a voltage step of 10 mV. The effect of annealing and illumination is revealed in Figure 5.16 for device B5-3. The J-V curves show instability at low electric field at both polarities which was reduced by annealing the devices at 200 °C for 1 hour with nitrogen flowing to prevent oxidation. Illumination causes a slight increase in the current at low electric field which is explained by other parallel mechanisms occurring such as the electron-hole generation in the dielectric bulk. The direct tunnelling closed form expression showed a better fitting at low electric field when 6.3 nm of Ta_2O_5 is considered as the sandwiched dielectric stack. The simulations in Figure 5.17 based on the in-house model (section 4.11) showed an excessive impact on the J-V curves with a reduction of 5 orders of magnitude when increasing the Al_2O_3 by 1 nm. In addition, the effect of resonant tunnelling in raising the asymmetry at positive polarity becomes less prominent.

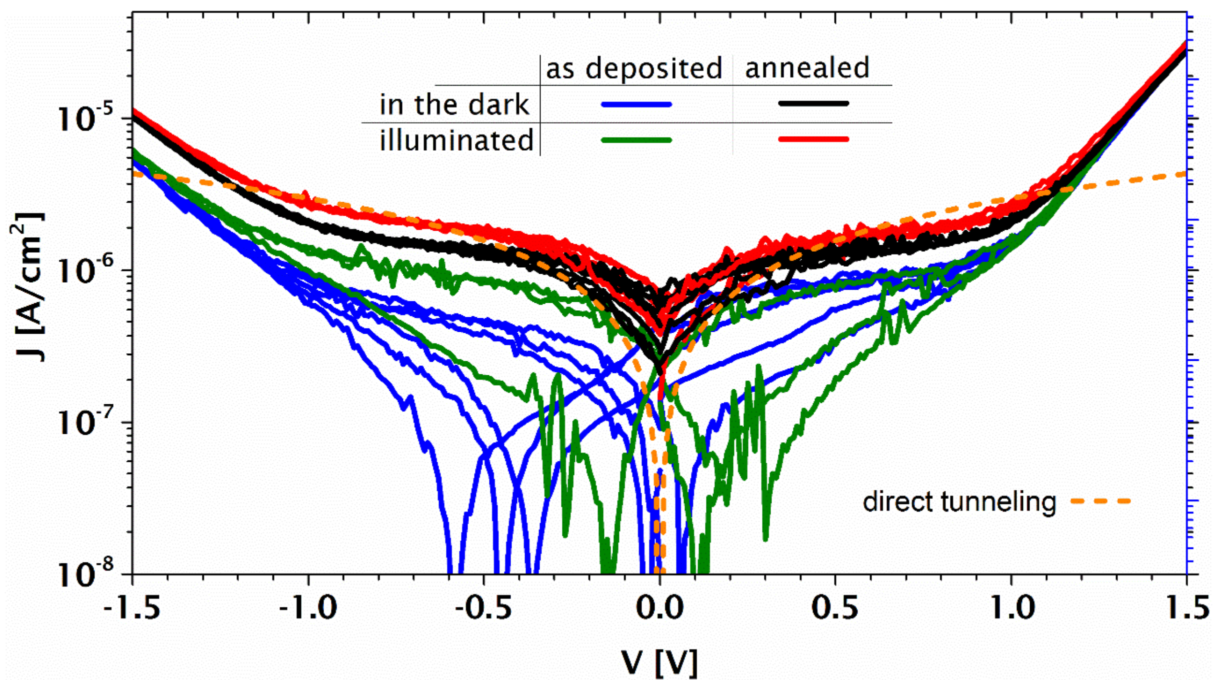

Figure 5.16 J-V characteristics for the same device B5-3 before and after annealing, in the dark and under illumination. The dashed orange curve represents the direct tunnelling closed form expression considering a 6.4 nm thick Ta_2O_5 dielectric and a 0.5 eV low barrier height between the Al and the Ta_2O_5.

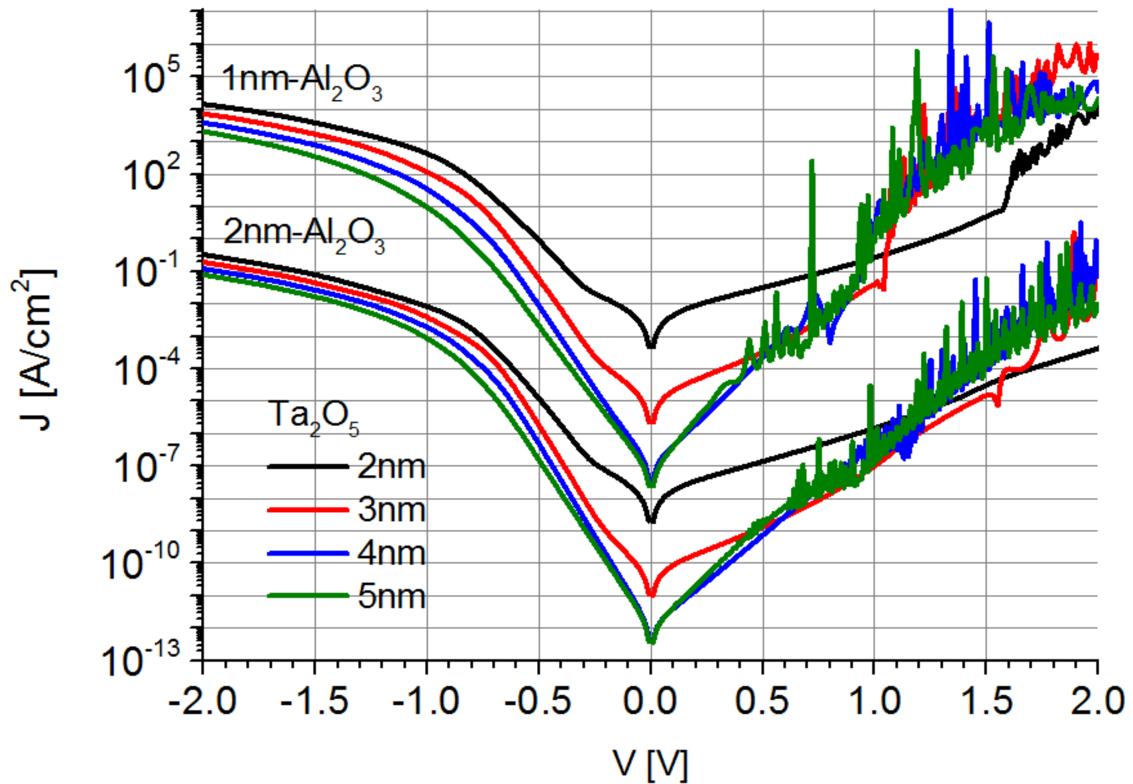

Figure 5.17 Simulated J-V curves for $Al/Al_2O_3/Ta_2O_5/Al$. The low barrier height was considered to be 0.45 eV (Work Function of Al: 4.2 eV, Electron affinities of Ta_2O_5 and Al_2O_3: 3.75 and 1.35 eV respectively).

The rectifying characteristics for the devices of batches 4 and 5 are shown in Figure 5.18. Larger asymmetry can be noticed for batch 5 at high voltage bias due to its double dielectric structure where tunnelling mechanisms are triggered. The small asymmetry observed for batch 4 of single dielectric structure can be attributed to the growth of Al native oxide. The native oxide was found to be 1.7 nm using the spectroscopic ellipsometry and expected to increase to 2-4 nm in several hours[126] and up to 5 nm after long time.[127] It is thought that even though the native oxide was minimised prior to oxide deposition, oxygen molecules from the deposited oxides diffuse to the Al. This is indicated by the native oxide observed at the interface with the top electrode in Figure 5.9 and Figure 5.10. In turn, the dynamic resistance (R_d) is not much changed as compared to the previous B1-4 of unetched native oxide and of similar oxide stack (1 nm Al_2O_3 and 4 nm Ta_2O_5), ~4×10^{10} Ω for B5-4 as compared to 2×10^{10} for B1-4. The deposition method (ALD for B1-4 and sputtering for B5-4) is another factor to consider. A considerable asymmetry coming from the larger current at opposite polarity can be noticed for the 4 nm-Ta_2O_5 for B5-4 and B5-5 which can be attributed to the possibility of resonant tunnelling at positive polarity exceeding FN tunnelling at negative polarity. The nonlinearity was sufficient to indicate that the devices show the typical

diode behaviour. The dynamic resistance (R_d) is still showing extremely high values making Al unsuitable for further use as a bottom contact for diodes designed for rectenna application.

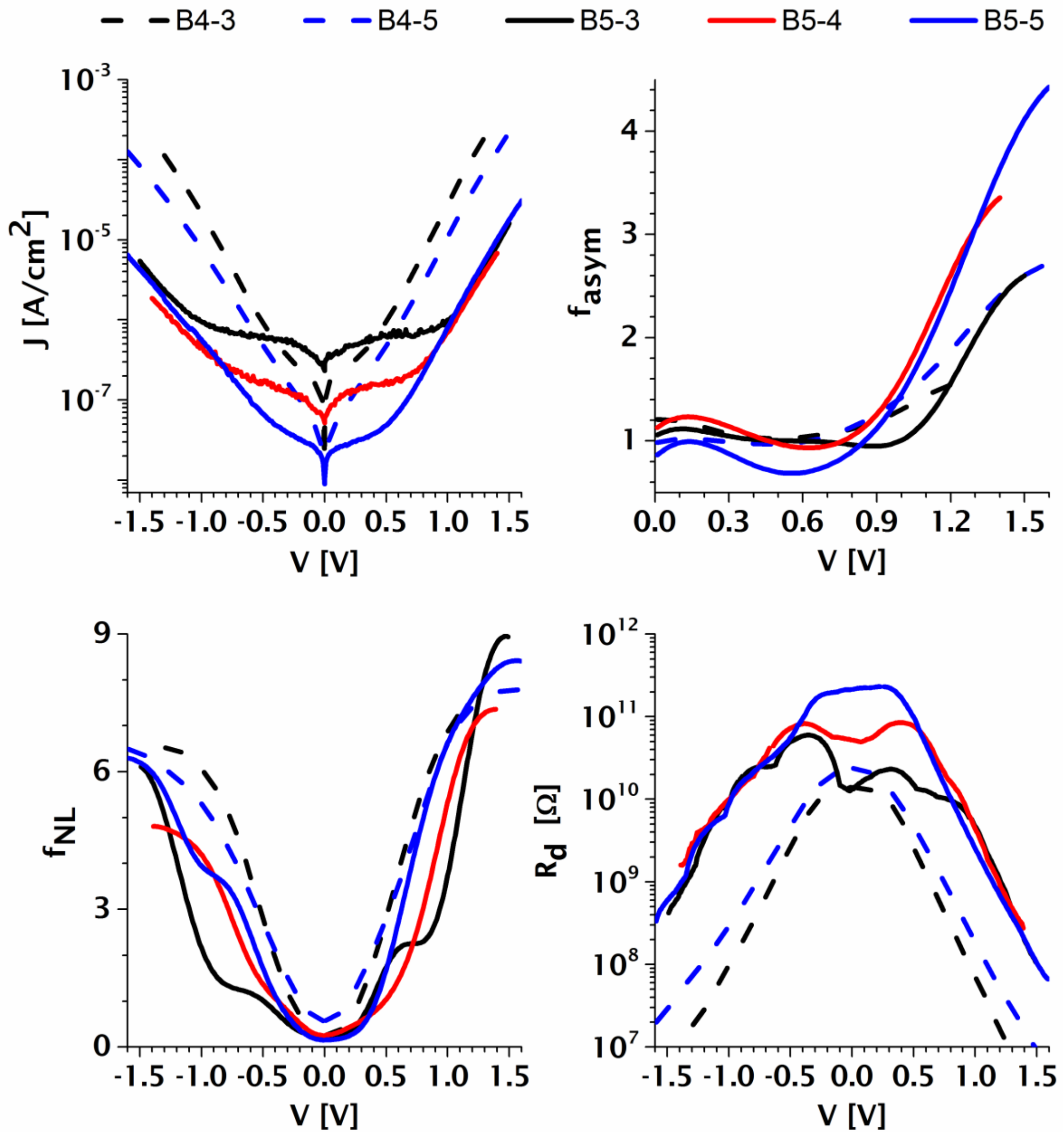

Figure 5.18 The J-V characteristics (a), the asymmetry plots (b), and the non-linearity plots (c) of selected B4 and B5 devices having 3 (black), 4 (blue), and 5 nm (red) low barrier oxide from batches 1 (red), 2 (blue), and 3 (green).

The occurrence of resonant tunnelling at positive polarity is indicated by the probability of more bound states in the wide and deep potential well between the dielectrics as in B5-4 band diagrams (Figure 5.19).[106,107] Resonant tunnelling is possible when the electrons are injected towards the Al/Al_2O_3 side at voltages larger than around 0.8 V. The simulated energy band diagrams show that Fowler-Nordheim (FN) tunnelling could occur when the electrons are injected from the

Al/Al_2O_3 side. This is the bottom contact in the fabricated devices where the J-V characteristics showed a good fit of the FN equation at high voltage regimes (depending on the device) with $R^2 > 0.995$ (Figure 5.20). Using FN plots for all samples, the low barrier height between Al and Ta_2O_5 was extracted at high electric field at negative and positive polarity and shown in Table 5.7. The values at positive polarity are close to the 0.45 eV expected in literature. The same values were found before and after annealing. It should be noted however, this is not necessarily FN tunnelling, and the temperature dependency needs to be investigated. Furthermore, FN plots were calculated considering the total thickness of the dielectric stack which is not straightforward for MIIM B5 devices.

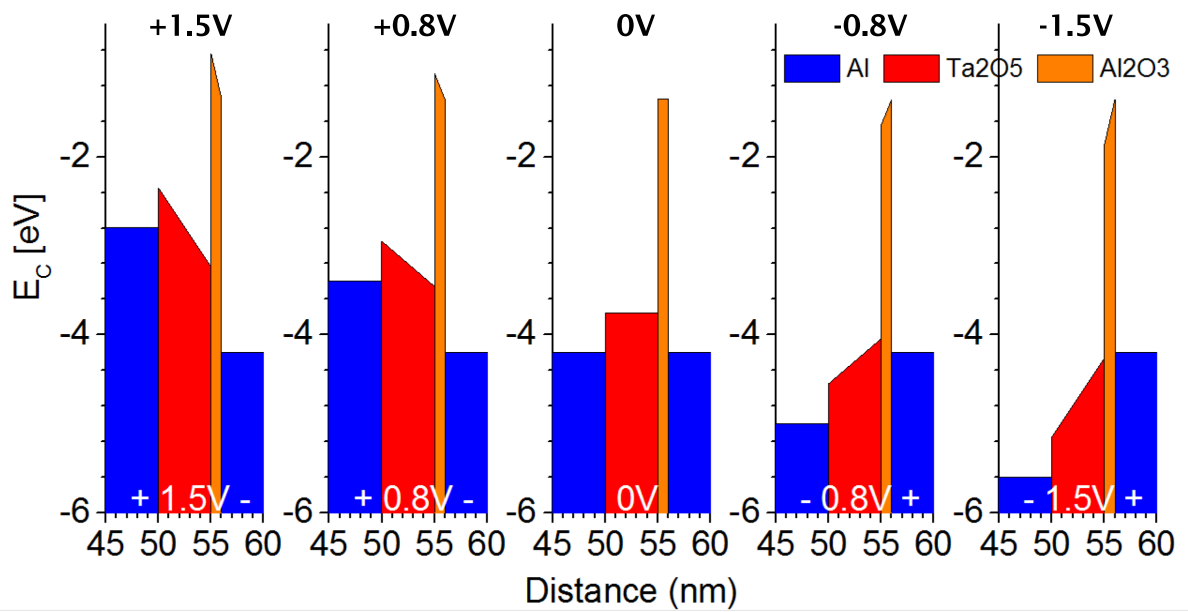

Figure 5.19 Simulated conduction band energy band diagrams of 50nm-Al/1nm-Al_2O_3/4nm-Ta_2O_5/50nm-Al structure. The voltage above each diagram represents the voltage applied at the same polarity as that of the J-V curves.

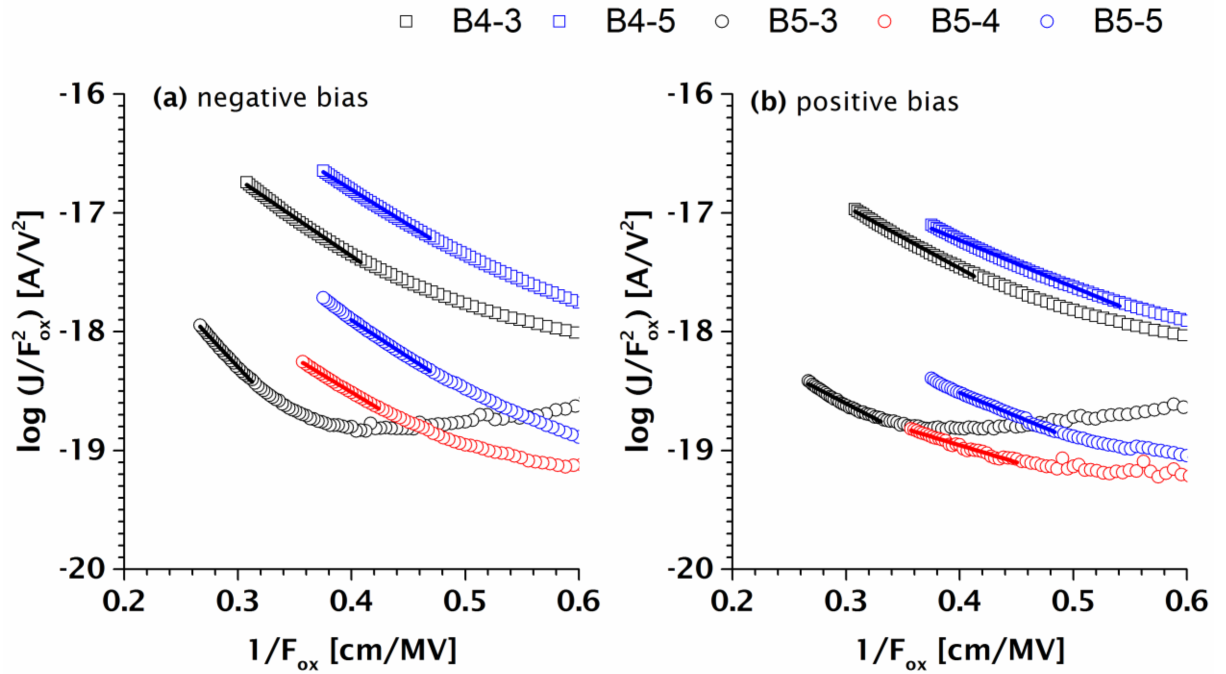

Figure 5.20 Fowler-Nordheim plot for the annealed devices of batch 5 showing a good fit at high electric field at both polarities.

Table 5.7 The slopes and intercepts of the linear fits of FN plots and the extracted barrier height $\varnothing_B$.

	Negative bias				Positive bias			
Device	Intercept	Slope	R^2	$\varnothing_B$ [eV]	Intercept	Slope	R^2	$\varnothing_B$ [eV]
B4-3	-15.4	-5.2	0.99604	0.39	-14.8	-6.5	0.99637	0.46
B4-5	-15.7	-3.9	0.99381	0.33	-14.4	-5.9	0.99881	0.43
B5-3	-17.1	-5.0	0.97906	0.38	-15.2	-10.2	0.99684	0.62
B5-4	-17.8	-2.9	0.97407	0.27	-16.2	-5.8	0.99827	0.42
B5-5	-16.9	-3.9	0.99746	0.33	-15.4	-6.2	0.99875	0.44

5.4.3 Optimal structure: choice of metal and dielectric thickness

Four different structures (6, 7, 8, and 9) were fabricated using different metals (Table 5.8) patterned using a shadow mask. The metals were varied keeping the same oxide structure in order to study the impact of work function dissimilarity on the device characteristics. 3 and 4 nm thick Ta_2O_5 are chosen with 1 nm of Al_2O_3 since the results in previous sections showed poor rectifying characteristics for thinner Ta_2O_5 and larger dynamic resistance for thicker Ta_2O_5. Thermal evaporation of the bottom and top metals was done downwards using Moorfield evaporator at a

deposition rate of ~10 Å/s and patterned by the use of a shadow mask. Only tungsten (W) was sputtered by the plasma group. All oxide layers were deposited using atomic layer deposition ALD1. All samples were annealed at 200 °C for 1 hour in closed Furnace with nitrogen flow to prevent oxidation. Annealing was previously shown to enhance the current stability at low voltages. The metals were chosen so as to vary the low and high barrier heights with the top and bottom metals respectively.

Table 5.8 The device structure of the fabricated devices of batches 6, 7, 8, and 9.

Batch	Device	Substrate CG [µm]	M1 50nm TE_E[1]	Native [Å]	I1 Al_2O_3 [nm]	I2 Ta_2O_5 [nm]	M2 50nm TE_E[1]
6	-	700	W[2]		1	3	Al
	64				1	4	
φ_B / EA [eV]			4.5		1.35	3.75	4.2
7	73		Ag		1	3	Al
	74				1	4	
φ_B / EA [eV]			4.7		1.35	3.75	4.2
8	83		Au		1	3	Al
	84				1	4	
φ_B / EA [eV]			4.8		1.35	3.75	4.2
9	93		Au		1	3	Cr
	94				1	4	
φ_B / EA [eV]			4.8		1.35	3.75	4.4

[1]Edwards Thermal Evaporation downwards. [2]Sputtered by plasma group, ~15 nm thick)

The energy band diagrams were simulated and shown in Figure 5.21 which shows the creation of a potential well when moving the bias towards positive polarity where the depth can be further tuned by the choice of metals. This potential well is necessary to have more bound states for resonant tunnelling to occur which is more likely to be dominant at positive polarity with (in order) batch 6, 9, 7, then 8. At negative polarity, however, no quantum well can be formed ruling out resonant tunnelling and suggesting FN tunnelling or step tunnelling with sufficient bending of the conduction band.

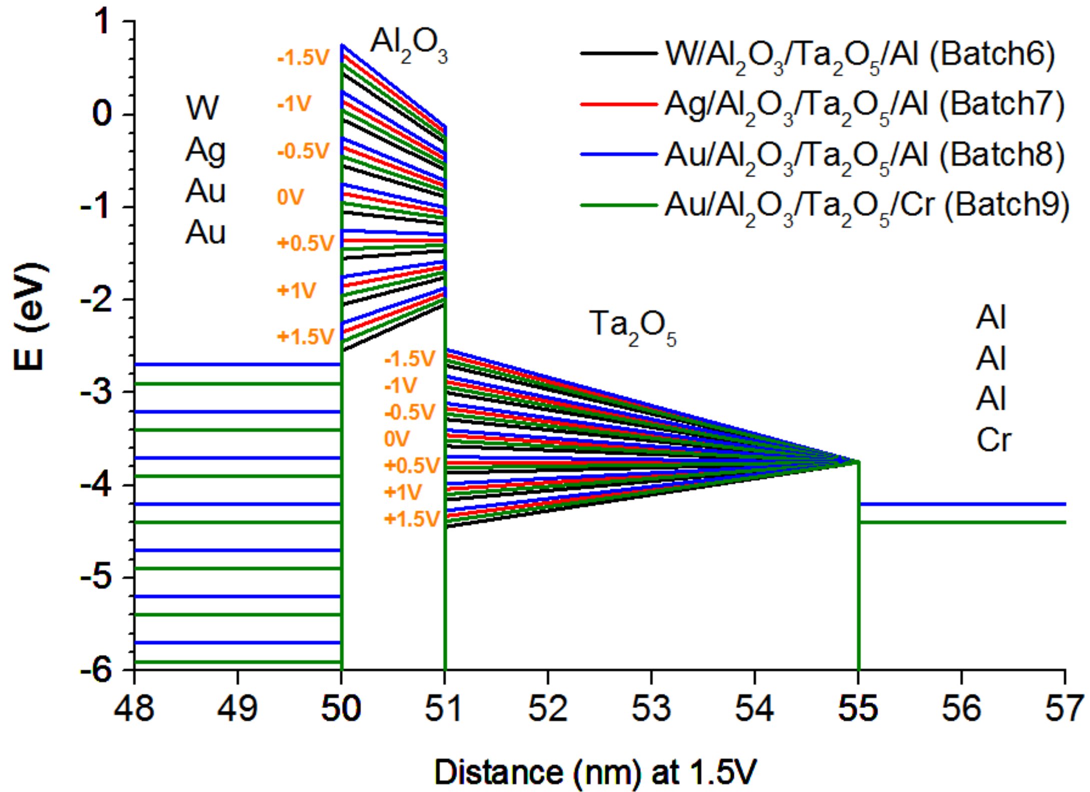

Figure 5.21 The energy band diagrams of the 4 batches at 0.5 V voltage increment from -1.5 to 1.5 V. The diagrams are shown in this way to further illustrate the structure effect on the potential well for enhancing resonant tunnelling.

The J-V measurements were done using the Agileant B1500 with a step of 10 mV at a sweep rate of 23 mV/s and the device rectifying characteristics shown in Figure 5.22. High asymmetry can be noticed at high voltage bias for batches 8 and 9 of Au bottom electrode due to its double dielectric structure. Large asymmetry at the positive polarity can be noticed for batches 8 and 9 especially with B9-4 of 4 nm thick Ta_2O_5 which can be attributed to the possible occurrence of resonant tunnelling. Batch 6 can be excluded from the analysis due to the very high dynamic resistance and poor rectification properties which is thought to be due to the insufficient thickness of the W metal. Batch 7 shows low dynamic resistance but almost no asymmetry and poor nonlinearity. Batch 8 and 9 show large asymmetry near zero bias and at high bias, while batch 9 has much better non-linearity near zero bias and at high bias. However, the dynamic resistance of both batches 8 and 9 is very large of 10^{10} and 3×10^{9} Ω respectively making for efficient coupling in THz rectennas. The barrier heights were extracted from the Fowler-Nordheim plots shown in Figure 5.23 indicating good fits only for batches 8 and 9 at high bias and found to be 0.73 and 0.72 eV respectively considering Ta_2O_5 as the dominant current limiting layer and using its thickness. Assuming electric field distribution in each dielectric according to Gauss law using

equations (4.19), the FN plots are replotted [Figure 5.23(c-f)] and the extracted barrier heights from each plot are shown in Table 5.9. Assuming an electron affinity of 3.75 eV, the extracted barrier heights across Al_2O_3 are consistent with the 4.8 eV literature value of work function of gold.

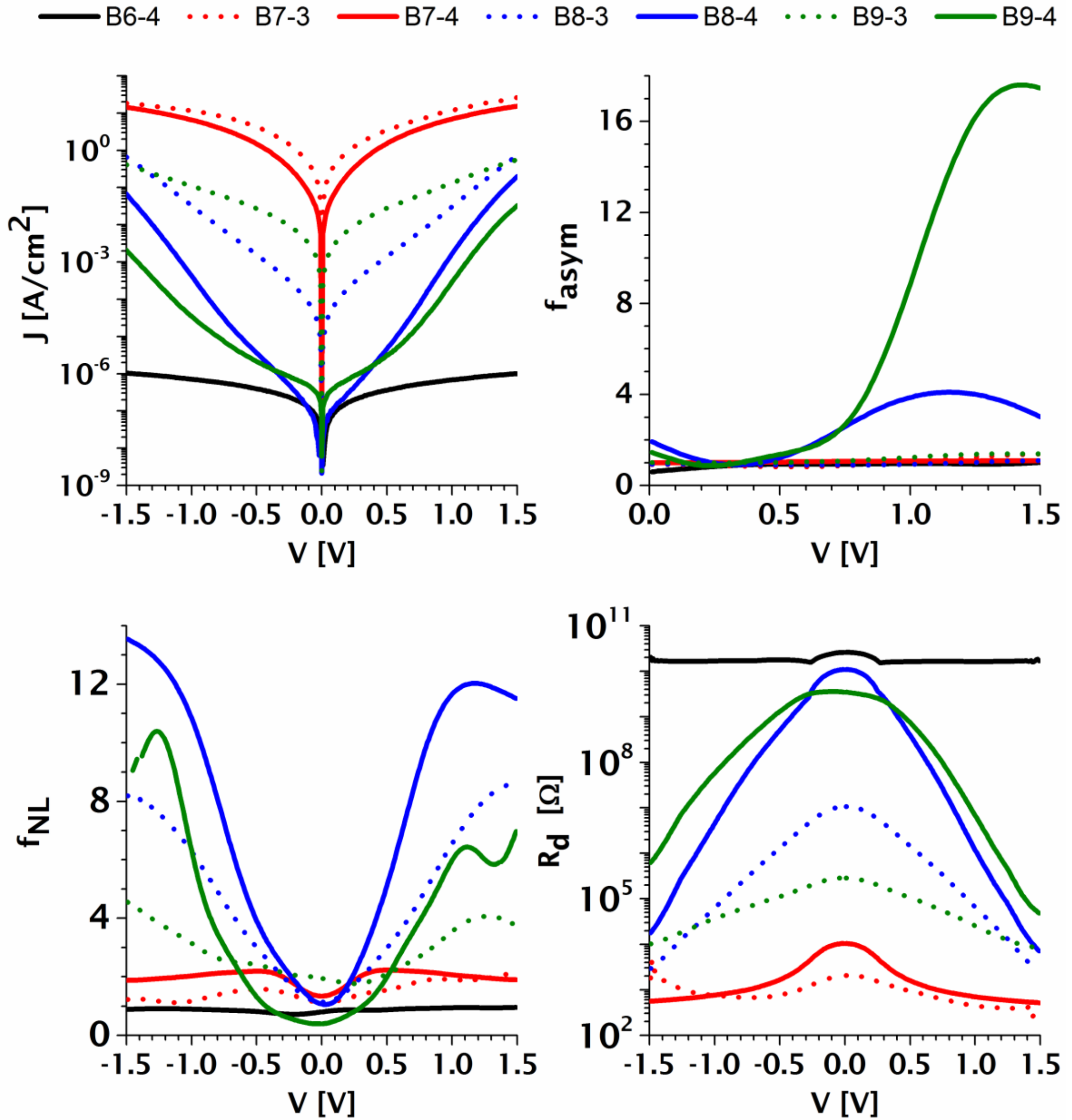

Figure 5.22 The rectifying characteristics versus the applied dc voltage for the 4 batches with Ta_2O_5 thickness of 3 (dashed) and 4 nm (solid).

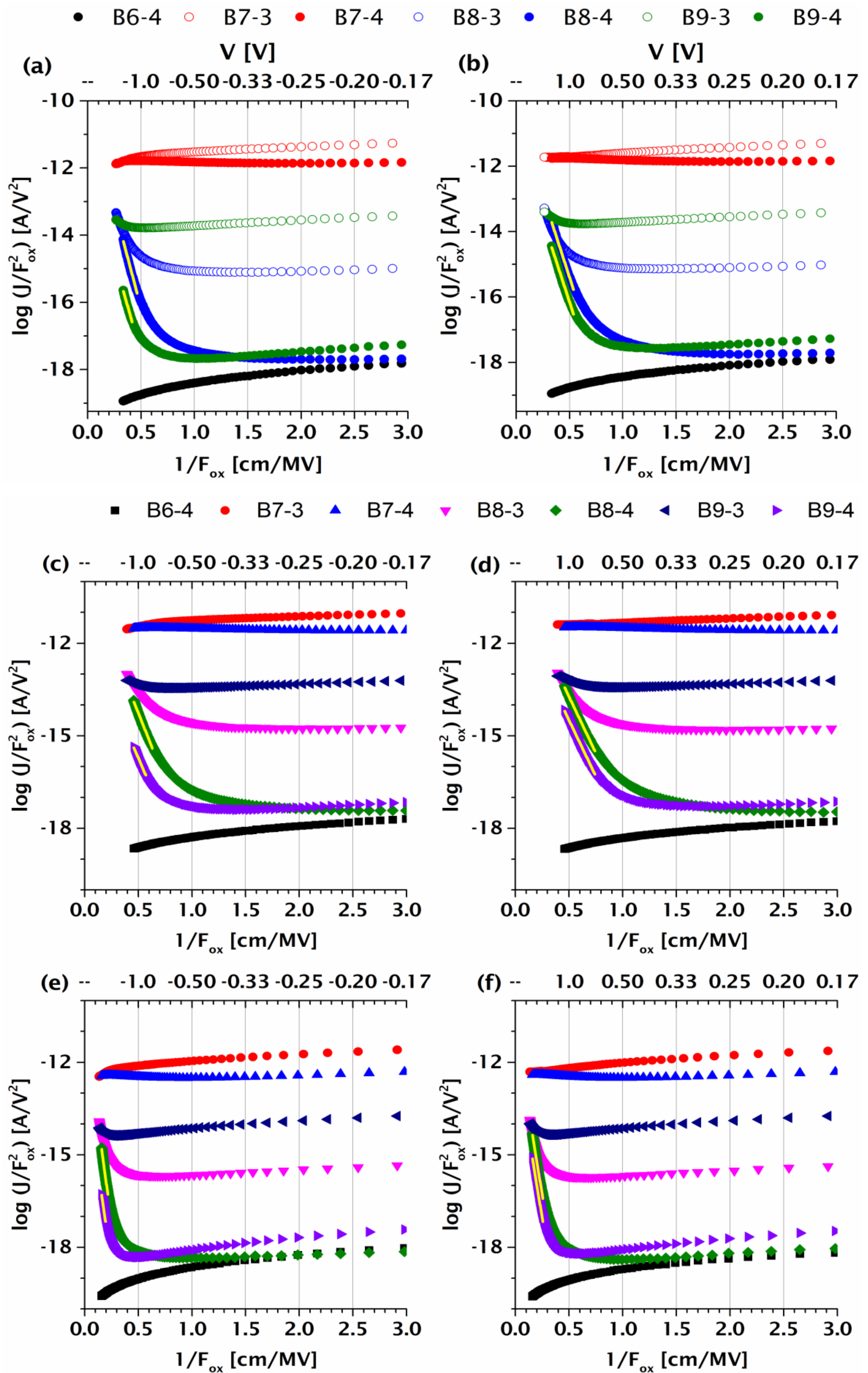
B6-4
B7-3
B7-4
B8-3
B8-4
B9-3
B9-4
(a)
V [V]
-- -1.0 -0.50 -0.33 -0.25 -0.20 -0.17
(b)
V [V]
-- 1.0 0.50 0.33 0.25 0.20 0.17
log (J/F²ox) [A/V²]
1/Fox [cm/MV]
(c)
(d)
(e)
(f)

Figure 5.23 Fowler-Nordheim plots for 7 devices of the four batches using Ta_2O_5 of dielectric stack total thickness (a and b), and individual layer voltage distribution across Ta_2O_5 (c and d) and A_2O_3 (e and f).

Table 5.9 Extracted barrier heights from each FN plot at negative and positive bias across each dielectric.

	B8-4				B9-4			
	Ta_2O_5		Al_2O_3		Ta_2O_5		Al_2O_3	
Bias	-	+	-	+	-	+	-	+
Intercept	-9.9	-10.1	-10.8	-11.0	-11.7	-10.9	-12.6	-11.8
Slope	-8.7	-7.3	-25.4	-21.1	-8.1	-7.3	-23.5	-21.0
R^2	0.99599	0.99619	0.99625	0.99619	0.99601	0.99582	0.99637	0.99582
$Ø_B$ [eV]	0.56	0.50	1.14	1.00	0.53	0.49	1.08	1.00

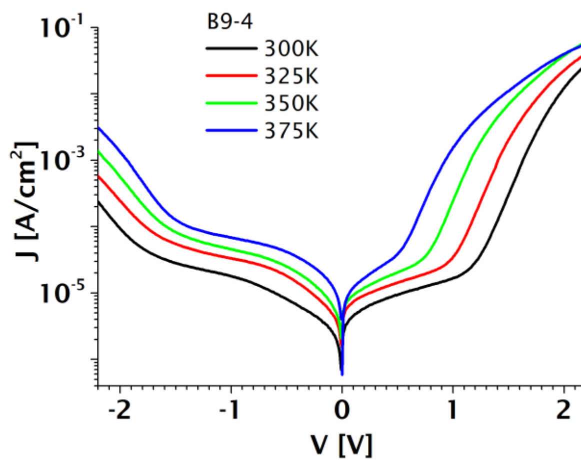

Figure 5.24 Temperature dependence of the J-V characteristics for the device B9-4 at 300, 325, 350, and 375 K.

The J-V characteristics of B9-4 showed considerable temperature dependence indicating the presence of thermal emission mechanisms.

5.4.4 Varying thicknesses of Cr-sandwiched dielectrics

Cr is less oxidising than Al, and it is desired to have electrodes of similar work function and lower barrier height for more bound states in the quantum well. As Al suffers from large dynamic resistance, Cr is used in this batch for the bottom and top electrodes. The oxides are grown using the ALD (ALD1), whereas Cr is deposited downwards using Edwards thermal evaporator at a rate of ~0.1 nm/s. The rate could not be increased, and the evaporation was done at 10 nm deposition intervals 5 times, leaving the equipment to cool down in between. Cr needs very high power to evaporate, unlike other metals like Al, Au, Ag.

Four different structures (6, 7, 8, and 9) were fabricated using different metals (Table 5.8) patterned using a shadow mask. The metals were varied keeping the same oxide structure in order to study the impact of work function dissimilarity on the device characteristics. 3 and 4 nm thick Ta_2O_5 are chosen with 1 nm of Al_2O_3 since the results in previous sections showed poor rectifying characteristics for thinner Ta_2O_5 and larger dynamic resistance for thicker Ta_2O_5. Thermal evaporation of the bottom and top metals was done downwards using Moorfield evaporator at a deposition rate of ~0.5 nm/s and patterned by the use of a shadow mask. All oxide layers were deposited using atomic layer deposition ALD1. All samples were annealed at 200 ºC for 1 hour in closed Furnace with nitrogen flow to prevent oxidation. Annealing was previously shown to enhance the current stability at low voltages. The metals were chosen so as to vary the low and high barrier heights with the top and bottom metals respectively.

Table 1. The structure of batch 10 devices.

Batch		Substrate CG [µm]	M1 50nm TE_E[1]	Native [Å]	I1 Al_2O_3 [nm]	I2 Ta_2O_5 [nm]	M2 50nm TE_E[1]
10a	Cr1-2	700	Cr	-	1	2	Cr
	Cr1-3			-	1	3	
	Cr1-4			-	1	4	
10b	Crh-2			-	0.5	2	
	Crh-3			-	0.5	3	
	Crh-4			-	0.5	4	
φ_B / EA [eV]			4.4	-	1.35	3.75	4.4

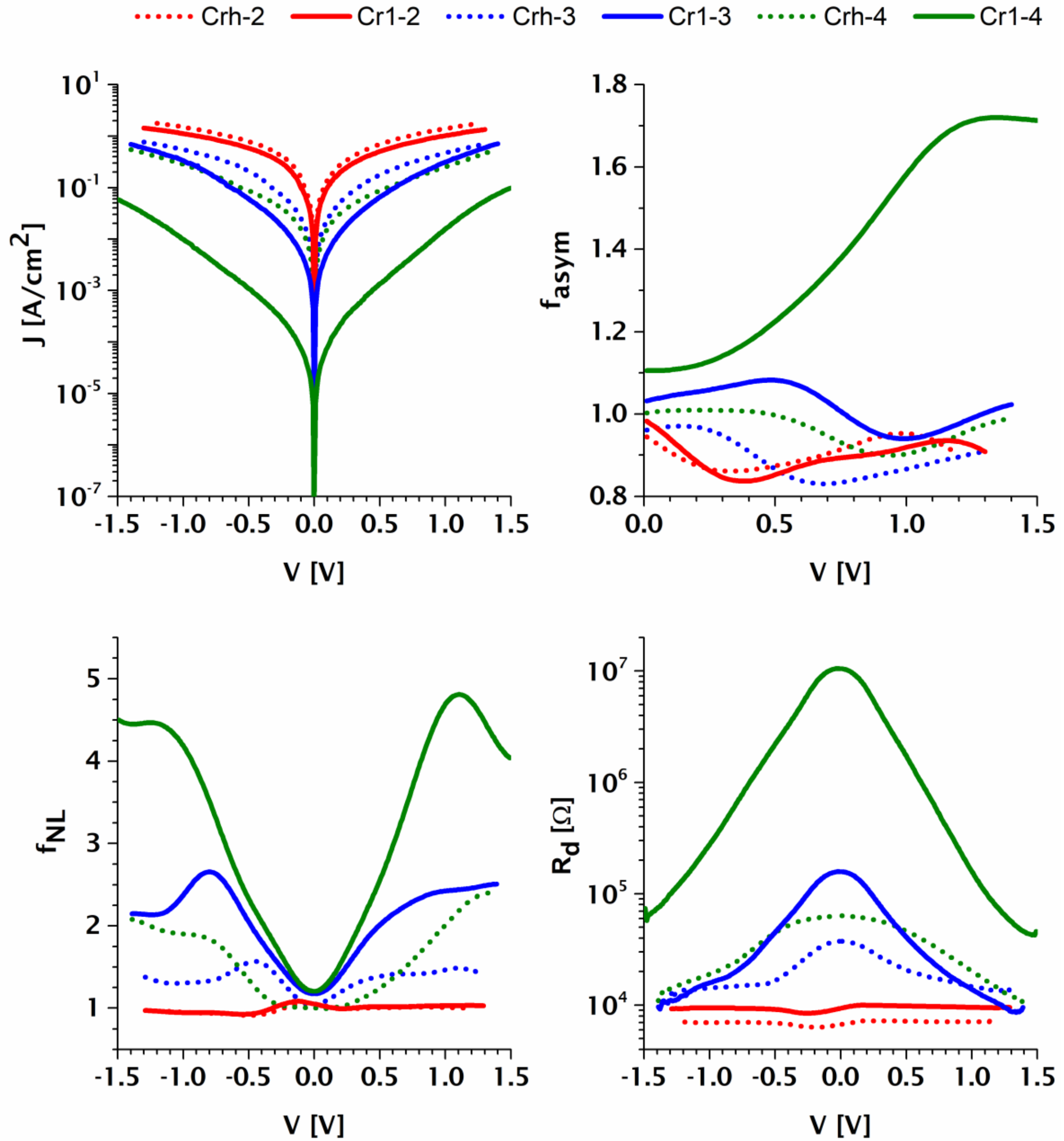

Figure 5.25 The dynamic resistance (a), the non-linearity (b), the asymmetry (c), and the current voltage curves for different dielectric thicknesses.

The rectifying characteristics (Figure 5.25) show some nonlinearity and very low asymmetry for all structures. Direct tunnelling can be assumed to be dominating at low voltages, which explains the low asymmetry in this region. At higher voltages Fowler Nordheim tunnelling could dominate at negative bias. The Al_2O_3 is thin enough for the electrons to tunnel through. However, in the opposite case, when electrons are injected from the Cr/Al_2O_3 side, electrons must tunnel across both dielectrics which make a larger barrier. This is further explained in the energy band diagrams (Figure 5.26). Lowering the Al_2O_3 thickness by half significantly reduces the tunnel distance and the dynamic resistance. However, the nonlinearity and asymmetry become lower than what is

expected from a diode. The J-V characteristics showed very small temperature dependence as shown in Figure 5.27 at 300, 325, 350, and 375K. These experimental observations indicate poor possibility of the occurrence of FN or resonant tunnelling.

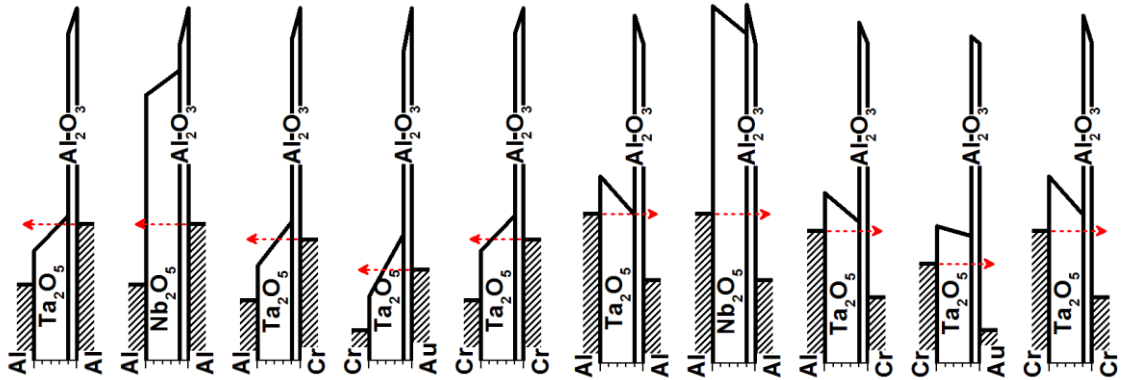

Figure 5.26 Energy band diagrams for different structures showing the conduction band and the electron injection.

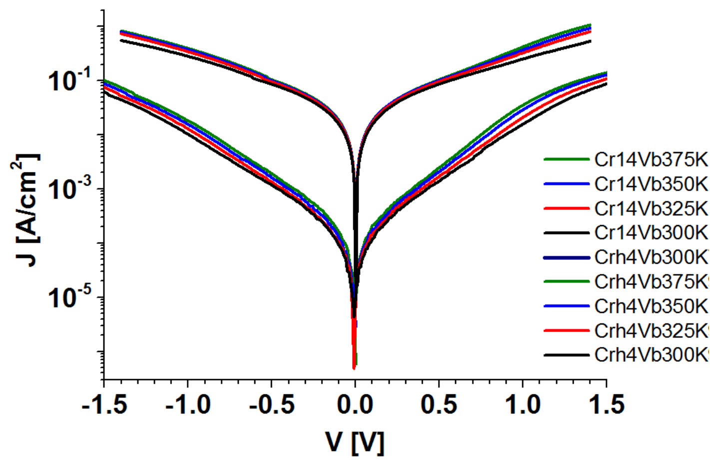

Figure 5.27 J-V characteristics at different temperatures 300, 325, 350, and 375K for the devices.

5.5 Summary

In summary, many attempts were done to fabricate MIIM devices focusing on getting any indication for resonant tunnelling and identifying the challenges in fabrication to tackle in the next chapter. Accurate thickness of ultra-thin layers and film homogeneity are examined using variable angle ellipsometry, whereas the surface roughness and topography are scanned using AFM, FF-OCT, and the confocal microscope. The repeatability of devices from the first batches B1 and B2 is questionable as devices of the same fabricated sample did not show a clear typical behaviour. Furthermore, while larger current should be for the devices of Ta_2O_5 thickness in this order: 1-, 2-, 3-, and 4-nm, this could be experimentally shown only for 2- and 4- nm. It is unknown what exactly the reason behind is but indeed due to the fabrication conditions. It could possibly be due to the shadowing effect on electrodes observed using FF-OCT and confocal microscope images, to the evaporation done at higher rate, or to the longer duration (>1 week) the samples were held for ALD deposition which could create thicker native oxide. An attempt to etch the native oxide was done, different metals and dielectrics were used, and the dielectric thicknesses were varied to notice any abrupt increase in current. J-V characteristics showed good stability against annealing and illumination with slight variation, which would be useful for rectenna operation during day and night and their durability for hot and cold weather. The results showed that maximum thicknesses of 1 and 4 nm for Al_2O_3 and Ta_2O_5 oxides should be used to avoid increasing the dynamic resistance and for an optimum use of resonant tunnelling as modelling suggests. The Cr/Al electrodes and the Al_2O_3/Ta_2O_5 dielectrics were selected mainly due to their more reliability in repeatability as noticed from the measurements. The Cr/Cr samples showed that halving Al_2O_3 thickness can significantly lower the dynamic resistance but also lower the rectifying performance, which needs to be checked for more devices. Temperature dependence of the J-V characteristics is observed for some devices, and this will be examined intensively for the devices in the next chapter to investigate the dominating conduction mechanism and any undesirable process.

6. Optimizing the structures for THz rectification

This section represents the second stage of experimental work, which includes state of the art tunnel devices with further understanding of the tunnelling and conduction mechanisms and the way these rectifiers can be tuned for better performance suited for THz energy harvesters.

6.1 Barrier tuning of atomic layer deposited Ta_2O_5 and Al_2O_3 in double dielectric diodes

The performance of ultrathin atomic layer deposited dielectrics of low (Al_2O_3) and high (Ta_2O_5) electron affinity (χ) is investigated in metal-insulator-(insulator)-metal [MI(I)M] diodes. The conduction mechanisms in 4 nm thick atomic layer deposited Al_2O_3 and Ta_2O_5 single barrier MIM diodes are first studied to show the dominance of tunnelling and thermally activated Poole–Frenkel emission respectively in these oxides. Varying the layer thickness of Ta_2O_5 with a 1 nm thick layer of Al_2O_3 shows evidence for resonant tunnelling in double barrier MIIM structures and is correlated with the simulated bound states in the quantum well formed between the two dielectrics. These findings demonstrate experimental work on barrier tuning of resonant tunnelling diodes with sufficient rectifying capability at a turn-on voltage as low as 0.32 V enabling their potential use in terahertz applications.

The device structure comprises of one or two dielectric layers of a few nanometres thickness sandwiched between two metal electrodes. The aim is to develop diodes with sufficiently nonlinear and asymmetric current density–voltage (J-V) characteristics, which can be achieved by the choice of the dielectrics and their thicknesses. Asymmetry is defined as the ratio of the current (I) at positive bias to that at negative bias at certain voltage $f_{asym} = I_+/I_-$. The dynamic resistance is defined as $R_d = dV/dI$. Nonlinearity is defined as the ratio of the static to dynamic resistance $f_{NL} = (V/I)/R_d$[128] and needs to be greater than about three.[2]

The conduction mechanisms dominating in 4 nm thick atomic layer deposited (ALD) Al_2O_3 and Ta_2O_5 are studied in metal-insulator-metal (MIM) structures. With 1 nm of the former and 1–4 nm thickness tuning of the latter, the effect of RT on metal-insulator-insulator-metal (MIIM) diode performance is investigated experimentally by studying the effect of varying the thickness of one layer in an MIIM structure.

6.1.1 Fabrication

Devices with lateral area of 100 × 100 μm^2 of structures presented in Table 6.1. were fabricated on cleaned Corning glass substrates. The top and bottom metal layers of 50 nm thickness were deposited by thermal evaporation through a shadow mask. The Al_2O_3 and Ta_2O_5 oxides were successively deposited over the bottom electrodes by ALD (ALD1) at a temperature of 200 °C

using deionized water as the oxidant for Ta_2O_5 and Al_2O_3 at 0.04 s/10 s pulse/purge time, tantalum ethoxide precursor for Ta_2O_5 at 0.3 s/2 s pulse/purge time, and trimethylaluminum (TMA) precursor for Al_2O_3 at 0.02s/5s pulse/purge time. The thicknesses of the dielectric layers were measured by variable angle spectroscopic ellipsometry using a *XLS-100 J.A. Woollam* instrument. The J-V measurements were done in the dark using an *Agilent B1500 Semiconductor Device Analyzer* on a temperature controlled heating stage. The voltage was swept from 0 V with 10 mV step size in negative and positive bias.

Table 6.1 Device structure and layer thickness.

Structure	Bottom contact	**Thickness (nm)**		Top contact
		Al_2O_3	Ta_2O_5	
S1	Au	4	—	Al
S2	Al	—	4	Al
S3	Cr	1	1	Al
S4	Cr	1	2	Al
S5	Cr	1	3	Al
S6	Cr	1	4	Al

6.1.2 Material Selection

The possible tunnelling mechanisms in each structure are illustrated schematically using the energy band diagrams shown in Figure 6.1 considering literature values for the work functions [4.2,[129] 4.4,[129] and 5.1 (Ref. [98]) eV for Al, Cr, and Au, respectively] and electron affinity, $q\chi$,[105] of 1.35 and 3.75 eV for Al_2O_3 and Ta_2O_5, respectively. These values and a dielectric constant of 10 (Ref. [130]) and 25,[131] for Al_2O_3 and Ta_2O_5, respectively, have been used for all theoretical calculations. When electrons are injected from the bottom electrode (right to left on the diagrams) at negative bias, the current in single barrier structures could be driven by direct or Fowler–Nordheim (FN)[132] tunnelling; the latter is depicted for the case of S2 in Figure 6.1. For double dielectric structures, this could turn into one-barrier step tunnelling[133] at sufficient negative bias as for S6 and S3. For opposite injection of electrons at positive bias, RT may occur in double barrier MIIM structures when the quantum well formed between the dielectrics becomes wide and deep enough to allow the formation of bound states[106] enabling resonant tunnelling. It is shown in Figure 6.1(b) that these could be achieved for S6 but not S3. Al_2O_3 has a large conduction band offset with Ta_2O_5, necessary to create the quantum well, which gets wider and deeper when it is thin enough (1 nm) and when Ta_2O_5 is thick enough (4 nm).

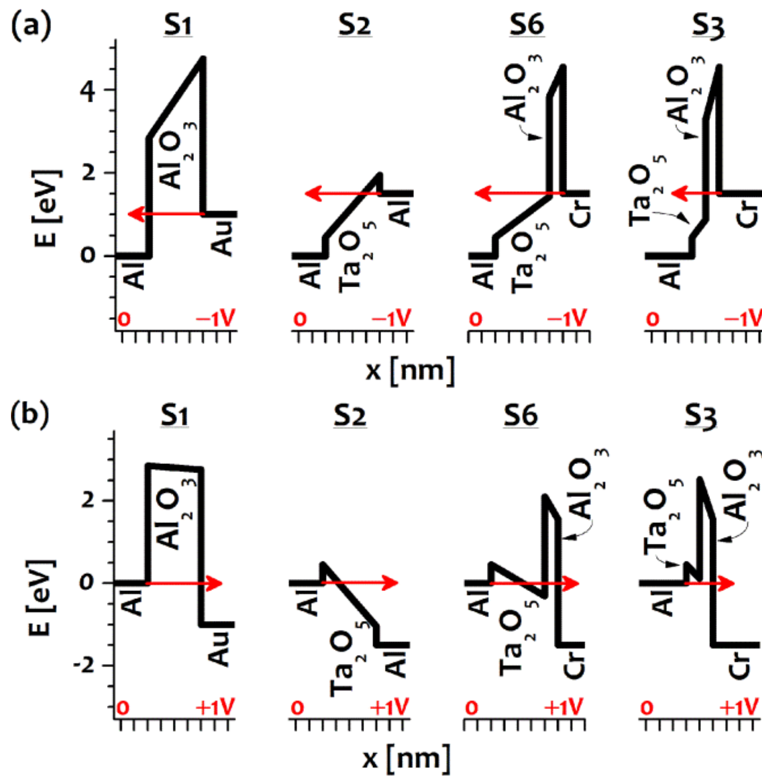

Figure 6.1 Energy band diagrams (conduction band) of four structures at −1 (a) and +1 V (b). Direction of electron injection is indicated by red arrows. Top electrode is always referred to zero. One tick on the x-axis corresponds to 1 nm.

Despite the advantage of Al work function to create a deep quantum well for RT at lower voltage, the AFM images of Figure 6.2 reveal a large root mean squared (RMS) surface roughness of 2.8 nm, which is not smooth enough for deposition of such thin dielectric layers. The metals Cr and Au serve better as bottom electrodes due to their ultra-smooth surface roughness of 0.42 and 0.44 nm (RMS) and their lower z-excursion peaks of 4.7 and 4.6 nm, respectively, which is necessary to avoid field intensification. These metals also have high melting point as compared to the bottom Al where the ALD growth of the oxides at 200 ºC on top of it might result in the formation of interfacial layer. In addition, a few nanometre thick native oxide layer growing on top of Al when exposed to air[134] is undesired. Despite its low surface roughness, using Au with its large work function as a bottom electrode in MIIM devices increases the metal-oxide energy barrier lowering the Fermi level of the emitter electrode so that no bound states in the quantum well could be formed in the 1.5 V voltage range. The metal Cr has a work function close to that of Al and has a native oxide of very small bandgap which does not create a large conduction band offset with Ta_2O_5 as Al. It is thus chosen as the bottom electrode for resonant tunnelling structures having the advantage of its ultra-smooth surface and the possibility of forming bound states in the quantum well within the applied voltage range when used in S6 structure [Figure 6.1(b)]. Using a few

nanometer thick Ta_2O_5 of large electron affinity (3.75 eV) and of large band offset with a 1 nm thick Al_2O_3 (2.4 eV) allows the quantum well to be tuned below the Fermi level of the emitting electrode with the applied bias.

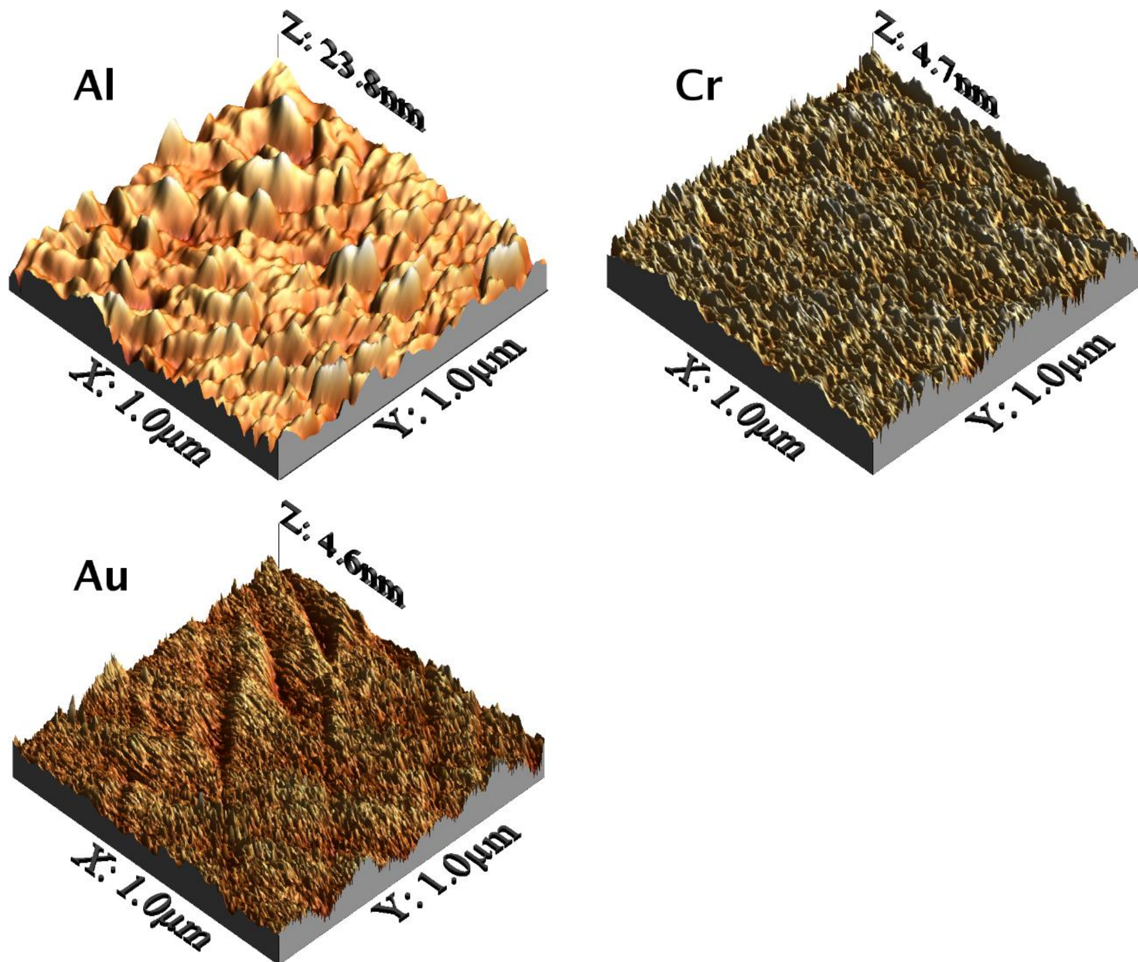

Figure 6.2 AFM images scanned at 1×1 μm^2 regions of the as-deposited bottom layers Cr, Au, and Al revealing an RMS average surface roughness of 0.42, 0.44, and 2.8 nm.

6.1.3 Results and discussion

6.1.3.1 Conduction mechanisms in the individual dielectrics

The possible presence of thermally activated mechanisms is first studied individually in the single barrier structures of Al_2O_3 and Ta_2O_5. The J-V characteristics show temperature insensitivity for S1 [Figure 6.3(a)] and strong temperature dependence for sample S2 [Figure 6.3(b)]. This indicates that the 4 nm thick Al_2O_3 and Ta_2O_5 are dominated by tunnelling and a thermal emission process, respectively, which is consistent with another study[135] done on 10 nm thick Al_2O_3 and

Ta_2O_5. The presence of thermally activated mechanisms Schottky emission (SE) and Poole–Frenkel emission (PFE) in S2 can be examined using the logarithmic plots of I/T^2 and I/V versus $V^{1/2}$ (Figure 6.4) which showed good linear fits with respect to their corresponding governing equations[136] $I_{SE} \propto T^2 exp(AV^{1/2}/kT - B)$ and $I_{PFE} \propto Vexp(AV^{1/2}/kT - B)$, respectively where A and B are constants, with a regression coefficient $R^2 > 0.995$ over the same voltage range at both polarities.

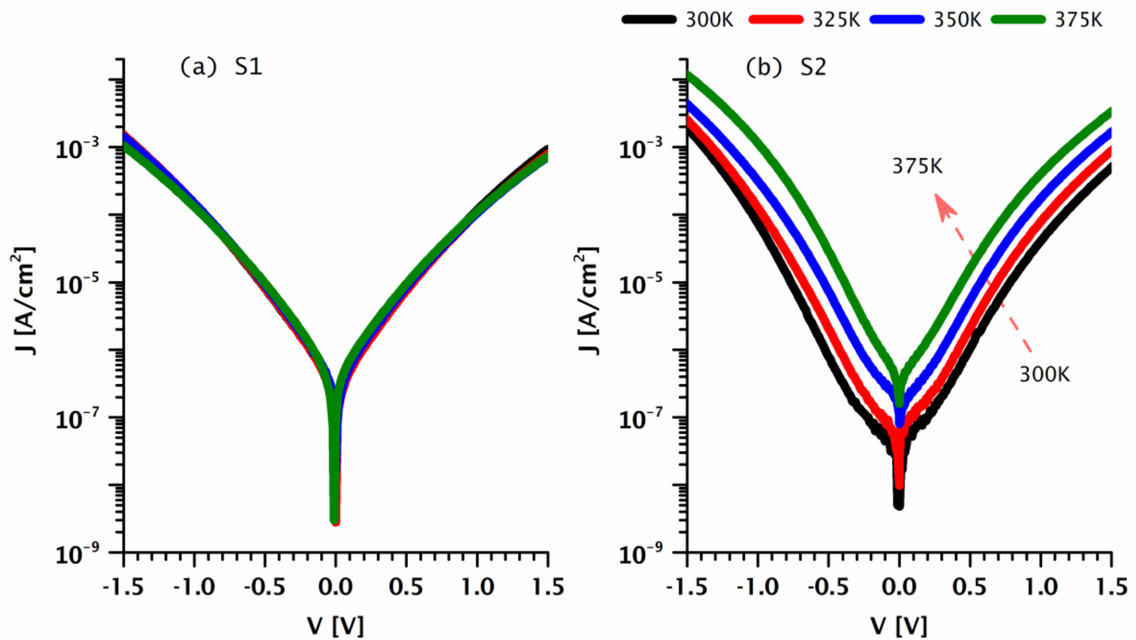

Figure 6.3 J-V characteristics of the MIM devices S1 (Al_2O_3) and S2 (Ta_2O_5), measured at 300, 325, 350, and 375 K.

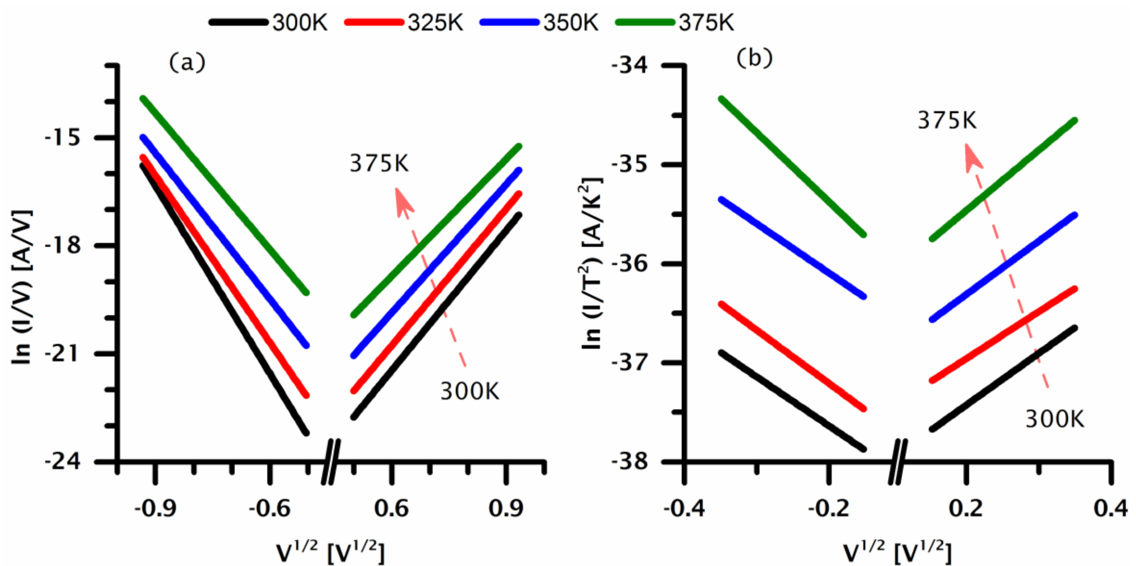

Figure 6.4 PFE (a) and SE (b) plots of the MIM device S2 (Ta_2O_5) at 300, 325, 350, and 375 K.

The average optical relative permittivity $\varepsilon_{r,opt}$, assumed to be equal to the square of the optical index of refraction n, of 50 nm thick ALD deposited Ta_2O_5 and Al_2O_3 on silicon substrates was found to be 3.14 and 5.23, respectively, as extracted from the spectroscopic ellipsometry measurements at room temperature in the 400-1200 nm wavelength range. The equivalent dynamic relative permittivity ε_r of the 4 nm thick Ta_2O_5 extracted from the slopes of the SE plots [Figure 6.4(b)] at 300 K in the 0.02-0.12 V voltage range were far larger than the optical values, and thus SE will be ruled out for this structure (S2). Only ε_r extracted from PFE plots for S2 was self-consistent with $\varepsilon_{r,opt}$ using a trap compensation factor[137] (CF) multiplied by kT in PFE equation ranging[138,139] from 1 to 2. This indicates the dominance of PFE in the 4 nm thick Ta_2O_5 ranging widely from 0.25 to 1.5 V at both polarities (Table 6.2). This dominance of thermal emission is expected for the high-k Ta_2O_5; it limits the diode speed implying the incompatibility of Ta_2O_5-based MIM devices to rectify at THz frequencies. Despite this, using the narrow-band Ta_2O_5 in MIIM structures has an advantage of creating a small barrier height for rectification to occur at lower V_{ON} in addition to the possibility of realising resonant tunnelling.

Despite the work function dissimilarity of 0.9 eV (Ref. [129]) in S1, no noticeable asymmetry could be observed due to the large barrier across the low-χ Al_2O_3 preventing the occurrence of FN tunnelling within the applied voltage range (Figure 6.1).

Table 6.2 Extracted CF when $\varepsilon_{r,PFE}$ is matched to $\varepsilon_{r,opt}$ (CF_m), the voltage range in which PFE fitting is done (V_{PFE}), and the trap depth at zero bias φ_{t0} for the 4 nm thick Ta_2O_5 at negative (−) and positive (+) polarities at 300 K.

Bias	**CF_m**	**V_{PFE} (V)**	**$q\varphi_{t0}$ (eV)**
−	1.35	0.25−1.5	0.9
+	1.81		0.53

The linear fit of the Arrhenius plots (Figure 6.5) is used to extract the activation energy (E_a) (Figure 6.6) associated with the dominant oxide trap in S2, such that $I_{PFE} \propto Vexp(-E_a/kT)$, where k is the Boltzmann constant and T is the temperature in K. The average trap depth at zero bias φ_{t0} extracted at positive bias for the 4 nm thick ALD Ta_2O_5 (Table 6.2) was equal to the 0.53 eV extracted for 10 nm thick ALD Ta_2O_5 in other studies.[135,111] PFE is a bulk limited process and should ideally be independent of voltage polarity. The polarity dependence apparent in Figure 6.3(b), therefore, could be related to the difference in interfacial roughness of the top and bottom

electrodes, which intensifies the electric field leading to lowering of the effective barrier height and hence increasing the current.[140]

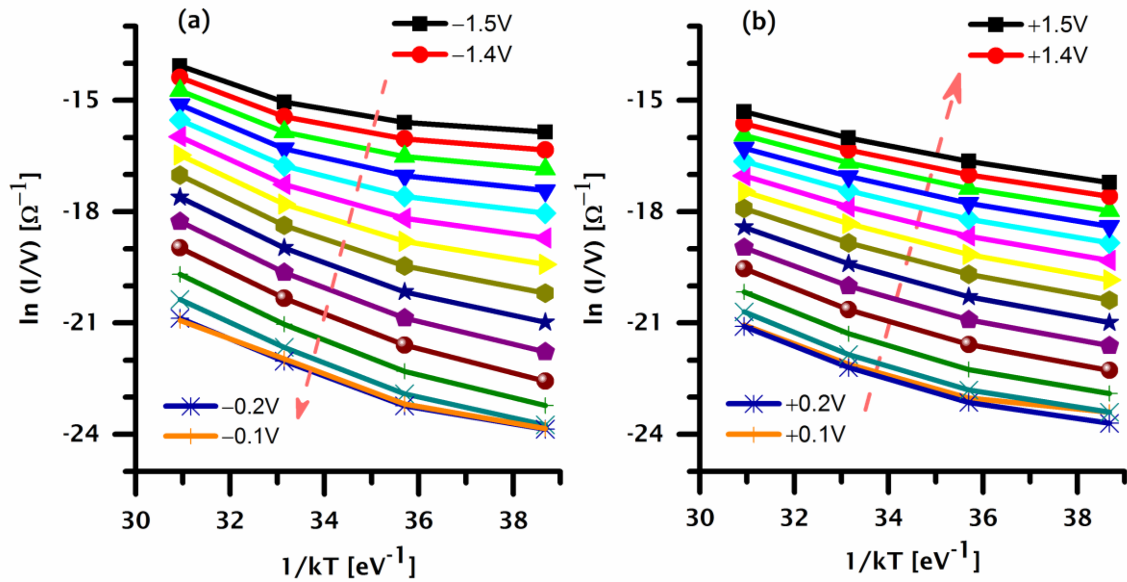

Figure 6.5 Arrhenius plots of the MIM device S2 from 0 to +1.5 (a) and to −1.5 V (b) at a 0.1 V step voltage.

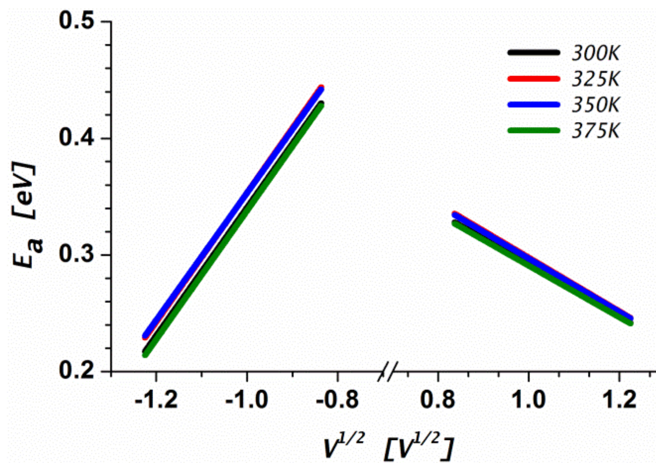

Figure 6.6 Activation energy (E_a) versus square root of voltage plots for the MIM device S2 at 300, 325, 350, and 375 K.

6.1.3.2 Barrier tuning of double dielectric diodes

The effect of varying the individual layer thickness of Ta_2O_5 with a 1 nm thick Al_2O_3 dielectric can be observed in the rectifying characteristics shown in Figure 6.7. It should be noted that the quantum well between the two dielectric layers becomes wider and deeper by either increasing the applied voltage or the thickness of the high-χ oxide (S6) giving rise to bound states in the

quantum well.[107] The abrupt increase in the J-V plots [Figure 6.7(a)] at positive bias of 0.32 V for the 4 nm thick Ta_2O_5 oxide could be attributed to RT. This possibility is supported by the band diagrams of Figure 6.1(b) which indicate the probable occurrence of RT at positive bias, when the energy of a bound state in the well is matched to the states neighbouring the Fermi level of the top Al charge injecting electrode.[141] This provides further evidence that the noticeable improvement in asymmetry [Figure 6.7(*b)*] and nonlinearity [Figure 6.7(c)] for S6 is associated with RT.

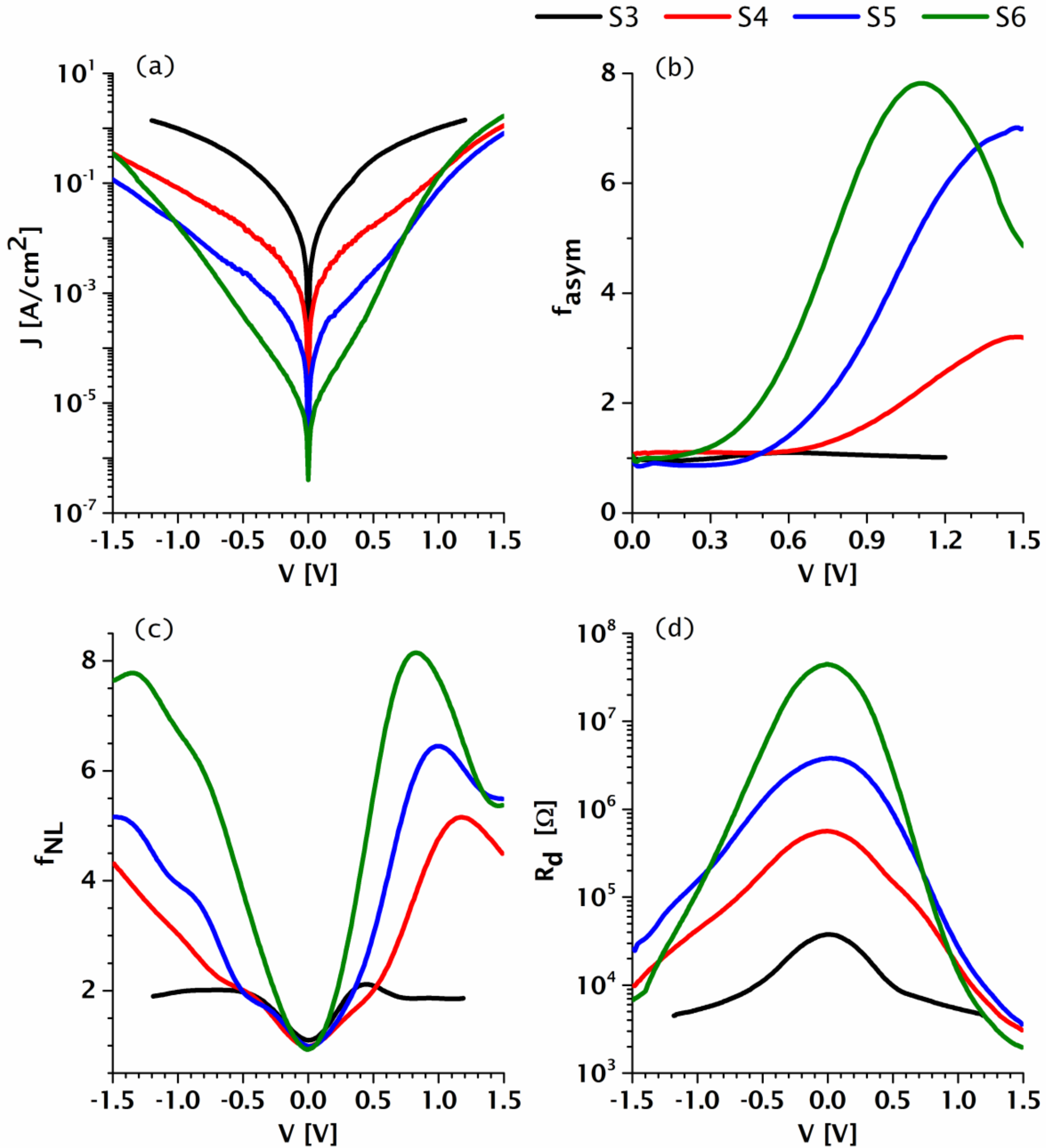

Figure 6.7 Rectifying characteristics of the MIIM devices (S3, S4, S5, and S6) showing the: (a) J-V characteristics, (b) asymmetry, (c) nonlinearity, and (d) dynamic resistance.

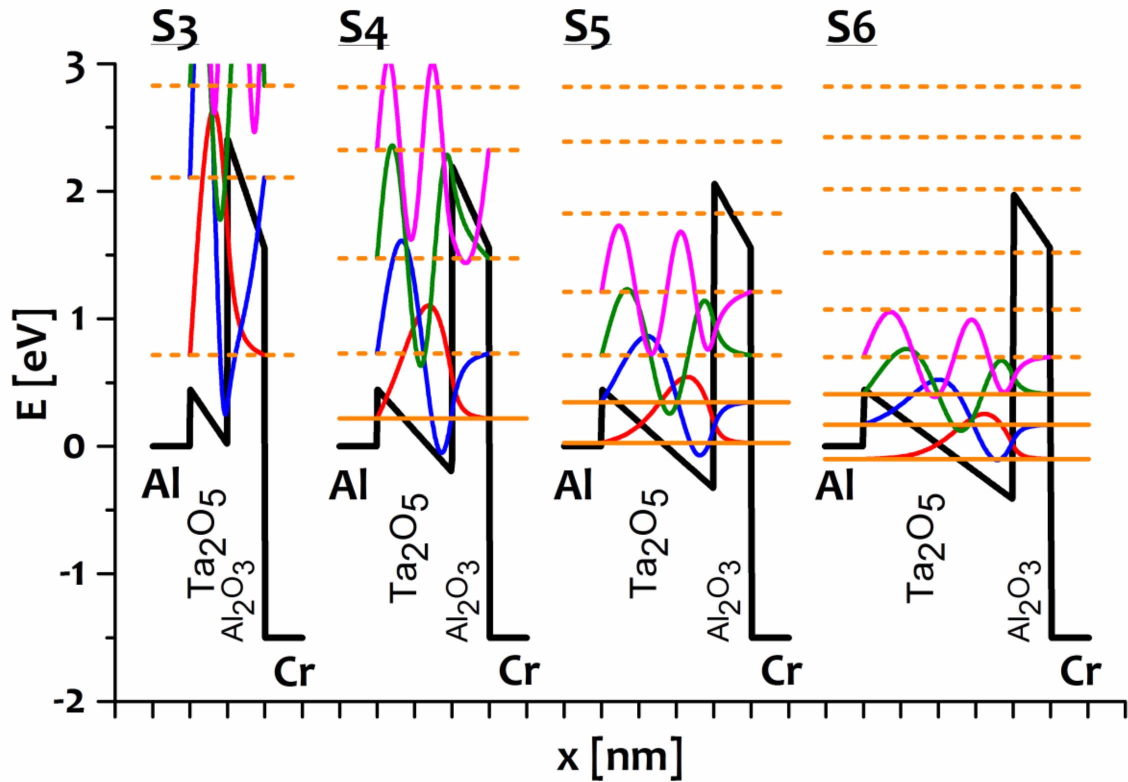

Figure 6.8 Simulated conduction band diagrams at +1.5 V showing 0, 1, 2, and 3 bound states (solid lines) for S3, S4, S5, and S6, respectively, using a work function difference of 0.2 eV (Ref. [129]). One tick on the x-axis corresponds to 1 nm.

Sample S3 shows inadequate nonlinearity and asymmetry because the width of the quantum well in the device with 1 nm thick Ta_2O_5 is insufficient to accommodate a bound state in the range of the applied voltage [Figure 6.1(b)]. Figure 6.8 shows the simulated conduction band diagrams, the wave function inside the dielectrics (sinusoidal waves), and the bound states for S3–S6 structures using an in-house model. The first bound state is predicted to be formed at an applied voltage of 0.98, 0.57, and 0.44 V for S4, S5, and S6, respectively. Briefly, we use the tunnelling current equations and Tsu-Esaki method[90] to calculate the bound states in the quantum well within the conduction band of Ta_2O_5. We calculate the transmission probability by the transfer matrix method (TMM), that is, solving the time independent Schrödinger equation for each slice of the Tsu-Esaki multibarrier oxide. The transmission probability is then integrated in the energy domain, applying the Fermi-Dirac statistics for occupancy of electrons in the metal contacts, to calculate the current density.

In order to observe resonant tunnelling, the quantum well (Figure 6.8) needs to be sufficiently wide and deep to accommodate at least one bound state. The model does not take into consideration the charge trapping predicted from the domination of PFE in the high-κ Ta_2O_5 of

defect nature. Other possibilities to explain the abrupt rise in the J-V characteristics are stress-induced leakage current[142] and soft breakdown.[143] However, as no such rise in current could be observed for the MIM structures (S1–S2), these mechanisms are unlikely to explain that observed for the MIIM structures (S3–S6) fabricated at similar conditions.

A voltage V_{ON} is defined as the point at which the current abruptly increases or at the knee in the asymmetry plots. For S4, S5, and S6, V_{ON} is found to be 0.71, 0.5, and 0.32 V at positive bias in reasonable agreement with the theoretical prediction of the formation of a bound state. The decrease in V_{ON} with Ta_2O_5 thickness is consistent with the associated increase in the depth of the quantum well at positive bias as illustrated in Figure 6.8. The larger current observed at positive bias for S4, S5, and S6 indicates that the overall asymmetry is regulated by the dominance of RT at positive bias over other conduction mechanisms. The effect of resonant tunnelling is enhanced in structure S6 with a quantum well accommodating a number of bound states, at a certain voltage, larger than that in other MIIM structures (Figure 6.8). For this device, the increase in nonlinearity [Figure 6.7(c)] and the drop in dynamic resistance [Figure 6.7(d)] were steeper at positive bias, where RT occurs [Figure 6.1(b)], than at negative bias, where step tunnelling occurs [Figure 6.1(a)], indicating the advantage of the prior mechanism in rectification. As the Ta_2O_5 thickness is varied, a trade-off is apparent between the asymmetry, nonlinearity, and low V_{ON} and the dynamic resistance [Figure 6.7(d)], which needs to be reduced for impedance matching in the THz rectenna. Accordingly, the choice of an optimum RT structure should take into consideration this trade-off depending on the application.

Atomic layer deposited Ta_2O_5 and Al_2O_3 oxides were used in single and double barrier structures to identify and optimize their rectifying performance. The dominant conduction mechanisms in 4 nm thick layers of Al_2O_3 and Ta_2O_5 were shown to be tunnelling in the former and PFE in the latter. There was self-consistent evidence for resonant tunnelling in double dielectric diodes arising from the noticeable enhancement in nonlinearity and asymmetry in agreement with the theoretical modelling. The effect of RT was tuned according to the individual thickness of the Ta_2O_5 layer resulting in a noticeable improvement in rectification as the quantum well becomes wider such as to accommodate more bound states. Enhanced rectifying characteristics were observed at a turn-on voltage as low as 0.32 V. It is feasible that exploitation of work function engineering can further reduce the turn-on voltage to allow the zero-bias rectification[48] necessary for energy harvesting in rectenna structures.

6.2 Improved rectification in MIIM tunnelling diodes via dielectric defects

Further understanding is needed to understand the dielectric properties where defects can play a major role especially in high-κ oxides such as Ta_2O_5. Tunnelling and thermionic emission

mechanisms are experimentally investigated using Ta_2O_5 and Al_2O_3 dielectrics with inert metal Au and the reactive metal Al electrodes. In this section, the domination of tunnelling, thermionic emission, and trap mediated charge transport are discussed according to the different single and double dielectric structures. The properties of Ta_2O_5 are tuned using sputtering and atomic layer deposition with different pulse and purge times. The rectifying characteristics of diodes containing Ta_2O_5 are analysed in terms of asymmetry, linearity, dynamic resistance and the turn-on voltage (V_{ON}).

6.2.1 Fabrication

Devices with 100^2 μm^2 lateral area were fabricated on cleaned Corning glass or silicon substrates by depositing 50 nm thick top and bottom metal layers by thermal evaporation at a rate of 4 Å/s and a pressure of 5×10^{-7} Torr. The electrodes were patterned through a shadow mask for S1b and by the lift-off process (described in section 6.3.1) for all other devices, as shown in Table 6.3. Al_2O_3 and Ta_2O_5 oxides were deposited using RF sputtering Sput2 (described in the introduction of chapter 5) at room temperature for the devices S3s and S5s. Atomic layer deposition (ALD) was used to deposit the oxides for the other devices: S1a, S1b, S2a, S3a, S4a, S5a, S6a, and S7a. Unlike ALD1 used solely for ALD in the previous section and chapter 5, ALD2 denotes the following conditions of ALD modifying the pulse and purge times (Table 6.3) to assess any influence on the rectifying performance as compared to ALD1-devices. ALD2 was done at a temperature of 200 ℃ using deionized water as the oxidant for Ta_2O_5 and Al_2O_3 at 0.04s/10s pulse/purge times, tantalum ethoxide precursor for Ta_2O_5 at 0.3s/2s pulse/purge time, and trimethylaluminium (TMA) precursor for Al_2O_3 at 0.02s/5s pulse/purge time. The J-V measurements were done in the dark on a temperature-controlled heating stage or in a Cryostat with liquid nitrogen cooling. Voltage was swept with 10 mV step size from 0 V from negative to positive bias, and from positive to negative bias.

Table 6.3 ALD pulse and purge times.

		ALD1		ALD2	
Oxide	Precursor	Pulse [s]	Purge [s]	Pulse [s]	Purge [s]
Al_2O_3	TMA	0.02	2	0.02	10
	H_2O	0.04	4	0.04	10
Ta_2O_5	Ta(O)$_5$	0.3	2	0.2	10
	H_2O	0.04	4	0.04	10

Table 6.4. Device structure and layer thickness: Substrate/M1/I1/I2/M2, where substrate could be glass (Gl) or Si, M1 and M2 are the bottom and top electrodes respectively, and I1 and I2 are the insulators.

Device	Subst.	M1	Dep.	t [nm]	I1	t [nm]	I2	M2
S1a	CG	Au	ALD2	1	Al_2O_3	4	Ta_2O_5	Al
S1b	CG	Au	ALD1	1	Al_2O_3	4	Ta_2O_5	Al
S2a	CG	Au	ALD2	1	Al_2O_3	3	Ta_2O_5	Al
S3a	CG	Au	ALD2	4	Ta_2O_5	1	Al_2O_3	Al
S3s	Si	Au	Sput	4	Ta_2O_5	1	Al_2O_3	Al
S4a	CG	Au	ALD2	3	Ta_2O_5	1	Al_2O_3	Al
S5a	CG	Au	ALD2	0.5	Al_2O_3	4	Ta_2O_5	Al
S6a	CG	Au	ALD2	0.5	Al_2O_3	3	Ta_2O_5	Al
S5s	Si	Au	Sput	0.5	Al_2O_3	4	Ta_2O_5	Al
S7a	CG	Au	ALD2	–	–	4	Ta_2O_5	Al

These mechanisms are not totally independent of each other. For the few nm thick dielectrics used here, tunnelling mechanisms are likely to play a major role. The conduction mechanism in tunnelling diodes could be influenced by trapping where the associated charge could reduce the electric field at the injecting electrode and thus limit the tunnelling current. For the trap-mediated thermal mechanisms, the commonly used theories usually assume relatively widely spaced traps with non-overlapping associated Coulombic potential wells. Such spacings are likely to be of the same order as the dielectric thicknesses so it is likely that the potential wells overlap, complicating the picture. The temperature dependence of the J-V characteristics in tunnelling diodes is related to the number of electrons incident on the barrier introducing a temperature-correction factor into the FN equation.[144] Temperature dependence has also been investigated in RT diodes,[145] and thermionic emission have shown to be affecting the rectifying characteristics.[146] It is worth noting that the first observance of RT with a charge transport faster than 10^{-13}s indicated clear temperature dependence of the J-V characteristics but was not explained.[28]

6.2.2 Results and discussion

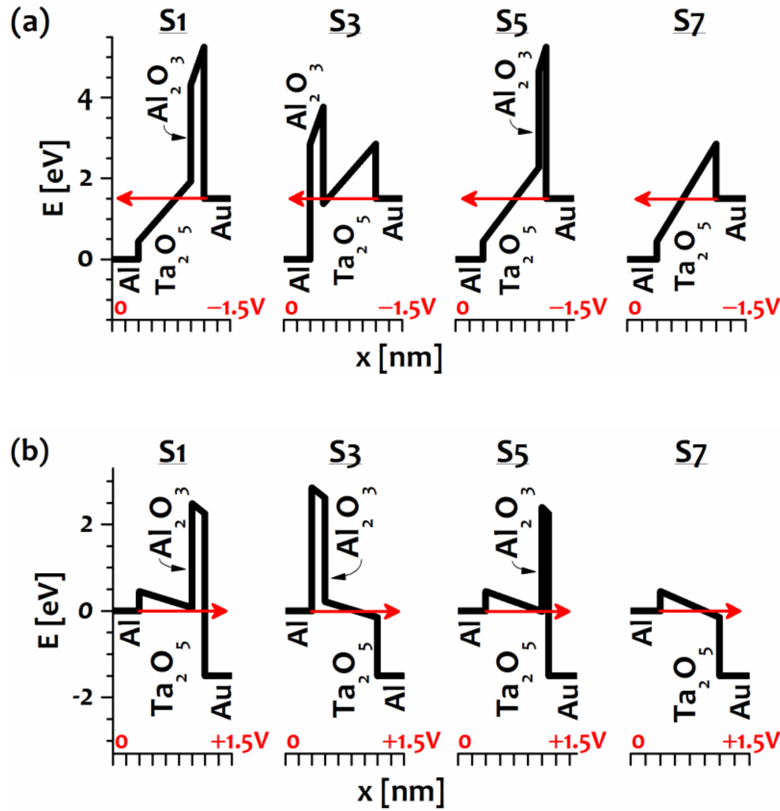

Figure 6.9 Band diagrams of structures S1, S3, S5, and S7 at negative (a) and positive (b) bias. Electron injection is indicated by the red arrow.

Figure 6.9 serves to illustrate the tunnelling paths in the band diagrams of these structures: the negative bias corresponds to Figure 6.9(a) where electrons are injected from the bottom Au electrode to the top Al electrode, whereas the positive bias corresponds to Figure 6.9(b) of opposite electron injection. At negative bias, FN tunnelling is predicted for structures S1, S5, and S7 where band bending shortens the effective distance for electrons to tunnel through, whereas resonant tunnelling is possible for S3 MIIM structure if any bound state can exist in the quantum well between the two dielectrics. At positive bias, resonant tunnelling is possible for MIIM structures S1 and S5 whereas FN tunnelling is predicted for S3. Halving the Al_2O_3 thickness in S5, as compared to S1, raises the possibility for resonant tunnelling to occur.

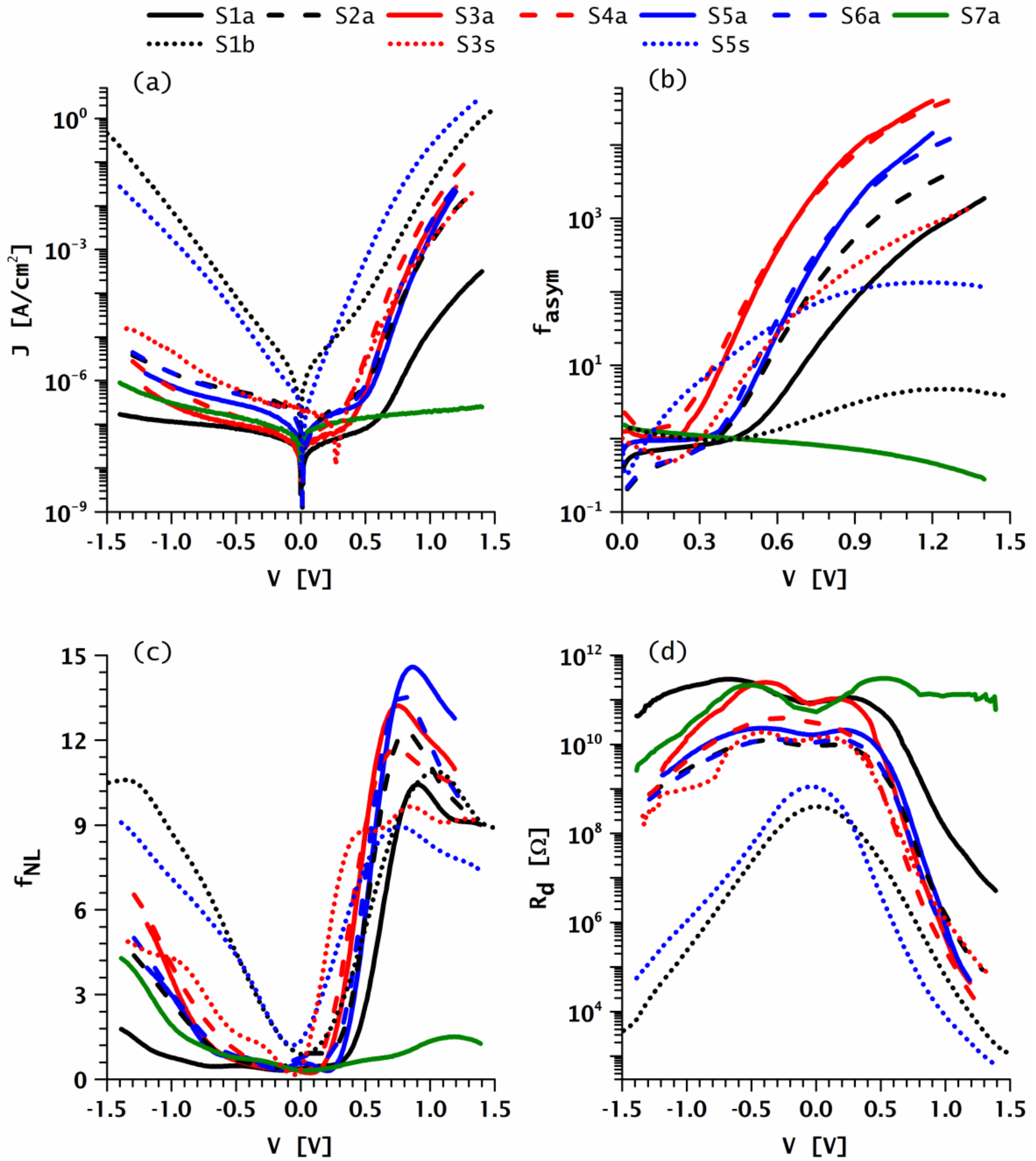

Figure 6.10 The rectifying characteristics of the Au/Ta_2O_5/Al_2O_3/Al structures showing the: J-V characteristics (a), asymmetry (b), non-linearity (c), and dynamic resistance (d).

The rectifying characteristics shown in Figure 6.10 are described by: (a) the asymmetry, defined as the ratio of the current at positive bias to that at negative bias at certain voltage: $f_{asym} = J_+/J_-$, (b) the dynamic resistance, defined as: $R_d = dV/dI$, and (c) the non-linearity, defined as the ratio of the static to dynamic resistance: $f_{NL} = (V/J)/(dV/dJ)$ which needs to be not less than three[2] for sufficient rectification in THz applications. Noticeably, very large asymmetry [Figure 6.10(a)] and non-linearity [Figure 6.10(b)] are observed at positive bias with ALD2 MIIM samples. Reducing Ta_2O_5 thickness by 1 nm did not reduce the dynamic resistance significantly as the

devices in previous sections. Such reduction could enhance the asymmetry and non-linearity as in the case of S2a comparable to S1a. Undesirably, all ALD2 samples suffer from very large dynamic resistance making them incompatible for THz rectennas, which require reducing the dynamic resistance and lowering V_{ON} as much as possible. However, these could be useful for applications not requiring low R_d and are helpful to understand the charge transport in tunnelling diodes and how to optimize them. Out of all these devices, S5s is characterized by the lowest V_{ON} of 0.14 V with sufficient rectifying non-linearity larger than 3 and sufficient asymmetry occurring at low voltage, making it compatible for THz rectennas. Different tunnelling mechanisms and thermal emissions dominating the conduction mechanism in the diodes are discussed in what follows. the negative bias of the J-V characteristics [Figure 6.10(a)].

The evidence for the domination of either Schottky emission (SE) or Poole-Frenkel emission (PFE)[147] requires a self-consistent dynamic permittivity from the slope of the plots[148] corresponding to their characteristic equations. This is not straightforward with multi-dielectric layers where current is dependent on more than one conduction mechanism and are correlated by the Maxwell-Wagner effect[103]. For this, it is necessary to study the conduction mechanisms dominating in the individual oxides. Typically, tunnelling dominates in Al_2O_3 and thermal emission in Ta_2O_5.[149]

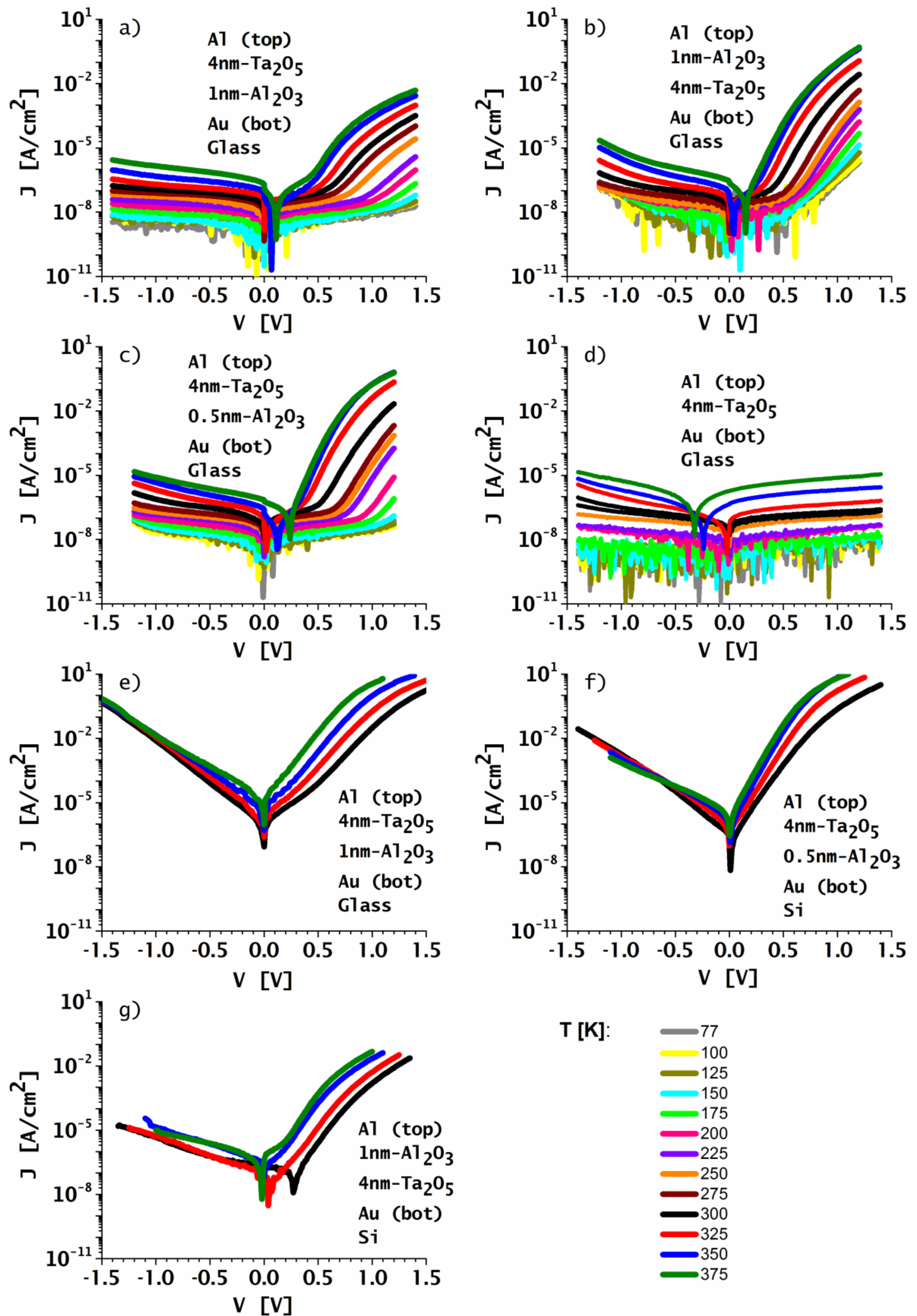

Figure 6.11 The temperature dependent J-V measurements of the devices measured using the cryostat (a-d) at 77K and 100-to-375K with 25K-step or using the heating stage (e-g) at 300-to-375K with 25K-step: S1a (a), S3a (b), S5a (c), S7a (d), S1b (e), S5s (f), and S3s (g).

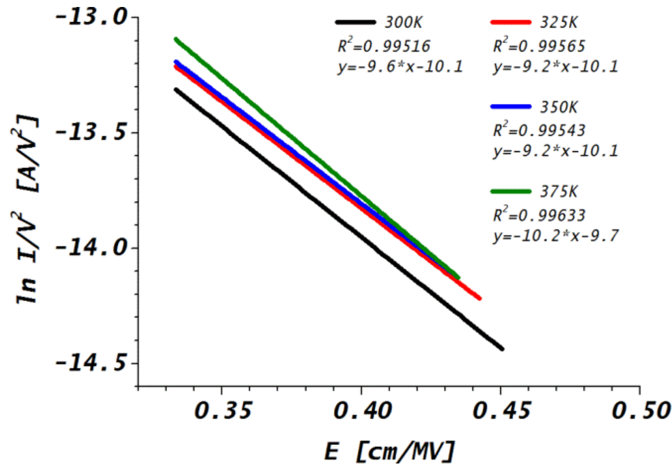

Figure 6.12 FN plot for S1b at negative polarity assuming Ta_2O_5 of total thickness equal to that of the sandwiched dielectric stack. The extracted barrier height is 0.59, 0.58, 0.58, and 0.62 eV at 300, 325, 350, and 375 K respectively.

The domination of FNT can be clearly observed in the temperature insensitive J-V region at negative polarity of the sputtered and the ALD1 samples: S1b, S5s, and slightly S3s [Figure 6.11(e,f,g)]. This explains why the energy trap depth diverges with opposite injection of electrons (found to be 0.6 and 1.7 eV at negative and positive polarities respectively for S1b).

Despite the good fitting of FNT plot for S1b at negative 1.1-1.4V bias range (Figure 6.12), the extracted barrier height of 0.6 eV is in agreement with Au work function of 4.8 eV[129] instead of the most reported 5.1 eV (Ref. [98]) assuming Al work function of 4.2 eV[129] and Ta_2O_5 electron affinity of 3.75 eV[105]. This could be reasonable due to the double barrier structure leading to extraction of a smaller effective barrier height. It can be noticed that the device S1a (ALD2) having the same structure as S1b (ALD1) failed to show FN behaviour – similarly for other structures [Figure 6.10(a)]. Temperature sensitivity at both polarities is illustrated in the J-V plots [Figure 6.11], showing noticeable insensitivity at negative polarity for S1b [Figure 6.11(e)] where FN dominates. However, the polarity-independent PFE was previously shown to be dominant in the 0.3-1.5V region for 4nm-Ta_2O_5,[149] which is close to V_{ON} of S1/S3/S5 indicating a possible role of the bulk defects and that there exists another polarity dependent conduction mechanism leading to asymmetry.

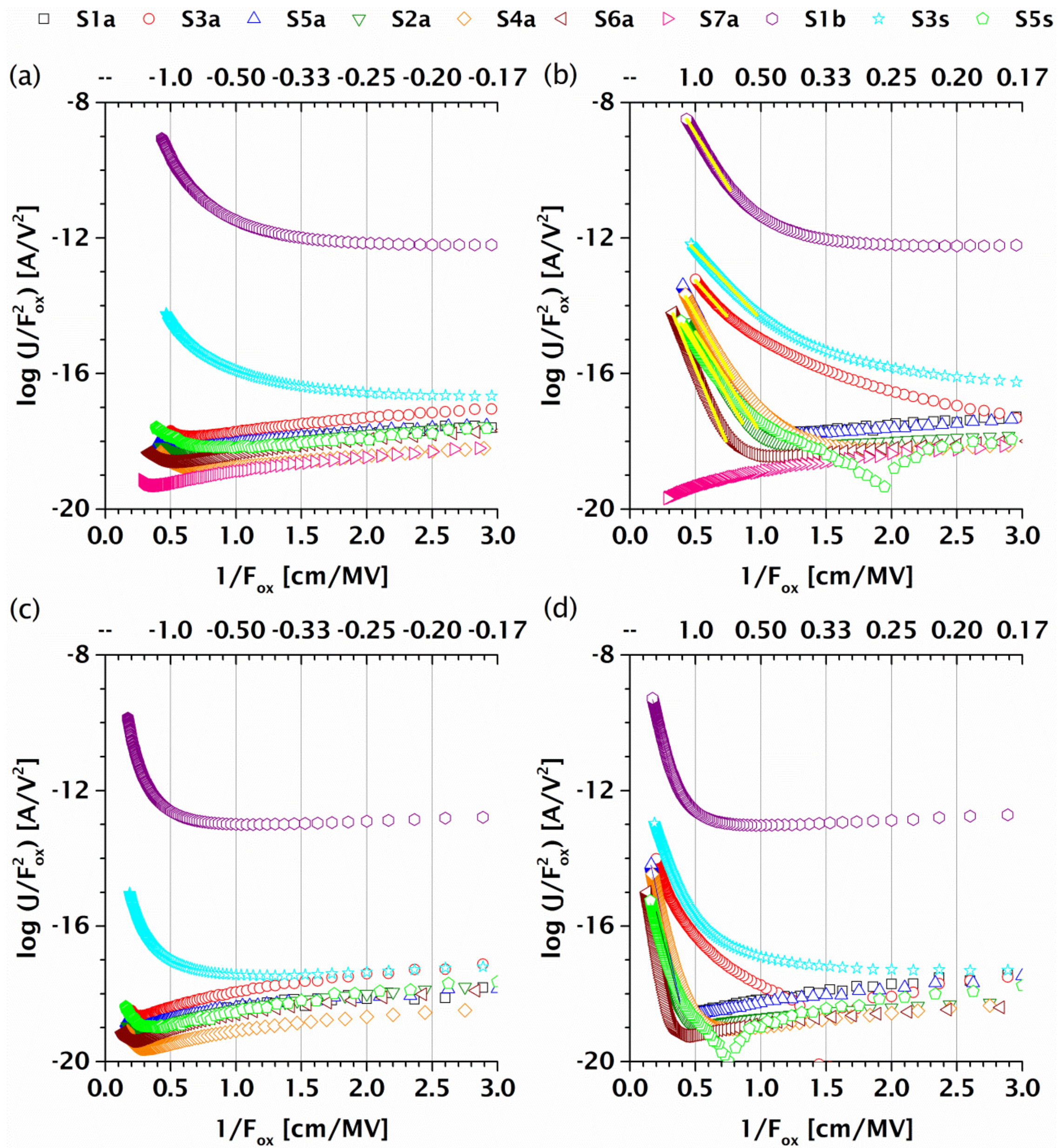

Figure 6.13 FN plots considering the electric field distribution across each dielectric Ta_2O_5 (a and b) and Al_2O_3 (c and d).

Table 6.5 The extracted barrier heights from FN plots across each dielectric.

	Al_2O_3							
Device	S1a	S5a	S5a	S5a	S4a	S4a	S1b	S5s
Intercept	-12.6	-11.2	-11.3	-11.2	-11.8	-11.8	-6.6	-13
Slope	-15.1	-18.3	-18.1	-18.3	-16	-16.5	-15.4	-14.8
R^2	0.99802	0.9973	0.99697	0.9973	0.99591	0.99797	0.99709	0.99518
$Ø_B$ [eV]	0.8	0.91	0.91	0.91	0.84	0.85	0.81	0.79

	Ta_2O_5							
Device	S1a	S3a	S2a	S4a	S6a	S1b	S3s	S5s
Intercept	-11.8	-11.1	-11.7	-10.9	-11.2	-5.8	-10.3	-12.2
Slope	-6	-4.4	-6.7	-6.7	-9.2	-6.3	-4.1	-6
R^2	0.99738	0.99598	0.99812	0.99724	0.99714	0.99826	0.99719	0.99555
$Ø_B$ [eV]	0.43	0.35	0.47	0.46	0.58	0.45	0.33	0.43

The bulk limited PFE, which would cause symmetrical current leakage at both polarities, is unlikely to explain the asymmetrical J-V characteristics observed for all devices, especially ALD2 (Figure 6.10). The conduction mechanism is thought to be limited by trap-to-trap Mott hopping lowering the current level and which, similar to PFE, does not have a major role in asymmetry. Consequently, the smaller non-linearity at negative polarity for S3s as compared to S1b and S5s could be attributed to the more defects present in the former where Mott-hopping dominates over FN. The conduction mechanisms are further investigated in S5a, S5s, and S1a devices of distinct behaviour of their J-V characteristics. The presence of defects is further evident by the dominance of SCLC at negative voltage for V < 0.9 V for S5s and at V < -0.3 and 0.4 V for S1a and S5a respectively indicating the large number of bulk defects in S1a and S5a. The parameters of defect related mechanisms PFE, SE, TAT, and SCLC are extracted based on plotting their corresponding equations. The fitted equations are compared with the experimental characteristics where they match in different regimes. Despite the good fitting, SE can be ruled out as $\varepsilon_{r,SE}$ extracted for all 3 devices is far away from the reliable 4.6-4.95 (optical) and 4.6 (PFE) extracted in another study. $\varepsilon_{r,PFE}$ extracted from the slopes of PFE plots is reasonable with S5s with a value of 4.83, whereas that of S5a is far below and S1a is a bit larger. The variation in extracted $\varepsilon_{r,PFE}$ for 2 devices of same ALD conditions but halved Al_2O_3 thickness is consistent with the increase of tunnelling probability with S5a of deeper potential well as expected from the energy band diagrams (Figure 6.9). This tunnelling mechanism is assisted by traps for V ≥ 0.7 V for all 3 devices, as evident from matching TAT tunnelling equations with the experimental J-V characteristics. Despite the

reasonable extracted parameters from PFE for S5s, PFE J-V curves do not match with experimental J-V for V > 1 V but only with TAT. Zooming in at the maximum positive voltage, the J-V curves for S5a and S1a are more likely to match TAT than PFE. Furthermore, when the 1 nm Al_2O_3 layer is not deposited (S7a), no linear fit for PFE could be found in any voltage region. These are all strong indications that the behaviour of experimental J-V characteristics is best described by TAT for V ≥ 0.7 V.

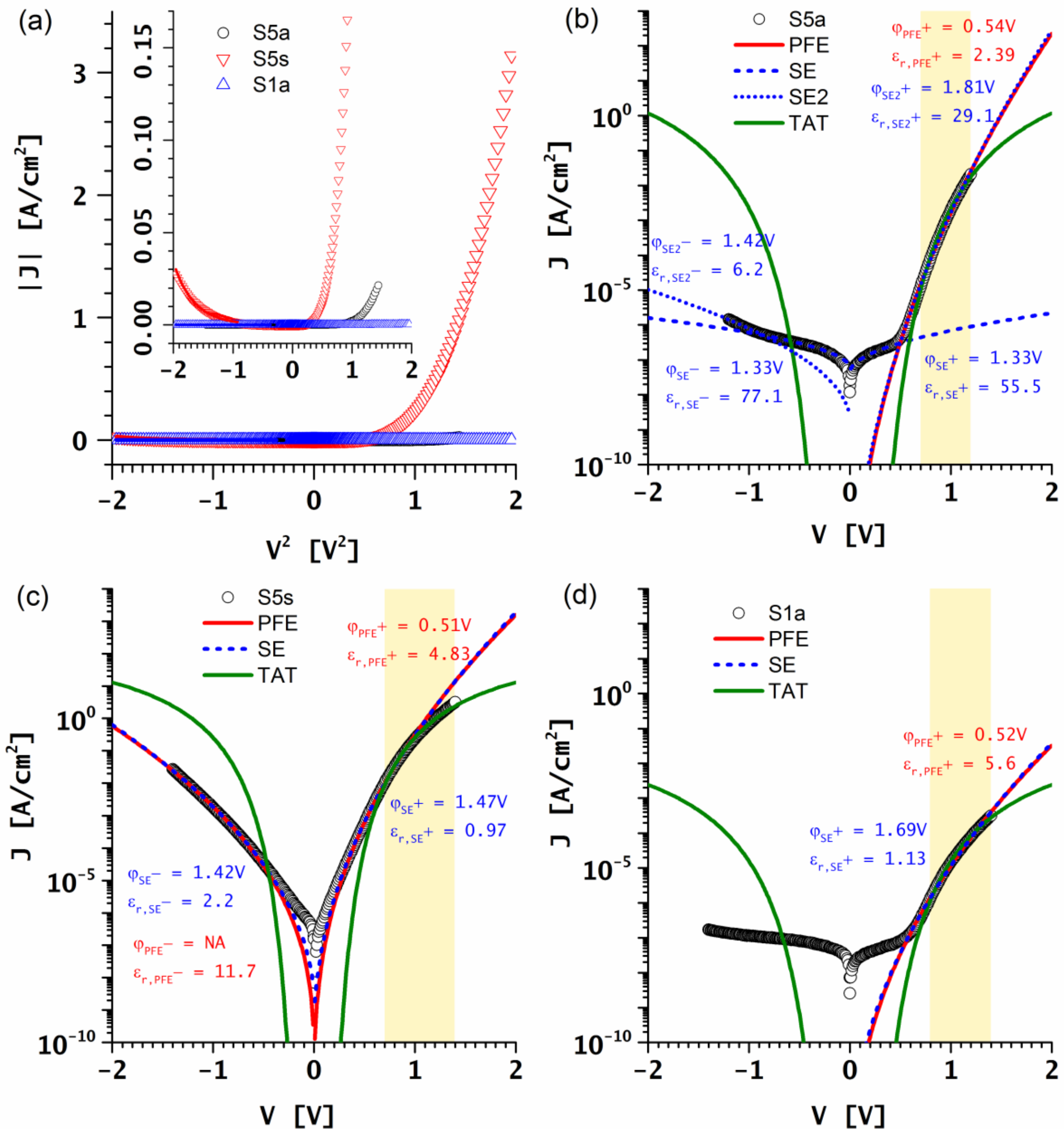

Figure 6.14 The J-V characteristics of S1a (a), S5s (b), and S5a (c), based on fitting the extracted parameters from the experimental J-V characteristics to the equation of PFE (ln(I/V)-$V^{1/2}$), SE (ln(I/T^2)-$V^{1/2}$), and TAT (ln(J)-V^{-1}). The J-V^2 characteristics of these 3 devices indicate no linearity over the applied voltage (d).

SE is also unlikely to dominate in ALD2 samples, due to the unreasonable small slope fittings obtained from SE plots. If the larger current at positive bias for all MIIM structures is explained by SE domination, the symmetrical behavior of the 4nm Ta_2O_5 MIM structure (S7a) rules out the domination of SE, since SE depends solely on the electrodes which are the same for all MIM and MIIM devices. The defect nature and high leakage current of the 4nm-Ta_2O_5 layer[150], is thought to be intensified in ALD2 resulting in the domination of TAT instead of FN tunnelling, expected at both polarities from the band diagrams (Figure 6.9). This shows further that S7a may be dominated by trap-to-trap hopping due to the large defects caused by the deposition conditions of ALD2. FNT expected from the band diagrams for S7a with larger band bending at negative bias is thought to be causing the slightly larger non-linearity at negative bias.

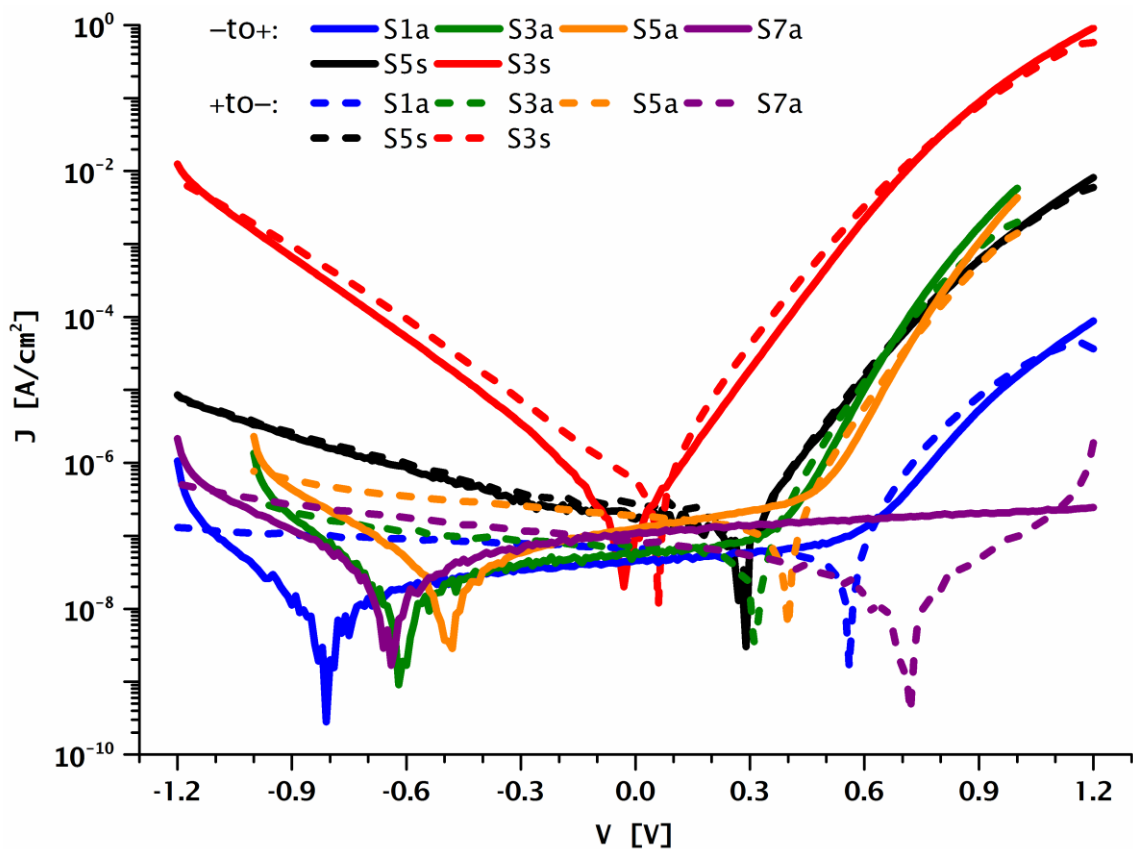

Figure 6.15 J-V characteristics of selected devices measured at negative sweep from maximum positive voltage to maximum negative voltage (+to-) and positive sweep from maximum negative voltage to maximum positive voltage (-to+).

This is known as trap assisted tunnelling (TAT), when the trap depth created below the conduction band minimum allows a shorter path for electrons to tunnel without entering the conduction band of the dielectric.[99] The ALD1 sample and the sputtered S5s of less traps, as indicated by the lower dynamic resistance [Figure 6.10(d)], are dominated by FN tunnelling at negative polarity. Due to

the presence of less traps in these two samples, TAT at positive polarity is not as steep as ALD2 MIIM samples. It's thought that traps in S1b and S5s are minimized due to the Al_2O_3 shield on top of Ta_2O_5 after exposing to air preventing oxygen vacancies to interact with Ta_2O_5 of defect nature as expected for S3a, S3s, and S4a. The presence of trap mediated charge transport in ALD2 samples is evident from the difference between the J-V characteristics at negative and positive sweeps (Figure 6.15), which indicates large number of traps in these samples. On contrary, this difference was slight for sputtered samples S3s and S5s indicating high quality oxides. The J-V characteristics can thus be tuned by controlling the defects in the oxides using different deposition properties which becomes critical with ultra-thin layers where more oxygen vacancies can be introduced in the bulk and the interface. It's thought that the lower quality of ALD2 oxides allows large number of oxygen vacancies to move towards the top Al layer post deposition, since Al is highly interactive with oxygen. These oxygen vacancies form an interfacial layer between Al and This, however, does not occur with opposite injection of electrons at positive polarity.

Tunnelling is revealed from the current reversal at low temperature (77K) and characterized by the large non-linearity at positive bias (at 300K). Thermal emission is indicated by the temperature dependence of the current, lowering V_{ON} with higher temperature. In fact, the temperature dependence of the J-V curves where FN could dominate is as strong as at positive polarity where RT dominates. The temperature dependence for all devices points to the existence of traps in the bulk of Ta_2O_5 where TAT could dominate. Furthermore, V_{ON} does not change significantly when Ta_2O_5 thickness is decreased to 3 nm, which suggests non-bulk mechanism, as tunnelling, dominating. Thus, at V_{ON}, current is thought to be increasing rapidly due to TAT.

Based on the analysis done on the different structures and on an analogous interpretation[151], the following two-step tunnelling process is suggested to explain the dominating conduction mechanism considering the traps as intermediate states. The electrons are injected from metal-to-traps through direct tunnelling and then from traps to the other electrode through TAT. This two-step process is thought to be occurring for some electrons in parallel to tunnelling mechanisms of others causing the current reversal: FNT with band bending of Ta_2O_5 or RT with bound states in the quantum well. At negative bias, these tunnelling and TAT mechanisms are followed by defects slowing down their transit time at the interface with Al containing oxygen vacancies. The transit time of the electrons does not get slower with opposite injection due to the inert nature of gold which does not absorb oxygen vacancies from the oxides (Ta_2O_5). Thus, it can be said that the major role in enhancing the rectifying performance lies in the quality of the oxide and the interactivity of the electrodes with oxygen.

MIIM diodes of Au and Al bottom and top electrodes respectively has been studied swapping the sandwiched Ta_2O_5 and Al_2O_3 oxides to show that the dominating conduction mechanism is not simply tunnelling mechanism or thermionic emission. The dominance of RT and FNT were evident from the analysis given to 6 MIIM and 1 MIM structure revealed from the J-V onset at 77K. Comparing the rectifying characteristics of devices fabricated with sputtering and different ALD deposition parameters, oxide quality shows significant role in tuning the diode for THz rectification. The interaction at the top of the high-k Ta_2O_5 with the top Al electrode is thought to be creating oxygen vacancies at the interface. When ALD purge time is increased, these vacancies increase significantly, resulting in impeding the current at negative polarity to the slow trap-to-trap Mott hopping, even after electrons tunnel with FNT or RT. These defects are of larger number for the samples of ALD2 than that of ALD1, lowering the current at both polarities, preventing tunnelling mechanisms (FN/RT) from occurring at negative polarity, but allowing them to occur at positive polarity. The same structures were further optimized for THz applications by minimizing the defect properties of Ta_2O_5 for less interaction post top Al deposition. A turn-on voltage of 0.14 V with sufficient asymmetry and non-linearity has been recorded for one of the devices (S5s) making it, with the evident RT mechanism dominating its conduction, suitable for low power applications as THz rectenna arrays.

6.3 The role of oxygen vacancies

Many attempts were done to fabricate MIIM diodes by depositing 1 nm-Al_2O_3 followed by 4 nm-Ta_2O_5 on top of Au, and all failed unlike the success of fabricating the same oxide stack on top of Al. This can be explained by the growth of native oxide, as indicated by the HR-TEM images in section 5.2, on top of bottom Al electrode and on bottom of top Al electrode which can be sufficient to prevent short circuits. S3s and S5s showed very good rectifying characteristics as shown in section 6.2. In this section, these structures are slightly modified with the aim to minimize the formation of native oxide on the bottom of top Al metal. g1, g3, and g5 devices are fabricated using Au inert metal as the bottom electrode and Cr of less oxidizing than Al, as the top electrode, to minimize the formation of native oxide. This allows better understanding of the conduction mechanisms in the structures.

In addition, no device of Al_2O_3 MIM diode was working despite the success of S1 in section 6.1. Plasmonic diode structures using 3, 4, and 5 nm ALD1-Al_2O_3 sandwiched between Au electrodes showed short circuit for all fabricated devices. Many MIM devices with 4 and 6 nm sputtered Al_2O_3 showed short circuit too, despite the success of Ta_2O_5 MIM devices.

Defects in the oxides are identified as oxygen vacancies present in the bulk material which could affect the optical and electronic properties of the oxides especially the high-k Ta_2O_5. Their number in the deposited dielectric depends on the growth conditions, which can control the properties of the oxides. Consequently, this alteration can result in significant change in the rectifying characteristics of the MIIM diodes as shown in section 4.6 between the devices of oxides deposited using different ALD growth parameters: ALD1 and ALD2. The presence of oxygen vacancies is unfavorable to device performance where it can lead to the domination of thermal mechanisms instead of tunnelling.

6.3.1 Fabrication

Devices of different structures are fabricated as shown in Table 6.6. Silicon substrates, of 2 nm native oxide (confirmed using ellipsometry), were cleaned with isopropanol and blown dry with a nitrogen gun. The oxides were deposited using sputtering using the same deposition conditions for S3s and S5s in section 6.2 (Sput2). The bottom and top metals (M1 and M2 respectively) were deposited using thermal evaporation and patterned using the lift-off photolithographic process. The cleaned substrates were fixed on a rotating vacuum chuck in the spin coater. The positive photoresist, Shipley S1813, was then dropped onto the sample using a syringe and spun at a rate of 1000 rpm (revolutions per minute) for 5 s (seconds) and at 5000 rpm for 55 s. This resulted in a uniform defect free photoresist layer of 1.2 µm thick.[152] The samples were then soft baked on a heating chuck at 115 ºC for 90 s to harden the resist. The samples were then placed in the mask aligner, where the mask was aligned to the substrate before exposing them to UV light for 20 s via the photomask. The exposed regions of the resist become soluble so that the required pattern stays after developing the samples in 1:1 solution of Microposit developer and deionized water. The samples were then rinsed in deionized water and blown dry with nitrogen. The samples were then fixed in a rotating sample holder inside a Moorfield thermal evaporator, where deposition is done upwards at a pressure lower than 5×10^{-7} torr and at a rate of 4 Å/s. The samples were then immersed in acetone which dissolves the photoresist till the metal above it is completely removed. The samples were then cleaned with acetone and isopropanol subsequently and then blown dry with a nitrogen gun.

Table 6.6 Device structure and layer thickness.

Structure		g1	g3	g5	S5s	S3s	c1	c3
Substrate		Si	Si	Si	CG	CG	Si	Si
Native oxide	t [nm]	2	2	2	-	-	2	2
		SiO_2	SiO_2	SiO_2	-	-	SiO_2	SiO_2
M1	t [nm]	80	80	50	80	80	120	120
		Au	Au	Au	Au	Au	Al	Al
Deposition		Sput	Sput	Sput	Sput	Sput	Sput	Sput
I1	t [nm]	1.5	6	6	0.5	4	1	4
		Al_2O_3	Ta_2O_5	Ta_2O_5	Al_2O_3	Ta_2O_5	Al_2O_3	Ta_2O_5
I2	t [nm]	6	1.5	-	4	1	4	1
		Ta_2O_5	Al_2O_3	-	Ta_2O_5	Al_2O_3	Ta_2O_5	Al_2O_3
M2	t [nm]	20	20	20	120	120	120	120
		Cr	Cr	Cr	Al	Al	Al	Al
M3	t [nm]	60	60	60	-	-	-	-
		Au	Au	Au	-	-	-	-

6.3.2 Results and discussion

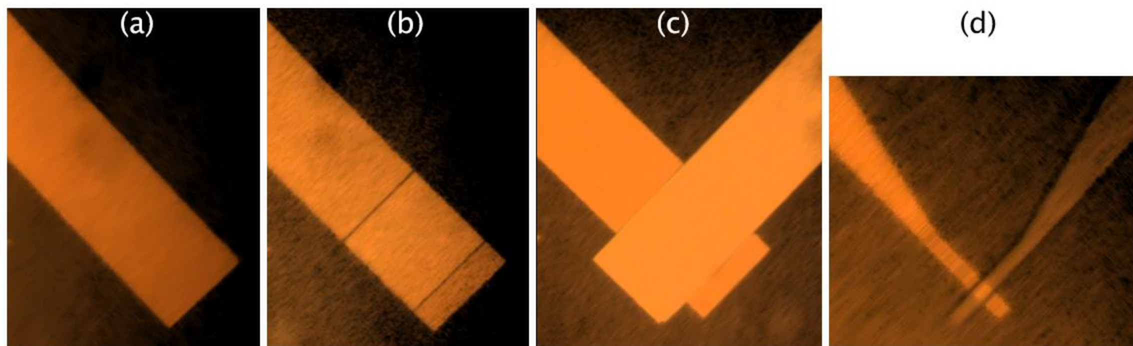

Figure 6.16 Microscope images of two devices fabricated using lift-off photolithography: 250×250 μm^2 device after M1 deposition (a), after developing (b), and after M2 deposition (c), and another 20×20 μm^2 device (d).

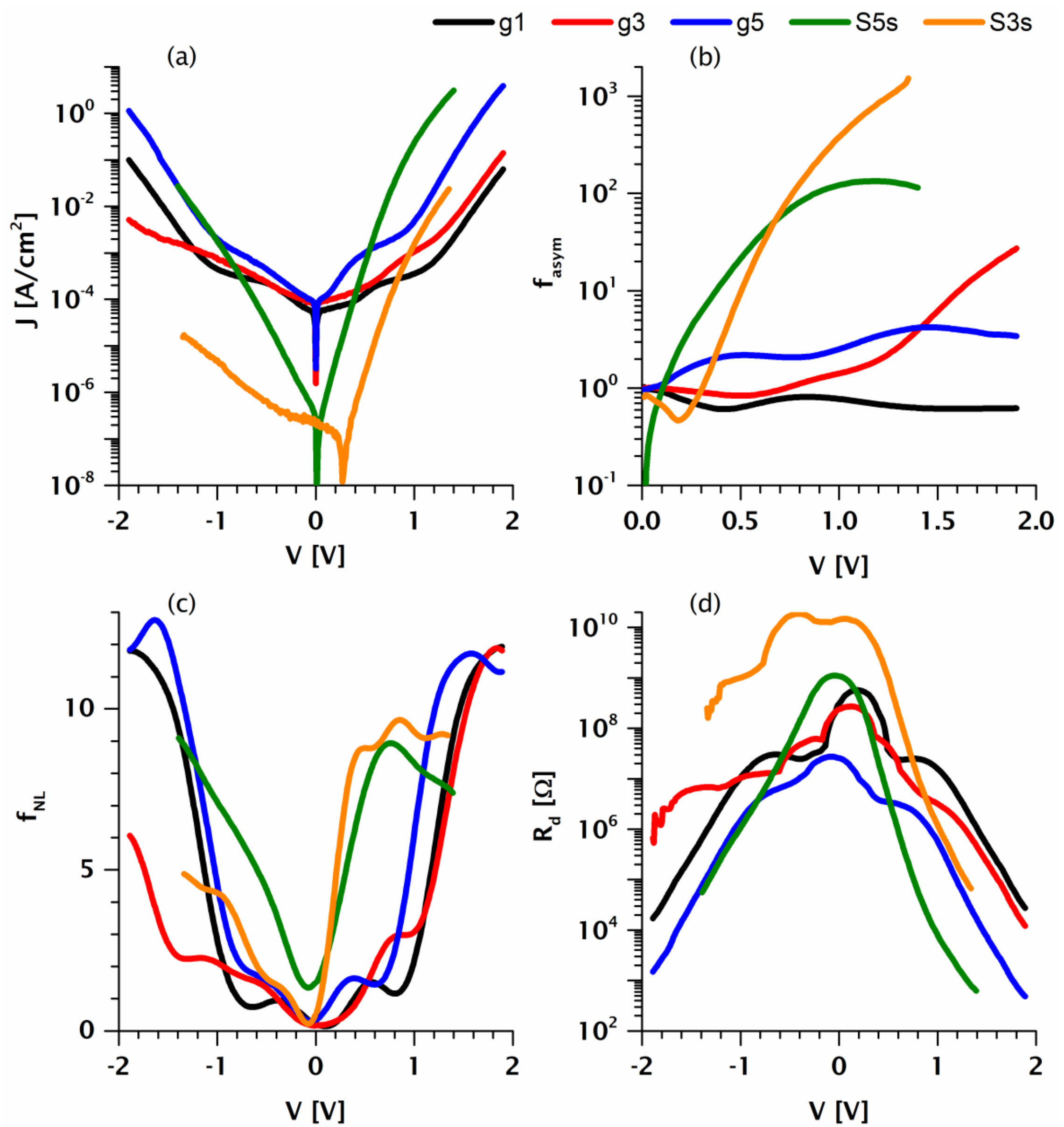

Figure 6.17 Rectifying characteristics of the MIIM devices (g1, g3, g5, S3s, and S5s) showing the: (a) J-V characteristics, (b) asymmetry, (c) nonlinearity, and (d) dynamic resistance.

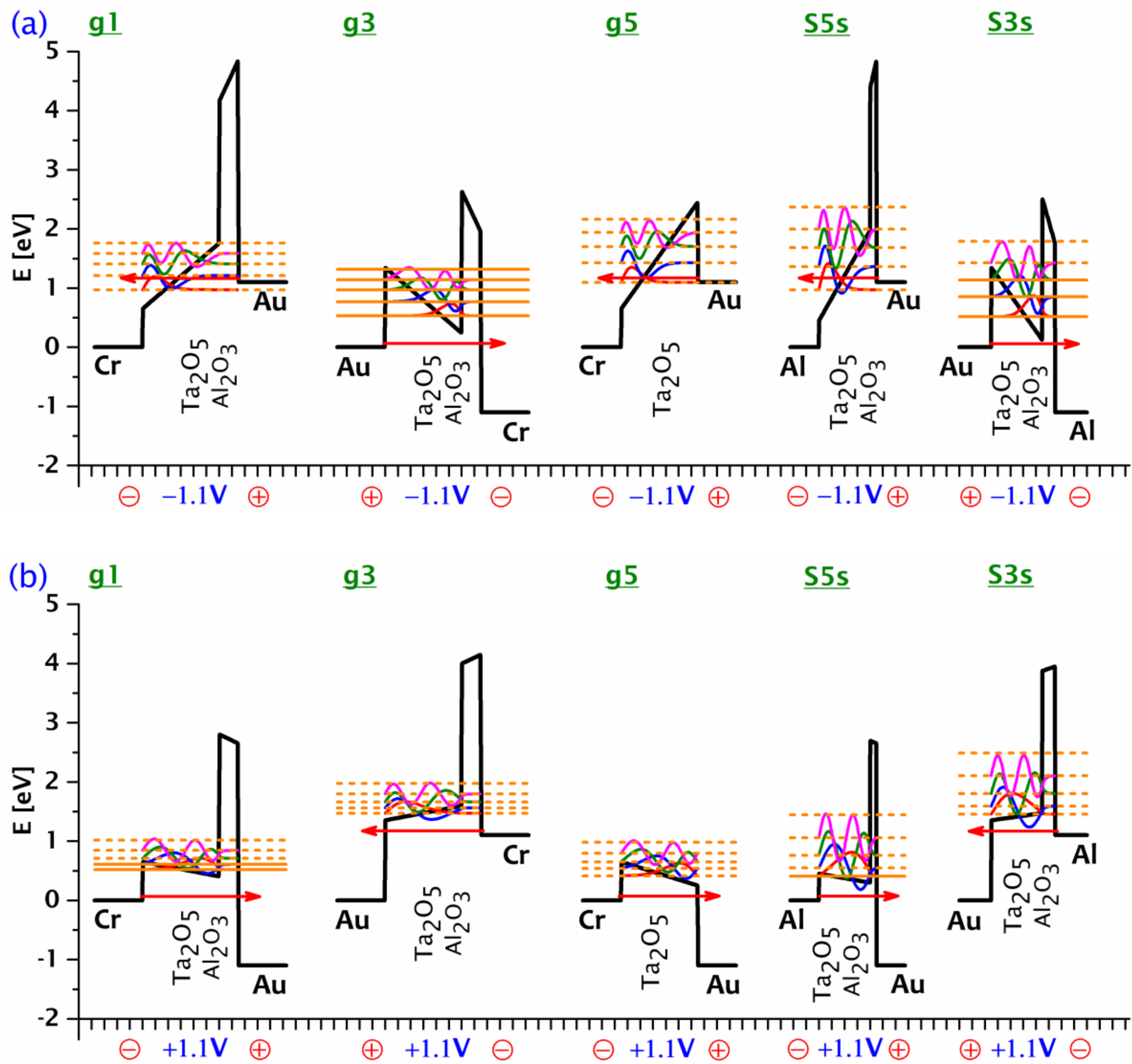

Figure 6.18 Simulated conduction band diagrams of the structures g1, g3, g5, S5s, and S3s at -1.1 (a) and +1.1 V (b) showing 0/2, 5/0, 0/0, 0/1, and 3/0 bound states (solid lines) for S3, S4, S5, and S6 respectively at negative/positive bias. One tick on the x-axis corresponds to 1 nm. The electrons move from an electrode to another as indicated by the red arrows. The red polarity symbols represent how the device is connected for the current-voltage measurements.

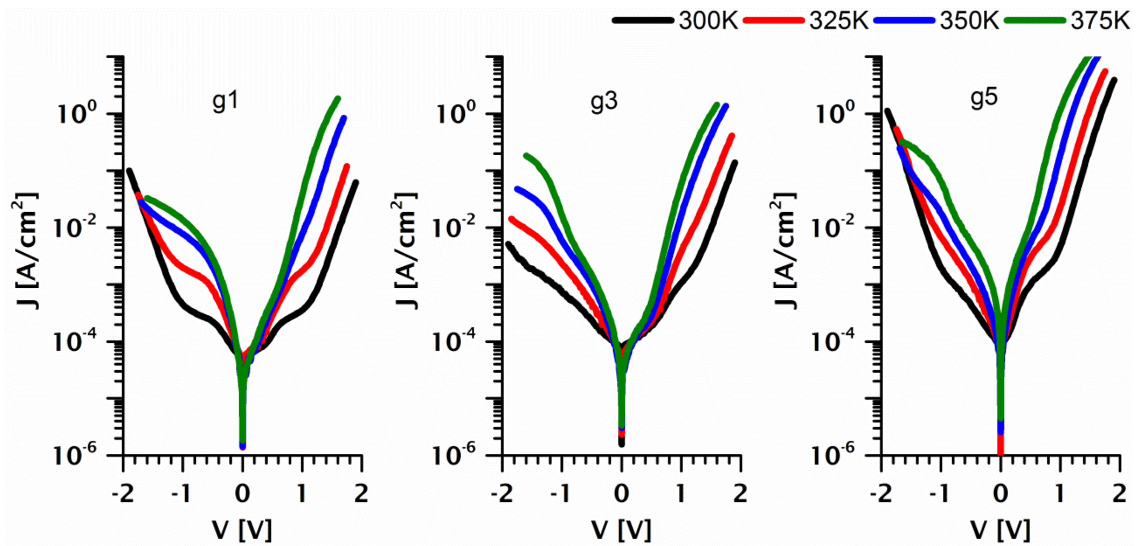

Figure 6.19 The temperature dependent J-V measurements of g1, g3, and g5 devices measured using the heating stage at 300, 325, 350, and 375 K.

Table 6.7 The reversal voltage for the devices S5s, S3s, g1, g3, and g5 at 300, 325, 350, and 375 K at negative (-) and positive (+) bias, defined as the voltage at which a non-linearity of 3 is achieved.

	S5s		S3s		g1		g3		g5	
T [K]	-	+	-	+	-	+	-	+	-	+
300	-0.33	0.16	-0.74	0.13	-1.01	1.06	-1.54	0.96	-0.88	0.83
325	-0.4	0.16	-0.67	0.04	-1.14	1.06	-1.01	0.6	-0.87	0.76
350	-0.53	0.13	-0.8	0.2	-1.47	0.54	-0.84	0.51	-0.72	0.57
375	-0.64	0.13	-0.92	0.18	-	0.49	-0.69	0.44	-0.67	0.4

The rectifying characteristics of g1, g3, g5, S5s, and S3s diodes are shown in Figure 6.17. The asymmetry and non-linearity were significantly better for S5s and S3s. The larger non-linearity is due to the smaller barrier of the dielectric stack in these structures, which was predictable from the model. However, it was not possible to fabricate the same oxides with exactly similar growth conditions sandwiched between Au and Cr despite the many attempts. It was not easy to get S5s and S3s too, and this can be explained by the native oxide filling the pinholes and preventing any metal excursion from creating short circuit between the electrodes. The reversal voltages for S3s and S5s was significantly lower than any other structures. A turn-on voltage of 0.13 and 0.16 V for S3s and S5s is accompanied by significant increase in asymmetry and non-linearity. For S3s and S5s, the nonlinearity reaches 8.8 at 0.42 and 0.7 V respectively whereas the asymmetry

increases steeply towards 10^3 and 10^2 scales respectively at larger voltages. It should be noted that the shift in J-V switching in S3s is possible to be brought to 0 V like other devices, if fabrication is repeated as this happened with some other devices in previous sections. S3s, however, suffers from large dynamic resistance. This is sensible as compared to S5s of 0.5 nm thinner Al_2O_3 barrier. However, this becomes not sensible at first as compared to 6nm-Ta_2O_5 and 6nm-Ta_2O_5/1.5nm Al_2O_3 and 1.5nm Al_2O_3/6nm-Ta_2O_5 structures, knowing that all oxides of these structures are grown by the same RF sputtering conditions. This can only be explained by the layer of native oxide grown on the bottom of Al (section 5.2) top electrodes in S5s and S3s structures, expected to be much thicker than that growing on the bottom of Cr. Samples S3s and S5s showed realistic rectifying characteristics at a turn-on voltage of 0.13 and 0.16 V, the lowest achieved in this work. This comprises good non-linearity of 3 and an asymmetry much better than that of MIM devices used successfully for THz rectennas.[2] The indications of tunnelling imply their potential use for THz electronics despite the large dynamic resistance.

As shown in the energy band diagrams (Figure 6.18), resonant tunnelling is more probable with g3 at negative polarity than g1 at positive polarity, and the difference in probability is due to the work function dissimilarity between the electrodes (0.7 eV). However, the non-linearity was much larger for g1 than for g3 and the reversal voltage was lower for g1 with +1.06 V for g1 at positive bias and -1.54 for g3 at negative bias. The band bending of g1 at negative bias is steep enough for FN tunnelling, unlike g3 at positive bias. However, the non-linearity and reversal voltage of g1 at negative bias are very close to those of g3 at positive bias. MIM device g5 could not get better characteristics at negative bias than at positive bias as predicted from the steeper band bending at negative bias. These are all indications that both resonant and FN tunnelling mechanisms are unlikely to be dominating but that does not rule them out. The large temperature dependence of g1, g3, and g5 structures (Figure 6.19) indicates the presence of thermal emissions. The J-V characteristics are drawn with the same scale showing larger current for g5 and consequently lower dynamic resistance [Figure 6.20(d)]. This consistency eliminates the thought of fabrication issues with Al_2O_3.

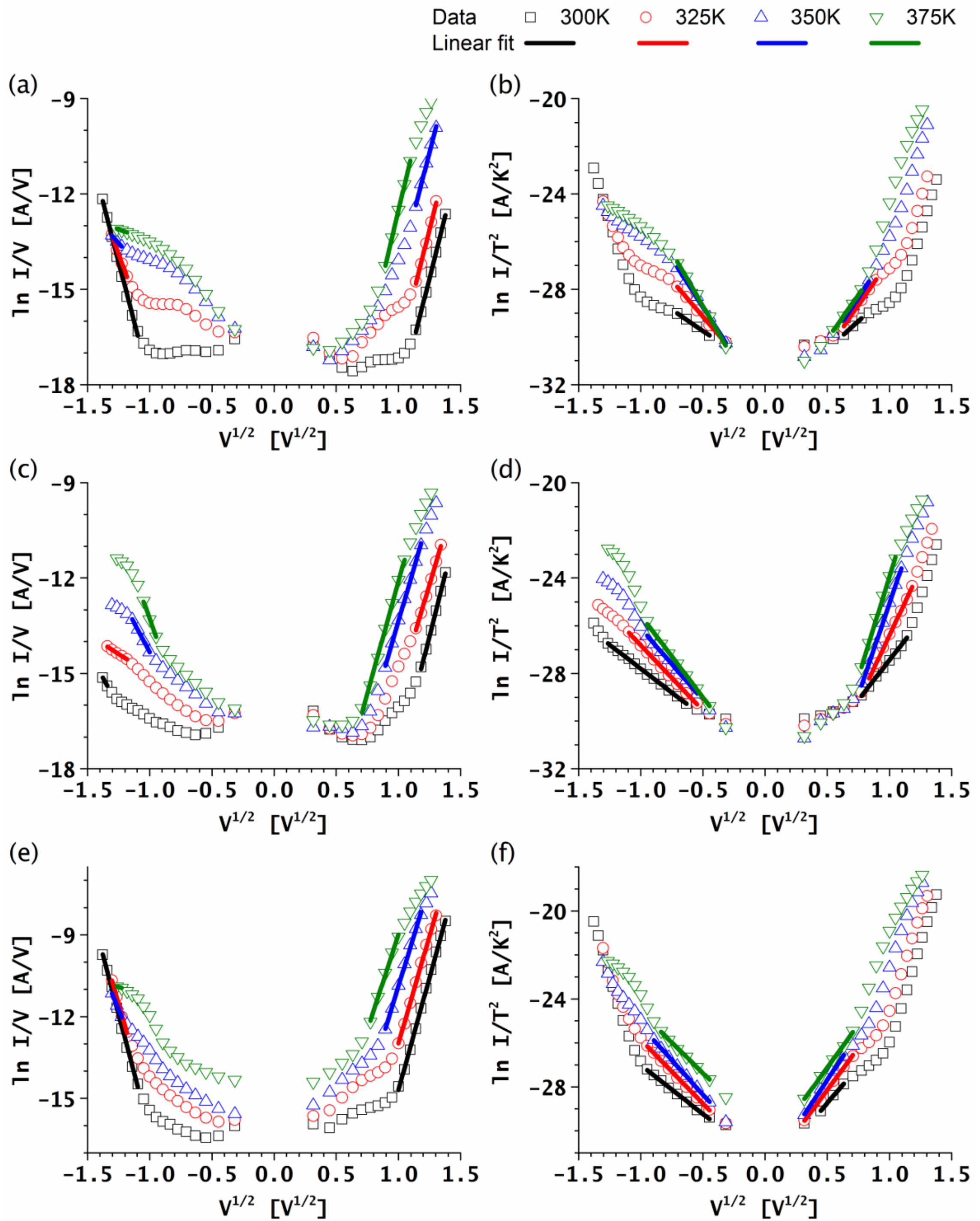

Figure 6.20 PFE (a, c, e) and SE (b, d, f) plots of the MIIM devices g1, g3, and g5 at 300, 325, 350, and 375 K.

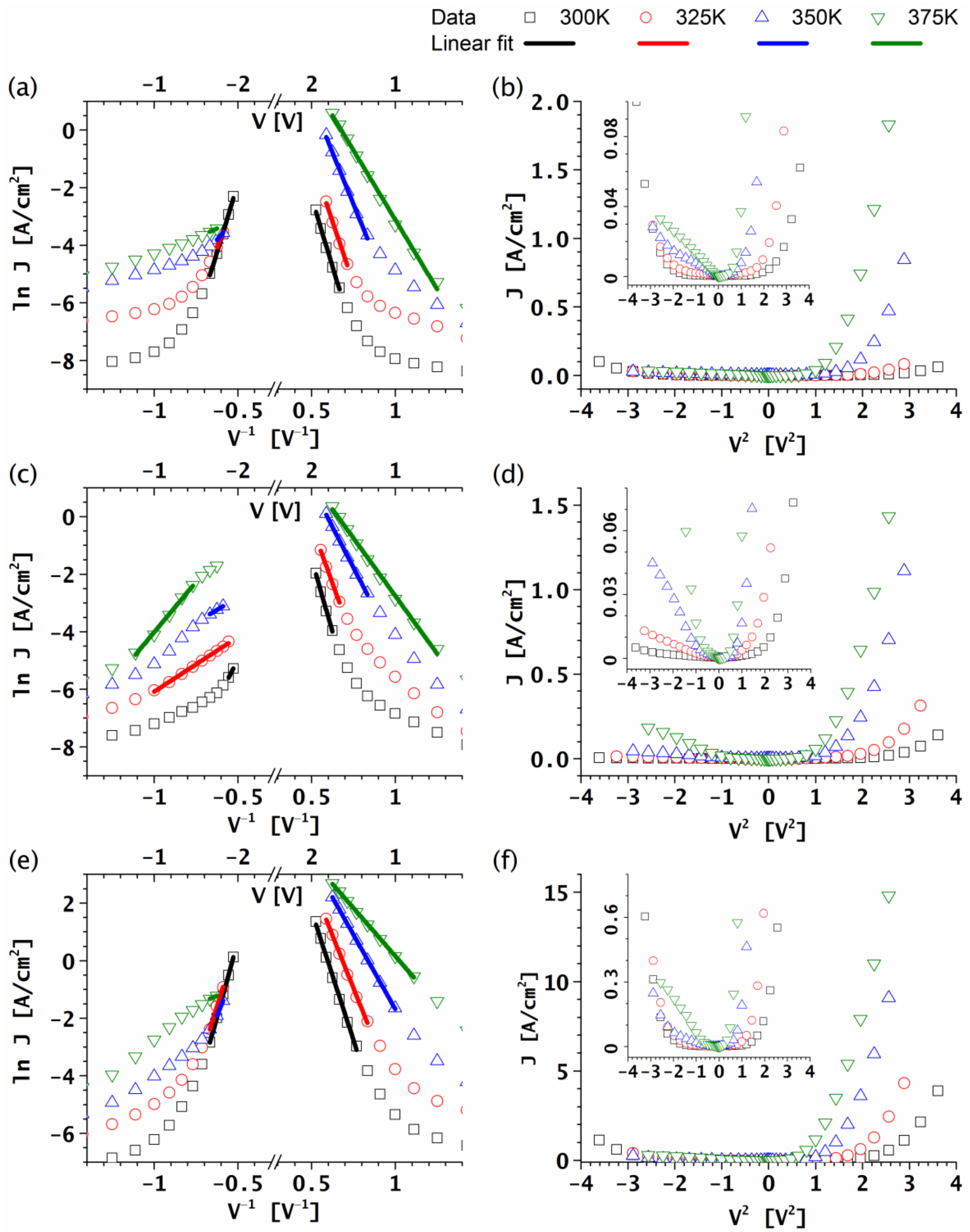

Figure 6.21 TAT (a, c, e) and SCL (b, d, f) plots of the MIIM devices g1, g3, and g5 at 300, 325, 350, and 375 K.

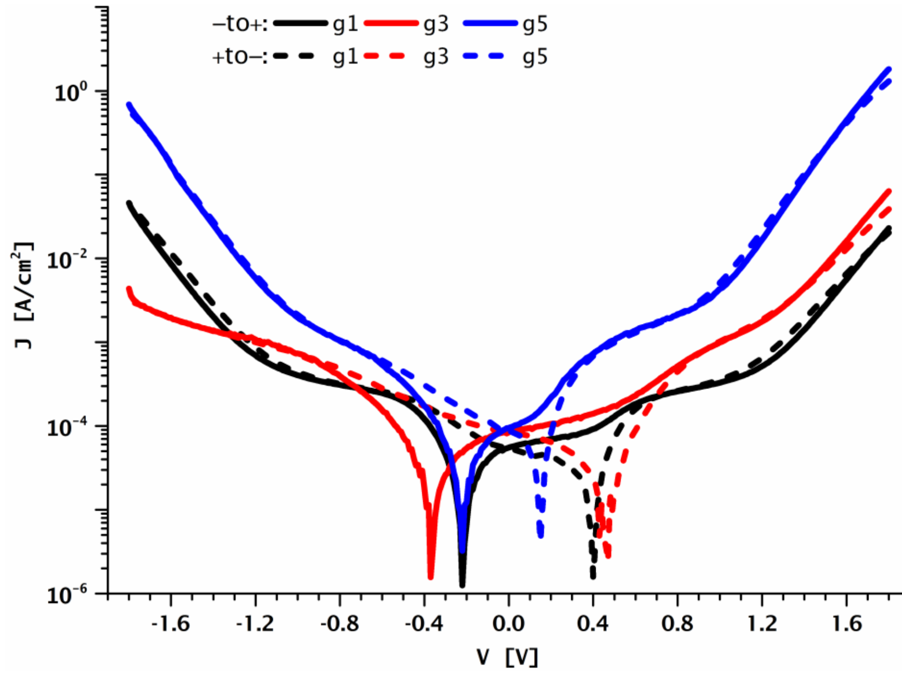

Figure 6.22 J-V characteristics of g1, g3, and g5 devices measured at negative sweep from maximum positive voltage to maximum negative voltage (+to-) and positive sweep from maximum negative voltage to maximum positive voltage (-to+).

The energy level for the trap depth of Ta_2O_5 can be extracted using different methods and could lead to different values depending on the growth conditions of the oxide. Extracting it from the J-V measurements, 0.7 eV was reported for 5.7 nm ALD deposited Ta_2O_5[153] whereas 0.58 eV was reported for 100 nm electron beam evaporation. 0.8 eV was reported using thermally stimulated current method, 2.2 eV using photoluminescence method for 100 nm CVD deposited Ta_2O_5,[154] and 1.5 eV using photoconductivity method for 520 and 80 nm sputtered Ta_2O_5.[155] As compared to these reported values, a trap depth of 1.2 eV extracted using PFE and SE plots at 300 K for devices g1, g3 and g5 can be considered to be consistent and reliable. Thus, these devices can be described by PFE for V > 1 V and by SE for V < 1 V. TAT can also describe the current at V > 1.4 V at positive polarity. Space charge limited (SCL) conduction is ruled out as J-V^2 plots could not be fitted in any voltage regime (Figure 6.21).

It is thought that the oxygen vacancies in g1, g3, and g5 play a major role in the conduction mechanism. The inert nature of Au electrode results in an interface with the oxide (Ta_2O_5 or Al_2O_3) free from any native oxide. The minor oxidising nature of Cr, as compared to Al, could result in the formation of very thin native oxide so that the absorption of oxygen vacancies by the Au electrode is almost zero whereas it is insignificant by Cr. Thus, the dielectrics in these structures (g1, g3, and g5) maintain their oxygen vacancies, and the conduction mechanism in each device is dominated by thermal emissions as shown previously. On the other hand, the devices which

have Al electrodes, such as S3s and S5s, absorb a significant amount of oxygen vacancies from the dielectrics creating a layer of oxygen vacancies affecting the charge transport.

Table 6.8 The structures of this section and the previous section (6.2) showing the change in the minimum switching voltage swept at opposite polarities ΔV_{sweep} .

<table>
<tr><td>M2</td><td colspan="3">Cr</td><td colspan="6">Al</td></tr>
<tr><td></td><td colspan="5">Sput2</td><td colspan="4">ALD2</td></tr>
<tr><td>I2
I1</td><td>6T
1.5A</td><td>1.5A
6T</td><td>6T</td><td>4T
0.5A</td><td>1A
4T</td><td>4T
1A</td><td>1A
4T</td><td>4T
0.5A</td><td>4T</td></tr>
<tr><td>M1</td><td colspan="9">Au</td></tr>
<tr><td>Device</td><td>g1</td><td>g3</td><td>g5</td><td>S5s</td><td>S3s</td><td>S1a</td><td>S3a</td><td>S5a</td><td>S7a</td></tr>
<tr><td>ΔV_{sweep} [V]</td><td>0.6</td><td>0.85</td><td>0.37</td><td>0</td><td>0.1</td><td>1.37</td><td>0.92</td><td>0.89</td><td>1.35</td></tr>
<tr><td>Suggested dominating mechanism</td><td colspan="3">PFE and TAT at $V > \sim 1V$
SE at $V < \sim 1V$</td><td colspan="2">TAT</td><td colspan="4">TAT</td></tr>
</table>

Overall, the structures S5s and S3s offer excellent rectification properties with the large non-linearity and asymmetry and a turn-on voltage of 0.13 and 0.16 V for S3s and S5s respectively. The dynamic resistance is lower with S5s in the 10^8-10^9 scale, which is still very large for efficient coupling with THz rectennas. This issue can also be reduced if the Al_2O_3 and Ta_2O_5 thicknesses are reduced as much as fabrication allows whilst maintaining the necessary ratio between Al_2O_3 and Ta_2O_5 thicknesses for resonant tunnelling to occur. The dynamic resistance could also be influenced by the presence of oxygen vacancies at the metal/dielectric interface, which have substantial thicknesses as indicated by HR-TEM images (section 5.2). This becomes critical for MIM/MIIM devices with ultra-thin dielectrics. This influence could help explain the disparity between experimental and theoretical results shown in Figure 6.23. The issue could be mitigated by selecting metals of a less oxidising nature, deposition techniques of ultra-high vacuum, and modifying the ALD conditions. Another suggestion is to deposit the bottom metal, the dielectrics, and the top metal consecutively in a cluster tool without breaking the vacuum.

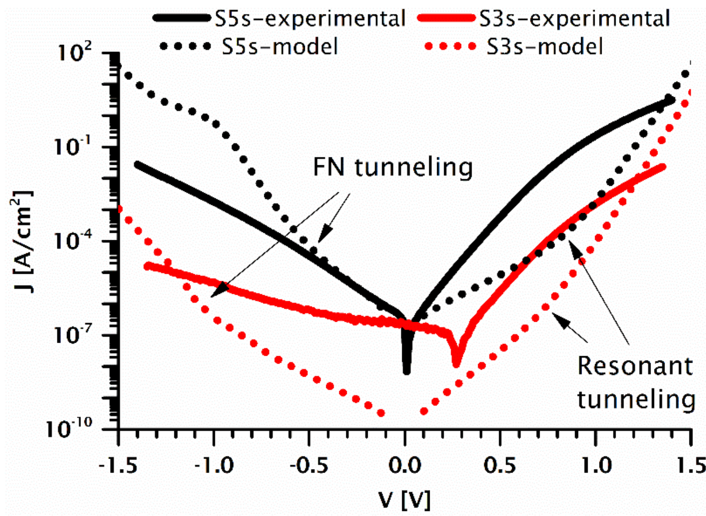

Figure 6.23 Comparison between experimental and modelled J-V characteristics for S5s and S3s devices. The onset of resonant and FN tunnelling is indicated by arrows for the modelled J-V curves.

Table 6.9 Extracted parameters from PFE, SE, and TAT plots of g1, g3, and g5 devices: ε_r trap depth ϕ_t and ϕ_{BTAT}.

			300K		325K		350K		375K	
			-	+	-	+	-	+	-	+
g1	PFE	R^2	0.9970	0.9988	0.9961	0.9964	0.9885	0.9979	0.9989	0.9998
		Intercept	-32.88	-33.99	-27.49	-32.59	-19.05	-29.69	-14.70	-28.99
		Slope	-14.98	15.47	-10.88	15.58	-4.40	15.20	-1.26	16.47
		ε_r	5.12	4.80	9.71	4.73	59.40	4.97	718.57	4.24
		ϕ_t	1.21	1.24	1.07	1.20	0.85	1.13	0.74	1.11
	SE	R^2	0.9975	0.9995	0.9985	0.9960	0.9987	0.9957	0.9975	0.9953
		Intercept	-31.54	-32.96	-32.18	-34.30	-32.81	-34.27	-33.22	-33.81
		Slope	-3.59	4.84	-6.07	7.52	-8.12	7.90	-9.03	7.44
		ε_r	22.33	12.25	7.81	5.08	4.36	4.61	3.53	5.19
		ϕ_t	1.18	1.21	1.19	1.25	1.21	1.25	1.22	1.24
	TAT	R^2	0.9961	0.9962	--	0.9945	--	0.9954	--	0.9949
		Intercept	7.68	7.26	5.09	7.57	0.52	8.21	-1.72	6.55
		Slope	19.09	-19.20	14.66	-17.18	6.93	-14.37	2.72	-9.66
		ϕ_{BTAT}	1.41	1.41	1.18	1.31	0.72	1.16	0.38	0.89

g3	PFE	R^2	--	0.9985	0.9975	0.9979	0.9987	0.9990	0.9970	0.9969
		Intercept	-25.03	-33.02	-17.57	-28.61	-21.72	-26.74	-24.39	-26.18
		Slope	-7.18	15.35	-2.54	13.13	-7.38	13.38	-11.10	14.07
		ε_r	22.29	4.88	177.56	6.66	21.09	6.42	9.32	5.81
		ϕ_t	1.01	1.22	0.82	1.10	0.92	1.05	0.99	1.04
	SE	R^2	0.9995	0.9961	0.9988	0.9990	0.9988	0.9986	0.9969	0.9990
		Intercept	-31.81	-34.11	-32.30	-37.51	-32.11	-40.40	-32.45	-40.76
		Slope	-4.01	6.67	-5.48	11.11	-6.00	15.34	-6.88	16.82
		ε_r	17.88	6.45	9.56	2.33	7.98	1.22	6.07	1.02
		ϕ_t	1.18	1.24	1.20	1.33	1.19	1.41	1.20	1.42
	TAT	R^2	--	0.9976	0.9978	0.9972	1.0000	0.9980	0.9953	0.9968
		Intercept	0.45	8.62	-2.29	7.82	-0.99	6.70	2.97	5.28
		Slope	10.88	-20.18	3.80	-16.21	3.61	-11.29	6.99	-8.03
		ϕ_{BTAT}	0.97	1.46	0.48	1.26	0.46	0.99	0.72	0.79
g5	PFE	R^2	0.9979	0.9988	0.9946	0.9987	0.9954	0.9975	--	0.9971
		Intercept	-33.42	-31.20	-31.57	-28.77	-25.46	-25.75	-12.51	-23.01
		Slope	-17.20	16.50	-16.03	15.79	-10.97	14.87	-1.28	14.02
		ε_r	4.86	5.28	5.59	5.77	11.93	6.50	882.86	7.31
		ϕ_t	1.23	1.17	1.18	1.11	1.02	1.03	0.69	0.96
	SE	R^2	0.9970	0.9941	0.9995	0.9971	0.9995	0.9981	0.9982	0.9984
		Intercept	-31.46	-32.06	-31.66	-31.96	-31.49	-31.93	-30.16	-31.01
		Slope	-4.45	6.66	-5.81	7.64	-6.27	8.50	-5.56	7.78
		ε_r	18.16	8.11	10.65	6.15	9.13	4.97	11.62	5.93
		ϕ_t	1.18	1.19	1.18	1.19	1.18	1.19	1.14	1.16
	TAT	R^2	0.9996	0.9965	0.9993	0.9985	--	0.9997	--	0.9996
		Intercept	11.25	10.69	10.15	10.02	6.99	8.68	0.52	6.85
		Slope	21.14	-17.92	18.81	-14.63	14.26	-10.36	2.78	-6.69
		ϕ_{BTAT}	1.75	1.56	1.61	1.37	1.34	1.09	0.45	0.81

6.4 Effect of area scaling

Rectification in rectennas converts the electromagnetic energy to DC power when the integrated MIM/MIIM diodes are scaled down to an active area as small as possible in order to increase the cut-off frequency as much as possible. The scaling down effect on rectifying performance is investigated on diodes of area: 20×20, 50×50, 100×100, 150×150, 200×200, 250×250 μm^2.

The J-V characteristics of different devices of Sput2 dielectrics (presented in previous sections) of different lateral area are shown in Figure 6.24. Current generally reduces as the active area is minimized which can be explained by the resistivity of the electrodes which increases with thinner cross-sectional area (A) of the metal lines having the same length (l) as described by the following relation:

$$R = \rho \frac{l}{A}$$

where ρ is the metal resistivity: 2.44, 2.65, and 100 for Au, Al, and Cr.

The drop in non-linearity as the active area is reduced can be indicated from the smaller J-V slopes. This is more obvious with g1 and g5 devices of Cr/Au electrodes than of c3 device of Al/Au electrodes, as the current in these devices is impeded by larger resistivity following the more resistive metal (Cr). The results are in agreement with another study[2] showing significantly lower nonlinearity and higher zero-bias impedance with Cr/Au MIM structures fabricated at nanoscale as compared to those at microscale. This consideration becomes crucial for nanostructures to keep good non-linearity, and thus metals of less resistivity are desired for THz rectifiers.

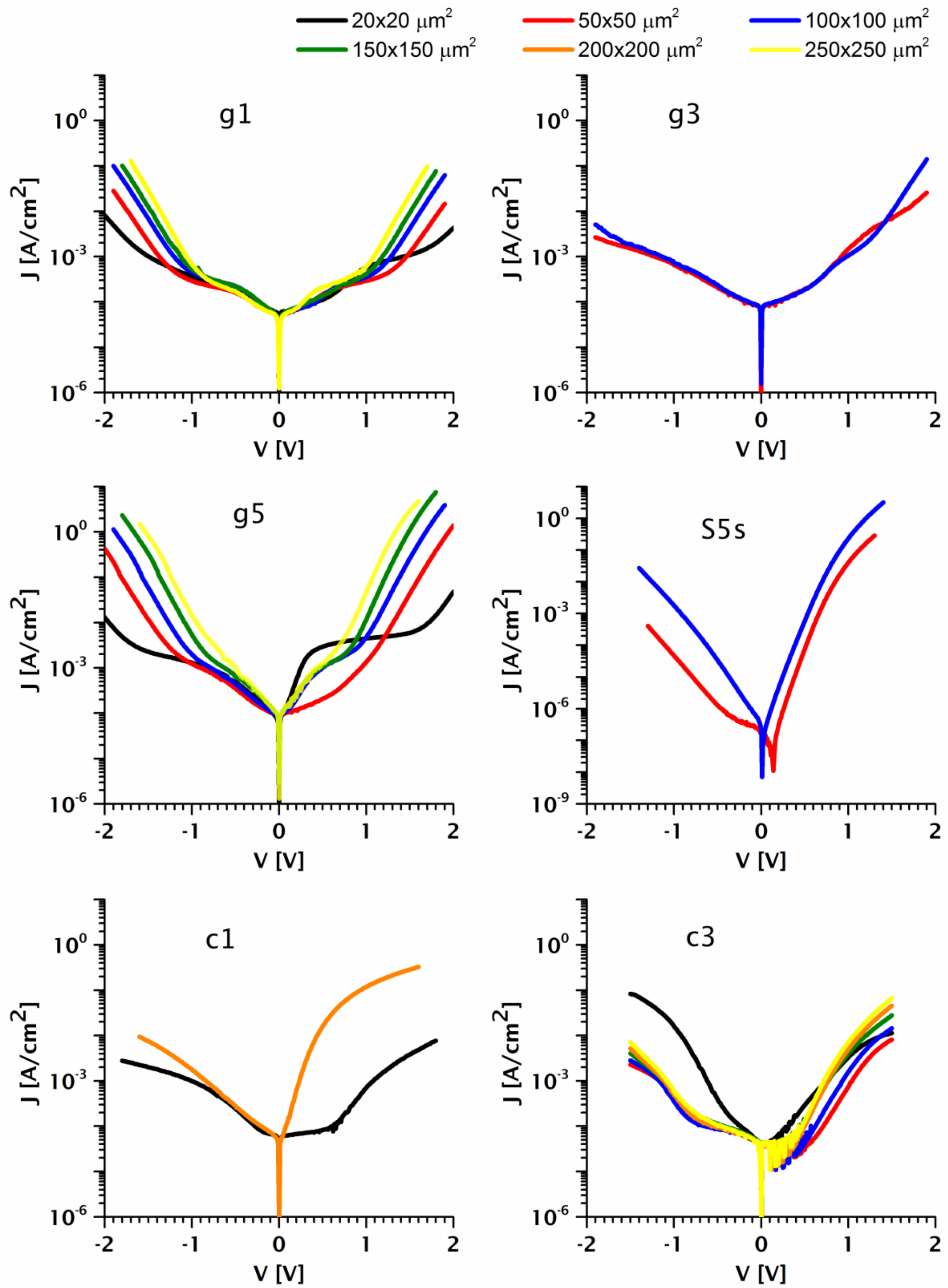

Figure 6.24 The J-V characteristics of different MIIM structures varying their lateral area.

6.5 Summary

In summary, this chapter shows state-of-the-art devices with enhancement in rectifying performance. It gives better understanding of thickness-tuning, fabrication conditions, and defect mechanisms. Conduction mechanisms in individual Al_2O_3 and Ta_2O_5 are studied showing the dominance of tunnelling in the former and undesirable thermal emission in the latter. However, engineering the structure using both oxides gave strong indications for resonant tunnelling with consistency in thickness varying. Motivated by the necessity to eliminate the native oxide issue, Au was used despite the smaller chance of resonant tunnelling as indicated from modelling. Fabricating the same structure by changing the oxide growth conditions lead to understanding the defect-related mechanisms with indications of tunnelling mechanisms in parallel. A fabricated device showed very good rectification at the lowest achieved turn-on voltage of 0.13 V. The trap assisted tunnelling equation fits well for a voltage regime around 1 V. The attempts to fabricate the same structures using Cr for top electrode could not be easily fabricated as those using Al, and those few devices which were successful had drastically different characteristics. This is further indication that the native oxide and oxygen vacancies play a major role in the conduction mechanism of MIM/MIIM of ultra-thin dielectrics. This also explains why it was never possible to match the experimental with the modelled J-V characteristics. A decrease in current at both polarities consistent with the area down-scaling is experimentally observed. This can be thought of as the same diode with the same rectifying performance in parallel to shunt resistor dissipating the current. This shunt resistor leading to lower non-linearity would decrease the responsivity for THz rectenna harvesters and detectors and could be critical for nanostructures. This issue can be tackled by increasing the film thickness and linewidth away from the active area.

7. Towards integrating the nanostructures in THz rectennas

This chapter concerns the design of 0.14/2 THz rectennas, with the efficiency considerations and area required for efficient coupling with antenna patches. The challenges in nanofabrication and the device structure are also described.

7.1 Fabricating the 0.14 THz rectennas

A fabrication scheme devised for THz rectennas using double dielectric structures with the photolithographic lift-off process. The design and the process flow were done based on the available facilities and simulations for the highest return loss of rectennas, which represents power reflected from the antenna.

Metal lift-off process was used to pattern the different layers of the rectenna structure on glass substrates using a designed photomask. Corning glass substrates were cleaned with Decon-90, acetone, isopropanol, and blown dry with Nitrogen gun. The metals of the top and bottom electrodes were deposited using thermal evaporation. The oxides were deposited using the atomic layer deposition ALD1.

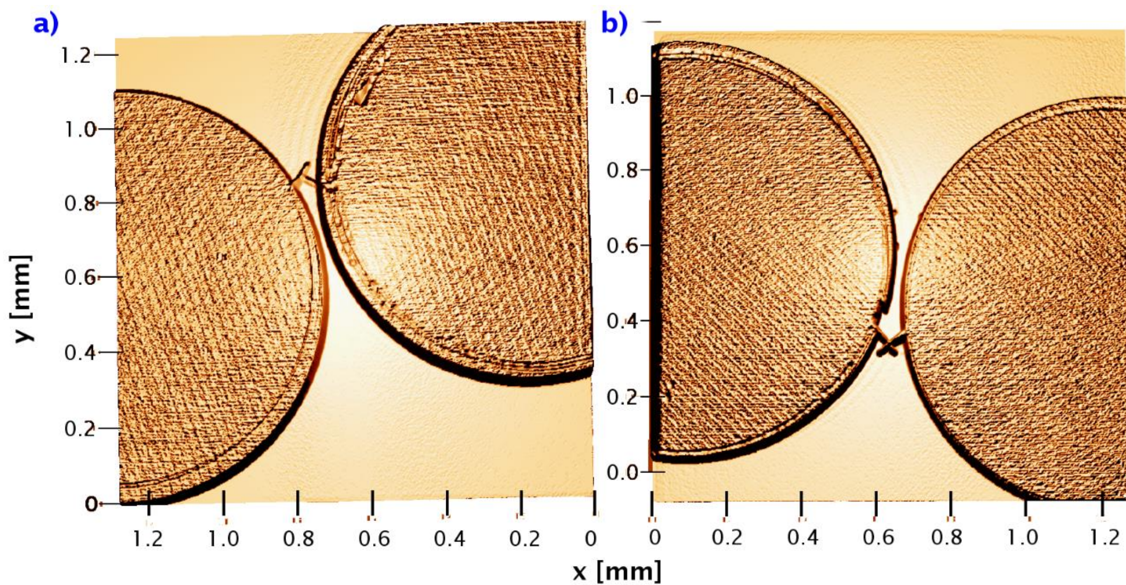

Figure 7.1 Confocal microscope images of selected fabricated rectenna circular patches with integrated rectifiers of an active area equal to 2µm×2µm (a) and 6µm×6µm (b).

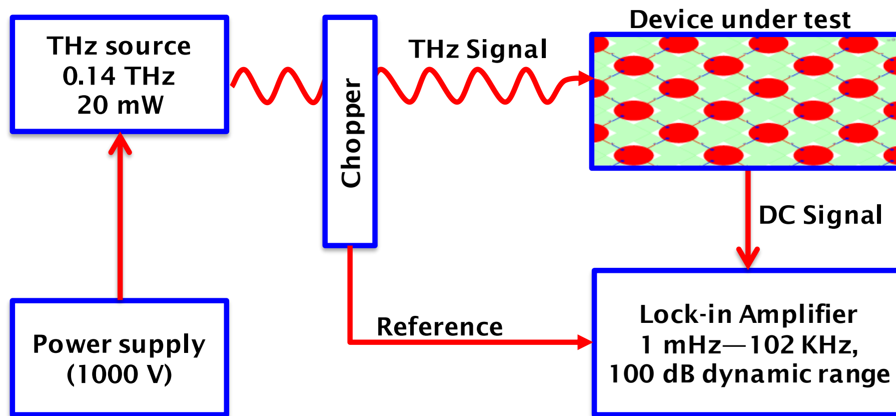

Figure 7.2 The set-up used to test the rectenna devices.

Rectenna devices were tested using a 0.14 THz generator as illustrated in the schematic (Figure 7.2) where the THz-induced current can be measured in the sub-nA or pA range. and no signal could be detected. We should be. The main issue was that the smallest possible diodes (2μm×2μm), successfully fabricated, are still relatively large to respond at THz frequencies.

7.2 Devising the 2 THz rectenna array[1]

The devised structures in this section show results based on simulation and could not be experimentally fabricated.[2]

The relatively high frequency of operation for THz rectennas leads to challenges not only in the rectification process but also in the fabrication of the nano rectifiers required for efficient THz-to-DC conversion. Infrared or optical antennas have not been extensively investigated before, since they require complicated fabrication facilities like the electron beam lithography (EBL). EBL patterning capability exceeds the two-micron limit of the optical lithography (Figure 3.5) making it possible to pattern sub-micron features of 100 nm. Patterning nano-scale rectifiers using EBL offer further advantages. It is maskless lithography technique with high resolution and good line width control. Nevertheless, it is expensive and suffers from very low throughput.

---

[1] The design was sent to the collaborating institutes in Taiwan for fabrication: National Tsing Hua University (NTHU) and National Nano Device Laboratories (NDL). The facilities in this section are those offered by these collaborators in contrast to previous sections.

[2] The project was ended by NTHU and NDL on 9th Jan 2018 due to funding issues.

7.2.1 Material choice

The available facilities allow the deposition of the following materials: Al_2O_3, Ta_2O_5, HfO_2, Ni, Al, Ti, W. The oxides can be sputtered with a minimum thickness of 2 nm. Ni (4.9 eV) offers excellent conductivity, where a thickness of 50 nm for the antenna patches is sufficient to avoid the skin depth at 2 THz. However, it is not favourable in resonant tunnelling structures due to its large work function. Thus, Ti of work function as low as 4.1 eV is chosen to maximize the dissimilarity, which is useful for FN tunnelling. Its high resistivity is still endurable in the application of micro-watt rectennas and can be neglected as compared to the >10 kΩ expected overall diode resistance obtained experimentally with more conductive metals. Ni, of excellent conductivity, is chosen as the bottom electrode for the rectifier and for the circular patches. Furthermore, it is possible to have high selectivity with these metals using proper etchants. There is a trade-off between the Ta_2O_5 and Al_2O_3 in terms of the domination of tunnelling and thermal emissions. Ta_2O_5 is chosen due to its large electron affinity resulting in steeper band bending describing tunnelling mechanisms and as it was intensively studied in this research. This makes rectification at lower turn-on voltage possible unlike Al_2O_3 and HfO_2. Thermal emissions can be reduced, and tunnelling mechanisms would be driven towards domination with the minimum possible ALD thickness of 2 nm. The bottom metal thickness needs to be kept as low as possible (50-70 nm) to reduce surface roughness and avoid short circuit between the electrodes which might happen at the edges. The recommended thickness for some metals taken as 5 skin depths to ensure high conductivity at 0.14 and 2 THz (Figure 7.3). 1000 nm is the maximum thickness possible to achieve. The recommended thickness for the available EBL is 300 nm to achieve 100 nm linewidth safely, and the metals which can be deposited are underlined (Ni, Al, W, and Ti). Based on these considerations and the fabrication capability, the rectenna structure is decided to be 50 nm thick Ti bottom metal and 300 nm thick Ni top metal.

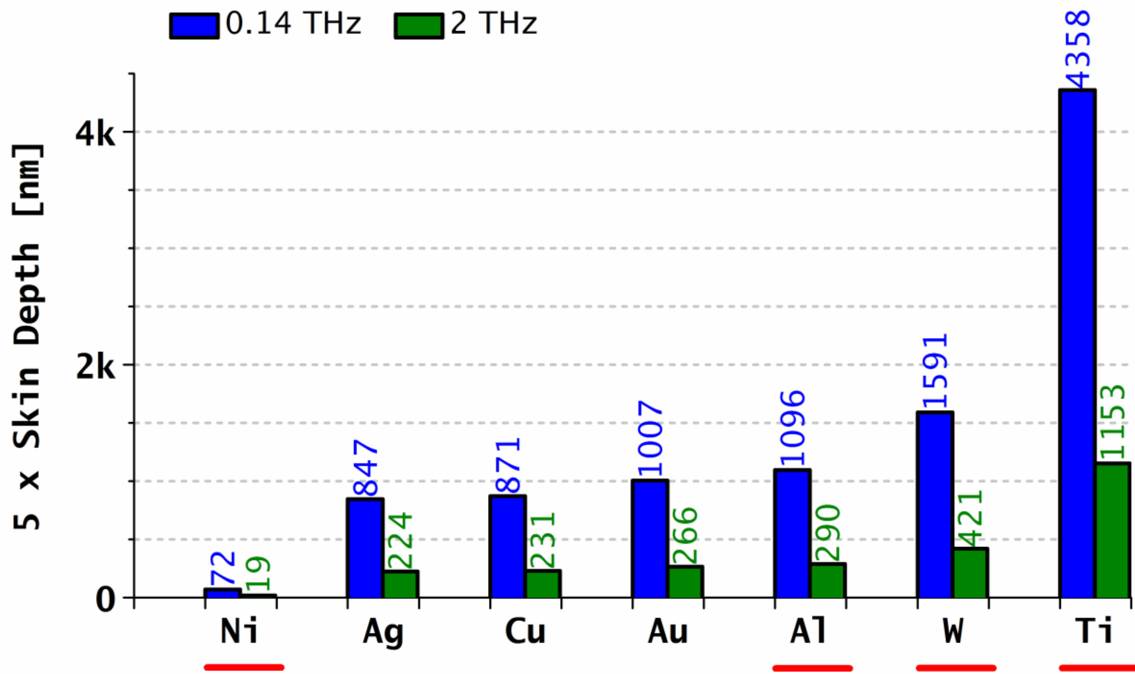

Figure 7.3 Five times the skin depth calculated using the resistivity of different metals.

7.2.2 Process flow

The fabrication of any of these tunnelling nanostructures is suggested. The dominating mechanism is based on FN tunnelling for FN2 or resonant tunnelling for the others (RT2, RT3, and RT4).

Table 7.1 Device structure

Structure	Bottom contact	Thickness (nm)		Top contact
		Al_2O_3	Ta_2O_5	
FN2	Ti	—	2	Ni
RT2	Ti	0.5	2	Ti
RT3	Ti	0.5	3	Ti
RT4	Ti	0.5	4	Ti

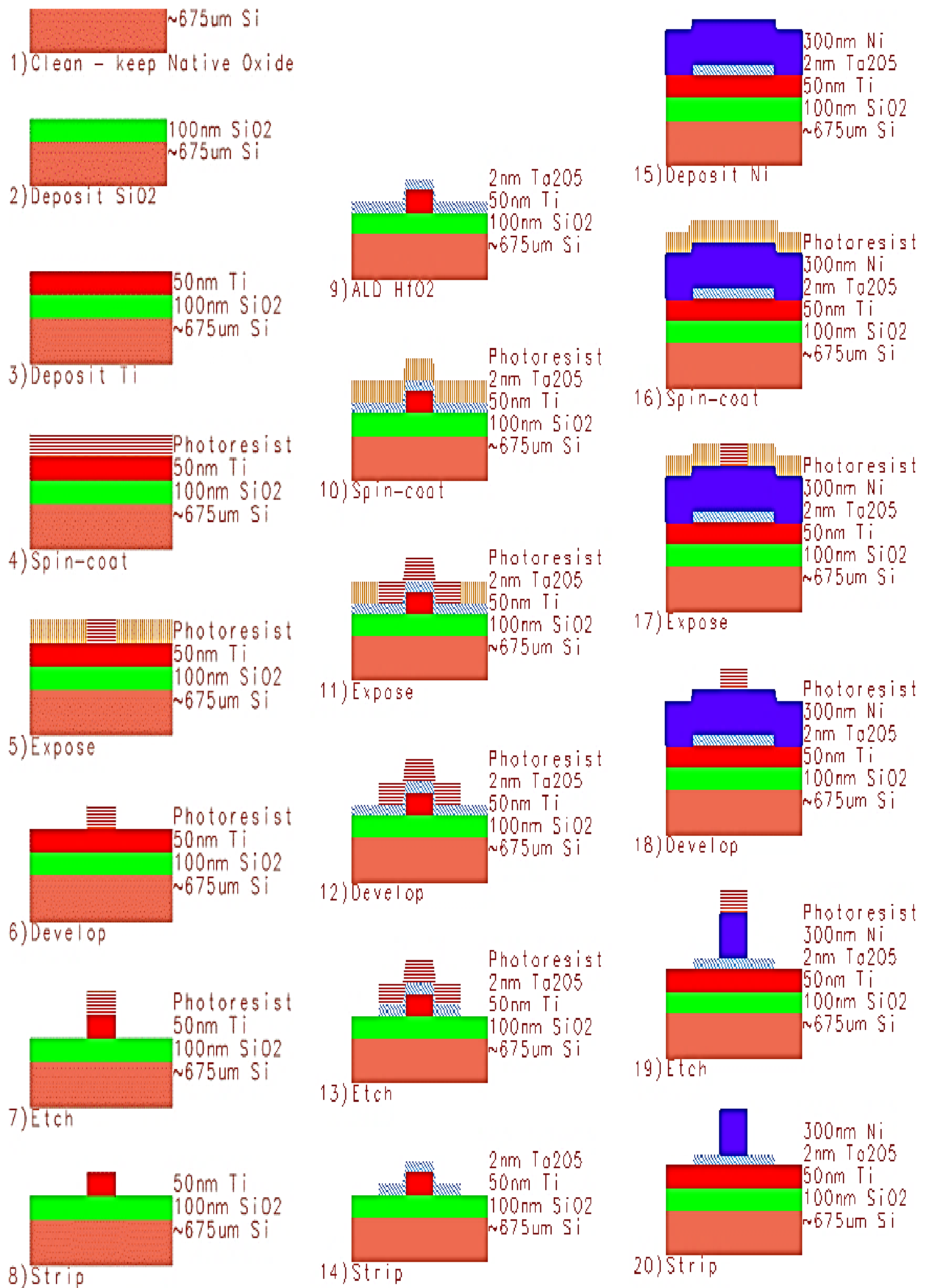

Figure 7.4 The process flow for patterning the layers of rectenna array FN2 at the cross-section of the integrated rectifier.

The process flow for the metal lift-off using e-beam lithography of the device FN2 is described in Figure 7.4. Steps 1-2 represent the standard cleaning procedure for the Si substrate. 100 nm thick SiO_2 is deposited over the whole surface of Si substrate to ensure proper isolation of the device. This is followed by the deposition and patterning of 300 nm thick Ti metal, 2 nm thick Ta_2O_5 oxide is deposited and patterned, and 300 nm thick Ni metal. The bottom metal needs to be deposited with the lowest possible surface roughness. The metal lift-off of the bottom and top metals is described by steps 3-8 and 15-20 respectively. The metal is deposited followed by spin coating the photoresist, exposing, developing, etching (with specific etchants for Ti or Ni), and stripping to get the pattern shown in Figure 7.5(a,c). Ta_2O_5 is then deposited allover the surface of the patterned bottom metal. The oxide is then patterned by spin coating the photoresist, exposing, developing, etching with specific etchants, and stripping to get the pattern shown in Figure 7.5(b). The other devices (RT2, RT3, and RT4) are fabricated using the same steps, using Ni instead of Ti for the bottom electrode, depositing additional 0.5 nm thick Al_2O_3, and varying the thickness of Ta_2O_5 accordingly.

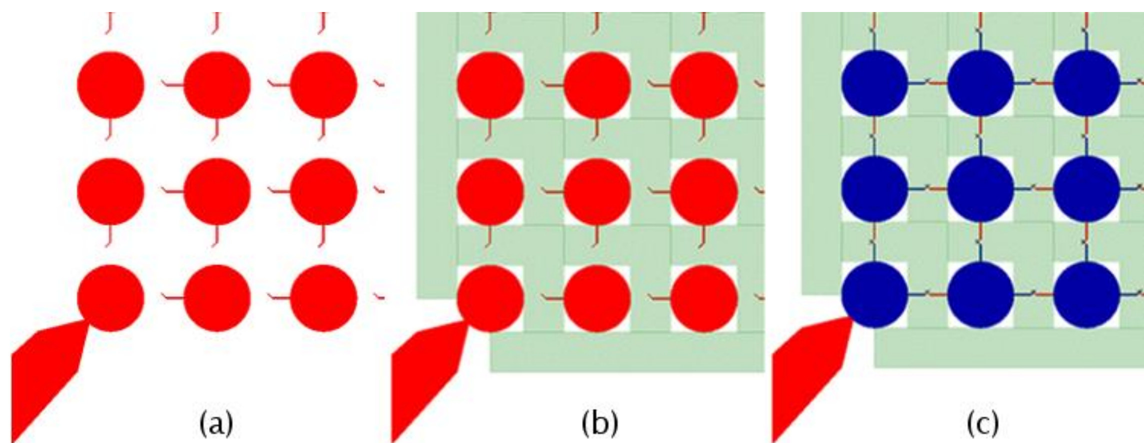

Figure 7.5 Top view of the patterned structure: a) the bottom electrode (red) at the corner of the array with the connection b) the oxide (green), and c) the top electrode (blue).

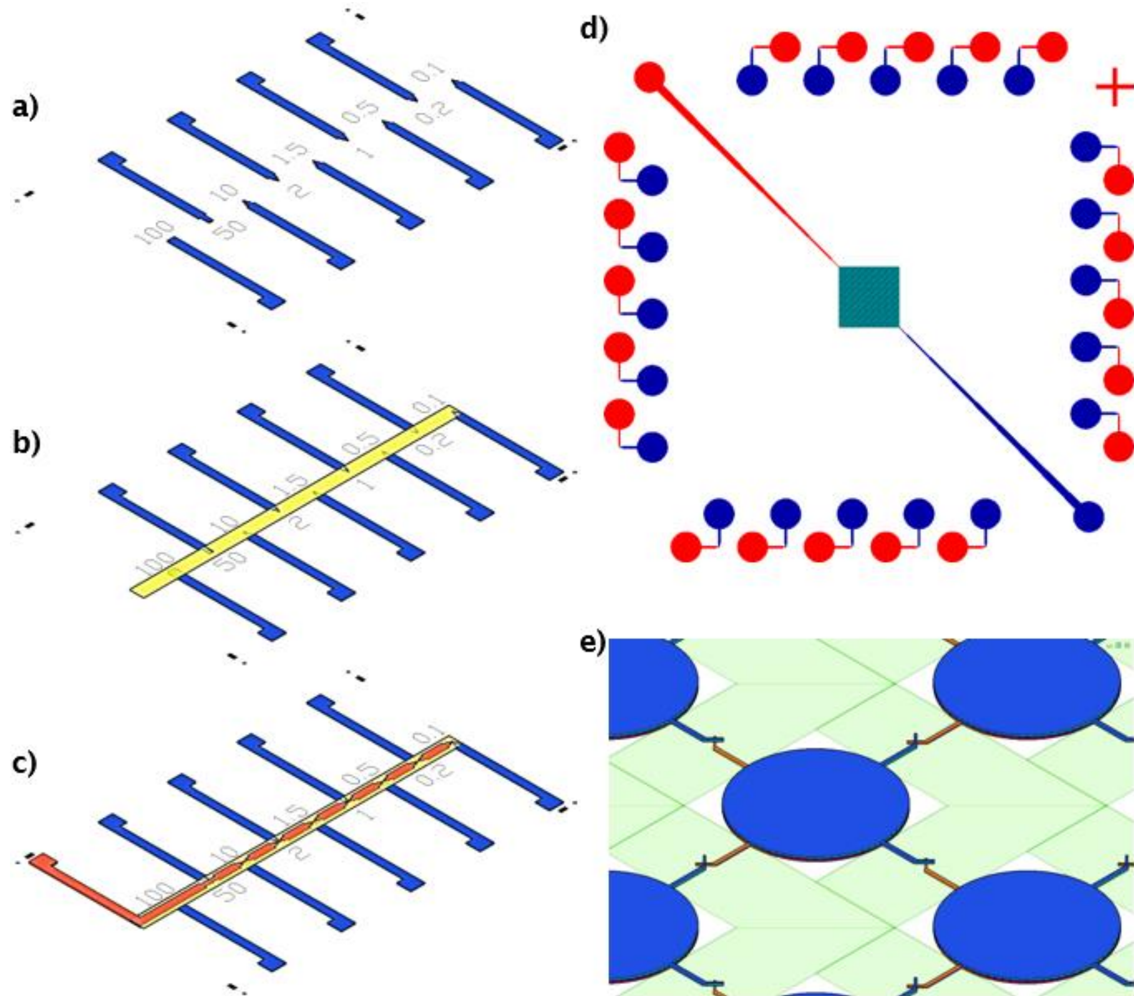

Figure 7.6 Fabricating the rectifying nanostructures of varying active area between 100×100 nm^2 and 100×100 μm^2: a) the bottom electrode (blue), b) the oxide(s) (yellow), and c) the top electrode (red). d) The rectenna array (of 14×14 mm^2 total actual size) connected to two metal lines for measurements and surrounded by rectifying nanostructures for dc measurements. e) Zoomed in image of the rectenna array.

7.2.3 Modelling the rectifying performance

The band diagrams of four different structures is shown in Figure 7.7. THz rectennas need a turn-on voltage as low as possible for efficient operation. At 0.2 V, the band bending of FN2 is not sufficient for FN tunnelling, and direct tunnelling would dominate at both polarities. This is would lead to poor rectification for the structures but might be sufficient to detect a signal. An additional 0.5 nm Al_2O_3 would offer resonant tunnelling at +0.56 V. Increasing Ta_2O_5 thickness to 3 and 4 nm would bring a bound state at smaller turn-on voltages of 0.29 and 0.2 V respectively. This would, however, increase the dynamic resistance.

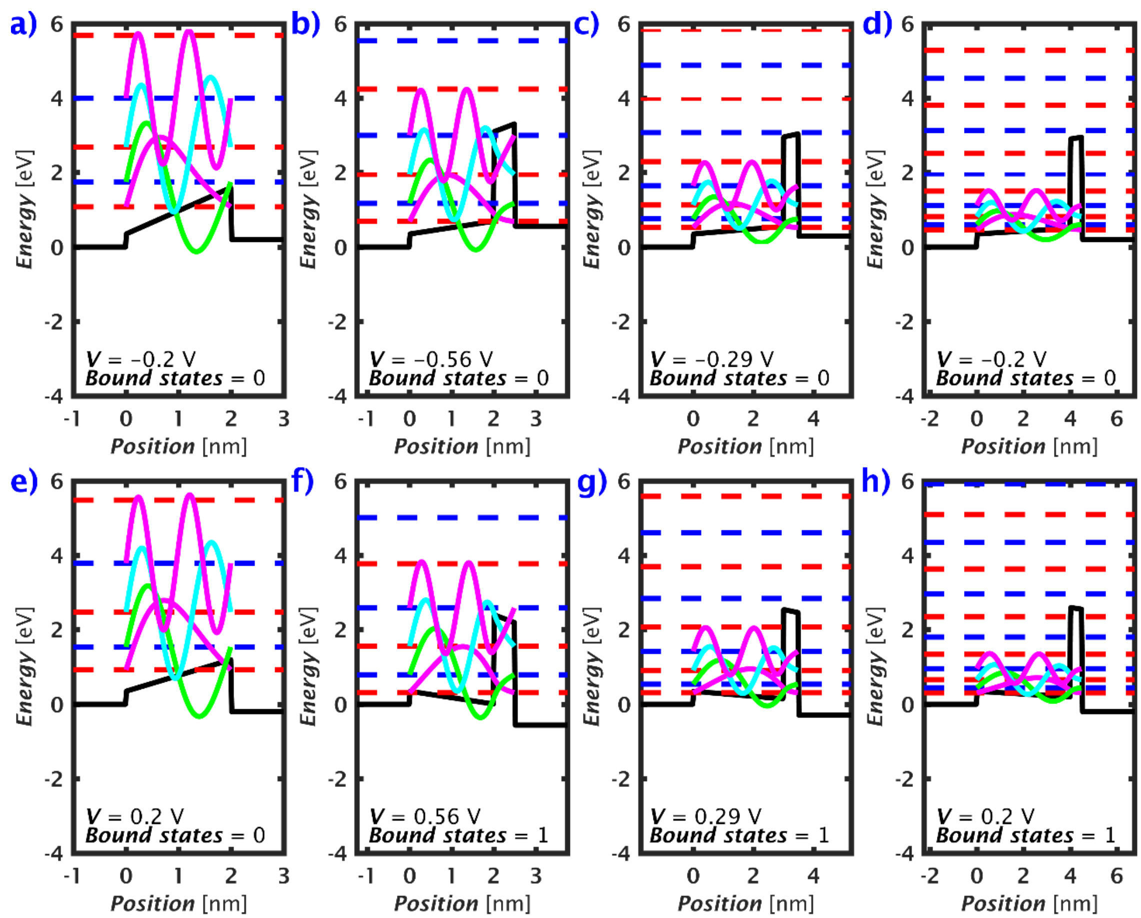

Figure 7.7 Conduction band diagrams simulated using the in-house model (described in section 4.11).

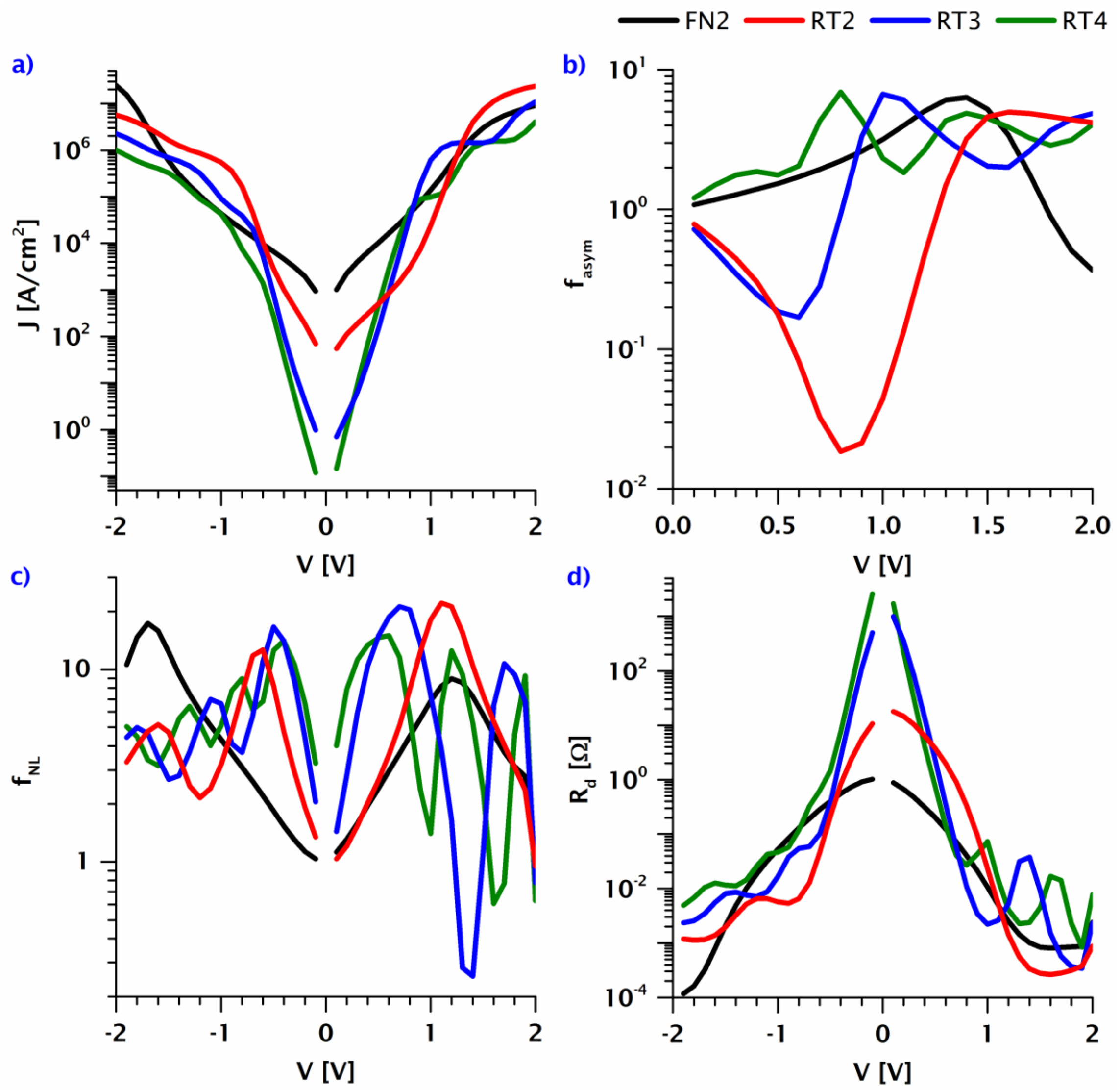

Figure 7.8 The rectifying characteristics of FN2, RT2, RT3, and RT4 structures simulated using the in-house model (described in section 4.11): the J-V characteristics (a), the asymmetry (b), the non-linearity (c), and the dynamic resistance (d).

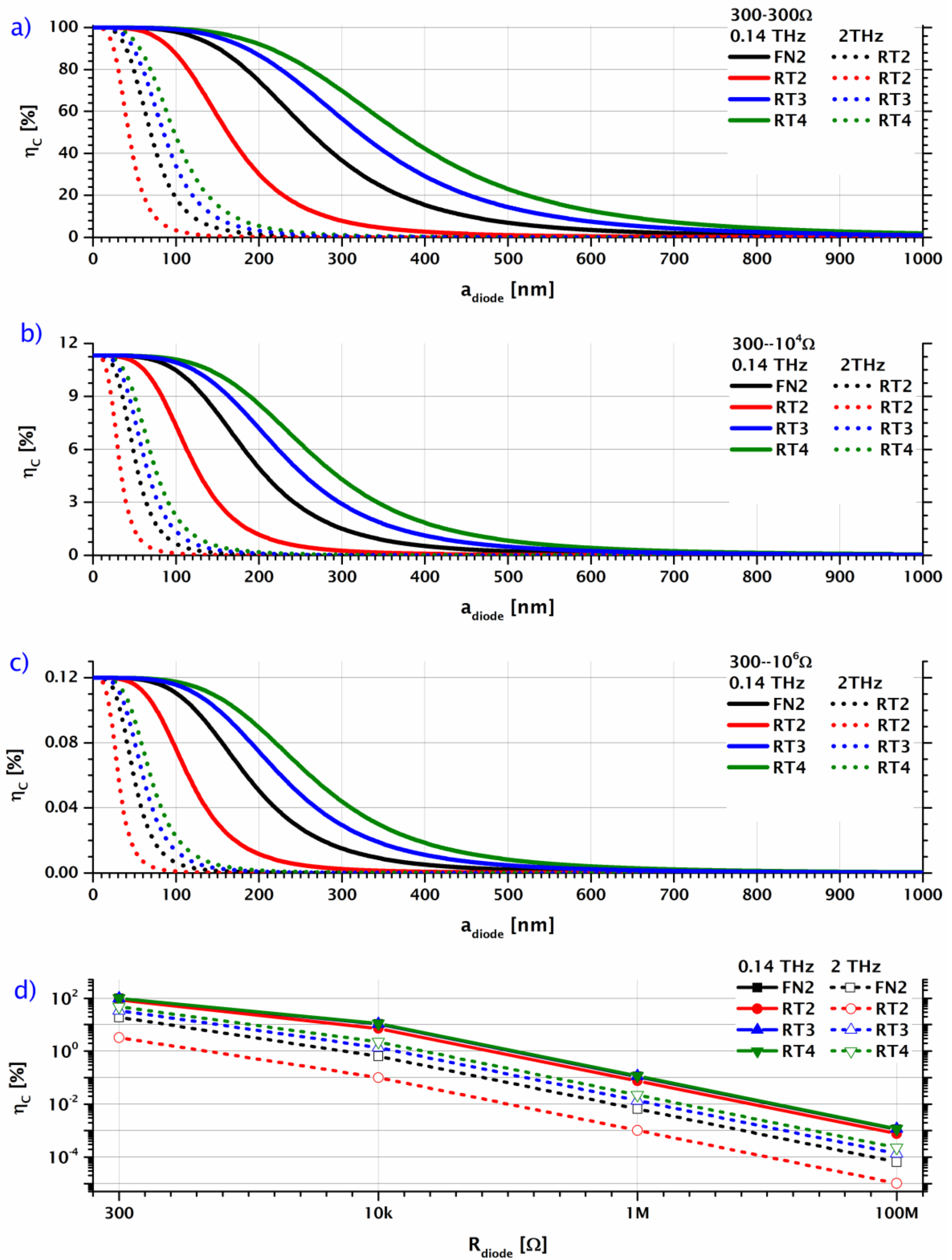

Figure 7.9 The diode-antenna coupling efficiency assuming an antenna impedance of 300 Ω. Calculations are based on equation (2.2) described in section 2.4.1.

The rectifying performance is studied in each structure, where the coupling efficiency is related to the materials used, their thicknesses, and the frequency at which the rectenna array operates. Considering the diode as a square of side a_{diode} and an area equal to a_{diode}^2, the efficiency drops

considerably with a_{diode} [Figure 7.9(a, b, c)]. This efficiency to a_{diode} drop increases with 2 THz as compared to 0.14 THz making the use of nanostructure (a_{diode} < 100 nm) essential to get measurable conversion efficiency. Assuming the impedance of the antenna patches to be 300 Ω (expected to be several hundreds[156] or less at THz[157]), the maximum achievable efficiency drops as the antenna-diode impedance mismatch is increased. It drops from 100% with zero mismatch [Figure 7.9(a)], to 11.5% with a 10^4 Ω diode impedance [Figure 7.9(b)], and to 0.12% with 10^6 Ω diode impedance [Figure 7.9(c)]. This is further illustrated in Figure 7.9(d) which shows an exponential relation between the efficiency and the diode impedance. 10^6 Ω of a good rectifier is realistic with the dynamic resistance of the devices fabricated in this work and the potential to be reduced to 10^4 Ω is put forward. The diode structure plays a major role as well. While FN2 performs better than RT2, the resonant tunnelling structures RT3 and RT4 of larger resonance probability are theoretically more efficient when integrated in THz rectennas.

8. Conclusions and suggestions for further work

Dielectric-based rectifying structures have been investigated thoroughly in this research, and THz energy harvesters have been devised. An update is given on the ongoing research on energy harvesters starting from those successful at radio and microwave frequencies to the attempts done at THz. Their applications are specified and the challenges in fabricating suitable rectifying nanostructures are discussed. These energy harvesters are still under research with only few successful figures so far not exceeding 1% efficiency. No model exists to simulate the overall characteristics of a rectenna. Instead, the rectenna components, the antenna and the rectifier are simulated separately taking into consideration the efficiency and the technological considerations for coupling them.

The antennas were simulated separately for maximum harvesting at 0.14 and 2 THz taking into consideration the materials used and the available fabrication facilities. An in-house model was used to simulate the rectifying characteristics which helped devising the structures towards maximum resonance. However, the characteristics of fabricated devices could not be matched with the model. The model calculates the current based on pure tunnelling mechanisms, whereas in real devices charge trapping could occur. This is evident from the temperature dependence of the rectifying characteristics of the fabricated devices. Trap assisted mechanisms have been indicated by fitting their equations, however, not ruling out tunnelling. In fact, strong indications for resonant tunnelling have been discussed and put forward. The devices have been optimised according to the individual layer thickness of the oxides and the metals chosen for the electrodes. The growth conditions of the oxides, using RF sputtering and different atomic layer deposition conditions, have shown significant impact on the rectifying characteristics. The growth of native oxide layer has been shown on HR-TEM images, surprisingly at the bottom of the top electrode. Fabrication was enhanced for better homogeneity and less surface roughness. An initial attempt was done to fabricate 0.14 THz rectenna elements, and this was a motive towards devising 2 THz rectenna arrays.

Two fabricated devices have shown outstanding rectifying performance at a turn-on voltage close to zero making them favourable for integration into THz rectennas. For MIIM devices S3s and S5s respectively, sufficient rectification occurs at V_{ON} of 0.13 and 0.16 V, where the non-linearity increases towards 0.42 and 0.7 V, increases and the asymmetry towards 10^3 and 10^2 scales at larger voltages. These devices, as all other devices in this work, suffer from a large dynamic resistance exceeding 1 MΩ. It is believed that this can be significantly lowered if the discussion on the results of this work are taken into consideration. This work provides a framework for optimising the structures according to the availability of materials and the methods of depositions.

More advanced techniques in the emerging nanotechnology would indeed improve the performance. For instance, depositing at ultra-low pressure and low deposition rate helped indeed enhance the surface roughness with generally better diode performance but could not obtain perfectly flat surface. Furthermore, the material properties of the electrodes and dielectrics need experimental investigation. For instance, literature values of the work functions and the electron affinities can vary: 5.15/4.9 eV for Ti, 4.1/4.33 eV for Ni, 4.2/4.4 eV for Al, 3.75/383 eV for Ta_2O_5, etc. The knowledge of these parameters according to specific deposition conditions helps in optimising the structures. It helps in understanding the dominant mechanism, which becomes not easily distinguishable using ultra-thin dielectrics. These, in addition to intensive high-resolution imaging are noteworthy to have full understanding of what is exactly being fabricated especially at the interface.

A trade-off between different parameters have been observed and discussed. The rectification capability of a diode is manifested in its nonlinearity (3 considered sufficient in this research) and its asymmetry (any small asymmetry can be sufficient for rectennas). Generally, diodes of good non-linearity require increasing Ta_2O_5 thickness which results in larger dynamic resistance. Similarly, those of low dynamic resistance exhibit very low non-linearity. Double dielectric structures have shown much better non-linearity and asymmetry which peaks with resonant tunnelling. Resonant tunnelling structures can additionally serve to enhance the coupling efficiency. Scaling down to 100 nm and below becomes essential for efficient coupling with antennas. However, this would worsen the non-linearity. A good design would involve scaling the area as much as possible to a limit where the non-linearity is sufficient for rectification. The fabrication of THz rectenna arrays using the conventional contact photolithography is not possible. The tunnelling nanostructures needed require using more advanced lithography techniques such as the electron beam lithography which is expensive. The ALD becomes necessary for resonant tunnelling nanostructures requiring ultra-thin oxides as thin as 0.5 nm with good homogeneity and pinhole-free layers. Any native oxide needs to be eliminated to minimize the dynamic resistance and ensure well defined interfaces with the metal. However, it is believed that this unwanted layer can serve to prevent the short circuit in the diodes of sandwiched oxides as thin as one nanometre.

Further work is needed to match the model with the experimental. Not much matching is reported in the literature, and the repeatability of any successful device becomes questionable when it comes to devices of extremely low current. This makes them sensitive to any variation in the deposition environment and any parameter involved in the fabrication process. This was evident from the significant change in the rectifying characteristics when the purge/pulse times were altered. Defects in the oxide bulk, in the form of oxygen vacancies, bring further complication to

the diode performance. These defects are thought to be serving as transport sites or stepping stones influencing the tunnelling mechanisms through the oxides. The reliability of CST simulations at THz cannot be examined with the lack/absence of experimental work on THz antennas. Designing the antenna needs to consider having it sufficiently broadband so that it picks up large range of THz frequencies. It must be low-loss so that it is able to transform the induced current in the patches into voltages large enough to turn on the rectifying diode.

Rectennas have been used successfully for radio and microwave to DC conversion. There have been some interesting attempts to demonstrate it for IR frequency radiation up to visible. However, and due to the technological hurdles, these devices are still proof-of-concept at THz. With the emerging nanotechnology techniques needed to fabricate the rectifying nanostructures, THz/IR energy scavenging becomes possible. Resonant tunnelling nanostructures have the potential to solve the issue of rectennas at THz frequencies taking the advantage of their easier integration and their ultra-fast transit time. Both resonant tunnelling nanostructures and THz antennas have not been extensively investigated before because of the complicated fabrication facilities they require such as EBL. This research provides further understanding on how to optimise the rectifying component of THz scavengers for better coupling efficiency.

References

[1]Y. Huang and S. Hall and Y. Shen, UK Patent No. 2484526 (A) (2012).

[2]B. Berland, NREL Subcontractor Final Report, ITN Energy Systems, Inc., Littleton Report No. NREL/SR-520-33263, 2003.

[3]E. H. Hauge and J. A. Støvneng, Reviews of Modern Physics **61** (4), 917 (1989).

[4]M. A. Green, K. Emery, Y. Hishikawa, W. Warta, and E. D. Dunlop, PROGRESS IN PHOTOVOLTAICS **22** (1), 1 (2014).

[5]D. H. Layer G. A. Jones, T. G. Osenkowsky, *National Association of Broadcasters Engineering Handbook 10th ed. chapter 1.1*, 10 ed. (Taylor & Francis, 2013).

[6]Viridian Solar UK, *A Guide to Solar Energy* http://www.viridiansolar.co.uk/Solar_Energy_Guide_5_2.htm *accessed on* 14/01/2014.

[7]Hahn-Meitner-Institut Berlin, *Heterogeneous Materials* http://www.helmholtz-berlin.de/zentrum/beispiele-wissenschaft/energie/solarenergie/materialien/index_en.html *accessed on* 14/01/2014.

[8]D. H. Auston and A. M. Glass, IEEE Journal of Quantum Electronics **8** (6), 541 (1972).

[9]D. H. Auston, Applied Physics Letters **26** (3), 101 (1975).

[10]Y. J. Ding, Opt Lett **29** (22), 2650 (2004).

[11]M. Bass, P. A. Franken, J. F. Ward, and G. Weinreich, Physical Review Letters **9** (11), 446 (1962).

[12]X. Yin, D. Abbott, and B. W.H. Ng, *Terahertz Imaging for Biomedical Applications : Pattern Recognition and Tomographic Reconstruction*. (Springer, New York, 2012).

[13]R. M. Woodward, V. P. Wallace, R. J. Pye, B. E. Cole, D. D. Arnone, E. H. Linfield, and M. Pepper, Journal of Investigative Dermatology **120** (1), 72 (2003).

[14]M. Kowalski and M. Kastek, IEEE Transactions on Information Forensics and Security **11** (9), 2028 (2016).

[15]S. May,"*Stealing the heat"* in *Gendercide* (The Economist, 2010), Vol. Technology Quarterly.

[16]D. M. Wu, P. L. Hagelstein, P. Chen, K. P. Sinha, and A. Meulenberg, Journal of Applied Physics **106** (9), 094315 (2009).

[17]R. L. Bailey, Journal of Engineering for Gas Turbines and Power **94** (2), 73 (1972).

[18]S. Hall, I. Z. Mitrovic, N. Sedghi, Y. C. Shen, Y. Huang, and J. F. Ralph, in *Functional Nanomaterials and Devices for Electronics, Sensors and Energy Harvesting*, edited by A. Nazarov et al. (Springer International Publishing, Switzerland, 2014), pp. 241.

[19]G. M. Elchinger, A. Sanchez, C. F. Davis, and A. Javan, Journal of Applied Physics **47** (2), 591 (1976).

[20]M. Sarehraz, PhD thesis, University of South Florida, 2005.

[21]P. C. D. Hobbs, F. R. Libsch, N. C. LaBianca, R. B. Laibowitz, and P. P. Chiniwalla, Optics Express **15** (25), 16376 (2007).

[22]S. Grover, O. Dmitriyeva, G. Moddel, and M. J. Estes, IEEE Transactions on Nanotechnology **9** (6), 716 (2010).

[23]M. Dagenais, K. Choi, F. Yesilkoy, A. N. Chryssis, and M. C. Peckerar,"*Solar spectrum rectification using nano-antennas and tunneling diodes"* in *Optoelectronic Integrated Circuits XII* (Society of Photo-optical Instrumentation Engineers, 2010), Vol. 7605, pp. 76050E.

[24]S. Bhansali, S. Krishnan, E. Stefanakos, and D. Y. Goswami,"*Tunnel Junction based Rectenna-A Key to Ultrahigh Efficiency Solar/Thermal Energy Conversion"* in *AIP Conference Proceedings* (American Institute of Physics, 2010), Vol. 1313, pp. 79.

[25]G. Moddel and S. Grover, *Rectenna solar cells*. (Springer, New York, 2013).

[26]S. Grover and G. Moddel, Solid State Electronics **67** (1), 94 (2012).

[27]M. Feiginov, K. Hidetoshi, S. Safumi, and A. Masahiro, Applied Physics Letters **104** (24), 243509 (2014).

[28]T. C. L. G. Sollner, W. D. Goodhue, P. E. Tannenwald, C. D. Parker, and D. D. Peck, Applied Physics Letters **43** (6), 588 (1983).

[29]F. E. Little, J. O. McSpadden, K. Chang, and N. Kaya, 1998 (unpublished).

[30]L. Fan J.O. McSpadden, K. Chang, IEEE Transactions on Microwave Theory and Techniques, Microwave Theory and Techniques, IEEE Transactions on, IEEE Trans. Microwave Theory Techn. (12), 2053 (1998).

[31]K. Buckle M. Sarehraz, T. Weller, E. Stefanakos, S. Bhansali, Y. Goswami, Subramanian Krishnan,"*Rectenna developments for solar energy collection"* (IEEE, Piscataway, NJ, USA, USA, 2005), p. 78.

[32]W. C. Brown, in *Raytheon Company, Wayland, MA, Tech. Rep. PT-4964, NASA Rep. CR-135194* (1977), p. 66.

[33]P. Koert, J. Cha, and M. Machina, presented at the SPS 91-Power from Space, 1991 (unpublished).

[34]B. J. Zwan, U.S. Patent No. 4,251,679 (1981).

[35]A.M. Marks,"*Device for conversion of light power to electric power"* (Google Patents, 1984).

[36]G. H. Lin, R. Abdu, and J. O'M. Bockris, Journal of Applied Physics **80** (1), 565 (1996).

[37]P. T. Landsberg and G. Tonge, Journal of Physics A: General Physics **12** (4), 551 (1979).

[38]W. C. Brown, presented at the 1976 IEEE-MTT-S International Microwave Symposium, 1976 (unpublished).

[39]M. W. Knight, H. Sobhani, P. Nordlander, and N. J. Halas, Science **332** (6030), 702 (2011).

[40]G. Moddel and S. Grover, *Rectenna Solar Cells, ch. 1*. (Springer New York, 2013).

[41]D. Y. Choi, S. Shrestha, J. J. Park, and S. K. Noh, International Journal of Communication Systems **27** (4), 661 (2014).

[42]G. N. Izmailov, Yu. A. Mityagin, V. N. Murzin, S. A. Savinov, S. S. Shmelev, and E. M. Apostolova, Measurement Techniques **56** (8), 856 (2013).

[43]K. S. Champlin and G. Eisenstein, IEEE Transactions on Microwave Theory and Techniques **26** (1), 31 (1978).

[44]L. E. Dickens, IEEE Transactions on Microwave Theory and Techniques **15** (2), 101 (1967).

[45]H. Kazemi, K. Shinohara, G. Nagy, W. Ha, B. Lail, E. Grossman, G. Zummo, W. R. Folks, J. Alda, and G. Boreman, 2007 (unpublished).

[46]V. Krozer, G. Loata, J. Grajal de la Fuente, and P. Sanz, presented at the Proceedings, IEEE Tenth International Conference on Terahertz Electronics, 2002 (unpublished).

[47]M. Dagenais, K. Choi, F. Yesilkoy, A. N. Chryssis, and M. C. Peckerar, 2010 (unpublished).

[48]N. Sedghi, I. Z. Mitrovic, J. F. Ralph, and S. Hall,"*Zero Bias Resonant Tunnelling Diode for Use in THz Rectenna"* in *18th Workshop on Dielectrics in Microelectronics* (WODIM 2014, Cork, Ireland, 2014).

[49]A. B. Hoofring, V. J. Kapoor, and W. Krawczonek, Journal of Applied Physics **66** (1), 430 (1989).

[50]I. Wilke, Y. Oppliger, W. Herrmann, and F. K. Kneubühl, Applied Physics A **58** (4), 329 (1994).

[51]M. R. Abdel-Rahman, F. J. Gonzalez, and G. D. Boreman, Electronics Letters **40** (2), 116 (2004).

[52]P. Esfandiari, G. Bernstein, P. Fay, W. Porod, B. Rakos, A. Zarandy, B. Berland, L. Boloni, G. Boreman, B. Lail, B. Monacelli, and A. Weeks, 2005 (unpublished).

[53]S. Krishnan, H. La Rosa, E. Stefanakos, S. Bhansali, and K. Buckle, Sensors and Actuators A: Physical **142** (1), 40 (2008).

[54]K. Choi, F. Yesilkoy, A. Chryssis, M. Dagenais, and M. Peckerar, IEEE Electron Device Letters **31** (8), 809 (2010).

[55]J. A. Bean, A. Weeks, and G. D. Boreman, IEEE Journal of Quantum Electronics **47** (1), 126 (2011).

[56]S. Zhang, L. Wang, C. Xu, D. Li, L. Chen, and D. Yang, ECS Solid State Letters **2** (1), 416 (2013).

[57]E. C. Kinzel, R. L. Brown, J. C. Ginn, B. A. Lail, B. A. Slovick, and G. D. Boreman, Microwave and Optical Technology Letters **55** (3), 489 (2013).

[58]Z. Zhu, S. Joshi, S. Grover, and G. Moddel, Journal of Physics D: Applied Physics **46** (18), 185101 (2013).

[59]M. N. Gadalla, A. Shamim, and M. Abdel-Rahman, Scientific Reports **4** (2014).

[60]R. A. Sainati, *CAD of Microstrip Antennas for Wireless Applications*. (Artech House, Inc., 1996), p.255.

[61]M. Hatzakis, Journal of The Electrochemical Society **116** (7), 1033 (1969).

[62]M. Hatzakis, B. J. Canavello, and J. M. Shaw, IBM Journal of Research and Development **24** (4), 452 (1980).

[63]B. J. Eliasson, University of Colorado, 2001.

[64]Riikka L. Puurunen, Journal of Applied Physics **97** (12), 121301 (2005).

[65]S.J. Moss and A. Ledwith, *Chemistry of the Semiconductor Industry*. (Springer Netherlands, 1989).

[66]W.S. Yang and S.W. Kang, Thin Solid Films **500** (1), 231 (2006).

[67]F. M. Wang and N. A. Melosh, Next Generation (Nano) Photonic and Cell Technologies for Solar Energy Conversion Ii **8111** (2011).

[68]F. M. Wang and N. A. Melosh, Nano Lett **11** (12), 5426 (2011).

[69]J. Antson T. Suntola, Patent No. FIN 52359, US 4058430 (priority Nov 29, 1974, publication Nov 15, 1977).

[70]R. L. Puurunen, Chemical Vapor Deposition **20** (10-12), 332 (2014).

[71]K. S. SreeHarsha, *Principles of Vapor Deposition of Thin Films*. (Elsevier Science, Amsterdam, 2006).

[72]Kurt J. Lesker Company, *Material Deposition Chart* https://www.lesker.com/newweb/deposition_materials/materialdepositionchart.cfm?pgid=0 *accessed on* 27/07/2017.

[73]American Lab, *Microscopy for Materials Characterization: Illuminating Structures With Light and Electrons* http://www.americanlaboratory.com/914-Application-Notes/167499-Microscopy-for-Materials-Characterization-Illuminating-Structures-With-Light-and-Electrons/ *accessed on* 28/07/2017.

[74]J. S Rigden, *Macmillan encyclopedia of physics*. (Simon & Schuster Macmillan, New York, 1996).

[75]C. Kisielowski, B. Freitag, M. Bischoff, and et al., Microsc Microanal **14** (5), 469 (2008).

[76]G. R. Brewer, in *Electron-Beam Technology in Microelectronic Fabrication* (Academic Press, 1980), p. 54.

[77]Veeco Instruments Inc. Digital Instruments CP-II User's Guide—Part I: Basic Imaging Techniques, xviii (2004).

[78]A. Rothen, Review of Scientific Instruments **16** (2), 26 (1945).

[79]*Guide to Using WVASE Spectroscopic Ellipsometry Data Acquisition and Analysis Software, ch. 13*. (J.A. Woollam Co., 2008).

[80]LOT-QuantumDesign GmbH, *Short introduction: Ellipsometry* https://lot-qd.de/en/products/spectroscopy/spectroscopic-ellipsometers/product/short-introduction-ellipsometry/ *accessed on*.

[81]R. M. A. Azzam and N. M. Bashara, *Ellipsometry and Polarized Light*, 1st ed. (North-Holland Publishing company, 1977).

[82]J.F. Moulder and J. Chastain, *Handbook of X-ray Photoelectron Spectroscopy: A Reference Book of Standard Spectra for Identification and Interpretation of XPS Data*. (Physical Electronics, 1995).

[83]R. W. Gurney, *Nuclear Levels and Artificial Disintegration*. (1929).

[84]L. Esaki, Physical Review **109** (2), 603 (1958).

[85]L. Esaki, Reviews of Modern Physics **46** (2), 237 (1974).

[86]J. G. Simmons, Journal of Applied Physics **34** (6), 1793 (1963).

[87]R. Holm, Journal of Applied Physics **22** (5), 569 (1951).

[88]R. Stratton, Journal of Physics and Chemistry of Solids **23** (9), 1177 (1962).

[89]N. Sedghi, J. W. Zhang, J. F. Ralph, Y. Huang, I. Z. Mitrovic, and S. Hall, presented at the 2013 Proceedings of the European Solid-State Device Research Conference (ESSDERC), 2013 (unpublished).

[90]R. Tsu and L. Esaki, Applied Physics Letters **22** (11), 562 (1973).

[91]J.S. Chen and M.D. Ker, IEEE Transactions on Electron Devices **56** (8), 1774 (2009).

[92]J. T. Y. Chang and E. J. McCluskey, presented at the Proceedings. 15th IEEE VLSI Test Symposium (Cat. No.97TB100125), 1997 (unpublished).

[93]V. Sedlakova, M. Chvatal, M. Kopecky, and J. Sikula, presented at the 2011 21st International Conference on Noise and Fluctuations, 2011 (unpublished).

[94]J. Bardeen, Physical Review Letters **6** (2), 57 (1961).

[95]W. A. Harrison, Physical Review **123** (1), 85 (1961).

[96]E. Schrödinger, Annalen der Physik **384** (4), 361 (1926).

[97]K. F. Schuegraf, C. C. King, and C. Hu,"*Ultra-thin silicon dioxide leakage current and scaling limit"* in *Dig. 1992 Symp. VLSI* (1992), pp. 18.

[98]S. M. Sze and K. K. Ng, *Physics of semiconductor devices*, 3rd ed. (Wiley-Interscience, Hoboken, N.J., 2007), p.137.

[99]C. Svensson and I. Lundström, Journal of Applied Physics **44** (10), 4657 (1973).

[100]S. A. Mojarad, K. S.K. Kwa, J. P. Goss, Z. Zhou, N. K. Ponon, D. J.R. Appleby, R. A.S. Al-Hamadany, and A. O'Neill, Journal of Applied Physics **111** (1), 014503 (2012).

[101]A. Miller and E. Abrahams, Physical Review **120** (3), 745 (1960).

[102]N. F. S. Mott and E. A. Davis, *Electronic processes in non-crystalline materials*. (Oxford: Clarendon Press, 1971., 1971).

[103]J. R. Jameson, P. B. Griffin, J. D. Plummer, and Y. Nishi, IEEE Transactions on Electron Devices **53** (8), 1858 (2006).

[104]K. B. P. Jinesh, University of Twente, 2010.

[105]R. G. Southwick, A. Sup, A. Jain, and W. B. Knowlton, IEEE Transactions on Device and Materials Reliability **11** (2), 236 (2011).

[106]N. Sedghi, J. F. Ralph, I. Z. Mitrovic, S. Hall, and P. R. Chalker, Applied Physics Letters **102** (9) (2013).

[107]Z. Wang, J. Ralph, N. Sedghi, I. Z. Mitrovic, and S. Hall, Journal of Vacuum Science & Technology B **31** (2) (2013).

[108]J. A. Bean, B. Tiwari, G. H. Bernstein, P. Fay, and W. Porod, Journal of Vacuum Science & Technology B: Microelectronics and Nanometer Structures Processing, Measurement, and Phenomena **27** (1), 11 (2009).

[109]T. J. Bright, J. I. Watjen, Z. M. Zhang, C. Muratore, A. A. Voevodin, D. I. Koukis, D. B. Tanner, and D. J. Arenas, Journal of Applied Physics **114** (8), 083515 (2013).

[110]K. Kukli, M. Ritala, R. Matero, and M. Leskelä, Journal of Crystal Growth **212** (3), 459 (2000).

[111]N. Alimardani, J. M. McGlone, J. F. Wager, and J. F. Conley, Journal of Vacuum Science & Technology A **32** (1) (2013).

[112]T. Gupta, in *Copper Interconnect Technology* (Springer New York, New York, NY, 2009), p. 99.

[113]I. H. Malitson, J. Opt. Soc. Am. **52** (12), 1377 (1962).

[114]R. S. Yan, Q. Zhang, O. A. Kirillov, W. Li, J. Basham, A. Boosalis, X. L. Liang, D. Jena, C. A. Richter, A. C. Seabaugh, D. J. Gundlach, H. L. G. Xing, and N. V. Nguyen, Applied Physics Letters **102** (12) (2013).

[115]I. H. Malitson, J. Opt. Soc. Am. **55** (10), 1205 (1965).

[116]C. Z. Tan, Journal of Non-Crystalline Solids **223** (1), 158 (1998).

[117]S. John, C. Soukoulis, M. H. Cohen, and E. N. Economou, Physical Review Letters **57** (14), 1777 (1986).

[118]C. Li, Y. Dong, Y. C. Shen, and J. A. Zeitler, Journal of Pharmaceutical Sciences **103** (1), 161 (2014).

[119]M. Ohring, in *Materials Science of Thin Films (Second Edition)* (Academic Press, San Diego, 2002), pp. 357.

[120]C. Brox-Nilsen, J. Jin, Y. Luo, P. Bao, and A. M. Song, IEEE Transactions on Electron Devices **60** (10), 3424 (2013).

[121]I. Horcas, R. Fernández, J. M. Gómez-Rodríguez, J. Colchero, J. Gómez-Herrero, and A. M. Baro, Rev Sci Instrum **78** (1), 013705 (2007).

[122]E. W. Cowell, N. Alimardani, C. C. Knutson, J. F. Conley, D. A. Keszler, B. J. Gibbons, and J. F. Wager, Adv Mater **23** (1), 74 (2011).

[123]N. Alimardani, E. W. Cowell Iii, J. F. Wager, J. F. Conley Jr, D. R. Evans, M. Chin, S. J. Kilpatrick, and M. Dubey, Journal of Vacuum Science and Technology A: Vacuum, Surfaces and Films **30** (1) (2012).

[124]P. Sharma, W. Zhang, K. Amiya, H. Kimura, and A. Inoue, Journal of nanoscience and nanotechnology **5** (3), 416 (2005).

[125]S. Parmanand, K. Neelam, K. Hisamichi, S. Yasunori, and I. Akihisa, Nanotechnology **18** (3), 035302 (2007).

[126]M. T. A. Saif, S. Zhang, A. Haque, and K. J. Hsia, Acta Materialia **50**, 2779 (2002).

[127]K. Wefers and C. Misra,"*Oxides and hydroxides of aluminum"* in *Alcoa technical paper, no. 19, rev.* (Alcoa Research Laboratories, 1987).

[128]P. Maraghechi, A. Foroughi-Abari, K. Cadien, and A. Y. Elezzabi, Applied Physics Letters **100** (11), 113503 (2012).

[129]C. J. Smithells, W. F. Gale, and T. C. Totemeier, *Smithells Metals Reference Book*, 8th ed. (Elsevier Butterworth-Heinemann, Amsterdam, 2004), pp.18.

[130]D. A. Buchanan, E. P. Gusev, E. Cartier, H. Okorn-Schmidt, K. Rim, M. A. Gribelyuk, A. Mocuta, A. Ajmera, M. Copel, S. Guha, N. Bojarczuk, A. Callegari, C. D'Emic, P. Kozlowski, K. Chan, R. J. Fleming, P. C. Jamison, J. Brown, and R. Arndt, International Electron Devices Meeting 2000, Technical Digest, 223 (2000).

[131]K. Kukli, M. Ritala, and M. Leskela, Journal of the Electrochemical Society **142** (5), 1670 (1995).

[132]R. H. Fowler and L. Nordheim,"*Electron Emission in Intense Electric Fields"* in *Proceedings of the Royal Society of London* (The Royal Society, 1928), Vol. 119, pp. 173.

[133]Y. Matsumoto, T. Hanajiri, T. Sugano, and T. Toyabe, Japanese Journal of Applied Physics, Part 1: Regular Papers and Short Notes and Review Papers **35** (2 Suppl. B), 1126 (1996).

[134]R. Winston Revie and Herbert Henry Uhlig, *Corrosion and corrosion control : an introduction to corrosion science and engineering*, 4th ed. (Wiley-Interscience, Hoboken, N.J., 2008), p.383.

[135]N. Alimardani, S. W. King, B. L. French, T. Cheng, B. P. Lampert, and J. F. Conley Jr, Journal of Applied Physics **116** (2), 024508 (2014).

[136]S. M. Sze, *Physics of semiconductor devices*. (Wiley-Interscience, 1969), p.496.

[137]W. R. Harrell and J. Frey, Thin Solid Films **352** (1–2), 195 (1999).

[138]A. G. Milnes, in *Deep impurities in semiconductors* (Wiley-Interscience, New York, 1973), pp. 99.

[139]R. A Ongaro and A. A Pillonnet, Revue de Physique Appliquée **24** (12), 1085 (1989).

[140]C. W. Miller, Z. P. Li, I. K. Schuller, and J. Åkerman, Applied Physics Letters **90** (4) (2007).

[141]L. L. Chang, L. Esaki, and R. Tsu, Applied Physics Letters **24** (12), 593 (1974).

[142]E. Rosenbaum and L. F. Register, Ieee Transactions on Electron Devices **44** (2), 317 (1997).

[143]M. Depas, T. Nigam, and M. M. Heyns, Ieee Transactions on Electron Devices **43** (9), 1499 (1996).

[144]M. Lenzlinger and E. H. Snow, Journal of Applied Physics **40** (1), 278 (1969).

[145]G. D. Shen, D. X. Xu, M. Willander, and G. V. Hansson, 1991 Proceedings IEEE/Cornell Conference on Advanced Concepts in High Speed Semiconductor Devices & Circuits, 84 (1991).

[146]G. Papp, M. Di Ventra, C. Coluzza, A. Baldereschi, and G. Margaritondo, Superlattices and Microstructures **17** (3), 273 (1995).

[147]J. Frenkel, Physical Review **54** (8), 647 (1938).

[148]S. M. Sze, Journal of Applied Physics **38** (7), 2951 (1967).

[149]I. Nemr Noureddine, N. Sedghi, I. Z. Mitrovic, and S. Hall, Journal of Vacuum Science and Technology B: Nanotechnology and Microelectronics **35** (1) (2017).

[150]G. S. Oehrlein, Journal of Applied Physics **59** (5), 1587 (1986).

[151]G. H. Parker and C. A. Mead, Applied Physics Letters **14** (1), 21 (1969).

[152]Microposit™ s1800™ series photoresists Data Sheet, 2006.

[153]M. Houssa, M. Tuominen, M. Naili, V. Afanas'ev, A. Stesmans, S. Haukka, and M. M. Heyns, Journal of Applied Physics **87** (12), 8615 (2000).

[154]G. B. Alers, R. M. Fleming, Y. H. Wong, B. Dennis, A. Pinczuk, G. Redinbo, R. Urdahl, E. Ong, and Z. Hasan, Applied Physics Letters **72** (11), 1308 (1998).

[155]J.H. Thomas III, Applied Physics Letters **22** (8), 406 (1973).

[156]I. Kocakarin and K. Yegin, *Glass Superstrate Nanoantennas for Infrared Energy Harvesting Applications*. (2013).

[157]F. P. García de Arquer, V. Volski, N. Verellen, G. Vandenbosch, and V. Moshchalkov, *Engineering the Input Impedance of Optical Nano Dipole Antennas: Materials, Geometry and Excitation Effect*. (2011), pp.3144.